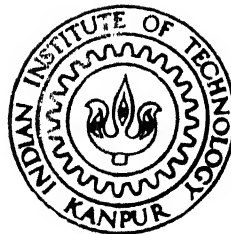


# MICROSTRUCTURAL AND TEXTURAL CHANGES DURING COLD ROLLING AND ANNEALING OF A $\text{Ni}_3\text{Al}(\text{B},\text{Zr})$ ALLOY

by  
BASUDEV BHATTACHARYA



Department of Materials and Metallurgical Engineering

**INDIAN INSTITUTE OF TECHNOLOGY KANPUR**

DECEMBER, 1996

TH  
MME / 1996 / 15

1408469 m

1996

D

BHA

MIC

# MICROSTRUCTURAL AND TEXTURAL CHANGES DURING COLD ROLLING AND ANNEALING OF A $\text{Ni}_3\text{Al}(\text{B},\text{Zr})$ ALLOY

by  
BASUDEV BHATTACHARYA



Department of Materials and Metallurgical Engineering

**INDIAN INSTITUTE OF TECHNOLOGY KANPUR**

DECEMBER, 1996

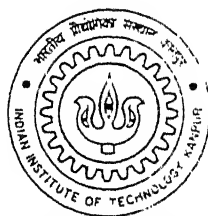


---

MICROSTRUCTURAL AND TEXTURAL  
CHANGES  
DURING COLD ROLLING AND ANNEALING  
OF A  $\text{Ni}_3\text{Al}(\text{B}, \text{Zr})$  ALLOY

A Thesis Submitted  
in Partial Fulfilment of the Requirements  
for the Degree of  
DOCTOR OF PHILOSOPHY

by  
BASUDEV BHATTACHARYA



Department of Materials and Metallurgical Engineering  
Indian Institute of Technology, Kanpur

December, 1996

11 JUL 1997/Management Eng.

CENTRAL LIBRARY  
I. I. T., KANPUR

No. A 423608

MME-1996-D-BAS-MIC

# Certificate



It is certified that the work contained in the thesis entitled **Microstructural and Textural Changes During Cold Rolling and Annealing of a  $\text{Ni}_3\text{Al(B.Zr)}$  Alloy**, has been carried out by Basudev Bhattacharya (*Roll No. 9220661*) under my supervision and that this work has not been submitted elsewhere for a degree.

18.12.1996

(Professor R.K. Ray)

Department of Materials and Metallurgical  
Engineering  
Indian Institute of Technology  
Kanpur - 208016

---

*To my departed Father  
who left long before I started  
my academic career*

and

*To my Mother  
and my two elder sisters  
who have always been  
an endless source of  
encouragement and love*

# Acknowledgements

I express my sincere gratitude to my thesis supervisor **Prof. R.K. Ray** for his excellent, careful and encouraging guidance throughout the present work. As a student, I not only acknowledge his immense help and appropriate suggestions. I also admire his outstanding capability of guiding a research problem in proper direction which I have felt at each and every step of my Ph.D. work.

I acknowledge the contribution of Dr. V.K. Sikka, *Group Leader, Oak Ridge National Laboratory, USA*, for providing a piece of continuous cast  $\text{Ni}_3\text{Al(B.Zr)}$  sheet on which the present work has been carried out. I am also grateful to Prof. G. Gottstein, *Director of Institut für Allgemeine Metallkunde und Metallphysik, RWTH, Aachen, Germany*, for his help during the texture measurements for this work. My thanks are also due to Prof. A. Ghosh, *IIT Kanpur*, who allowed me to use a transformer of his laboratory for doing the necessary heat treatments.

Among the laboratory staff members, my sincere thanks are due to Mr. A. Biswas (*Engineering Metallurgy Lab*), Mr. K.P. Mukherjee (*Physical Metallurgy Lab*), Mr. U.S. Singh (*X-ray Lab*), Mr. P.K. Pal (*SEM Lab*), Mr. C. Bharthwal (*TEM Lab*) and Mr. B.K. Jain (*Material Testing Lab*) for their various helps. I am also thankful to Mr. H.C. Srivastava (*Heat Treatment Lab*) who assisted me in carrying out the experimental part. Special thanks are due to Mr. Sadgopan (*Graphic Arts*) who helped me at a crucial stage while taking the print out of the thesis.

Among my friends, I am grateful to S. Ghosh Chowdhury for his valuable help during my work. My thanks are also due to N.K. Nath, T.K. Roy, G.G. Roy, S. Suwas, A. Saha, M. Sujata, and S. Ghosh, for not only their help and assistance at various situations, it is mainly because they made my stay at IIT Kanpur a memorable pleasure. My thanks are due to Santanu and Bikas who gave me valuable assistance during my work. Among the

---

others. I am thankful to Sanjib, Kallol, Sudarshan, Bivash, Arindam, Pradyot and Pallab who all made a wonderful and friendly neighbouring atmosphere during my stay period at H207, Hall-5, IIT Kanpur.

Finally, at the mature stage of my student life, I most gratefully acknowledge the Herculean task carried out by my Mother for my proper bringing up and providing an excellent opportunity for my higher study, against all the odds, without which I would have not been able to come upto this stage. I also acknowledge the contribution of my two elder sisters who, along with my mother, always inspired me for study and actively built a steady platform for giving me a well secured academic career.

**Basudev Bhattacharya**

9220661

# ● *Contents*

List of Figures	IV
List of Tables	XVII
Synopsis	XIX
Chapter 1 Introduction	1
Chapter 2 Literature	7
2.1 Ni <sub>3</sub> Al Intermetallic Compound	9
2.2 Unit Cell and Crystal Structure of Ni <sub>3</sub> Al	11
2.3 Ordering Behaviour of Ni <sub>3</sub> Al	11
2.4 Defects in Ni <sub>3</sub> Al : Dislocations and Planar Faults	25
2.5 Deformation Modes in Ni <sub>3</sub> Al	32
2.6 Mechanical Properties	33
2.6.1 Effect of Grain Size, Temperature and Alloy Addition	35
2.6.2 Yield Stress anomaly	38
2.6.3 Ductility of Ni <sub>3</sub> Al and its Improvement	48
2.7 Diffusion in Ni <sub>3</sub> Al	57
2.8 Annealing of Cold Worked Ni <sub>3</sub> Al : Recovery and Recrystallization	60
2.9 Development of Texture During Processing	67
2.9.1 Deformation Texture in FCC Metals	67
2.9.2 Cold Rolling Texture in Ni <sub>3</sub> Al	68
2.9.3 Annealing Texture of FCC Materials	70
2.9.4 Annealing Texture of Ni <sub>3</sub> Al	70
2.10 Two Phase Ni <sub>3</sub> Al Alloys	71
2.11 Scope of the Present Work	73
Chapter 3 Experimental	77

3.1 Alloy Preparation	78
3.2 Cold Rolling	78
3.3 Annealing	79
3.3.1 Isochronal Annealing	79
3.3.2 Isothermal Annealing	79
3.4 Microstructural Characterization	80
3.4.1 Optical Microscopy	80
3.4.2 Scanning Electron Microscopy (SEM)	80
3.4.3 Transmission Electron Microscopy (TEM)	81
3.5 Microhardness Measurements	81
3.6 X-ray Diffraction Study	82
3.6.1 Long Range Order Parameter (S)	83
3.6.2 Strain Parameter	83
3.7 Measurement and Representation of Texture	84
3.8 Differential Scanning Calorimetry (DSC)	90
Chapter 4 Deformation Behaviour	91
4.1 Microstructure	92
4.1.1 Starting Material	92
4.1.2 Cold Rolled Material	95
4.1.2.1 Optical and Scanning Electron Micrographs	95
4.1.2.2 Transmission Electron Micrographs	101
4.2 X-ray Diffraction Analysis	118
4.2.1 X-ray Line Profiles	118
4.2.1.1 Starting Material	118
4.2.1.2 Cold Rolled Material	121
4.2.2 Order Parameter	123
4.2.3 Strain Parameter and Microhardness	129
4.3 Cold Rolling Texture	129
4.4 Discussion of Deformation Results	147
4.4.1 Changes in Order and Structure of $\text{Ni}_3\text{Al}$ with Rolling	147
4.4.2 Textural Changes	158



<b>Chapter 5 Annealing Behaviour</b>	<b>168</b>
<b>5.1 Isochronal Annealing</b>	<b>169</b>
5.1.1 Optical Microstructures	169
5.1.2 XRD Line Profiles	173
5.1.3 Order Parameter (S)	173
5.1.4 Strain Parameter and Microhardness	173
<b>5.2 Isothermal Annealing</b>	<b>178</b>
5.2.1 Optical and SEM Microstructures	178
5.2.2 XRD Line Profiles	187
5.2.3 Order Parameter (S)	187
5.2.4 Strain Parameter and Microhardness	197
<b>5.3 TEM Microstructures</b>	<b>197</b>
<b>5.4 Recrystallization Kinetics</b>	<b>229</b>
5.4.1 Analysis of Recrystallized Volume Fraction Data	229
5.4.2 Analysis of Differential Scanning Calorimetry (DSC) Data	235
<b>5.5 Textural Changes During Annealing</b>	<b>239</b>
<b>5.6 Discussion of Annealing Results</b>	<b>253</b>
5.6.1 Recovery and Reordering	253
5.6.2 Recrystallization and Precipitation	255
5.6.3 Mechanism of Recrystallization and Precipitation	258
5.6.4 Discontinuous Reactions	259
5.6.5 Recrystallization Kinetics	264
5.6.6 Textural Changes	266
<b>Chapter 6 Conclusions</b>	<b>268</b>
<b>References</b>	<b>272</b>

# ● *List of Figures*

No.	Figure Caption	Page
<b>Chapter 1</b>		
1.1	Yield strength versus test temperature for Ni <sub>3</sub> Al alloys, two superalloys and type 316 stainless steel [3]	5
<b>Chapter 2</b>		
2.1	Aluminium - Nickel binary phase diagram [6]	10
2.2	Unit cell of Ni <sub>3</sub> Al (L1 <sub>2</sub> crystal structure)	12
2.3	Schematic diagram of a BCC superlattice composed of two simple cubic sub-lattices	13
2.4	Variation of long range order parameter with temperature	13
2.5	Long range order parameter S as a function of temperature for stoichiometric Ni <sub>3</sub> Al (with and without boron addition) [16]	16
2.6	XRD intensity profiles of the hypostoichiometric boron doped Ni <sub>3</sub> Al alloy when subjected to anneals at 1000° and 1200°C [16]; (a) (100) and (110) superlattice reflections, (b) (111), (200) and (220) fundamental reflections	17
2.7	Structural relationship between L1 <sub>2</sub> and L1 <sub>2</sub> - derivative superlattice structures [17]; (a) L1 <sub>2</sub> , (b) DO <sub>22</sub> , (c) DO <sub>23</sub> and (d) DO <sub>22</sub> structure with an APB on (001)	18
2.8	The long range order parameter of cold worked Ni <sub>3</sub> Al as a function of annealing time [19]	20
2.9	XRD line profiles of Ni <sub>3</sub> Al powders with milling time [21]	21

2.10	Variation of long range order parameter as a function of milling time on the basis of (110) and (200) reflections [22]	22
2.11	Variation of long range order parameter as a function of rolling deformation of $\text{Ni}_3\text{Al(B)}$ [25]	23
2.12	Variation of long range order parameter as a function of rolling strain of $\text{C}_3\text{Au}$ [26]	24
2.13	Slip system and APB in $\text{L1}_2$ structure: (a) (111) plane and $\langle 111 \rangle$ directions in $\text{L1}_2$ (FCC) structure. (b) (010) plane of $\text{L1}_2$ structure. (c) a $\frac{1}{2}[\bar{1}01]$ dislocation on (111) plane, producing an APB, and (d) two $\frac{1}{2}[\bar{1}01]$ dislocations on (111) plane separated by an APB	26
2.14	The atomic arrangement and the nature of planar faults on the (111) plane in an $\text{A}_3\text{B}$ compound with $\text{L1}_2$ structure and stacking sequence ...abc/abc.... Large, medium and small circles represent atoms on a, b and c layers, respectively [29]	28
2.15	Intrinsic ( $\text{DO}_{19}$ ) and extrinsic ( $\text{DO}_{24}$ ) faults associated with a Frank sessile in the $\text{L1}_2$ structure [30]	30
2.16	Atomic arrangement and possible dissociation schemes for $[\bar{1}10]$ dislocation on (111) in the $\text{L1}_2$ structure: (a) types of dissociation. (b) six-fold. (c) four-fold. (d) two-fold (APB splitting) and (e) two-fold (SISF splitting) [38-40]	31
2.17	XRD line profiles of $\text{Ni}_3\text{Al(B)}$ at different degrees of cold rolling [25]	34
2.18	Yield strength versus temperature for stoichiometric $\text{Ni}_3\text{Al}$ of three different grain sizes [54]	36
2.19	Hardness versus (grain size) $^{-0.5}$ for $\text{Ni}_3\text{Al}$ and $\text{Ni}_3\text{Al+B}$ [54]	36
2.20	Yield strength versus (grain size) $^{-0.8}$ for $\text{Ni}_3\text{Al}$ at room temperature [55]	37
2.21	Changes in yield stress with temperature for boron - doped $\text{Ni}_3\text{Al}$ of different grain sizes [56]	37
2.22	Temperature dependence of 0.2% flow stress in $\text{Ni}_3\text{Al}$ : (a) with addition of Sn [59], (b) with addition of Hf [60]	39
2.23	Relation between 0.2% flow stress measured at 77K and the solute concentration in ternary $\text{Ni}_3\text{Al}$ : (a) with addition of B-subgroup elements [59], (b) with addition of transition elements [60]	40
2.24	Temperature dependence of the 0.2% flow stress of (a) the $\text{Ni}_3\text{Al}$ alloys and (b) the $\text{Ni}_3\text{Ga}$ alloys [14]	41

2.25a	Effect of alloying additions upon the temperature dependence of the flow stress of $\gamma'$ [48]	43
2.25b	Microstrain yield stress as a function of temperature in $\text{Ni}_3\text{Al}$ [48]	43
2.26	The axial 0.2% flow stress as a function of temperature for five orientations of $\text{Ni}_3(\text{Al},\text{Nb})$ single crystals [64]	44
2.27	Schematic representation of cross slip of a screw dislocation pair from the slip plane into a cube plane [66]	46
2.28	Illustration of the cross slip pinning showing the successive positions of a superlattice screw dislocation on $\{111\}$ by the <i>dynamical breakaway</i> from pinning points on $\{010\}$ ; $b$ is the Burgers vector [68]	46
2.29a	The oval shaped core configuration of the $\frac{1}{2}[\bar{1}01]$ superpartial [69]	47
2.29b	A schematic view of the partial cross slip of one superpartial from the $(111)$ to the $(010)$ plane [69]	47
2.30	Comparison of tensile ductility of IC145 ( $\text{Ni}-21.5\text{Al}-0.5\text{Hf}-0.1\text{B}$ at.%) rested in vacuum and air [73]	49
2.31	Temperature dependence of the percentage elongation of a $\text{Ni}_3\text{Al}$ base alloy with 8 wt.% Cr [74]	49
2.32a	Typical tensile shear stress - shear strain curve of $\text{Ni}_3\text{Al}$ single crystal at room temperature [71]	51
2.32b	Tensile and compressive stress - strain curves of homogenized stoichiometric $\text{Ni}_3\text{Al}$ polycrystal at room temperature [71]	51
2.33a	Plot of room temperature tensile properties as a function of boron concentration for $\text{Ni}_3\text{Al}$ (24 at.% Al) [2]	53
2.33b	Plot of room temperature tensile properties as a function of aluminium concentration [2]	54
2.34	Temperature dependence of $D_{\text{Ni}}^*$ in pure $\text{Ni}_3\text{Al}$ [99]	59
2.35	Time for 50% recrystallized volume fraction of 50% cold rolled $(\text{Co}_{78}\text{Fe}_{22})_3\text{V}$ annealed above and below $T_c$ [108]	63
2.36	The fraction recrystallized versus annealing time for 90% cold rolled $\text{Cu}_3\text{Au}$ [112]	63
2.37a	Arrhenius plots showing temperature dependence of the time for 50% recovery and recrystallization [112]	64

2.37b	Schematic Arrhenius plots of migration rates for grain boundaries in the ordered and disordered states [112]	64
2.38	Hardness of cold deformed $\text{Ni}_3\text{Al}$ as a function of annealing time at various temperatures. Arrows denote the starting of recrystallization [23]	65
2.39	Standard $\{111\}$ pole figures showing (a) copper type texture and (b) $\alpha$ -brass type texture [121]	69
2.40	Texture of cold rolled $\text{Ni}_3\text{Al(B)}$ after annealing at $950^\circ\text{C}$ for 1hr [119]; (a) $\{111\}$ pole figure. (b) corresponding ODF	72
2.41	Solid solution strengthening of $\text{Ni}_3\text{Al}$ by the addition of Zr [60]	74
2.42	Microhardness versus temperature for isochronal annealing of 85% cold rolled (a) IC15 and (b) IC50 [127]	75

## Chapter 3

3.1	Schematic representation of three Euler angles $\phi_1, \phi, \phi_2$ ; (a) sample frame $S$ and crystallite frame $C$ . (b) Transformation of sample frame into crystallite frame [131]	86
3.2	Schematic presentation of Euler space [131]	87
3.3	Schematic presentation of the FCC rolling texture in the first subspace of three dimensional Euler angle space [138]	88
3.4	Main FCC rolling texture components schematically shown in two dimensional $\phi_2$ sections of Euler space [138]	89

## Chapter 4

4.1a	Optical micrograph of cast $\text{Ni}_3\text{Al(B,Zr)}$ (flat sheet surface)	93
4.1b	Optical micrograph of cast $\text{Ni}_3\text{Al(B,Zr)}$ (longitudinal surface)	93
4.2a	Optical micrograph of homogenized $\text{Ni}_3\text{Al(B,Zr)}$ alloy (sheet plane)	94
4.2b	Optical micrograph of homogenized $\text{Ni}_3\text{Al(B,Zr)}$ alloy (longitudinal plane)	94
4.3	SAD pattern taken from the thin foil of homogenized alloy shows superlattice spots along with the fundamental spots	96

4.4a Optical micrograph of 15% cold rolled material	97
4.4b Optical micrograph of 25% cold rolled material	97
4.4c Optical micrograph of 35% cold rolled material	98
4.4d Optical micrograph of 45% cold rolled material	98
4.4e Optical micrograph of 45% cold rolled material (at lower magnification)	99
4.4f Optical micrograph of 55% cold rolled material	99
4.4g Optical micrograph of 65% cold rolled material	100
4.4h Optical micrograph of 73% cold rolled material	100
4.5a SEM micrograph of homogenized material	102
4.5b SEM micrograph of 45% rolled material	102
4.5c SEM micrograph of 65% rolled material	103
4.5d SEM micrograph of 73% rolled material	103
4.6a TEM micrograph of 35% rolled material	104
4.6b SAD pattern of the thin foil area shown in Figure 4.6a	105
4.6c Indexing of the SAD pattern shown in Figure 4.6b	105
4.7a TEM micrograph of the 35% rolled material showing the twin bands	106
4.7b Twin bands in the same material as shown above	106
4.8a TEM micrograph of 45% rolled material	107
4.8b Corresponding SAD pattern of the above area indicating ordered $L1_2$ structure	107
4.9a Microbands in thin foil of 45% rolled material	108
4.9b Twin bands in thin foil of 45% rolled material	108
4.9c Shear bands in thin foil of 45% rolled material	109

4.10a	Twin bands in thin foil of 65% rolled material	111
4.10b	Twin bands in thin foil of 73% rolled material	111
4.10c	SAD pattern of the area shown in Figure 4.10b	112
4.10d	Indexing of the SAD pattern shown in Figure 4.10c	112
4.11a	Cellular substructure in thin foil of 73% rolled material	113
4.11b	Corresponding SAD pattern of the area shown above	113
4.12a	TEM micrograph of 65% rolled material showing a combination of twinned and untwinned regions	114
4.12b	SAD pattern taken from the region <i>A</i> in Figure 4.12a	115
4.12c	SAD pattern taken from the region <i>B</i> in Figure 4.12a	115
4.13a	TEM micrograph of 35% rolled material	116
4.13b	SAD pattern of the area shown in Figure 4.13a	117
4.13c	Indexing of the SAD pattern shown in Figure 4.13b	117
4.14	X-ray diffraction profiles of the initial material in different conditions	119
4.15	A few selected peaks from the X-ray line profiles of the homogenized alloy	120
4.16	X-ray diffraction profiles of the $\text{Ni}_3\text{Al}(\text{B.Zr})$ alloy rolled at different strain levels	122
4.17	XRD line profiles at different degrees of cold reduction showing (100) and (200) reflections	124
4.18	XRD line profiles at different degrees of cold reduction showing (110) and (220) reflections	125
4.19	Scheme for determination of the integrated intensity of a $\gamma'$ XRD peak: (a) an isolated peak, (b) determination of $2A$ from $\gamma/\gamma'$ combination	127
4.20	Variation of order parameter as a function of rolling deformation	128
4.21	Variation of strain parameter as a function of rolling deformation	130
4.22	Variation of microhardness as a function of rolling deformation	131

4.23a {111} pole figure of the homogenized material	132
4.23b Corresponding ODF of the homogenized material	132
4.24a {111} pole figure of the 25% rolled material	134
4.24b {111} pole figure of the 35% rolled material	134
4.24c {111} pole figure of the 45% rolled material	135
4.24d {111} pole figure of the 55% rolled material	135
4.24e {111} pole figure of the 65% rolled material	136
4.24f {111} pole figure of the 73% rolled material	136
4.25a ODF of 25% rolled material	137
4.25b ODF of 35% rolled material	137
4.25c ODF of 45% rolled material	138
4.25d ODF of 55% rolled material	138
4.25e ODF of 65% rolled material	139
4.25f ODF of 73% rolled material	139
4.26 $\beta$ -fibre (maximum intensity) plots of cold rolled $\text{Ni}_3\text{Al}(\text{B},\text{Zr})$	143
4.27 $\beta$ -fibre orientation plots of cold rolled $\text{Ni}_3\text{Al}(\text{B},\text{Zr})$	144
4.28 $\alpha$ -fibre plots of cold rolled $\text{Ni}_3\text{Al}(\text{B},\text{Zr})$	145
4.29 $\tau$ -fibre plots of cold rolled $\text{Ni}_3\text{Al}(\text{B},\text{Zr})$	146
4.30 $\text{DO}_{22}$ (ordered tetragonal) structure of $\text{Ni}_3\text{Al}$	150
4.31 Comparison of the XRD profiles of the two homogenized alloys, $\text{Ni}_3\text{Al}(\text{B})$ [25] and $\text{Ni}_3\text{Al}(\text{B},\text{Zr})$	153
4.32 XRD line profiles of 35%, 45% and 55% cold rolled materials	155
4.33a Twin bands in thin foil of 73% cold rolled material	156



4.33b	SAD pattern of the area shown in Figure 4.33a	157
4.33c	Indexing of the SAD pattern indicates a tetragonal structure	157
4.34	$\beta$ -fibre plots of pure Ni at different levels of cold rolling [150]	161
4.35	$\beta$ -fibre plots of single phase $\text{Ni}_3\text{Al(B)}$ at different levels of cold rolling [50]	162
4.36	TEM micrograph of 73% rolled $\text{Ni}_3\text{Al(B,Zr)}$ shows high density of twin bands nearby the $\gamma$ regions	164

## Chapter 5

5.1a	Optical micrograph after isochronal annealing at 700°C	170
5.1b	Optical micrograph after isochronal annealing at 800°C	170
5.1c	Optical micrograph after isochronal annealing at 900°C	171
5.1d	Optical micrograph after isochronal annealing at 1000°C	171
5.1e	Optical micrograph after isochronal annealing at 1100°C	172
5.1f	Optical micrograph after isochronal annealing at 1200°C	172
5.2	XRD line profiles of isochronally annealed samples	174
5.3	XRD line profiles of a few selected isochronally annealed samples ( <i>recorded at a slower scanning speed</i> )	175
5.4	Variation of order parameter (S) with isochronal annealing	176
5.5	Variation of strain parameter with isochronal annealing	177
5.6	Variation of microhardness with isochronal annealing	177
5.7	Optical micrograph after annealing at 700°C for 16 hr	179
5.8a	Microstructure after annealing at 900°C for 5 min	180
5.8b	Microstructure after annealing at 900°C for 1.5 hr	180
5.8c	Microstructure after annealing at 900°C for 5 hr	181

5.8d Microstructure after annealing at 900°C for 15 hr	181
5.9a Recrystallized microstructure after annealing at 1000°C for 10 hr	182
5.9b Recrystallized microstructure after annealing at 1200°C for 1.5 hr	182
5.10a SEM micrograph after annealing at 1100°C for 5 min	184
5.10b SEM micrograph after annealing at 1100°C for 10 min	184
5.10c SEM micrograph after annealing at 1100°C for 20 min	185
5.10d SEM micrograph after annealing at 1100°C for 30 min	185
5.10e SEM micrograph after annealing at 1100°C for 1 hr	186
5.10f SEM micrograph after annealing at 1100°C for 2 hr	186
5.11a XRD line profiles of isothermally annealed samples at 800°C	188
5.11b XRD line profiles of isothermally annealed samples at 900°C	189
5.11c XRD line profiles of isothermally annealed samples at 1000°C	190
5.11d XRD line profiles of isothermally annealed samples at 1100°C	191
5.11e XRD line profiles of isothermally annealed samples at 1200°C	192
5.12a A few selected XRD peaks after annealing at 800°C	193
5.12b A few selected XRD peaks after annealing at 1000°C	194
5.13a Variation of order parameter (S) with isothermal annealing at 800°C	195
5.13b Variation of order parameter (S) with isothermal annealing at 900°C	195
5.13c Variation of order parameter (S) with isothermal annealing at 1000°C	195
5.13d Variation of order parameter (S) with isothermal annealing at 1100°C	196
5.13e Variation of order parameter (S) with isothermal annealing at 1200°C	196
5.14 Variation of strain parameter with isothermal annealing at five temperatures	198

5.15	Variation of microhardness with isothermal annealing at five temperatures ( <i>The error bars are omitted in order to maintain the clarity of the diagram</i> )	199
5.16a	TEM micrograph showing a partly recovered area after annealing at 700°C for 16 hr	201
5.16b	Corresponding SAD pattern of the area shown in Figure 5.16a	201
5.17a	Recovery after annealing at 700°C for 16 hr	202
5.17b	Formation of subgrain after annealing at 700°C for 16 hr	202
5.18a	Retained twin bands after annealing at 700°C for 16 hr	203
5.18b	Retained twin bands after annealing at 700°C for 16 hr	203
5.19a	TEM micrograph showing diffuse twin bands after annealing at 700°C for 16 hr	204
5.19b	Partly recovered area showing the disappearance of fine twin bands after annealing at 700°C for 16 hr	204
5.20a	Cellular precipitation in the recrystallized subgrains ( <i>annealed at 700°C for 16 hr</i> )	205
5.20b	Cluster of subgrains with cellular precipitates near the cold worked regions ( <i>annealed at 700°C for 16 hr</i> )	205
5.20c	SAD pattern of the cold worked region in Figure 5.20b	206
5.20d	SAD pattern of the cluster of subgrains in Figure 5.20b	206
5.21a	A recrystallized subgrain with cellular precipitates inside ( <i>annealed at 700°C for 16 hr</i> )	207
5.21b	A cluster of subgrains with cellular precipitates ( <i>annealed at 700°C for 16 hr</i> )	207
5.21c	A subgrain with cellular precipitates grows by consuming the highly deformed matrix ( <i>annealed at 700°C for 16 hr</i> )	208
5.22a	A recrystallized grain containing cellular precipitates advancing into a cluster of small cells and subgrains ( <i>annealed at 700°C for 16 hr</i> )	208
5.22b	SAD pattern of the recrystallized grain in Figure 5.22a	209
5.22c	SAD pattern of the cluster of subgrains and cells in Figure 5.22a	209

5.23a	Interface between a growing recrystallized grain and deformed matrix ( <i>annealed at 800°C for 30 min</i> )	211
5.23b	Isolated dislocations and precipitate particles along the interface between a recrystallized grain and cold worked region ( <i>annealed at 800°C for 1 hr</i> )	211
5.24	Morphology of the discontinuous precipitation inside a recrystallized grain ( <i>annealed at 800°C for 1 hr</i> )	212
5.25a	Two recrystallized grains and the adjacent deformed region ( <i>annealed at 800°C for 30 min</i> )	213
5.25b	SAD pattern of the deformed region in Figure 5.25a	213
5.25c	SAD pattern of the grain A in Figure 5.25a	214
5.25d	SAD pattern of the grain B in Figure 5.25a	214
5.26	A partially recrystallized region after annealing at 900°C for 5 min	215
5.27a	A small recrystallized grain with a rod-like feature inside ( <i>annealed at 900°C for 5 min</i> )	216
5.27b	Recrystallized grains with fine striations ( <i>annealed at 900°C for 5 min</i> )	216
5.28a	A recrystallized grain adjacent to the deformed matrix ( <i>annealed at 900°C for 5 min</i> )	218
5.28b	SAD pattern of the recrystallized grain in Figure 5.28a	218
5.29a	Dislocations within a recrystallized grain ( <i>annealed at 900°C for 5 min</i> )	219
5.29b	Precipitations within a few recrystallized grains ( <i>annealed at 900°C for 5 min</i> )	219
5.30a	A cluster of recrystallized grains ( <i>annealed at 1000°C for 2 min</i> )	220
5.30b	Growth of the newly formed grains ( <i>annealed at 1000°C for 2 min</i> )	220
5.30c	SAD pattern of the grain at the centre in Figure 5.30b	221
5.30d	Faults within the recrystallized grains ( <i>annealed at 1000°C for 2 min</i> )	221
5.31a	Parallel dislocation lines within recrystallized grain ( <i>annealed at 1000°C for 2 min</i> )	222
5.31b	A partly recrystallized region after annealing at 1000°C for 2 min	222

5.32	A recrystallized grain with high density of globular precipitates inside ( <i>annealed at 1000°C for 2 min</i> )	223
5.33a	A grain with precipitates inside ( <i>annealed at 1000°C for 2 min</i> )	224
5.33b	SAD pattern of the grain in Figure 5.33a	224
5.34	Moiré fringe like features developed during recovery ( <i>annealed at 1000°C for 2 min</i> )	225
5.35a	Parallel bands of $\gamma$ regions ( <i>annealed at 1000°C for 2 min</i> )	226
5.35b	SAD pattern of the thin foil area shown in Figure 5.35a	226
5.36a	A cluster of $\gamma$ subgrains ( <i>annealed at 1000°C for 2 min</i> )	227
5.36b	Magnified image of the subgrain <i>A</i> in Figure 5.35a	227
5.36c	Magnified image of the boundary <i>B</i> in Figure 5.35a	228
5.36d	Magnified image of the feature <i>C</i> in Figure 5.35a	228
5.37	Plots of recrystallized volume fraction with annealing time at five annealing temperatures	231
5.38	Plots of $\ln\{\ln[1/(1-X)]\}$ versus $\ln t$ at five annealing temperatures when $X$ is the recrystallized volume fraction and $t$ is the annealing time	232
5.39	Variation of $n$ ( <i>Avrami exponent</i> ) with temperature	234
5.40	$\ln k$ versus $1/T$ plots for the determination of activation energy	234
5.41	DSC thermograms of 73% cold rolled material at the two heating rates 30°C/min and 10°C/min	237
5.42	DSC thermograms of all the cold rolled samples at a fixed heating rate 20°C/min	238
5.43a	{111} pole figure after annealing at 900°C for 4 min	241
5.43b	{111} pole figure after annealing at 900°C for 10 min	241
5.43c	{111} pole figure after annealing at 900°C for 1 hr	241
5.43d	{111} pole figure after annealing at 900°C for 3 hr	242

5.43e {111} pole figure after annealing at 900°C for 10 hr	242
5.43f {111} pole figure after annealing at 900°C for 15 hr	243
5.43g {111} pole figure after annealing at 900°C for 25 hr	243
5.44a ODF after annealing at 900°C for 4 min	244
5.44b ODF after annealing at 900°C for 10 min	245
5.44c ODF after annealing at 900°C for 1 hr	245
5.44d ODF after annealing at 900°C for 3 hr	246
5.44e ODF after annealing at 900°C for 10 hr	246
5.44f ODF after annealing at 900°C for 15 hr	247
5.44g ODF after annealing at 900°C for 25 hr	247
5.45 $\beta$ -fibre plots of the annealed samples	248
5.46 $\alpha$ -fibre plots of the annealed samples	250
5.47 $\tau$ -fibre plots of the annealed samples	251
5.48a Cube RD-rotation plots of the annealed samples	252
5.48b Cube TD-rotation plots of the annealed samples	252
5.49 Schematic representation of the <i>pucker mechanism</i> of lamellar precipitation [156]	256
5.50 Schematic diagram showing the interaction between recrystallization and precipitation as a function of the temperature of annealing [159]	261

## ● *List of Tables*

No.	Table Caption	Page
<b>Chapter 2</b>		
2.1	Properties of nickel, iron and titanium aluminides	9
2.2	Fault energies in $\text{Ni}_3\text{Al}$ ( $\text{mJ}/\text{m}^2$ )	29
2.3	Mechanical properties of $\text{Ni}_3\text{Al}$	33
2.4	Tensile properties of $\text{Ni}_3\text{Al}$	35
2.5	Activation energies and frequency factors of diffusion of Ni and Al in $\text{Ni}_3\text{Al}$	58
2.6	Parameters of the recrystallization kinetics of $\text{Ni}_3\text{Al}$	67
<b>Chapter 4</b>		
4.1	Compositions of the two phases (atomic percent)	92
4.2	Peak positions and lattice parameters of $\gamma'$ and $\gamma$ phases	121
4.3	Theoretical relative intensities of the XRD lines of $\text{L}_{12}$ , $\text{DO}_{22}$ and $\gamma$ phases	152
4.4	X-ray intensities of the different lines for 45% cold rolled sample	154

## Chapter 5

5.1 Chemical composition of different phases during isothermal annealing (at. %)	183
5.2 $n$ values determined for all temperatures	233
5.3 Calculated $\ln k$ values at different temperatures	233
5.4 Activation energy ( $Q$ ) values at different stages	235
5.5 Recrystallized volume fraction with annealing time at 900°C	249



## ● *Synopsis*

The ordered intermetallic compounds constitute the major strengthening phases in Ni and Co-base superalloys. Since many of these intermetallic compounds maintain long range ordered structures almost upto their melting points, they impart significant high temperature strengthening effect to the matrix materials. For the last few decades, superalloys have been developed and used successfully in gas turbines, aircraft engines, diesel engines, turbochargers etc. which normally operate at high temperatures (700° - 1200°C) and under severe atmospheric conditions. Attempts have been going on for the last few years to develop the intermetallic compounds themselves as high temperature structural materials and these have resulted in the successful production and specialized application of a number of such materials.

Among the various intermetallic materials, the aluminide family, primarily represented by the trinickel aluminide,  $\text{Ni}_3\text{Al}$ , has shown an excellent promise because of its high temperature strength and resistance against hot corrosion and oxidation etc. However, poor polycrystalline ductility was found to be an inherent drawback of this material. This difficulty has now been tackled by boron-addition, and it has been observed that micro-alloying with boron enhances the room temperature polycrystalline ductility of slightly hypostoichiometric  $\text{Ni}_3\text{Al}$  to a great extent.

Ternary additions of several elements such as Hf, Cr, Fe, Cu, Zr, Ti, W, Co etc. in  $\text{Ni}_3\text{Al}$  have also been found to produce remarkable improvement in properties like strength, toughness, hot corrosion resistance, hot and cold workability, creep and fatigue strength etc.

With a view to exploiting the full potential of this material, a number of studies have been carried out on many aspects of single phase  $\text{Ni}_3\text{Al(B)}$ .

During the processing of  $\text{Ni}_3\text{Al(B)}$  through thermomechanical routes the material will be subjected to both cold deformation and annealing. These will promote the development of specific crystallographic textures in the material, which will ultimately affect its mechanical properties. Only recently some systematic work has been carried out on the development of deformation and recrystallization textures and related aspects in single phase  $\text{Ni}_3\text{Al(B)}$ . This work has been, by no means, quite exhaustive and more research is needed to clarify texture formation during processing of this alloy.

More recently, substantial attention is being paid to the development of two-phase  $\text{Ni}_3\text{Al}$ -base alloys which, along with ordered  $\text{Ni}_3\text{Al}$  ( $\gamma'$ ), also contain a Ni-base disordered FCC phase ( $\gamma$ ). Such a two-phase material is expected to exhibit a better combination of strength and ductility; at the same time, selected ternary additions could enhance the material properties even further. Very little work, however, has been carried out in these areas till date, leaving ample scope for more scientific work, especially on the textural aspects of the material during processing. For this reason, a systematic attempt has been made in the present work to investigate in detail the development of cold rolling and annealing textures in a two-phase  $\text{Ni}_3\text{Al(B,Zr)}$  alloy, with a composition similar to what is known as an IC50 alloy. Investigations have also been carried out on other important aspects such as the evolution of microstructure, structural stability, ordering behaviour and recrystallization kinetics etc.

The alloy used in the present investigation was obtained in the form of a continuously cast sheet of  $\sim 1$  mm thickness, with the nominal composition Ni-21.8Al-0.34Zr-0.1B in atomic percent. The cast material was homogenized by annealing in vacuum ( $< 10^{-4}$  Pa) at  $1150^\circ\text{C}$  for 24 hrs. The homogenized alloy was cold rolled in a 2-high laboratory rolling mill, to different levels of percentage reduction, upto a maximum of 73%. Subsequently, the 73% rolled alloy was annealed, first isochronally followed by isothermal annealing. Isochronal

annealing was done for 1 h each at several temperatures ranging from 500° to 1200°C. while isothermal annealing was carried out upto full recrystallization at five different temperatures ranging from 800° to 1200°C.

Microstructural characterization was carried out from the cast and homogenized as well as the deformed and recrystallized samples using optical and scanning electron microscope (SEM). A selected number of samples, both in the deformed and partially recrystallized conditions, were also extensively studied using a transmission electron microscope (TEM).

A thorough X-ray diffraction study was carried out on the initial material as well as on the deformed and annealed samples at different stages of processing. Integrated intensities of the relevant peaks were measured from each of the XRD profiles for the determination of long range order parameters  $S_{100/200}$  and  $S_{110/220}$ , based on the intensity ratios of the 100/200 and 110/220 reflection pairs respectively. Strain parameter values were calculated by measuring the ratios of the half intensity breadths of the (111) and (200) lines in the XRD profile at any stage to the corresponding breadths of the same lines in the original homogenized sample. The microhardness values of all the samples were also determined in the usual manner.

The kinetics of recrystallization was studied from the plots of volume fraction recrystallized versus time at particular annealing temperatures and the values of different parameters such as 'n' (Avrami exponent) and 'Q' (activation energy) determined therefrom. Differential scanning calorimetric (DSC) study was conducted on all the deformed samples, in order to have an idea about the energy release during the annealing treatment. Crystallographic textures were determined for all the deformed and a few isothermally annealed (at 900°C) samples using both (111) pole figures and orientation distribution functions (ODF).

The results of the present investigation indicate that the starting material, i.e. the homogenized alloy, has a distinct two phase microstructure with islands of disordered FCC Ni-rich  $\gamma$  phase distributed within the ordered  $\text{Ni}_3\text{Al}$  ( $\gamma'$ ) matrix. At the initial stages

of deformation, the  $\gamma$  islands get elongated along the rolling direction and align themselves along the deformation bands. At later stages, when a high density of shear bands form, the  $\gamma$  islands get further aligned along the shear bands. The TEM micrographs reveal the presence of numerous twins along with highly dislocated substructure from a deformation level of 35% onwards. Neither deformed  $\gamma$  nor the  $L1_2$  structure of  $\gamma'$  are expected to deform by twinning. From X-ray diffraction and microstructural evidences these twins have been related to a possible structural transformation in  $\gamma'$  from  $L1_2$  to  $DO_{22}$  since the  $DO_{22}$  structure is known to deform by twinning only. The  $L1_2 \rightarrow DO_{22}$  transformation most probably takes place between 35% and 45% cold deformation. During this range of rolling deformation both the strain parameter and the microhardness values decrease abruptly indicating a strain-induced transformation. At this level of deformation the order parameter  $S_{100/200}$ , characteristic of the  $L1_2$  structure of  $Ni_3Al$ , becomes zero whereas the parameter  $S_{110/220}$  starts showing an increase. The  $S_{110/220}$  parameter reaches a maxima after 55% rolling, beyond which it decreases again.

Significant textural changes occur in this material with the progress of cold rolling. A pure metal type texture is produced at the initial stage of cold rolling. This changes into an alloy type texture characterized by a strong  $B_s \{011\} \langle 211 \rangle$  component after 35% rolling. The overall texture intensity decreases till 55% deformation and then shows an increase at 65% and 73% deformation. The final texture again appears to be alloy type. It is known that in FCC materials the deformation mode governs the formation of crystallographic texture. Therefore, the two phases in the present alloy,  $\gamma'$  and  $\gamma$ , whose deformation modes are not likely to be of the same type, are expected to develop different kinds of texture, the combined effect of which is actually reflected in the overall texture of the material. The  $B_s/S \{168\} \langle 211 \rangle$  component has been found to be the strongest component after 35%, 45% and 73% rolling reductions.

TEM micrographs show that at the initial stages of annealing a 'de-twinning' process

seems to operate whereby the high density twins of the 73% cold rolled material disappear within a very short period of time. X-ray diffraction results indicate that the above phenomenon is also accompanied by a reordering process which changes the  $DO_{22}$  structure of the cold rolled material back to the original  $L1_2$ . A level of ordering, characteristic of the original homogenized sample, is established quickly during the recovery stage and this changes only a little during subsequent recrystallization. The transformation from the  $DO_{22}$  back to the  $L1_2$  structure appears to weaken the texture of the 73% cold rolled material even before significant amount of recrystallization has taken place.

Recrystallization appears to start at the shear band regions containing deformed  $\gamma$  islands. The high nucleation rate within the shear bands and the heterogeneous nucleation sites provided by the fine  $\gamma'$  particles inside the  $\gamma$  islands, all lead to the formation of a high density of small recrystallized grains. During annealing at the lower temperatures of 700° and 800°C the interfaces between the deformed  $\gamma$  regions and the  $\gamma'$  matrix appear to act as reaction fronts for combined recrystallization and precipitation. As a result, the recrystallized  $\gamma$  grains contain a discontinuous (cellular) precipitation inside. Annealing at the intermediate temperature of 900°C leads to the formation of both discontinuous and a fine globular precipitation inside the  $\gamma$  grains. At the higher annealing temperature of 1000°C, recrystallization of  $\gamma$  grains appears to precede the formation of fine globular precipitates inside the grains. Careful examination of the SAD patterns indicate that these precipitates – whether cellular or globular – are nothing but of  $Ni_3Al$  ( $\gamma'$ ).

After the recrystallization of the deformed  $\gamma$  regions is almost over, in the second stage of recrystallization, the deformed  $\gamma'$  regions start to recrystallize. The microstructure of the final annealed material appears to consist of

- nearly 50% by volume of recrystallized  $\gamma$  grains with  $\gamma'$  precipitates within.
- nearly 50% by volume of recrystallized  $\gamma'$  grains and
- a very small fraction of recrystallized pure  $\gamma$  grains without any precipitates inside.

That recrystallization here is a two stage process has also been corroborated by the activation energy data obtained from the recrystallization kinetics studies. The measured activation energy ( $Q$ ) values have been found to be more or less independent of the annealing temperature, but very much dependent on the volume fraction of material recrystallized. Thus a  $Q$  value of about 117 kJ/mole is obtained when the volume fraction recrystallized is  $< 0.5$  whereas  $Q$  has a value of 274 kJ/mole for recrystallization volume fractions of 0.5 and more. Evidently the lower activation energy relates to the initial recrystallization of the deformed  $\gamma$  regions which is followed in the next stage by the recrystallization of the deformed  $\gamma'$  grains, which is sluggish at the beginning and needs a higher activation energy.

As mentioned earlier, drastic weakening of the deformation texture appears to take place during the recovery stage. The texture at the beginning of recrystallization process is already very weak and it remains so till the progress of recrystallization is complete. A high density of randomly oriented nuclei seems to contribute towards this phenomenon. The final texture is not much different from the random, indicating that the material will be nearly isotropic at the end of the deformation and recrystallization processing.<sup>1</sup>

# CHAPTER 1

## INTRODUCTION

## ● *Introduction*

High temperature structural materials constitute an important group of materials which are specifically designed for high temperature applications, such as aircraft engines, gas turbines, diesel engine turbochargers etc. The ever increasing need for energy conservation demands the designing of fuel efficient engines or turbines which can operate at even higher temperatures. Such materials find applications in other fields also, namely, for the manufacture of marine turbines, reactors, coal gasification plants, chemical industry, heat exchangers, exhaust valves, satellite propulsion systems, rockets and missiles etc.

The desirable properties for a high temperature material are:

- High melting point and adequate strength at service temperatures.
- Structural and dimensional stability.
- Excellent creep and fatigue resistance.
- Excellent corrosion and oxidation resistance, both at ambient and high temperatures.
- High strength to weight ratio, which is a primary necessity for aerospace applications.
- Easy processing and fabricability.

It has indeed been a great challenge for the materials engineers to design advanced high temperature structural materials with satisfactory level of performance. Alloys based on high melting refractory metals with superior creep strength had been considered earlier, but



their poor oxidation resistance restricted their scope. Ceramic materials have excellent dimensional stability and environmental resistance along with a high strength to weight ratio. However, the extremely poor toughness of these materials has limited their industrial application. Hybrids of ceramics and metals, known as cermets, and the advanced structural ceramics are still under vigorous investigation. The most successful high temperature materials developed until now are the Ni-base superalloys in which the nickel aluminide ordered intermetallic compound,  $\text{Ni}_3\text{Al}$ , actually constitutes the main strengthening phase. Later, research activities have been focussed on the development of high temperature materials based on the ordered intermetallics themselves, such as the aluminides of Ni and Ti.

The elevated temperature mechanical strength and creep resistance of  $\text{Ni}_3\text{Al}$  has been found to be highly satisfactory due to restricted diffusion in ordered structure. The unique property of  $\text{Ni}_3\text{Al}$  is its positive temperature coefficient of flow stress: the flow stress increases with temperature up to  $700^\circ\text{C}$ .  $\text{Ni}_3\text{Al}$  is also highly oxidation resistant due to its ability to form adherent oxide surface films that protect the base metal from environmental attack.

A major drawback of polycrystalline  $\text{Ni}_3\text{Al}$  intermetallic compound is its brittleness which leads to intergranular fracture. This is essentially a grain boundary phenomenon as the single crystal of  $\text{Ni}_3\text{Al}$  has been found to be sufficiently ductile. In fact, the polycrystalline brittleness of this material had delayed its commercialization. Aoki and Izumi [1] were the first to observe that microalloying with boron improved the ductility of polycrystalline  $\text{Ni}_3\text{Al}$ . Later, Liu *et al* [2] showed that a precise control of boron addition, alloy stoichiometry and thermomechanical treatment could produce in  $\text{Ni}_3\text{Al}$  tensile elongations exceeding 50% at room temperature. They also observed that the fracture was basically transgranular in nature in boron doped  $\text{Ni}_3\text{Al}$ .

It is now an established fact that boron doped hypostoichiometric (slightly Ni-rich)  $\text{Ni}_3\text{Al}$  is an excellent structural material with adequate room temperature ductility. Along with other attractive properties, an important characteristic of  $\text{Ni}_3\text{Al}$  is that it shows a good

deal of flexibility in material designing. Addition of several elements such as Cr, Hf, Zr, Fe, Co, W, Ti, Nb etc. to  $\text{Ni}_3\text{Al}$  impart solid solution strengthening and improve cold and hot workability, hot corrosion resistance etc. The combination of suitable alloying additions and processing techniques are expected to lead to superior material properties for  $\text{Ni}_3\text{Al}$ , even better than the superalloys. Figure 1.1 compares the yield strength variations with temperature for a few materials, namely, 316 stainless steel, Hastelloy X and IN-713C (all superalloys),  $\text{Ni}_3\text{Al(B)}$  and advanced nickel aluminides. It is clearly seen that the advanced aluminides have a distinct edge over the other high temperature materials [3].

A large number of two-phase advanced nickel aluminides have also been designed, the most important among these being  $\text{Ni}_3\text{Al(B,Zr)}$ . Basically it is a hypostoichiometric alloy, consisting mainly of the ordered  $\text{Ni}_3\text{Al}$  ( $\gamma'$ ), with a minor fraction of disordered Ni-base solid solution ( $\gamma$ ) phase. Boron has been added to improve its cold workability and zirconium for solid solution strengthening. The commercial designation of this alloy is IC50, and this is generally used as a base alloy for the development of other advanced nickel aluminide compositions.

The thermomechanical processing of  $\text{Ni}_3\text{Al}$  and related intermetallics could involve both cold deformation and annealing treatments. However, very little systematic study has so far been carried out in this direction. The processing of nickel aluminides is also expected to have pronounced effect on the development of textures in these materials. Since textures are known to affect the mechanical properties very significantly, investigations into these aspects is also of utmost importance. Although some work in this area has recently been carried out on single phase  $\text{Ni}_3\text{Al(B)}$  alloys, very little information is available on the deformation and annealing behaviour of two-phase  $\text{Ni}_3\text{Al}$ -base alloys. The present work was therefore undertaken to carry out a systematic study of the microstructural and textural changes that occur during cold rolling and subsequent annealing in a two-phase  $\text{Ni}_3\text{Al(B,Zr)}$  alloy.

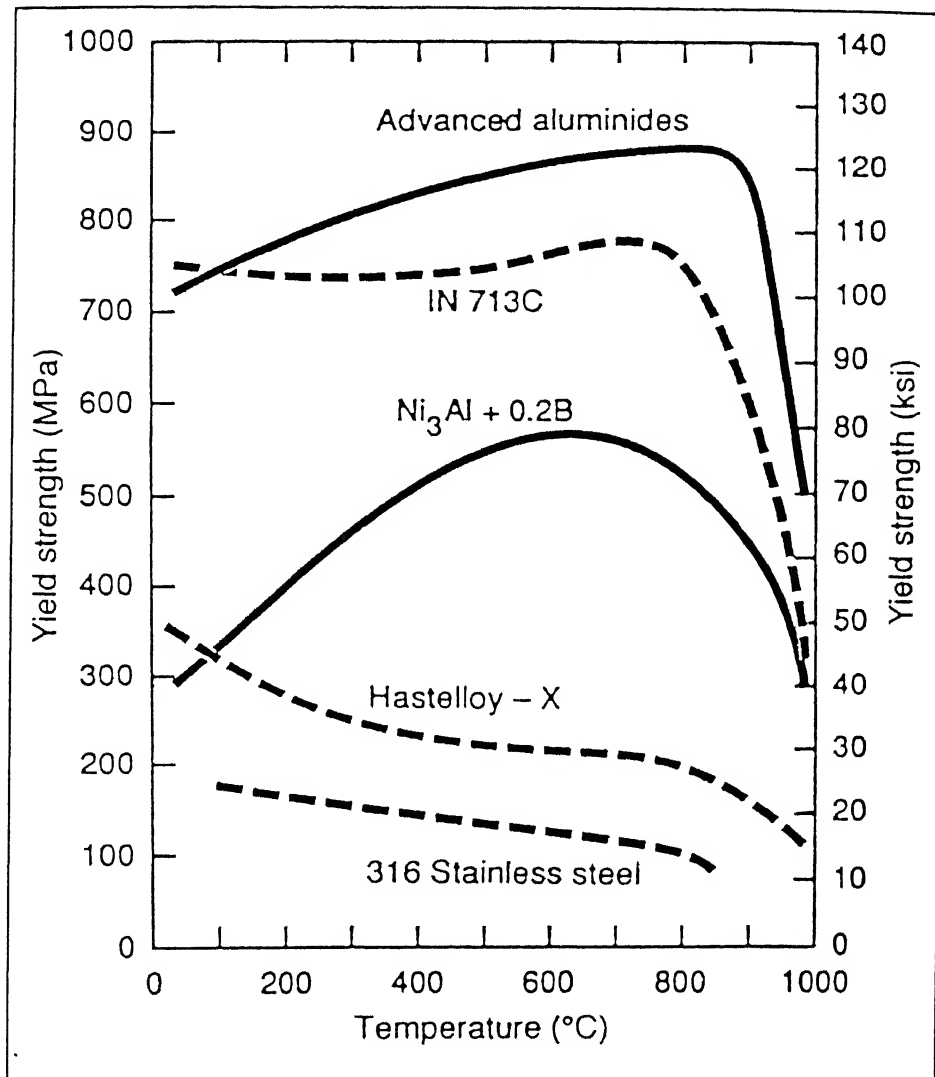


Figure 1.1 Yield strength versus test temperature for Ni<sub>3</sub>Al alloys, two superalloys and type 316 stainless steel [3]

Several characterization techniques have been used for this purpose. The structural stability of the alloy and changes in the ordered state as a function of cold rolling and annealing treatments have been thoroughly investigated using standard XRD techniques. Microstructural changes have been recorded by optical, scanning and transmission electron microscopy. The development of textures during cold deformation and annealing has been investigated by measuring pole figures and ODFs (Orientation Distribution Functions). The kinetics of recrystallization was carefully studied in the usual manner by analysing the results pertaining to the progress of recrystallization. Measurements of strain parameter and microhardness values at different stages of processing and some heat release experiments using a Differential Scanning Calorimeter (DSC) were also undertaken. The results have been analysed carefully and discussed and appropriate conclusions were drawn therefrom.

# CHAPTER 2

## LITERATURE

## ● *Literature*

Ordered intermetallic compounds constitute an important class of materials. They usually exhibit remarkable structural stability, along with excellent high temperature mechanical properties. The aluminides, such as nickel aluminide, titanium aluminide and iron aluminide show good corrosion and oxidation resistance.  $\text{Ni}_3\text{Al}$  based intermetallic compounds constitute the main strengthening phase in the Ni and Co base superalloys. Quite naturally, for the last few years, these materials have received considerable attention from materials engineers and scientists. The ongoing research has opened a new horizon for the future generation of high strength materials.

The technological importance of the aluminides is due basically to their excellent structural stability upto the order - disorder transformation temperatures. The transformation temperature is often quite high, sometimes the material is ordered even upto its melting point. Another important advantage of the aluminides is their high strength to weight ratio, essentially for titanium aluminides. The transformation temperature ( $T_c$ ), melting point ( $T_m$ ), density ( $\rho$ ) and Young's modulus ( $E$ ) of a few important aluminide intermetallics are listed in Table 2.1 [4].

**Table 2.1** Properties of nickel, iron and titanium aluminides

<i>Alloy</i>	<i>Crystal Structure</i>	<i>T<sub>c</sub>(°C)</i>	<i>T<sub>m</sub>(°C)</i>	<i>ρ(gm/cc)</i>	<i>E(GPa)</i>
Ni <sub>3</sub> Al	L1 <sub>2</sub> (ordered FCC)	1390	1390	7.5	179
NiAl	B2 (ordered BCC)	1640	1640	5.86	294
Fe <sub>3</sub> Al	DO <sub>3</sub> (ordered BCC)	540	1540	6.72	141
	B2 (ordered BCC)	760	1540	—	—
FeAl	B2 (ordered BCC)	1250	1250	5.56	261
Ti <sub>3</sub> Al	DO <sub>19</sub> (ordered HCP)	1100	1600	4.2	145
TiAl	L1 <sub>0</sub> (ordered tetragonal)	1460	1460	3.91	176
TiAl <sub>3</sub>	DO <sub>22</sub> (ordered tetra)	1350	1350	3.4	—

## 2.1 Ni<sub>3</sub>Al Intermetallic Compound

An intermetallic compound can be defined as an intermediate phase in an alloy system, having a narrow range of composition and relatively simple stoichiometric proportions, in which the nature of the atomic binding can vary from metallic to ionic [5]. An intermediate phase can form by a congruent transformation, or an incongruent, for instance, a peritectic transformation. Figure 2.1 shows the aluminium - nickel binary phase diagram [6]. At 75 atomic percent Ni, the intermetallic compound ( $\gamma'$ ) is formed, within a limited solubility range. This phase is basically the product of a peritectic reaction taking place at 1395°C which is actually quite close to the melting point for that composition.

The Ni<sub>3</sub>Al single crystal is sufficiently ductile; however, the polycrystalline Ni<sub>3</sub>Al, like the other intermetallic compounds, is extremely brittle which is an inherent limitation of the material. However, it was later found out that polycrystalline Ni<sub>3</sub>Al can be made substantially ductile at room temperature by boron addition [1, 2]. This discovery actually led to the technological application of this intermetallic compound, and practically Ni<sub>3</sub>Al is now on commercialization stage. The salient features of Ni<sub>3</sub>Al, its properties, ordering behaviour, cold rolling and annealing characteristics, the effect of boron on the ductility and related phenomena and textural changes during processing of this material are discussed in the following sections.

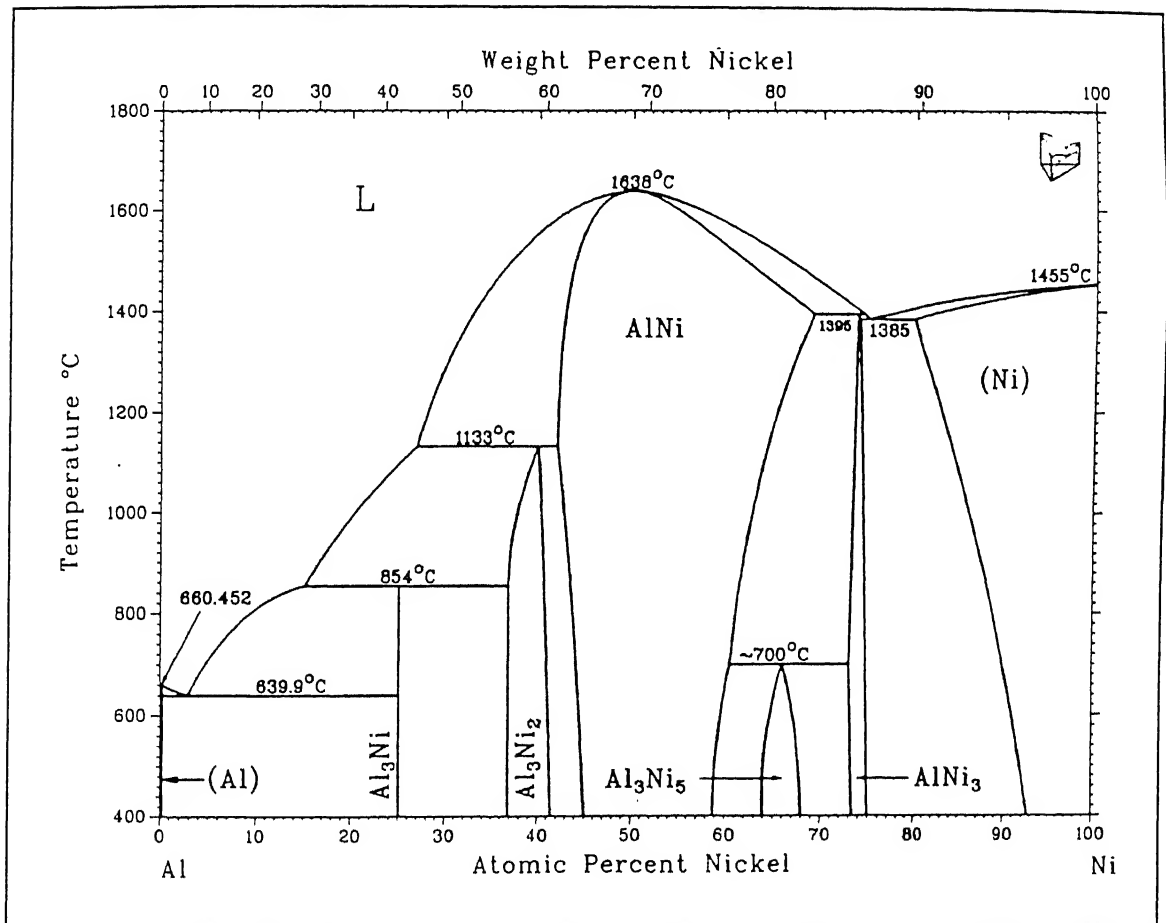


Figure 2.1 Aluminium - Nickel binary phase diagram [3]



## 2.2 Unit Cell and Crystal Structure of Ni<sub>3</sub>Al

The unit cell of the  $\gamma'$  Ni<sub>3</sub>Al phase is shown in Figure 2.2. It is basically a face centered cubic structure, in which the Al atoms occupy the corner sites leaving the face centered positions to the Ni atoms. The ordered superlattice structure is composed of four interpenetrating simple cubic sub-lattices. The prototype of this structure is Cu<sub>3</sub>Au, and its Strukturbericht designation is L1<sub>2</sub> [7]. The atom positions are:

$$\text{Al} - 000$$

$$\text{Ni} - \frac{1}{2}0\frac{1}{2}, \frac{1}{2}\frac{1}{2}0, 0\frac{1}{2}\frac{1}{2}$$

The lattice parameter of stoichiometric Ni<sub>3</sub>Al has been reported as 3.561 Å [8].

## 2.3 Ordering Behaviour of Ni<sub>3</sub>Al

An ordered intermetallic compound remains ordered upto a critical temperature, known as *order-disorder transformation temperature*. The coherent scheme of order which extends over a large region of the lattice is usually known as *long range order*. The basic condition of the ordering phenomenon is that a particular type of atom should be surrounded or neighbored by different types of atoms. In a superlattice, generated by the sub-lattices of two kinds of atoms A and B, the atoms occupy specific positions allotted for them. This is schematically shown in Figure 2.3. Therefore, if  $p$  is the probability that a right position for an A atom is filled by an A atom, and  $r$  is the fraction of the lattice sites that is occupied by A atoms in the state of perfect order, then the long range order parameter can be given by the relation [7]

$$S = (p - r)/(1 - r) \quad (2.1)$$

where  $S$  varies from 0 to 1. Figure 2.4 shows how the long range order parameter varies with temperature. The nature of the curve shown in this Figure is analogous to the variation of saturation magnetization with temperature.

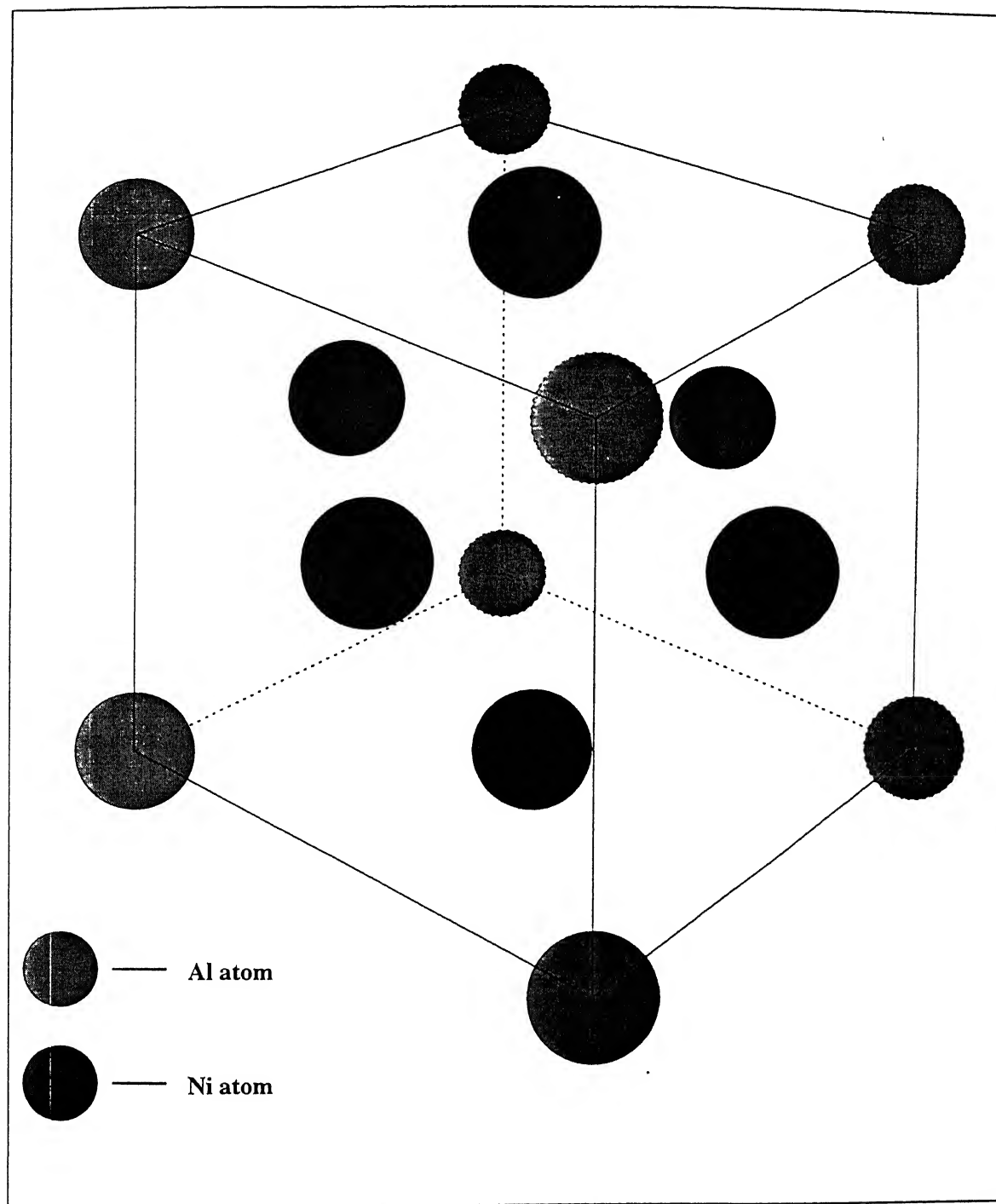


Figure 2.2 Unit cell of  $\text{Ni}_3\text{Al}$  (L1<sub>2</sub> crystal structure)

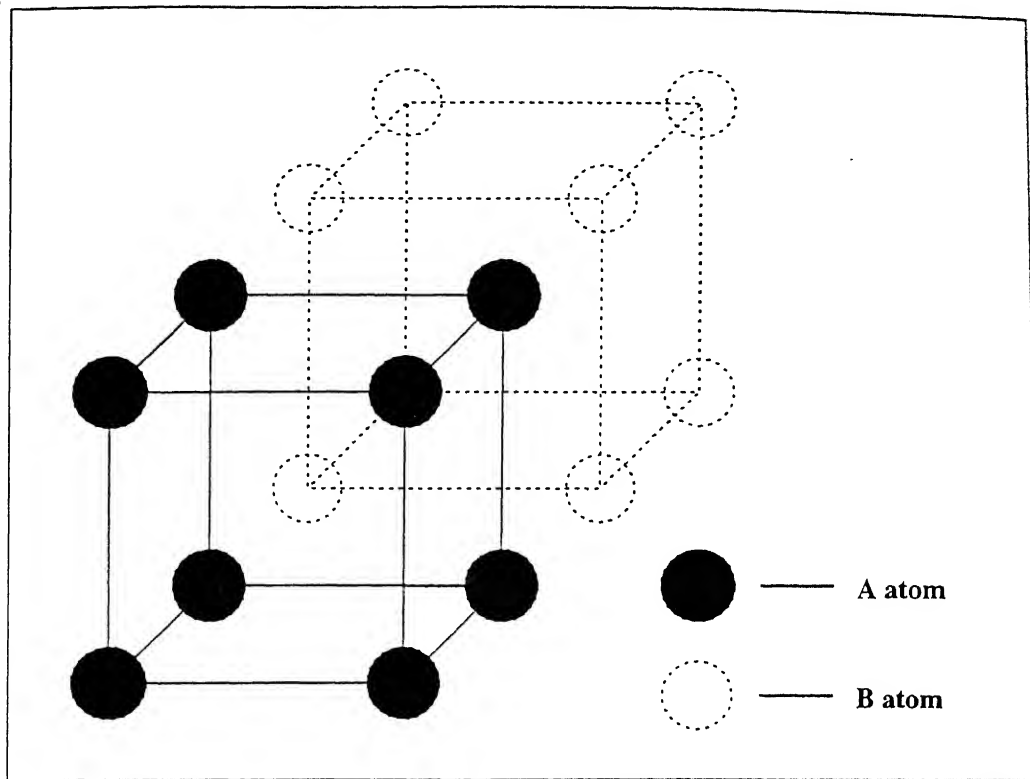


Figure 2.3 Schematic diagram of a BCC superlattice composed of two simple cubic sub-lattices

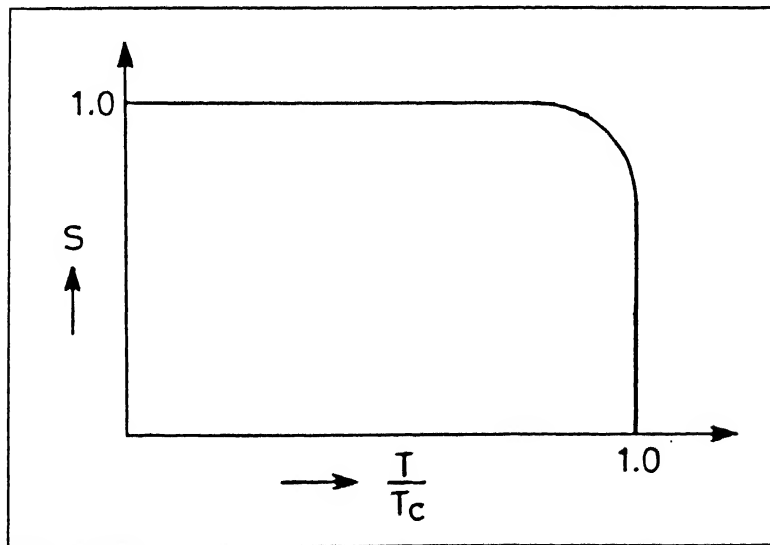


Figure 2.4 Variation of long range order parameter with temperature

In the absence of long range order, a *short range order* can exist, which maintains the condition that dissimilar atoms should attract one another preferentially [9]. Many of the intermetallic compounds have their order-disorder transformation temperatures close to their respective melting points, and sometimes the transformation temperature lies in the liquid zone of the phase diagram. In the latter case the material directly freezes into the fully ordered state, and holds its strength nearly upto its melting point.  $\text{Ni}_3\text{Al}$  is an intermetallic compound of this kind which retains its strength upto a high temperature level.

Extensive investigations have been carried out on the ordering behaviour of  $\gamma'$   $\text{Ni}_3\text{Al}$ . The stability of the ordered structure depends on a few important parameters, such as temperature, stoichiometry, alloying addition and amount of plastic deformation.

As mentioned earlier,  $\text{Ni}_3\text{Al}$  retains its ordered structure nearly upto its melting point. Guard and Westbrook [10] reported the presence of the (100) superlattice peak even at  $1000^\circ\text{C}$ . According to Corey and Lisowsky [11], off-stoichiometric Ni-rich  $\text{Ni}_3\text{Al}$  having 22.5% Al became disordered at above  $1100^\circ\text{C}$ . Stoeckinger and Newmann [12] reported on the basis of (100)/(200) and (300)/(400) intensity ratios that the long range order was maintained upto nearly  $1320^\circ\text{C}$ , in case of both stoichiometric and non-stoichiometric single crystals. It was later supported by Pope and Garin [13].

The effect of composition on the ordering behaviour of  $\text{Ni}_3\text{Al}$  was studied in detail by Stoeckinger and Newmann [12]. They reported that off-stoichiometric  $\text{Ni}_3\text{Al}$  having less than 23 atomic percent Al contained disordered  $\gamma$  (Ni-rich solid solution) phase along with the  $\gamma'$  phase at  $1100^\circ\text{C}$ . The binary Ni-Al phase diagram (Figure 2.1) shows that the solubility of Al in the terminal  $\gamma$  solid solution increases considerably at high temperatures. Therefore, it is quite natural that lower the Al content of the alloy, closer will be the composition to the  $\gamma$  region and higher will be the volume fraction of disordered  $\gamma$  phase at higher temperatures.

Noguchi *et al* [14] also reported that alloy stoichiometry affected the stability of the ordered structure of  $\text{Ni}_3\text{Al}$ . They suggested that increasing the minority component (Al in this

case) lowered the stability of  $L1_2$  structure, with respect to the  $DO_{22}$  structure. It was supposed to be due to the presence of anti-structure defects which are actually created when one particular kind of atom occupies positions in different sub-lattices. Masahashi *et al* [15] reported that the addition of carbon and boron, in both stoichiometric and non-stoichiometric  $Ni_3Al$ , intensified the superlattice reflections. They suggested that the strongly attractive interaction between Ni atom and the interstitials stabilizes the  $L1_2$  structure of  $Ni_3Al$ . They also observed that pure, stoichiometric  $Ni_3Al$  was not fully ordered and the order parameter was determined as 0.88; however the addition of Be, which occupied the Al sites, enhanced the ordering of  $L1_2$  structure.

Ramesh *et al* [16] obtained some interesting results while measuring the order parameters of stoichiometric and Ni-rich off-stoichiometric  $Ni_3Al$  with and without boron. In their experiments, the long range order parameter,  $S$ , was computed on the basis of the intensity ratios of the (100)/(200) and (110)/(220) reflection pairs. They found that the  $L1_2$  structure of stoichiometric  $Ni_3Al$  attained a maximum stability at about 600°C (Figure 2.5); the order parameter was then close to the theoretical value. Above 600°C, however, splitting of the (100), (110), (111), (200) and (220) peaks indicated a structural transformation which, according to them, could be from  $L1_2$  to  $DO_{22}$  structure (Figure 2.6). It was suggested by Yamaguchi *et al* [17] that the ordered  $DO_{22}$  or  $DO_{23}$  superlattice structures can be derived from  $L1_2$  by introducing one  $\frac{1}{2}[110]$  APB on every (001) plane or every alternate (001) plane respectively (Figure 2.7). It therefore appears that the earlier concept of structural stability of  $Ni_3Al$  is not absolutely true; at a high temperature the ordering behaviour of  $Ni_3Al$  can be altered.

It has been reported by several investigators that the ordered  $L1_2$  crystal structure of  $Ni_3Al$  could be made disordered by heavy plastic deformation. Corey and Potter [18] and Clark and Mohanty [19] recorded, respectively, the (100)/(200) and (110)/(220) intensity ratios of filed  $Ni_3Al$  powders and reported significant disordering effect due to plastic

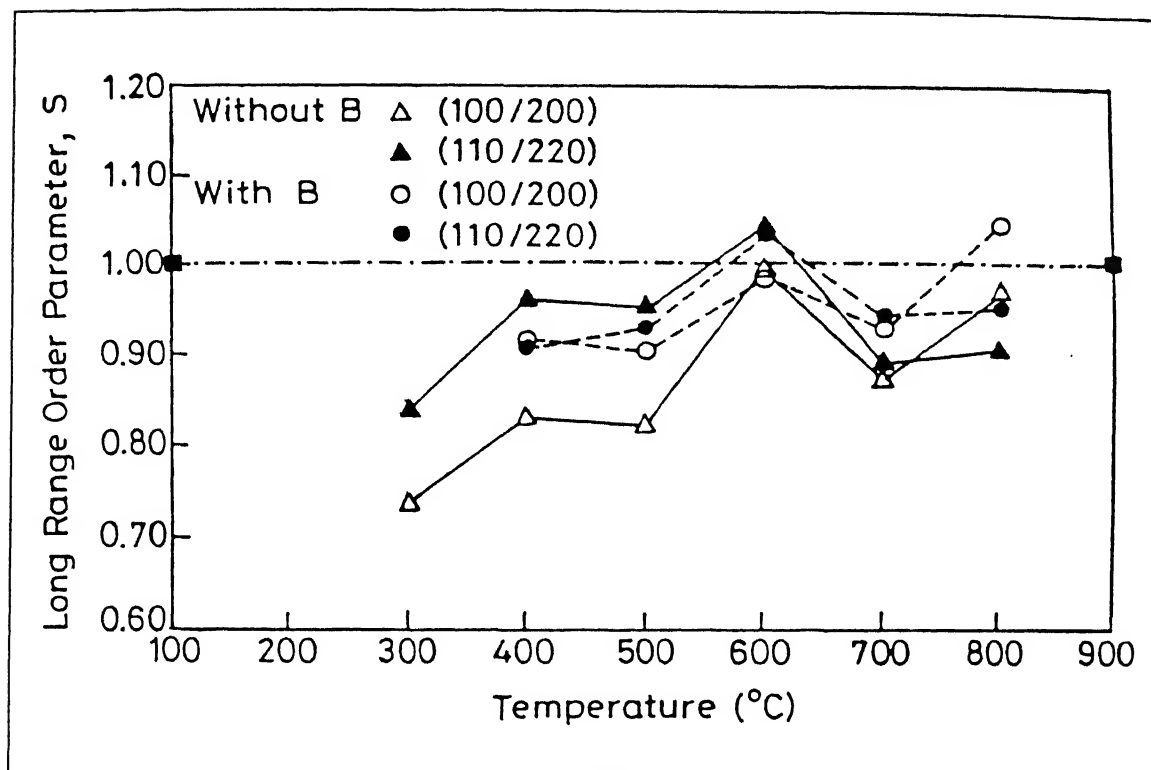


Figure 2.5 Long range order parameter  $S$  as a function of temperature for stoichiometric  $\text{Ni}_3\text{Al}$  (with and without boron addition) [16]

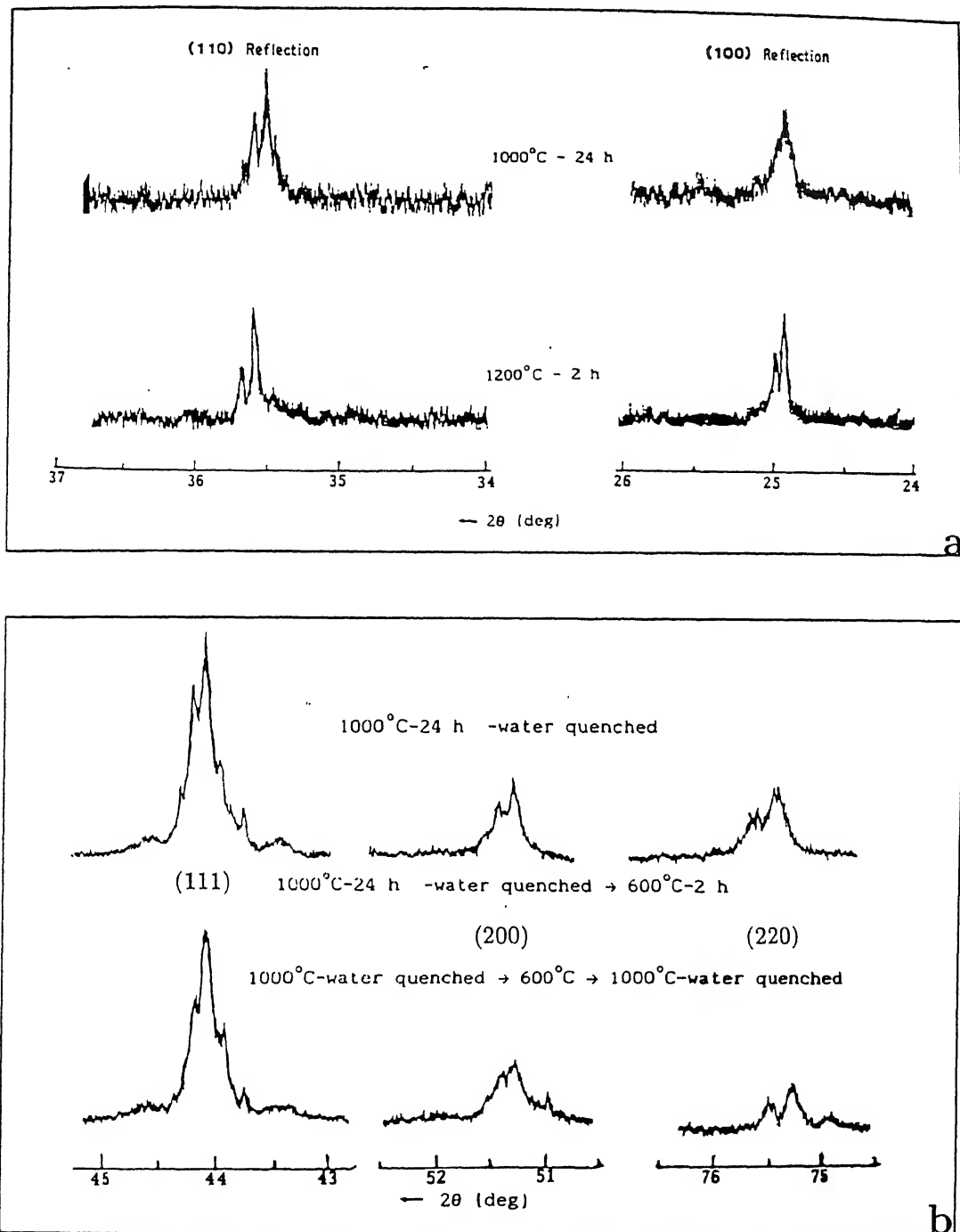


Figure 2.6 XRD intensity profiles of the hypostoichiometric boron doped  $\text{Ni}_3\text{Al}$  alloy when subjected to anneals at  $1000^\circ$  and  $1200^\circ\text{C}$  [16]; (a) (100) and (110) superlattice reflections, (b) (111), (200) and (220) fundamental reflections

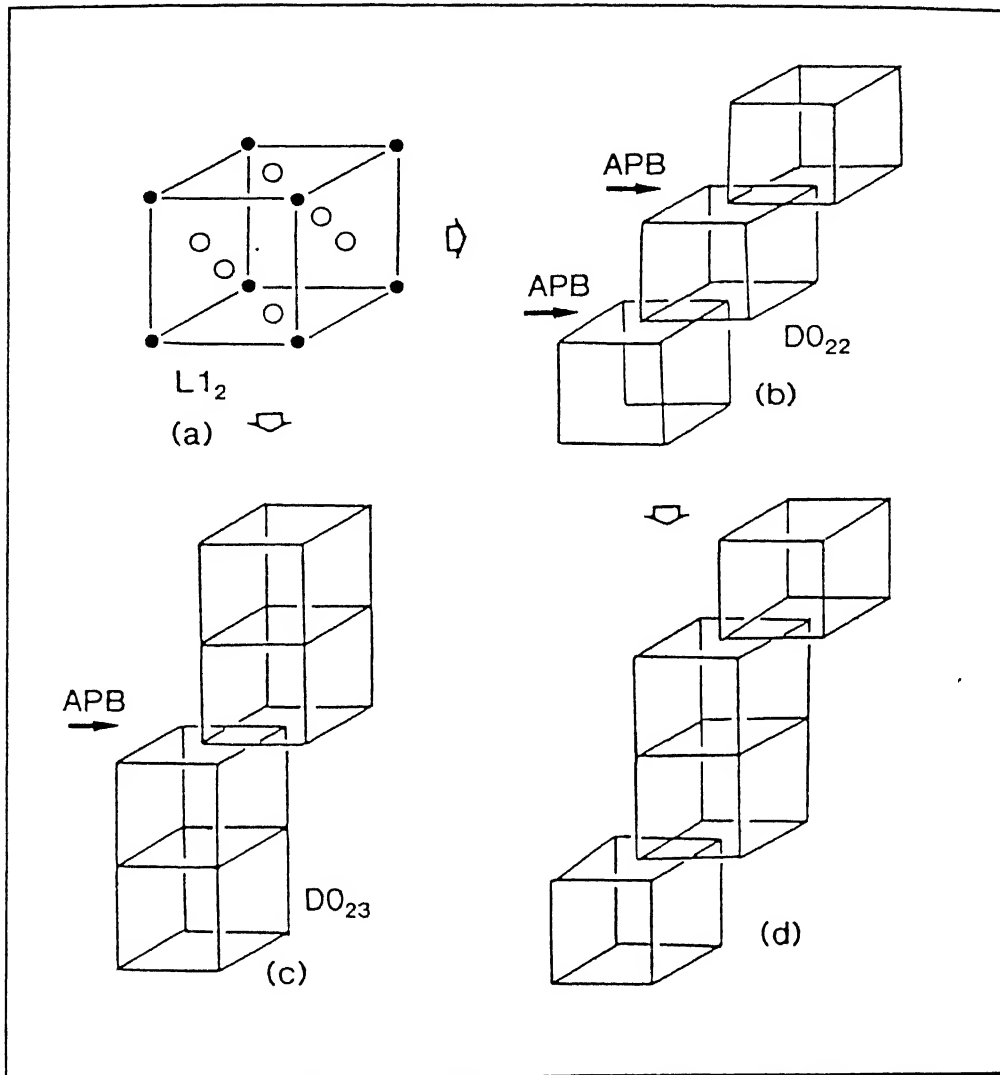


Figure 2.7 Structural relationship between  $L1_2$  and  $L1_2$  - derivative superlattice structures [17]; (a)  $L1_2$ , (b)  $DO_{22}$ , (c)  $DO_{23}$  and (d)  $DO_{22}$  structure with an APB on (001)



deformation by filing. In the above two cases the (100) and (110) superlattice line intensities decreased to very low values, as an effect of filing. Complete disappearance of those peaks after filing was also reported by Ramesh *et al* [16]. Clark and Mohanty [19] observed that on isothermal annealing of the filed powders, a moderate degree of long range order again developed (Figure 2.8) after short recovery times at all temperatures, followed by a slow increase towards the equilibrium degree of order on longer annealing at the respective temperatures. This kind of behaviour was also reported by Corey and Potter [18] for  $\text{Ni}_3\text{Al}$  and Ward and Mikkola [20] for  $\text{Cu}_3\text{Au}$ .

Jang and Coch [21] investigated the disordering effect of  $\text{Ni}_3\text{Al}$  powders caused by ball milling in a vibratory mill. They found that the superlattice lines disappeared with increasing milling time (Figure 2.9). Gialanella *et al* [22] also reported similar disordering effect of ball milling. They measured the (110) and (200) integrated intensity ratios with milling time while carrying out investigation on off-stoichiometric  $\text{Ni}_3\text{Al}$  powder and found a steady decrease of order parameter, followed by complete disordering after 8 hours of milling time (Figure 2.10). Baker *et al* [23], using the (100) and (110) selected area diffraction spot patterns in a TEM, also came to the conclusion that partial disordering of ordered  $\text{Ni}_3\text{Al}$  takes place by cold rolling. Ball and Gottstein [24] reported that the long range order parameter in  $\text{Ni}_3\text{Al(B)}$  reduced to 0.6 after 70% cold rolling from the initial value of nearly unity. Ghosh Chowdhury *et al* [25] found that the intensity of the (100) superlattice reflection gradually decreased during cold rolling and finally disappeared after 65% reduction of off-stoichiometric boron doped  $\text{Ni}_3\text{Al(B)}$  (Figure 2.11). On the other hand, the intensity of the (110) superlattice line decreased and reached a finite value at high strain levels. In a much earlier work, Wassermann [26], who measured the long range order parameter on the basis of 100/200 and 110/220 reflection pairs, observed that  $\text{Cu}_3\text{Au}$ , another  $\text{L}_{12}$  alloy, underwent complete disordering on rolling deformation (Figure 2.12).

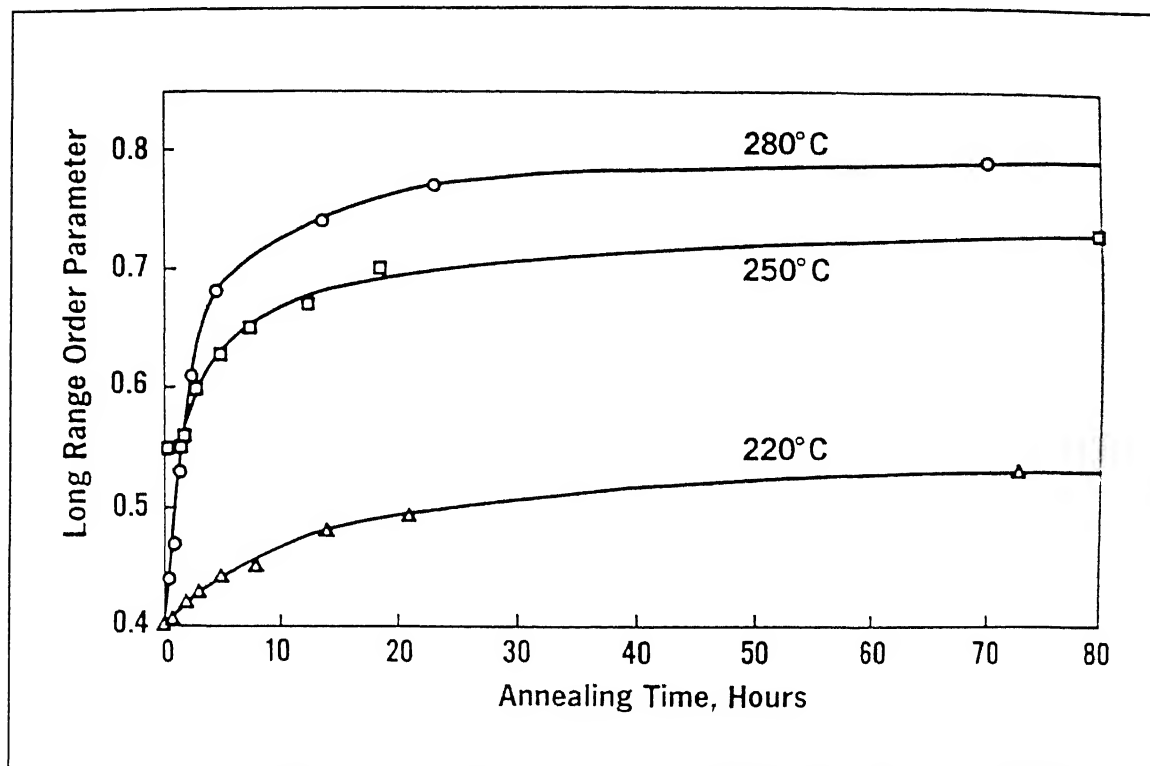


Figure 2.8 The long range order parameter of cold worked  $\text{Ni}_3\text{Al}$  as a function of annealing time [19]

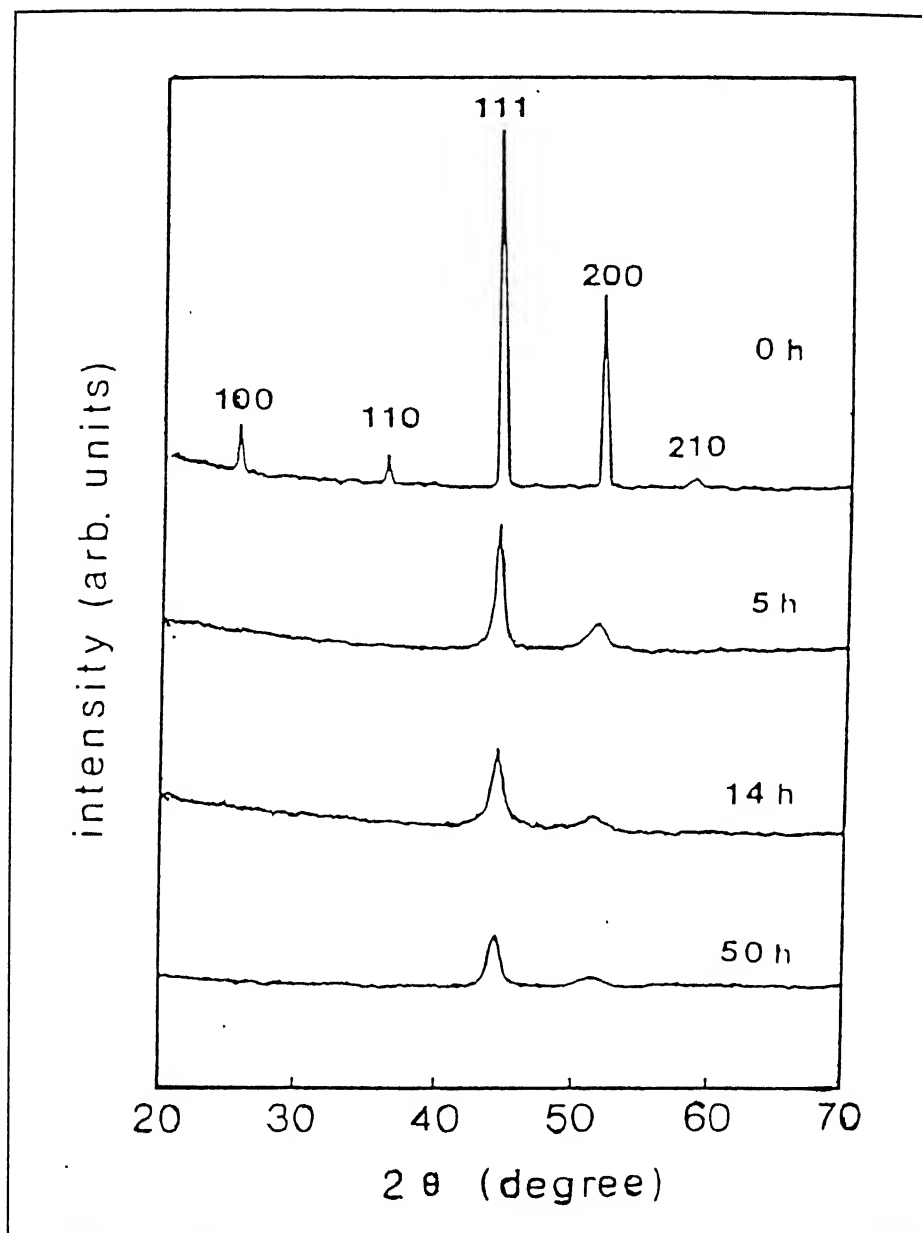


Figure 2.9 XRD line profiles of  $\text{Ni}_3\text{Al}$  powders with milling time [21]

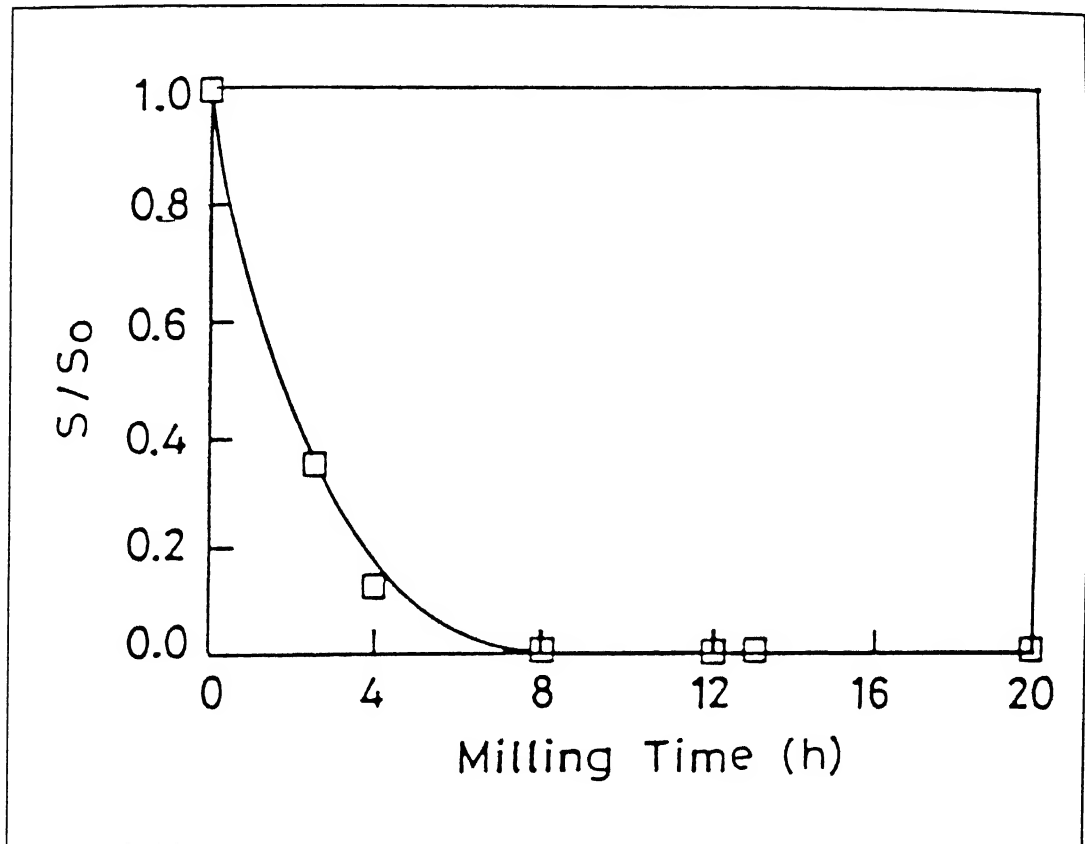


Figure 2.10 Variation of long range order parameter as a function of milling time on the basis of (110) and (200) reflections [22]

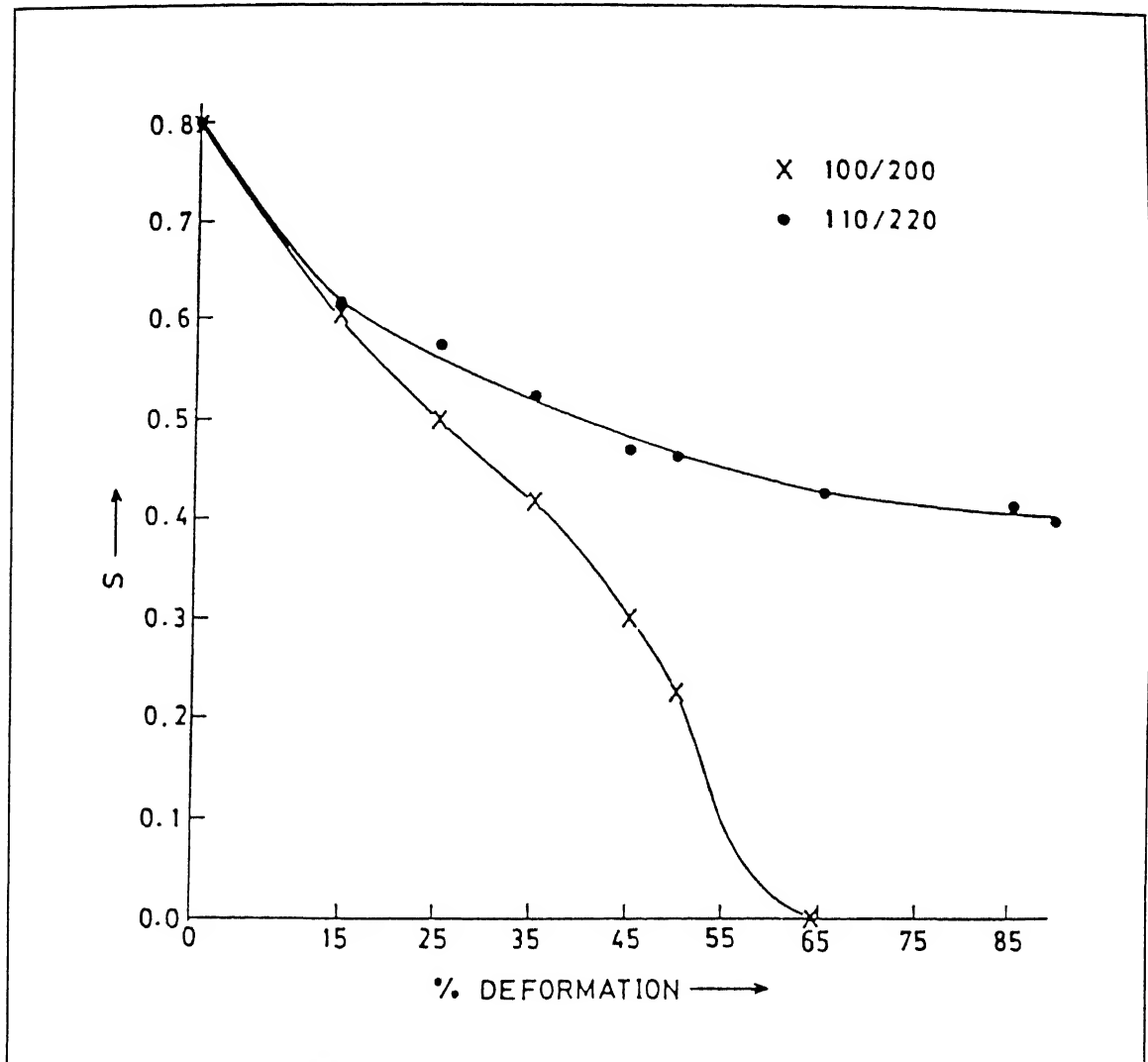


Figure 2.11 Variation of long range order parameter as a function of rolling deformation of  $\text{Ni}_3\text{Al(B)}$  [25]

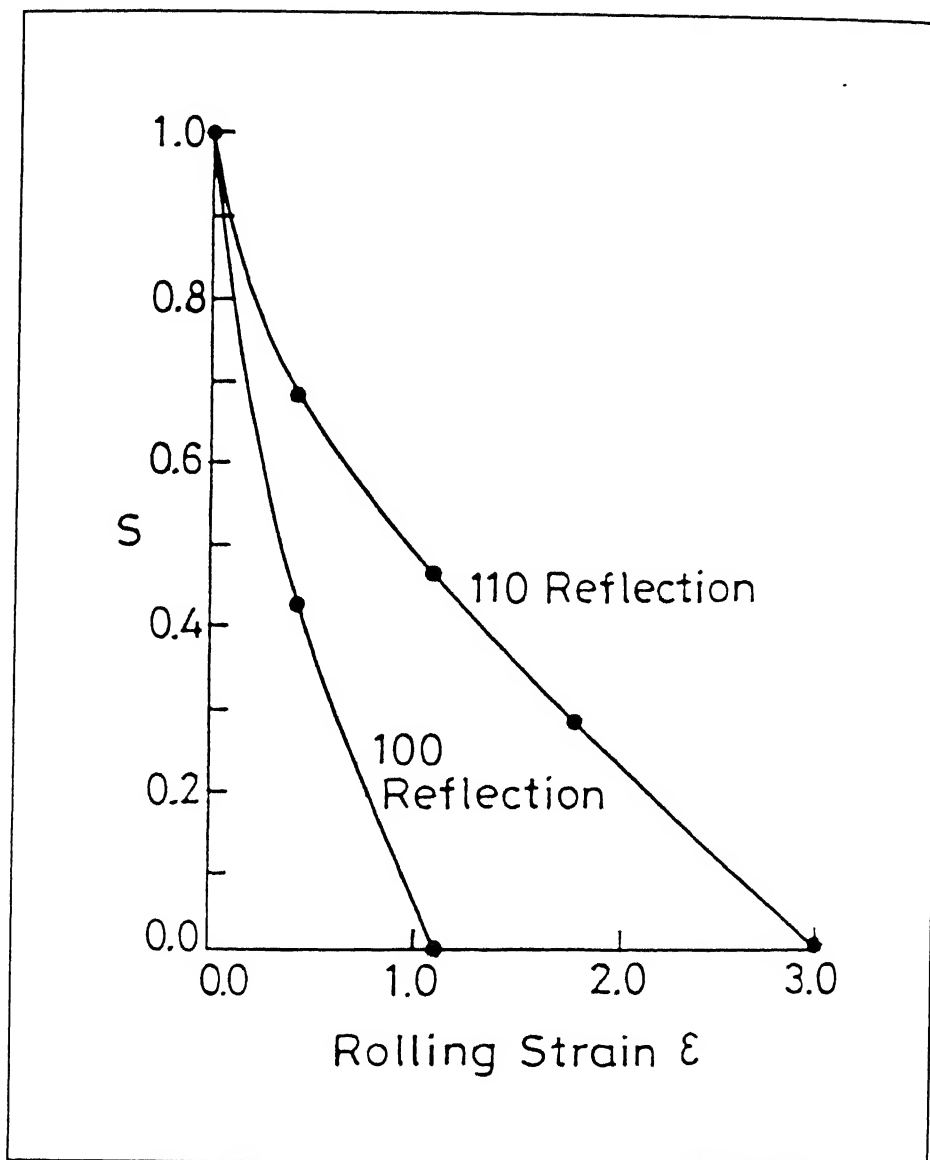


Figure 2.12 Variation of long range order parameter as a function of rolling strain of  $C_3Au$  [26]

## 2.4 Defects in Ni<sub>3</sub>Al : Dislocations and Planar Faults

In FCC metals and alloys, the most common slip system is of the  $\{111\} \langle 110 \rangle$  type with  $\frac{a}{2}[110]$  being the Burgers vector of a single dislocation (Figures 2.13a and 2.13b). In the L1<sub>2</sub> ordered crystal structure, however, a dislocation with Burgers vector  $\frac{a}{2}[110]$  introduces an antiphase boundary as shown in Figure 2.13c. Thus, in the same ordered structure, the introduction of another dislocation of the same kind (as shown in Figure 2.13d) will terminate the APB and the long range ordering would be established once again. Therefore, a dislocation in a disordered structure is actually equivalent to a partial dislocation in an ordered structure. The whole unit, consisting of two dislocations is known as a superdislocation, and the individual dislocations are known as the superpartials.

The dissociation of the superpartials is dependent on the elastic energy associated with the dislocations and the energy value of the planar faults which actually separate the superpartial dislocations. The elastic energy of a dislocation is proportional to the square of the magnitude of its Burgers vector [27]. If a superdislocation of Burgers vector  $\vec{b}$  dissociates into two superpartials of Burgers vectors  $\vec{b}_1$  and  $\vec{b}_2$ , the change in elastic energy will be proportional to  $b_1^2 + b_2^2 - b^2$ . Therefore, dissociation is possible when

- $\vec{b}_1 + \vec{b}_2 = \vec{b}$ , and
- $b_1^2 + b_2^2 < b^2$

The two dissociated superpartials are separated by a planar fault region, and the width of that region is inversely proportional to the energy associated with that planar fault. As a result, the decrease in elastic energy during a dissociation process is compensated by the creation of a planar fault region. The width of the planar fault is decided by the balance between the strain energy of dissociated dislocations and the energy value of the respective planar fault. The overall concept is that the dissociation is easier for a lower specific energy value of the planar faults.

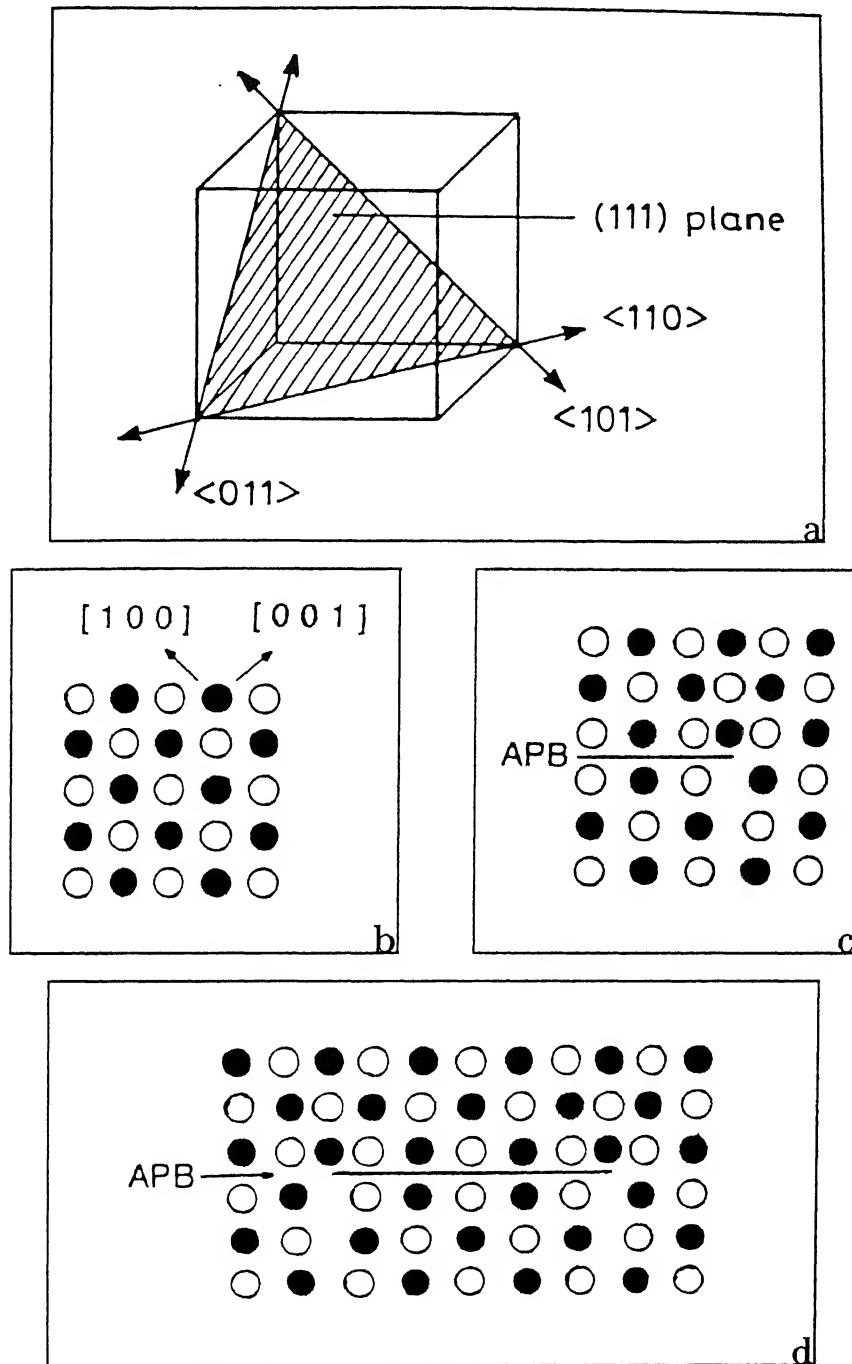


Figure 2.13 Slip system and APB in  $L1_2$  structure; (a)  $(111)$  plane and  $\langle 111 \rangle$  directions in  $L1_2$  (FCC) structure, (b)  $(010)$  plane of  $L1_2$  structure, (c) a  $\frac{1}{2}[\bar{1}01]$  dislocation on  $(111)$  plane, producing an APB, and (d) two  $\frac{1}{2}[\bar{1}01]$  dislocations on  $(111)$  plane separated by an APB



The existence of four types of planar faults on the  $\{111\}$  planes of the  $L1_2$  structure have so far been reported [28]. These are

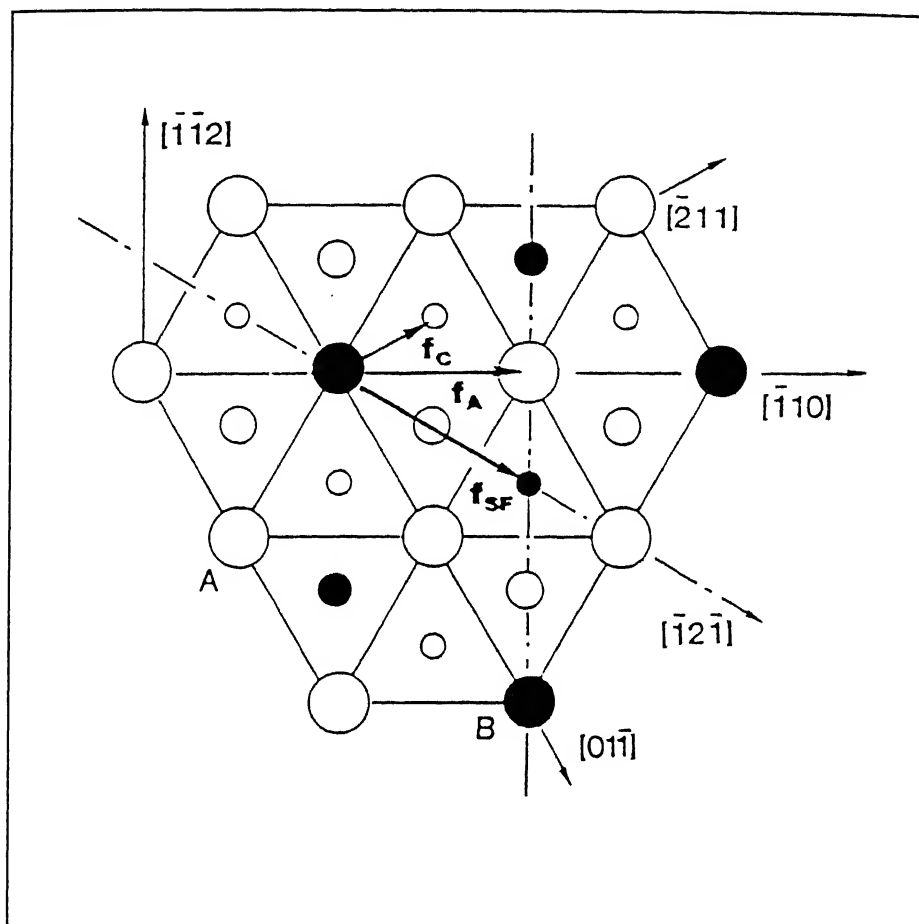
- (a) Antiphase Boundary (APB)
- (b) Complex Stacking Fault (CSF)
- (c) Superlattice Intrinsic Stacking Fault (SISF)
- (d) Superlattice Extrinsic Stacking Fault (SESF)

Figure 2.14 illustrates the nature of APB, CSF and SISF [29] on  $\{111\}$  planes of an  $A_3B$  type intermetallic alloy. In this Figure, three successive layers of  $(111)$  planes have been shown. The large, medium and small circles represent atoms on  $a$ ,  $b$  and  $c$  layers respectively, when the stacking sequence of  $(111)$  planes is  $abc/abc$ . When the top layer  $a$  is displaced by the vector  $f_A = \frac{1}{2}[\bar{1}10]$ , as shown in the diagram, with respect to the layer  $b$ , the configuration of the atom neighbours across the fault is changed, producing an APB. The basic arrangement of the atoms is not changed when the lattice sites are randomly occupied by A and B atoms. Therefore, an APB only exists in an ordered lattice, which simply places the like atoms side by side, violating the nearest neighbour relationship.

A CSF is created when the top layer  $a$  is displaced by the vector  $f_C = \frac{1}{6}[\bar{2}11]$ , with respect to the layer  $b$ , thereby placing the B atoms in the  $a$  layer directly above the A atoms in the  $b$  layer. This results in a local HCP type stacking, similar to the ordinary stacking faults in FCC structures. The additional feature is that a CSF involves the effect of wrong bonds (i.e. the violation of nearest neighbour relationship).

SISF is formed when the top layer  $a$  is shifted by the vector  $f_{SF} = \frac{1}{2}[\bar{1}2\bar{1}]$ , so that the B atoms of the two layers lie directly one above another. As a result, a change occurs in the stacking sequence from  $abc/abc$  to  $abc/bc$ . Such type of faults are low energy faults because they change the stacking sequence but do not violate the nearest neighbour relationship.

SESF can be produced when one layer shifts by a vector  $\frac{1}{3}[\bar{1}2\bar{1}]$  and the layer above



**Figure 2.14** The atomic arrangement and the nature of planar faults on the (111) plane in an  $A_3B$  compound with  $L1_2$  structure and stacking sequence  $\dots abc/abc\dots$

Large, medium and small circles represent atoms on  $a$ ,  $b$  and  $c$  layers, respectively [29]

shifts by either  $\frac{1}{3}[2\bar{1}\bar{1}]$  or by  $\frac{1}{3}[11\bar{2}]$ , resulting in a change in stacking sequence from  $abc/abc$  to  $bcac/bcac$ . This fault also does not violate the nearest neighbour relationship. The superlattice faults in the  $L1_2$  structure have the following characteristics [30]:

SISF = 4 layers of  $\text{SnNi}_3$  ( $\text{DO}_{19}$ ) structure

SESF = 7 layers of  $\text{TiNi}_3$  ( $\text{DO}_{24}$ ) structure

SISF + SESF = 10 layers of  $\text{VCo}_3$  structure

and  $\text{CSF} = \text{APB} + \text{SISF}$ , which indicates that the energy of complex faults should be larger than that of APB. Figure 2.15 schematically shows the difference between the SISF and SESF associated with a Frank sessile in  $L1_2$  lattice.

The specific energies of APB, CSF and SISF in  $\text{Ni}_3\text{Al}$  are displayed in Table 2.2 [31-36]. These values actually determine the relative stability of the planar faults, which plays a key role in dislocation dissociation on  $\{111\}$  planes. Of course, the dissociation of dislocations are more complex here due to the large Burgers vector involved [37]. Various dissociation models have been proposed [38-40], which are illustrated in Figure 2.16.

**Table 2.2** Fault energies in  $\text{Ni}_3\text{Al}$  (mJ/m)

$\gamma_{APB}$ (111)	$\gamma_{CSF}$ (010) (111)		$\gamma_{SISF}$ (111)	Reference
111±15	90±5		10±5	31
156	28	259	96	32
142	83		13	33
180±20		206±30		34
175		225		35
170		240		36

Out of the different types of faults, APBs are the most common in  $\text{Ni}_3\text{Al}$  [41, 42], while SISF dissociation is also observed [41, 43, 44]. Straight screw dislocations are frequently observed as dipoles in  $\text{Ni}_3\text{Al}$  [45, 46]. Veyssière *et al* [47] observed APB and CSF coupled dissociations in  $\text{Ni}_3\text{Al}$  at high temperatures.

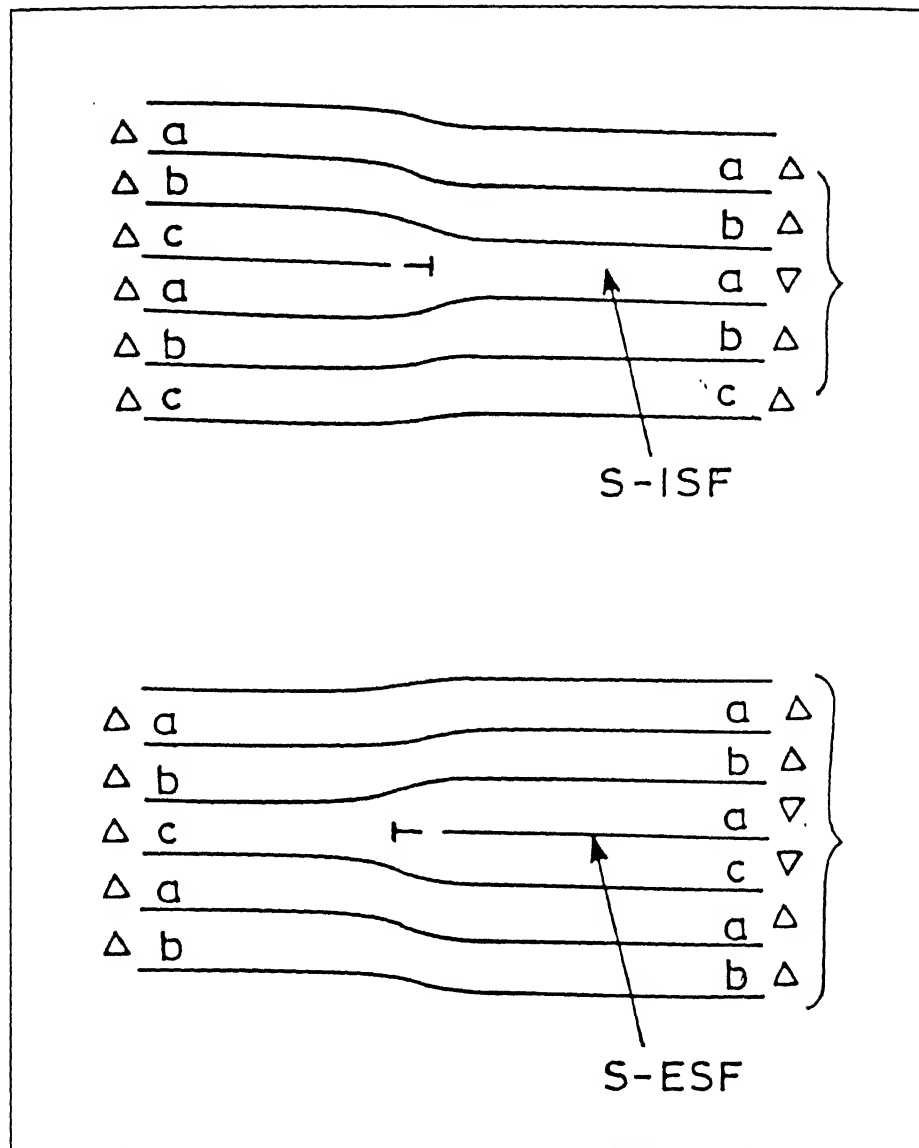
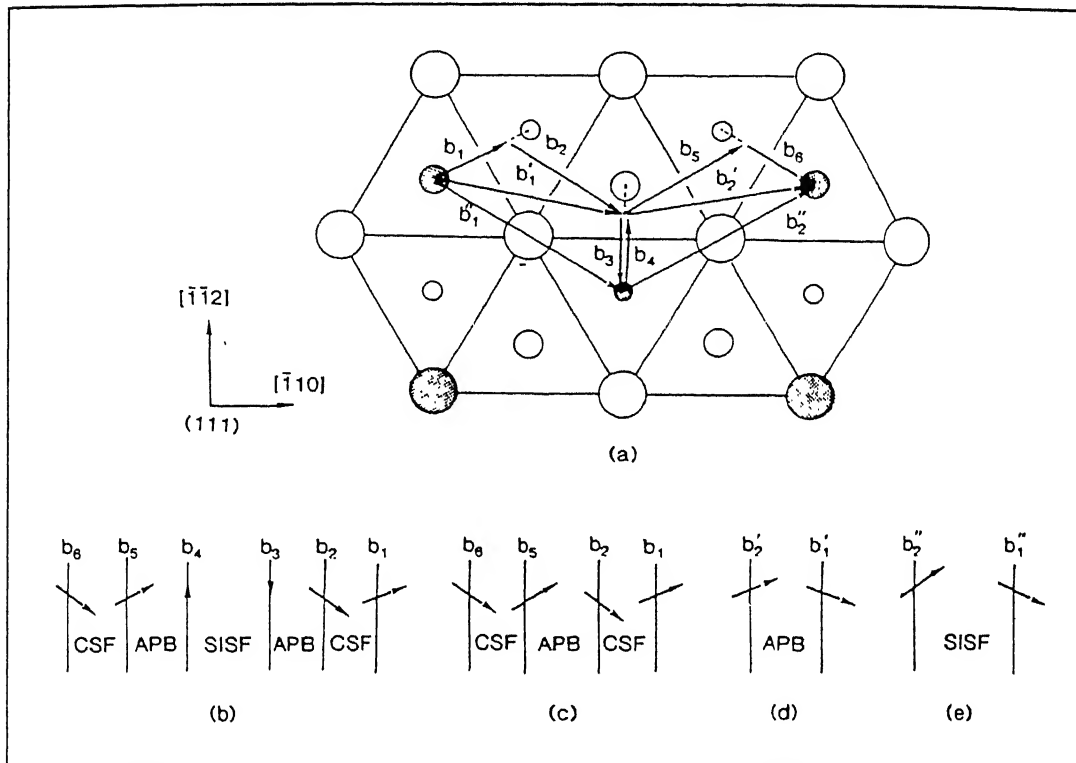


Figure 2.15 Intrinsic ( $DO_{19}$ ) and extrinsic ( $DO_{24}$ ) faults associated with a Frank sessile in the  $L1_2$  structure [30]



**Figure 2.16** Atomic arrangement and possible dissociation schemes

for  $[\bar{1}10]$  dislocation on  $(111)$  in the  $L1_2$  structure;

(a) types of dissociation, (b) six-fold, (c) four-fold,

(d) two-fold (APB splitting) and (e) two-fold (SISF splitting) [38-40]

## 2.5 Deformation Modes in Ni<sub>3</sub>Al

Ni<sub>3</sub>Al, like other FCC materials, deforms by  $\{111\}\langle 110 \rangle$  slip at room temperature. Significant changes in deformation behaviour are noticed at higher temperatures, and also at room temperature with higher deformation levels.

At higher temperatures, there is a changeover from  $\{111\}\langle 110 \rangle$  octahedral slip to  $\{001\}\langle 110 \rangle$  cubic slip [48], which actually results in flow stress increment. Yamaguchi and Umakoshi [28] reported that the CRSS for  $\{001\}\langle 110 \rangle$  slip obeys Schmid's law while that for  $\{111\}\langle 110 \rangle$  slip depends on crystal orientation. Another difference is that the flow stress for cubic slip is very much sensitive to the strain rate, whereas that for octahedral slip has negligible strain rate sensitivity.

Twinning could be another possible mode of deformation in ordered Ni<sub>3</sub>Al. A twin can be produced if the Shockley partials move on consecutive  $\{111\}$  planes [49]. However, due to this movement, a CSF will be produced simultaneously, but the existence of such faults has never been found in Ni<sub>3</sub>Al at low temperature as they are associated with higher fault energy. The primary twin system in L1<sub>2</sub> structure is  $\{111\}\langle \bar{1}21 \rangle$  which requires atomic shuffling on every other twin plane, leading to low mobility of twinning dislocations. The shear stress in the complimentary twin system is twice as large but it requires no atomic shuffling. The evidence of CSF at higher temperature [47] was correlated with the concept that the required atomic shuffling is not difficult at that temperature which may lead to twin formation.

Twinning was observed by Ghosh Chowdhury *et al* [50] during the cold rolling of Ni<sub>3</sub>Al(B). They reported a structural transformation from L1<sub>2</sub> to DO<sub>22</sub> crystal structure after 65% cold rolling. DO<sub>22</sub> is basically an ordered tetragonal structure which deforms by twinning,  $\{112\}$  being the principal twin plane. They proposed that Ni<sub>3</sub>Al with L1<sub>2</sub> structure deforms by slip at lower deformation level. After a certain rolling deformation, the material undergoes a strain induced structural transformation (from L1<sub>2</sub> to DO<sub>22</sub>) and the resulting DO<sub>22</sub> struc-

ture deforms by twinning at still higher levels of deformation. Figure 2.17 shows the X-ray intensity profiles of their  $\text{Ni}_3\text{Al(B)}$  samples cold rolled by different amounts. The gradual changes in the XRD patterns indicate the structural transformation which was essentially complete at around 65% deformation.

## 2.6 Mechanical Properties

$\text{Ni}_3\text{Al}$  is a structural intermetallic material with good oxidation resistance. Strength of the  $\text{Ni}_3\text{Al}$  family of materials is quite high. Grala [51] reported tensile data of  $\text{Ni}_3\text{Al}$ , tested at several conditions. For different situations, yield strength of  $\text{Ni}_3\text{Al}$  varied from 100 to 150 MPa, and tensile strength from 170 to 340 MPa. However, the percentage elongation was not very satisfactory. Later, superior material development techniques boosted the mechanical properties of this alloy. Schulson *et al* [52] observed the dramatic effect of boron doping on the percentage elongation of  $\text{Ni}_3\text{Al}$ . The mechanical properties investigated by them on a number of  $\text{Ni}_3\text{Al}$  samples are listed in Table 2.3.

**Table 2.3 Mechanical Properties of  $\text{Ni}_3\text{Al}$**

<i>Alloy</i>	<i>Grain Size (<math>\mu\text{m}</math>)</i>	<i>Yield Strength (MPa)</i>	<i>Hardness (RA-60Kg)</i>	<i>Elongation (%)</i>
$\text{Ni}_3\text{Al}$	$3\pm 0.3$	$947\pm 21$	$69.9\pm 0.9$	0.0
	$10\pm 1$	$413\pm 14$	$60.2\pm 0.9$	$0.6\pm 0.4$
	$75\pm 5$	$155\pm 3$	$50\pm 1.5$	$0.2\pm 0.2$
	$827\pm 99$	$137\pm 3$	$45\pm 2.9$	compression
$\text{Ni}_3\text{Al} + \text{B}$	$2.7\pm 0.8$	$887\pm 100$	$66.3\pm 1.1$	$22.7\pm 2.2$
	$10\pm 0.8$	$454\pm 41$	$58.9\pm 1.2$	$20.5\pm 7.3$
	$75\pm 5$	$272\pm 5$	$51.9\pm 0.8$	compression
	$831\pm 71$	$277\pm 8$	$53.1\pm 0.5$	compression

Fujita *et al* [53] tested a number of specimens of  $\text{Ni}_3\text{Al}$  with and without boron, at room temperature as well as elevated temperatures. The room temperature testing data are shown in Table 2.4, which also shows the effect of boron addition. They further studied the effect

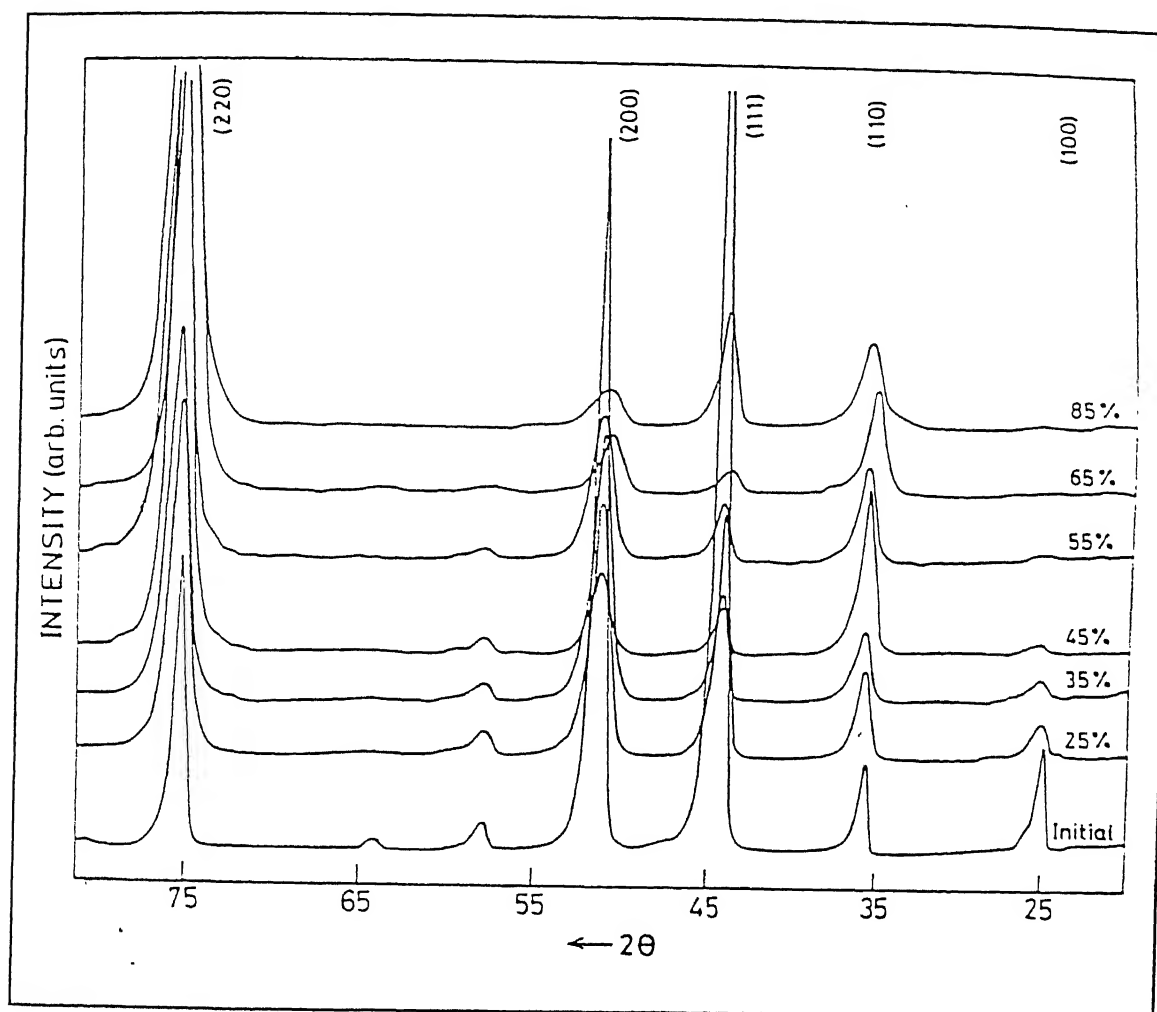


Figure 2.17 XRD line profiles of  $\text{Ni}_3\text{Al(B)}$  at different degrees of cold rolling [25]



of several alloying additions, and observed that the high temperature tensile properties were nearly comparable or even better than those of commercial Inconel 713C alloy.

**Table 2.4** Tensile properties of Ni<sub>3</sub>Al

Composition	0.2% Proof Stress (MPa)	Tensile Strength (MPa)	Elongation (%)	R.A. (%)
Ni <sub>3</sub> Al	150	—	2.3	3.4
Ni <sub>3</sub> Al+0.05B(wt%)	170	610	33.7	42.3
Ni <sub>3</sub> Al+0.1B(wt%)	240	910	27.8	29.6

### 2.6.1 Effect of Grain Size, Temperature and Alloy Addition

The effects of grain size and temperature on the mechanical properties of Ni<sub>3</sub>Al were studied by several investigators [54-57]. Weihs *et al* [54] carried out extensive studies on the effect of temperature and grain size on the yield strength of a boron doped and stoichiometric Ni<sub>3</sub>Al. They found that grain size played a vital role at higher temperature, and larger grain boundary area drastically softened the material (Figure 2.18). They also recorded microhardness data with grain size and found that boron actually reduced the magnitude of the Hall-Petch slope (Figure 2.19). Schulson *et al* [55] reported that the room temperature yield strength  $\sigma_y$  did not obey the Hall-Petch relation, rather it was observed to maintain a linear relationship with  $d^{-0.8}$ , where  $d$  indicates the grain size in  $\mu\text{m}$  (Figure 2.20).

Takeyama and Liu [56] worked on the ductility of boron doped Ni<sub>3</sub>Al, and reported that a smaller grain size gave the best results (Figure 2.21) within the range of 600° – 700°C. above which the material with larger grain size underwent premature fracture. Kim *et al* [57] observed that increasing grain size decreased the fracture strain. Srivatsan and Sriram [58] also carried out a number of tensile tests in different environments and concluded that aqueous environment drastically reduced the strength of Ni<sub>3</sub>Al.

Ochiai *et al* [59] investigated the effect of alloying with B-subgroup elements (e.g. Si, Ga, Ge, In, Sn, Sb etc.) and observed remarkable enhancement in tensile properties of Ni<sub>3</sub>Al

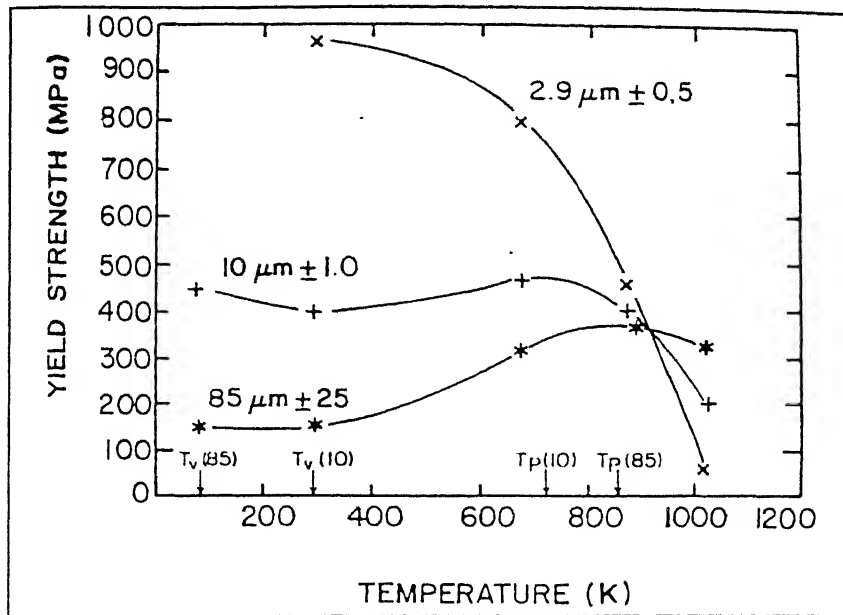


Figure 2.18 Yield strength versus temperature for stoichiometric  $\text{Ni}_3\text{Al}$  of three different grain sizes [54]

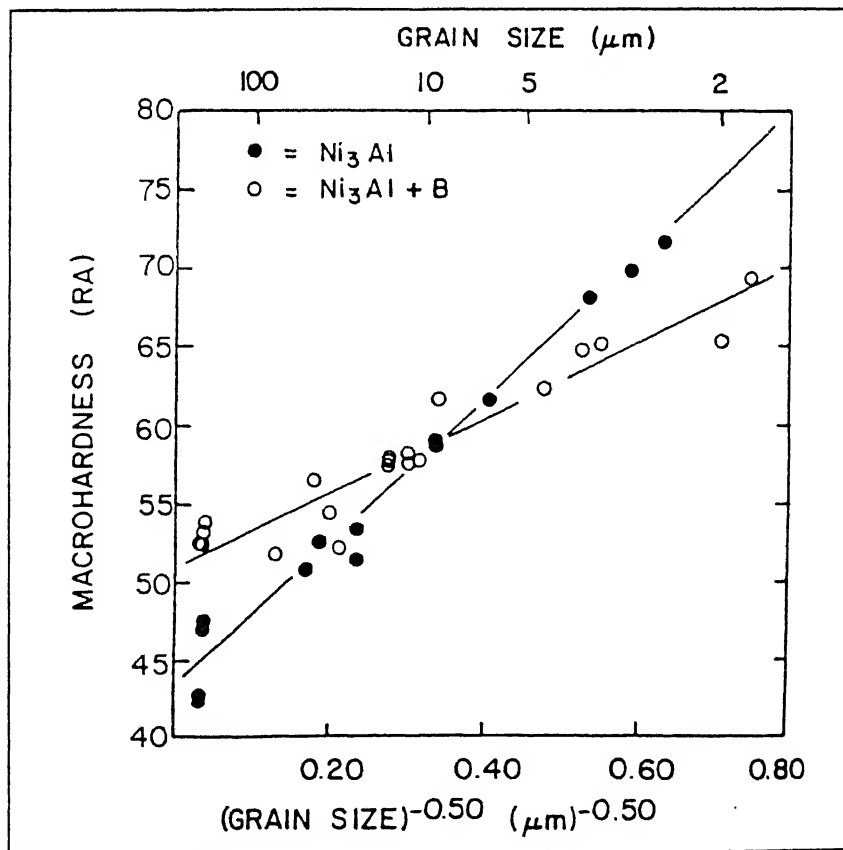


Figure 2.19 Hardness versus  $(\text{grain size})^{-0.5}$  for  $\text{Ni}_3\text{Al}$  and  $\text{Ni}_3\text{Al}+\text{B}$  [54]

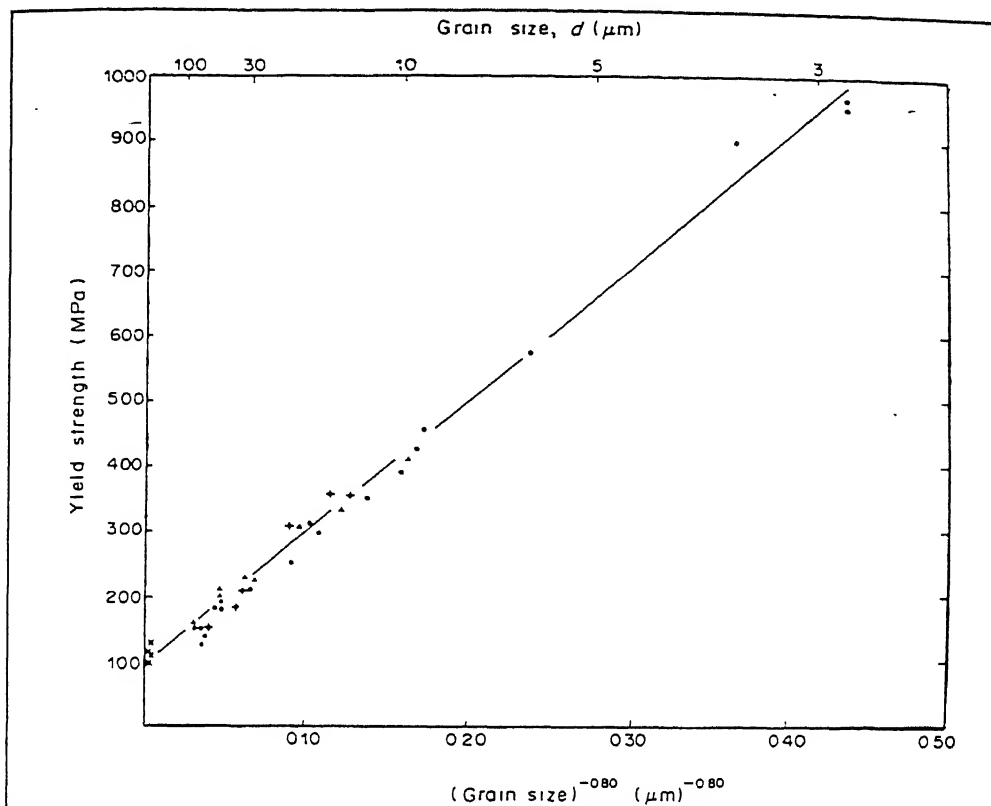


Figure 2.20 Yield strength versus  $(\text{grain size})^{-0.8}$  for  $\text{Ni}_3\text{Al}$  at room temperature [55]

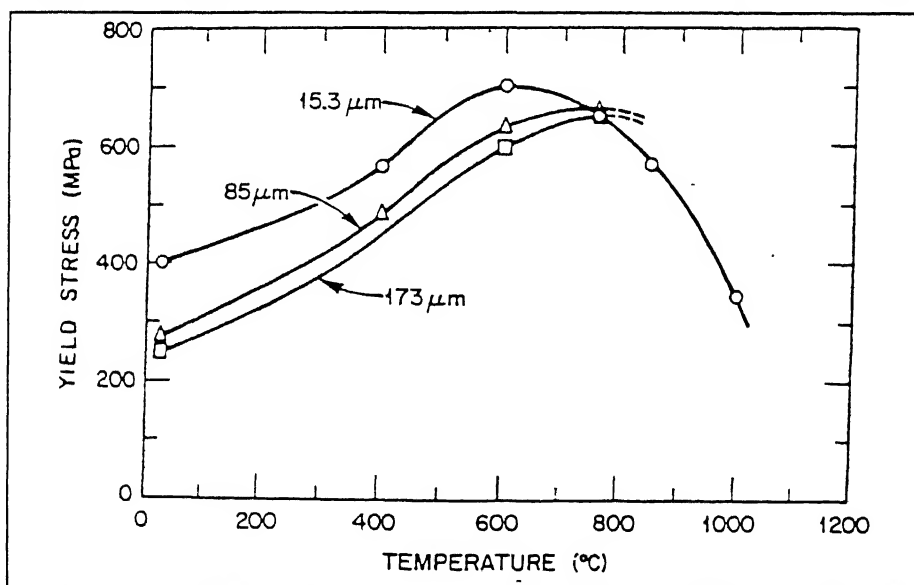


Figure 2.21 Changes in yield stress with temperature for boron - doped  $\text{Ni}_3\text{Al}$  of different grain sizes [56]

by addition of a third element. Mishima *et al* [60] who studied the effect of alloying with transition metals (e.g. Ti, Zr, Hf, V, Nb, Mo, Ta, W etc.), also reported excellent improvement of mechanical properties through alloying. These effects are shown in Figure 2.22, which actually features the effects on flow stress of  $\text{Ni}_3\text{Al}$  by the addition of Sn (a B-subgroup element) and Hf (a transition element). The next set of diagrams (Figures 2.23a and 2.23b) illustrates the enhancement of flow stress at a fixed temperature by the alloying addition (both B-subgroup and transition elements), and compares the solid solution strengthening ability of the different solutes. In another study, Mishima *et al* [61] measured the Young's modulus of  $\text{Ni}_3\text{Al}$  as a function of solute concentration: and found that the B-subgroup elements, in general, decreased the Young's modulus while the transition elements (except Hf) enhanced the elastic modulus.

Srivatsan *et al* [62] observed the influence of cold deformation and annealing on the tensile behaviour of  $\text{Ni}_3\text{Al}$  alloyed with boron and zirconium. Using different strain rates, they observed a tremendous increase in the tensile strength, upto about 1850 MPa.

## 2.6.2 Yield Stress Anomaly

$\text{Ni}_3\text{Al}$  shows a substantial increase in yield strength with temperature, in case of both single crystal and polycrystalline materials. This phenomenon was first detected by Flinn [63] in polycrystalline  $\text{Ni}_3\text{Al}$ . Figure 2.24a shows the yield stress variation of  $\text{Ni}_3\text{Al}$  with temperature where a peak can be seen at around  $800^\circ\text{C}$ . The peak height and position are not fixed, they depend on several parameters such as crystal orientation, alloy stoichiometry, solute addition, grain size and strain rate. Figure 2.24a actually shows the effect of alloy stoichiometry on the peak height. Figure 2.24b shows similar behaviour exhibited by another  $\text{L1}_2$  intermetallic alloy,  $\text{Ni}_3\text{Ga}$  [14]. In both the cases, higher concentrations of the minority component, i.e. Al or Ga, have been found to increase the peak height. Noguchi *et al* [14] attributed this phenomenon to the significant defect hardening effect in the Al or Ga rich intermetallic

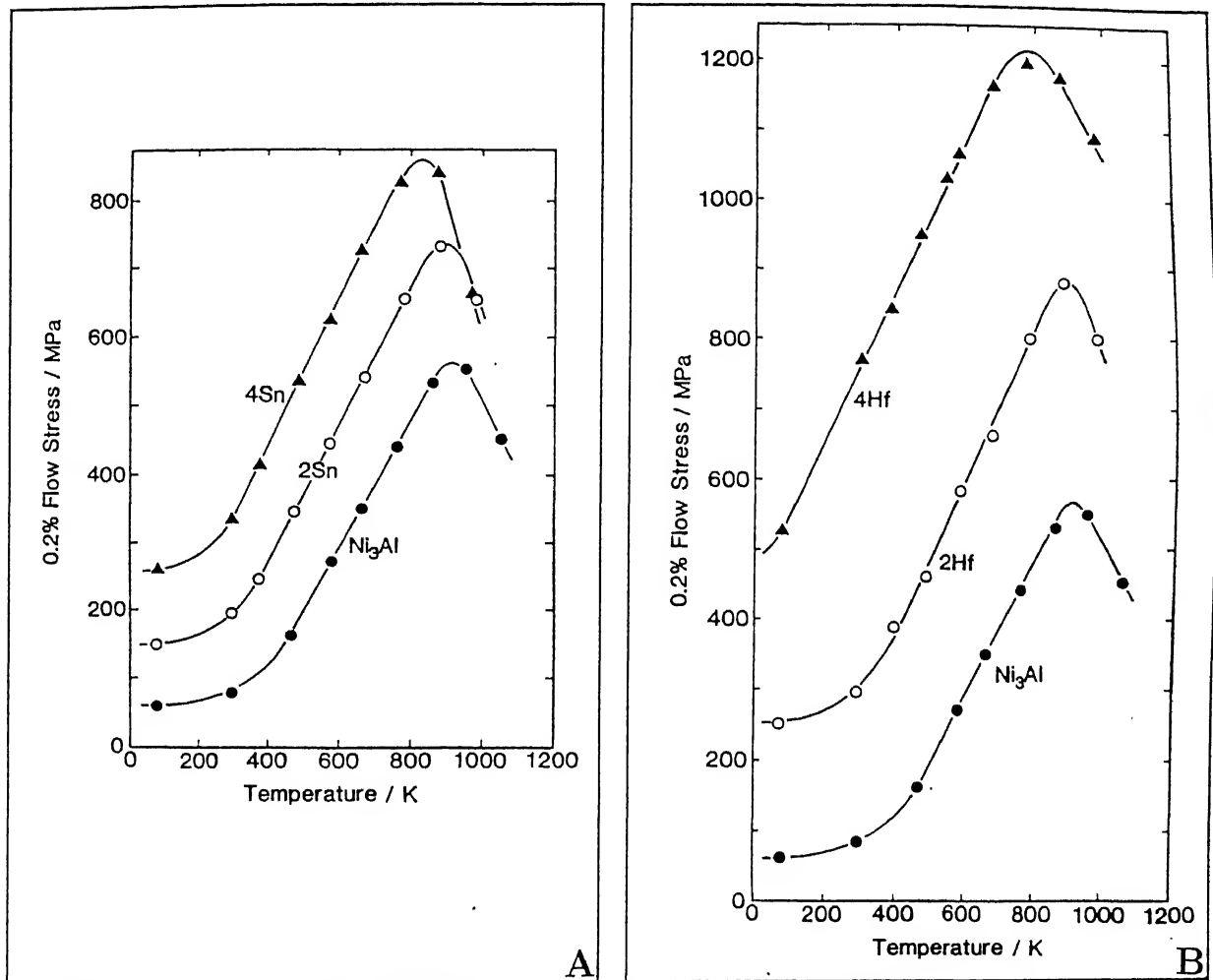
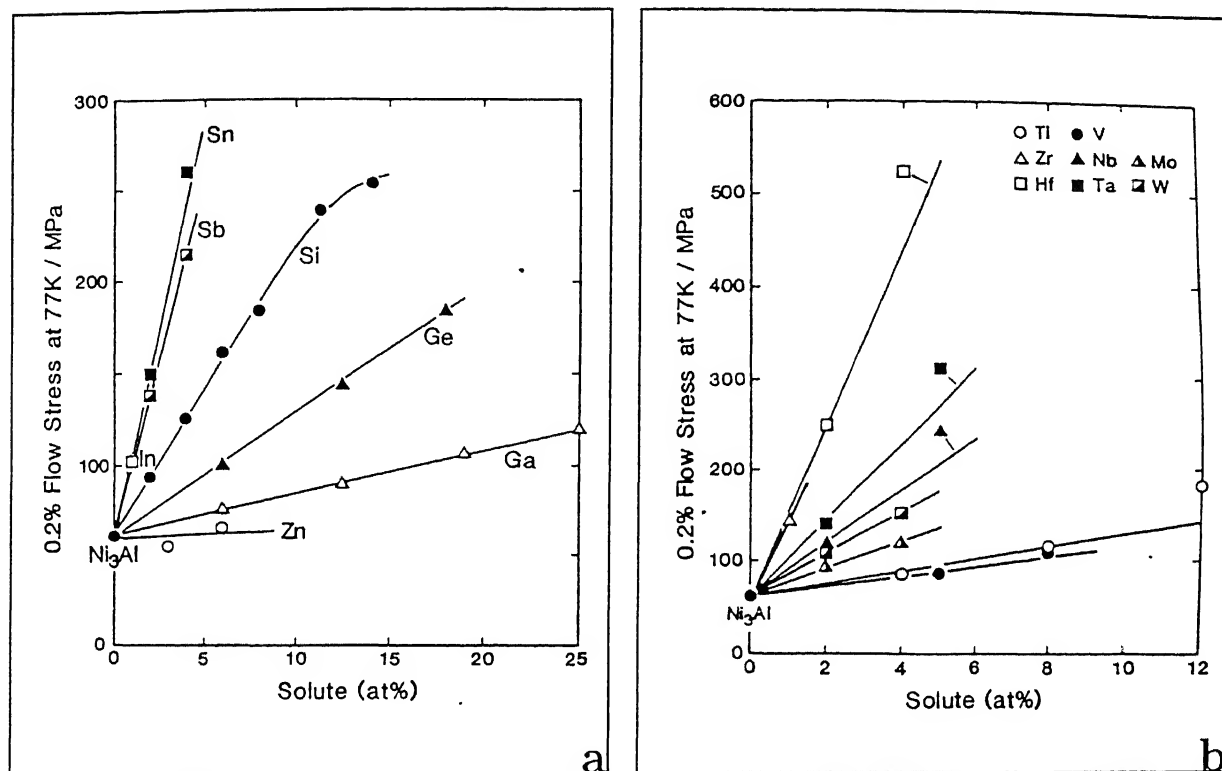


Figure 2.22 Temperature dependence of 0.2% flow stress in  $\text{Ni}_3\text{Al}$ :

(a) with addition of Sn [59], (b) with addition of Hf [60]



**Figure 2.23** Relation between 0.2% flow stress measured at 77K and the solute concentration in ternary  $\text{Ni}_3\text{Al}$ ;  
 (a) with addition of B-subgroup elements [59],  
 (b) with addition of transition elements [60]

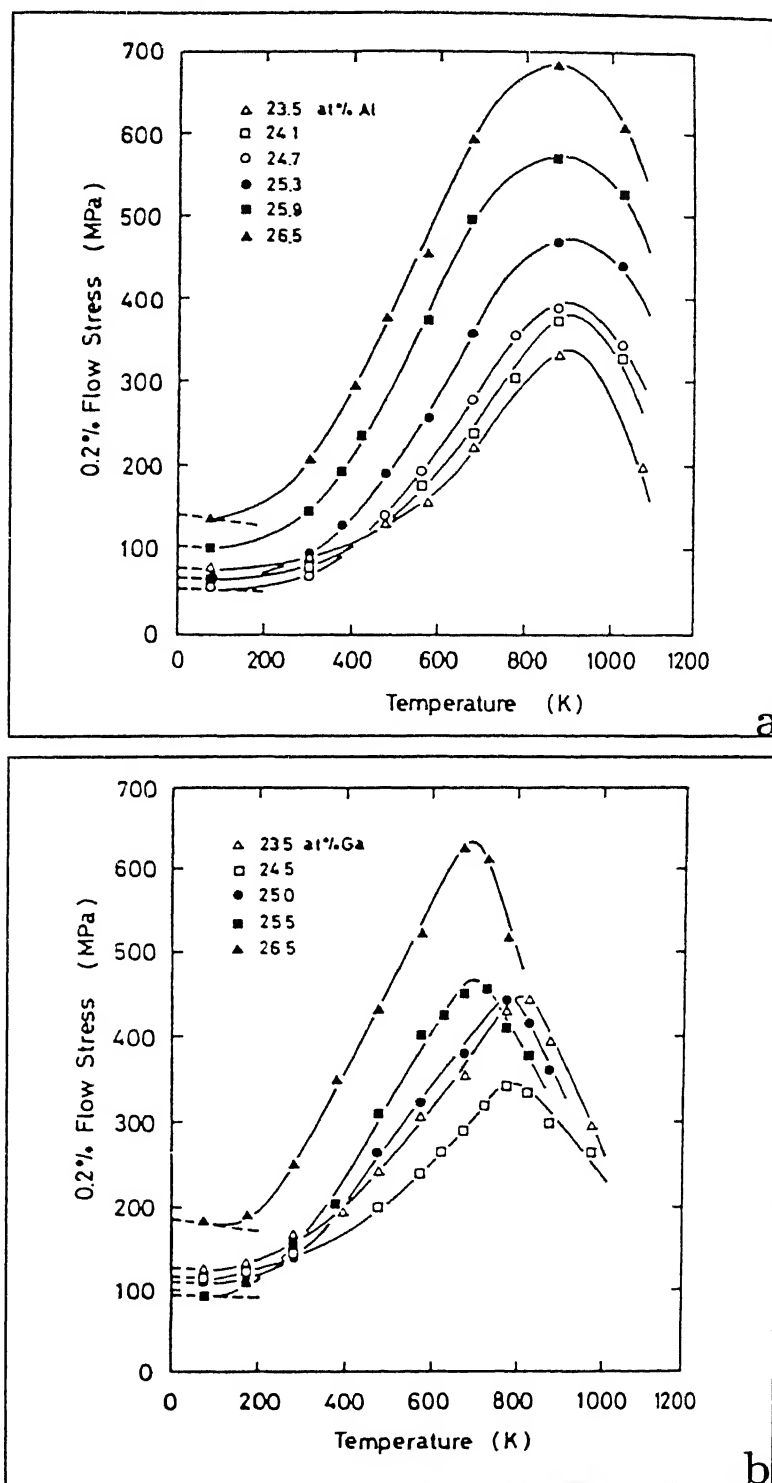


Figure 2.24 Temperature dependence of the 0.2% flow stress of  
(a) the  $Ni_3Al$  alloys and (b) the  $Ni_3Ga$  alloys [14]

alloys.

Thornton *et al* [48] found that alloying additions substantially altered the flow stress peak height and position (Figure 2.25a). They also observed the effect of microstrain on the temperature dependence of flow stress. Figure 2.25b schematically shows their experimental results, which indicate that at a very low strain level, the flow stress remains constant throughout a wide range of temperatures. The peak flow stress was found to increase at higher strain levels. They suggested that at very low strains, the dislocations are sufficiently mobile at constant stress, irrespective of the testing temperature.

Lall *et al* [64] observed that the flow stress of  $\text{Ni}_3(\text{Al.Nb})$  single crystals changed under the combined influence of temperature and orientation. They carried out compression tests along various crystallographic directions and found that the compression axis was an important factor which altered the flow stress peak height and position (Figure 2.26). Umakoshi *et al* [65] also performed flow stress measurements on  $\text{Ni}_3(\text{Al.Ti})$  as a function of temperature, orientation, strain rate and sense of the applied uniaxial stress. They found that the CRSS for  $(111)[\bar{1}01]$  slip depends on the sense of the applied stress also, apart from temperature and orientation of the samples. They further observed that the CRSS for octahedral slip  $(111)[\bar{1}01]$  is strain rate independent, but the CRSS for cubic slip  $(001)[\bar{1}10]$  is highly dependent on strain rate.

Several mechanisms have been suggested so far to explain the anomalous yield stress behaviour of  $\text{Ni}_3\text{Al}$ . The core configurations and mobilities of dislocations on  $\{111\}$  and  $\{001\}$  planes have been advanced as the most important factors. Kear and Wilsdorf [66] were the first to propose a *cross-slip* mechanism in which a screw dislocation moving on  $\{111\}$  glide planes may partially cross slip on to the energetically favourable  $\{001\}$  planes (Figure 2.27), thereby reducing the mobility of the dislocation as a whole. This leads to an increase in the flow stress of the material. This effect is much more prominent at higher temperatures as the thermal energy facilitates the cross slip process.



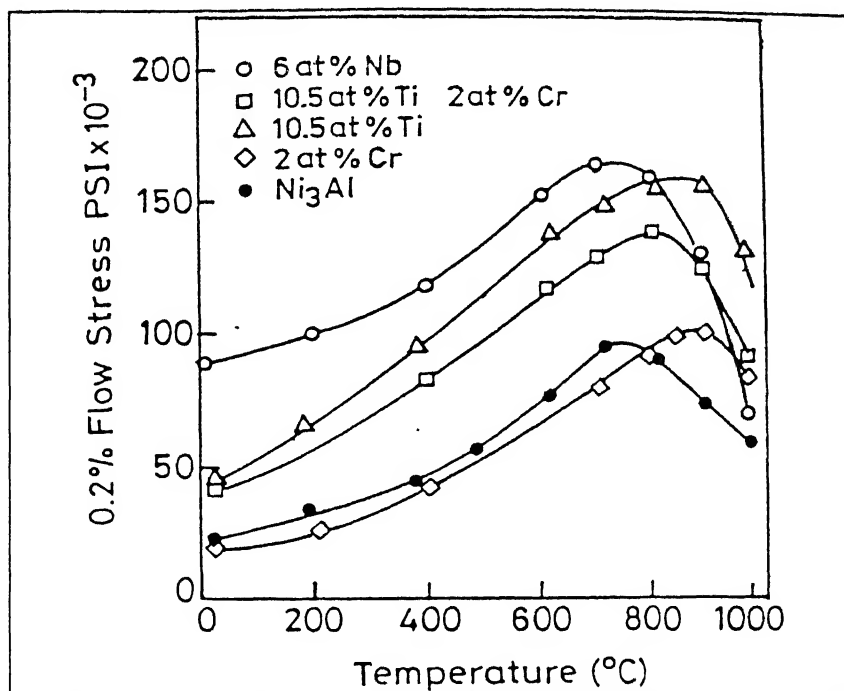


Figure 2.25a Effect of alloying additions upon the temperature dependence of the flow stress of  $\gamma'$  [48]

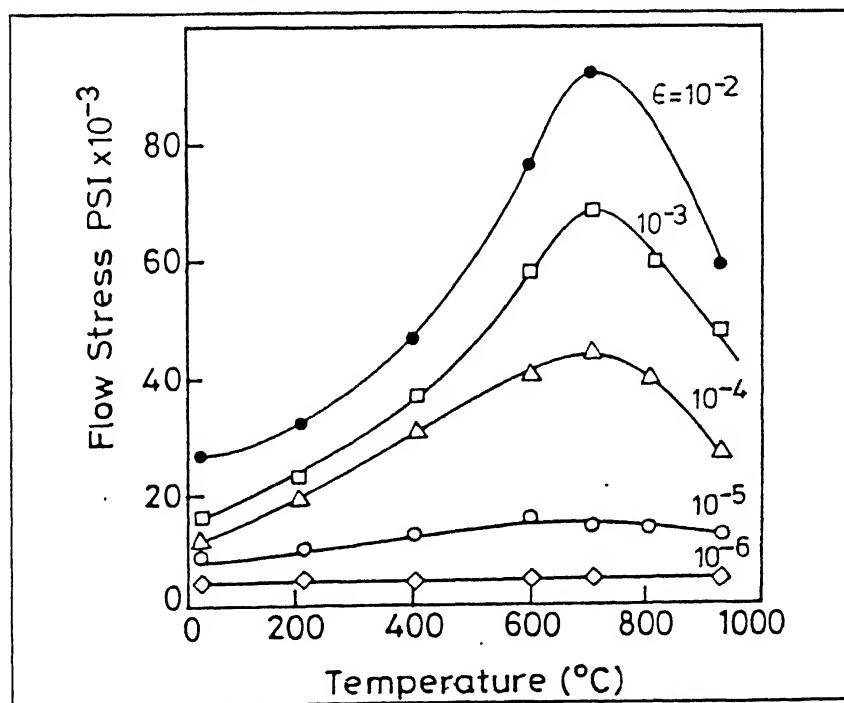


Figure 2.25b Microstrain yield stress as a function of temperature in  $\text{Ni}_3\text{Al}$  [48]

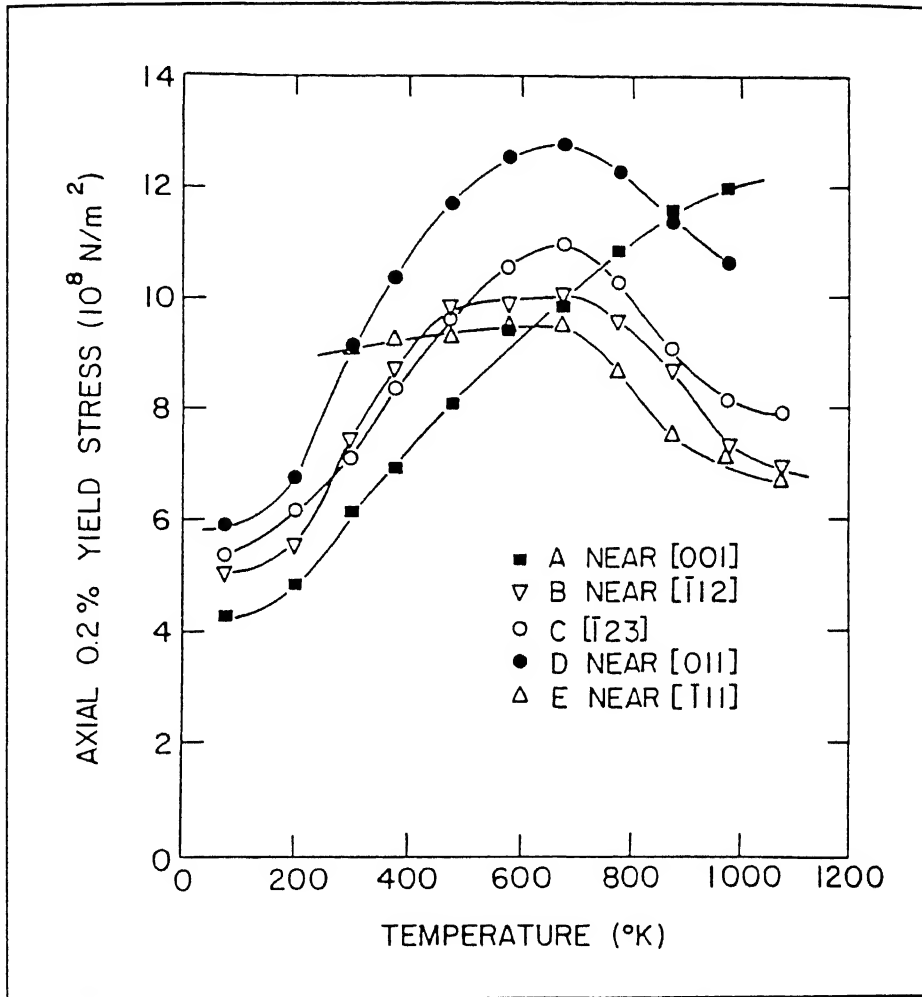


Figure 2.26 The axial 0.2% flow stress as a function of temperature for five orientations of  $\text{Ni}_3(\text{Al,Nb})$  single crystals [64]

Flinn [63] suggested that a screw dislocation pair, separated by APB, can reduce its energy by changing the common plane from the octahedral slip plane to a cube plane. The driving force for this process is the lowering of APB energy on (010) glide plane. Cohen and Bever [67] explained the line broadening features in strained  $\text{Cu}_3\text{Au}$  in terms of an increase in antiphase boundaries in  $\{100\}$  and  $\{111\}$  planes. It means that during plastic deformation of ordered  $\text{L}_{12}$  alloy, the formation of APB on cubic planes can enhance the flow stress which is much more prominent at higher temperatures due to the ease of cross slip.

Using the concept of Flinn [63], Takeuchi and Kuramoto [68] illustrated a *dynamical breakaway* model, which is schematically shown in Figure 2.28. In this model, the superlattice dislocations extensively move on the  $\{111\}$  planes. The free motion of the dislocations is inhibited by a periodic distribution of pinning points, which are locations where  $\{010\}$  cross slip takes place. As a result, the dislocations bow out near the obstacles. The mean distance between the pinning points,  $l$ , is inversely proportional to the frequency of the  $\{010\}$  cross slip. The number of pinning points the frequency of the  $\{010\}$  cross slip. The numbening an Arrhenius relation, thereby increasing the flow stress of the material.

Paidar *et al* [69] added the concept of core configuration of dislocations to explain the anomalous yield behaviour of  $\text{Ni}_3\text{Al}$ . According to them, the core configuration of the superpartials will be such that their movement on the cube plane  $\{001\}$  will be difficult enough, leading to an increase in the flow stress (Figure 2.29a). They suggested that the oval shaped core of a  $\frac{1}{2}[\bar{1}01]$  superpartial lies on the (111) plane. When cross-slip of the superpartial takes place on the (010) plane, the oval shaped dislocation core, lying on (111) or  $(1\bar{1}1)$  plane effectively impedes the dislocation motion. The *cross-slip pinning* model (Figure 2.29b) suggested by them illustrates that cross slip takes place rather partially, instead of a complete transfer to the cube plane, as suggested by Kear and Wilsdorf [66]. Hirsch [70] proposed another model in which the barriers to slip were identified as edge dislocation dipoles formed at the ends of screw segments which have cross slipped into the  $\{010\}$  planes.

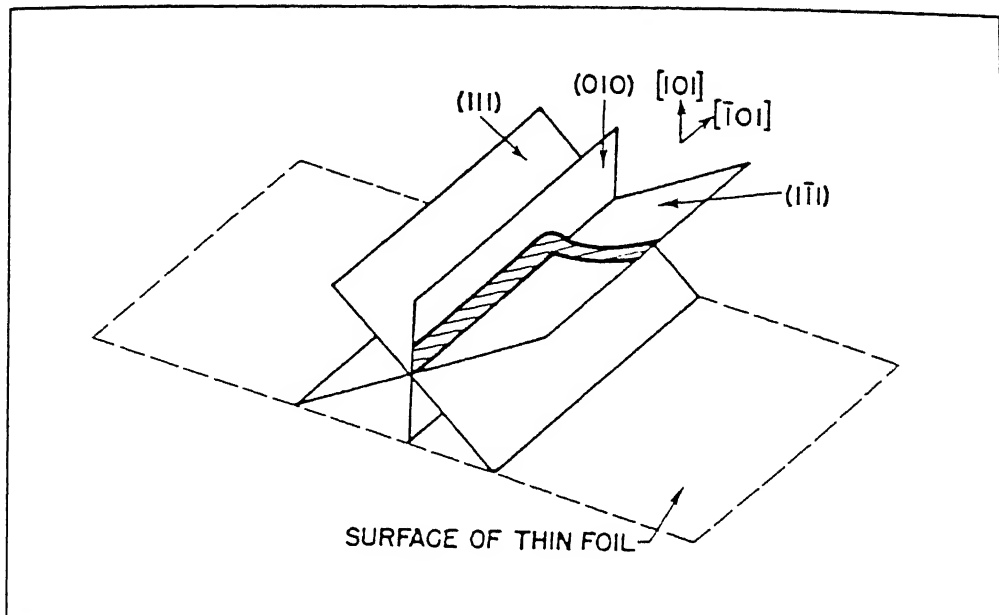


Figure 2.27 Schematic representation of cross slip of a screw dislocation pair from the slip plane into a cube plane [66]

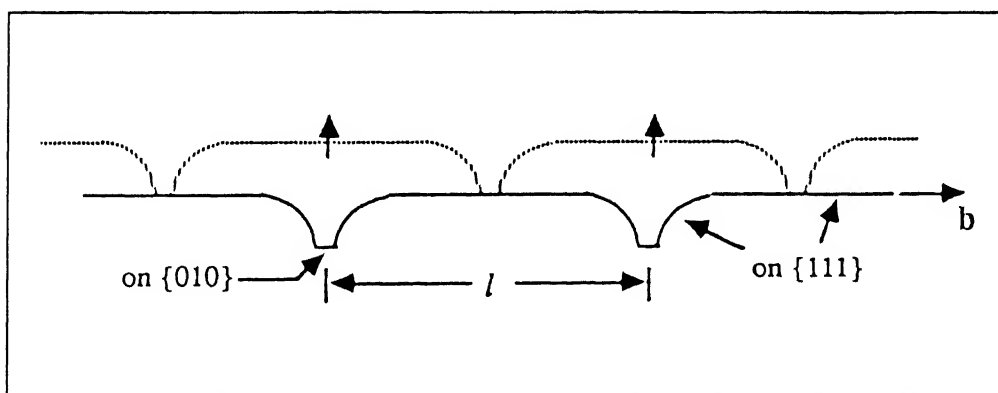


Figure 2.28 Illustration of the cross slip pinning showing the successive positions of a superlattice screw dislocation on  $\{111\}$  by the *dynamical breakaway* from pinning points on  $\{010\}$ ;  $b$  is the Burgers vector [68]

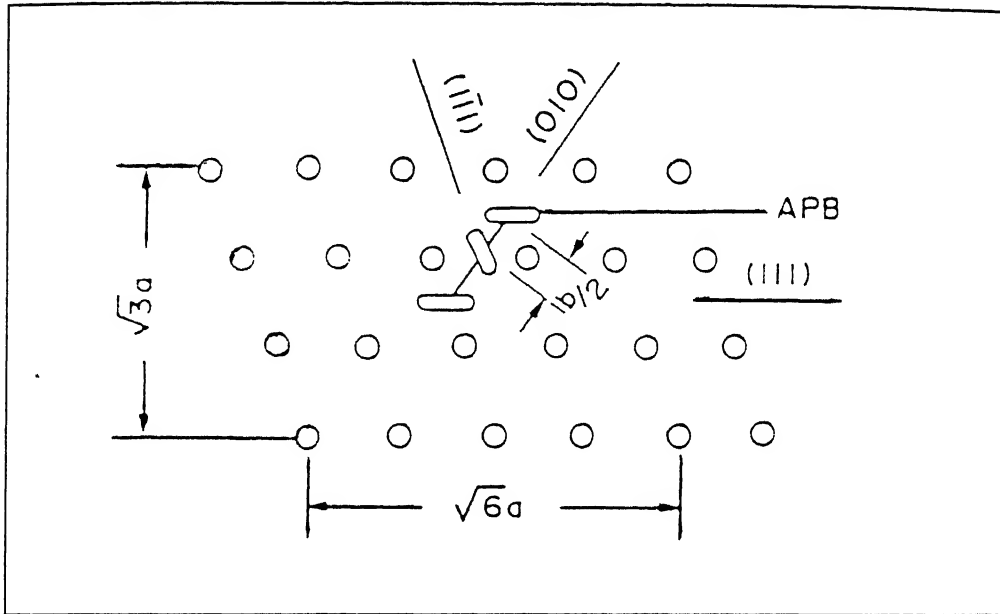


Figure 2.29a The oval shaped core configuration of the  $\frac{1}{2}[\bar{1}01]$  superpartial [69]

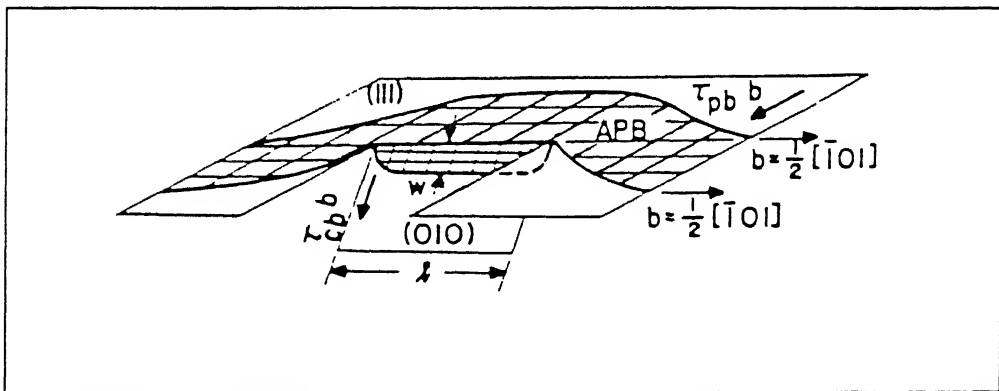


Figure 2.29b A schematic view of the partial cross slip of one superpartial from the (111) to the (010) plane [69]

### 2.6.3 Ductility of $\text{Ni}_3\text{Al}$ and its Improvement

Brittleness has been found to be an inherent problem for polycrystalline  $\text{Ni}_3\text{Al}$  intermetallics. Despite high strength and good corrosion resistance its fabricability is extremely poor due to the tendency of cleavage fracture at grain boundary regions. On the other hand,  $\text{Ni}_3\text{Al}$  single crystal exhibits a good amount of ductility [71]. The suggested reasons for the poor ductility of polycrystalline  $\text{Ni}_3\text{Al}$  may be classified as [4, 72]:

- Intrinsic factors like weak grain boundary cohesion, poor cleavage strength and insufficient slip system.
- Extrinsic factors like impurity segregation to grain boundaries and environmental embrittlement.

Liu and Sikka [73] investigated the ductility of an off-stoichiometric  $\text{Ni}_3\text{Al}$  alloy ( $\text{Ni}_{21.5}\text{Al}_{0.5}\text{Hf}_{0.1}\text{B}_{0.1}$  at.%), and found that its tensile ductility is extremely poor within the temperature range of  $600^\circ - 800^\circ\text{C}$ . It gradually reaches a negligible value, then again improves with increasing temperature, as shown in Figure 2.30. It is interesting to note that the tensile ductility of  $\text{Ni}_3\text{Al}$  is minimum at the same temperature range in which the alloy shows the peak flow stress. Substantial improvement was achieved when the same alloy was tested in vacuum, although the nature of variation of ductility with temperature did not change.

The temperature dependence of the ductility of  $\text{Ni}_3\text{Al}$  was thoroughly studied by Choudhury *et al* [74]. They observed a massive enhancement of tensile ductility at above  $900^\circ\text{C}$ , while carrying out experiments on the tensile properties of an off-stoichiometric alloy, doped with 8 at.% Cr. Figure 2.31 illustrates the abrupt enhancement of elongation at above a certain temperature level, leading to superplastic behaviour.

According to Liu *et al* [2], poor grain boundary cohesion and environmental embrittlement are the most important reasons for the brittleness of polycrystalline  $\text{Ni}_3\text{Al}$ . Several

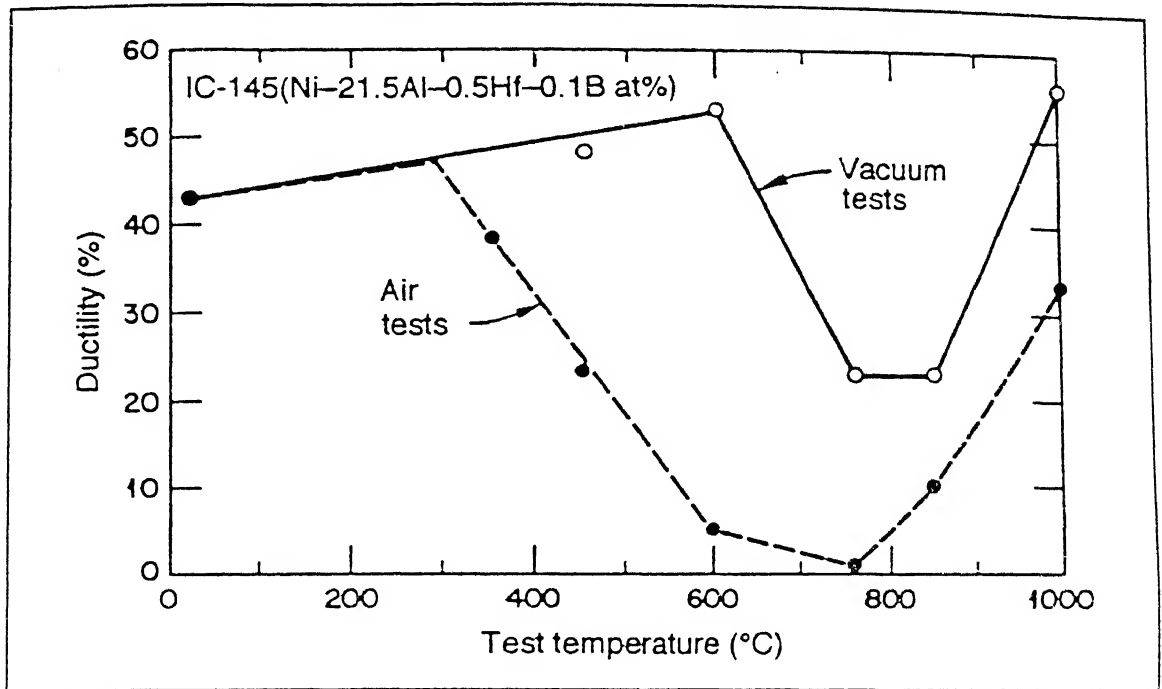


Figure 2.30 Comparison of tensile ductility of IC145 (Ni-21.5Al-0.5Hf-0.1B at.%) tested in vacuum and air [73]

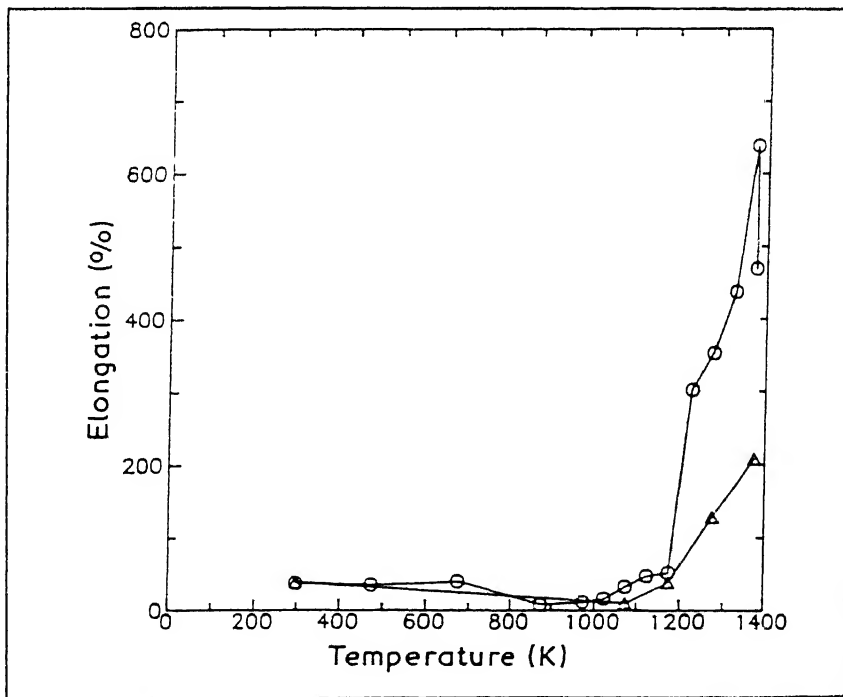


Figure 2.31 Temperature dependence of the percentage elongation of a Ni<sub>3</sub>Al base alloy with 8 wt.% Cr [74]

explanations have been put forward to account for this phenomenon. Takasugi and Izumi [75] observed that alloys having large valency difference between the constituent atoms were more prone to intergranular fracture. According to them, the heterogeneous distribution of electronic charge due to A-B bonding actually governed the grain boundary cohesive strength. Takasugi *et al* [76] observed the effect of ternary additions and found that third elements such as Mn and Fe which have similar electronic bonding nature as Ni prevented grain boundary fracture when they substituted for Al sites in  $\text{Ni}_3\text{Al}$  alloy. Taub and Briant [77], proposed that the electronegativity difference between the atoms of the constituent elements actually governs the grain boundary cohesion strength. King and Yoo [78] suggested that fewer dislocation reactions at an ordered grain boundary locks the dislocation motion, thereby creating strain inhomogeneity which ultimately leads to fracture. Vitek *et al* [79], using computer simulation, suggested that the grain boundaries of strongly ordered  $\text{L1}_2$  compounds must contain microvoids, which could act as nuclei for cracks causing cleavage fracture. Chiba *et al* [80] emphasized that higher ordering energy increases the tendency for intergranular fracture. Messmer and Briant [81] considered the role of chemical bonding and found that a strong embrittling element such as S drew charge from the host atom while forming bonds with it. As a result, less charge would be available for the formation of metal-metal bond, thereby lowering the cohesive force. In contrast, elements like B or Ni created an opposite effect in order to maintain the cohesive force at the grain boundary region.

Aoki and Izumi [71], in their experiments on  $\text{Ni}_3\text{Al}$  single crystals, observed nearly 100% tensile elongation at room temperature. The typical shear stress-strain curve is shown in Figure 2.32a, which indicates substantial ductility of the material. However, as mentioned before, the problem was with the polycrystalline ductility, and the experimental results were quite disappointing for the polycrystalline  $\text{Ni}_3\text{Al}$  samples. This material showed almost no tensile elongation; however, a little bit ductility was obtained during compression test



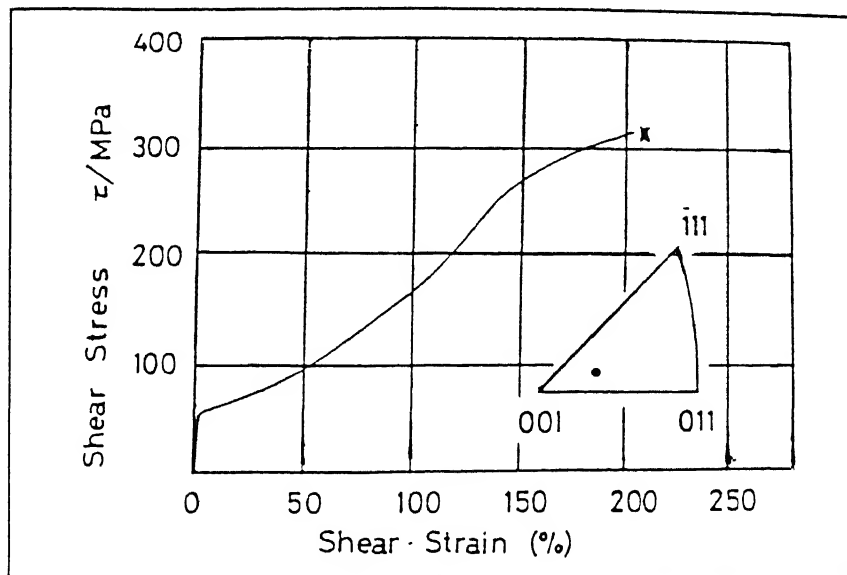


Figure 2.32a Typical tensile shear stress - shear strain curve of  $\text{Ni}_3\text{Al}$  single crystal at room temperature [71]

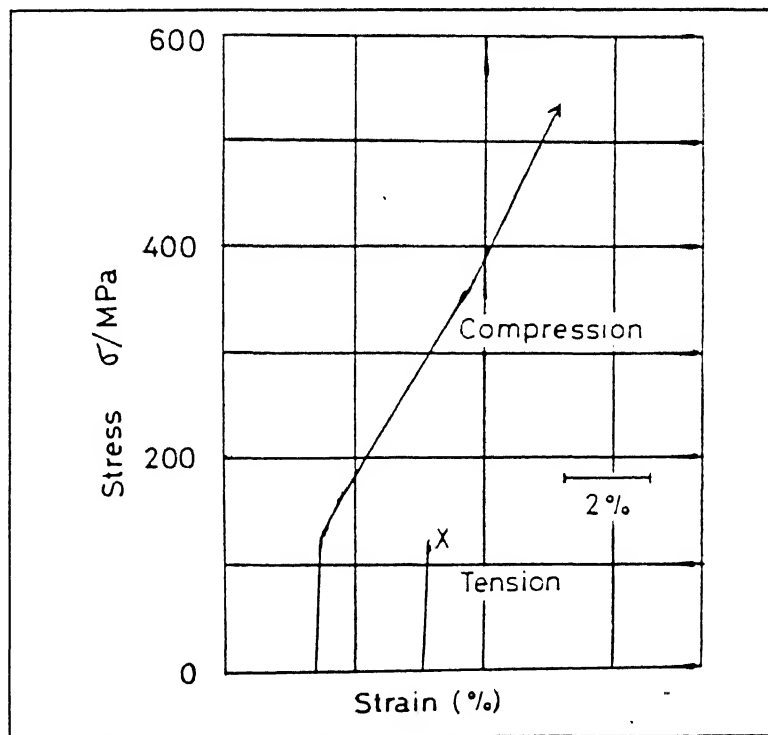


Figure 2.32b Tensile and compressive stress - strain curves of homogenized stoichiometric  $\text{Ni}_3\text{Al}$  polycrystal at room temperature [71]

CENTRAL LIBRARY  
IIT KANPUR

Vol. A 123608

(Figure 2.32b).

Several methods have been suggested to overcome the brittleness problem of polycrystalline  $\text{Ni}_3\text{Al}$ , the most important among which are enumerated below.

**I. Alloying with Boron :** In order to improve the ductility of polycrystalline  $\text{Ni}_3\text{Al}$ , microalloying with small amounts of other elements has been tried. The main aim always was how to alter the grain boundary chemistry, thereby improving the cohesive strength. Aoki and Izumi [1] noticed for the first time that boron could significantly improve the ductility of polycrystalline  $\text{Ni}_3\text{Al}$ , by changing the fracture mode from intergranular to transgranular.

Liu *et al* [2] carried out a systematic study of B-doped  $\text{Ni}_3\text{Al}$  and achieved tensile elongation of more than 50% by precisely controlling the alloy stoichiometry, the dopant concentration and the thermomechanical treatment. The effects of boron concentration and alloy stoichiometry on the room temperature tensile properties of  $\text{Ni}_3\text{Al}$  are shown in Figures 2.33a and 2.33b respectively. It was observed that boron addition was effective only in case of the hypostoichiometric (Ni-rich)  $\text{Ni}_3\text{Al}$ , not in the stoichiometric or the hyperstoichiometric (Al-rich) alloy. Impurity segregation at the grain boundary is definitely harmful, but this is not the only cause of embrittlement as the impurity free  $\text{Ni}_3\text{Al}$  also undergoes intergranular fracture [82, 83]. Koch *et al* [84] used rapid solidification technique in order to suppress the impurity segregation, even then the  $\text{Ni}_3\text{Al}$  foils became brittle. Therefore, it appears that poor grain boundary cohesion is an intrinsic limitation of this alloy, which could be solved by boron addition.

Boron has a strong tendency to segregate at grain boundary regions in  $\text{Ni}_3\text{Al}$ , particularly for the hypostoichiometric alloy, and this alters the grain boundary cohesive energy. The energy necessary to cause fracture ( $\gamma_f$ ) may be expressed by the following relationship:

$$\gamma_f = 2\gamma_s - \gamma_g \quad (2.1)$$

where,  $\gamma_s$  and  $\gamma_g$  are surface energy and grain boundary energy respectively. Liu *et al* [2]

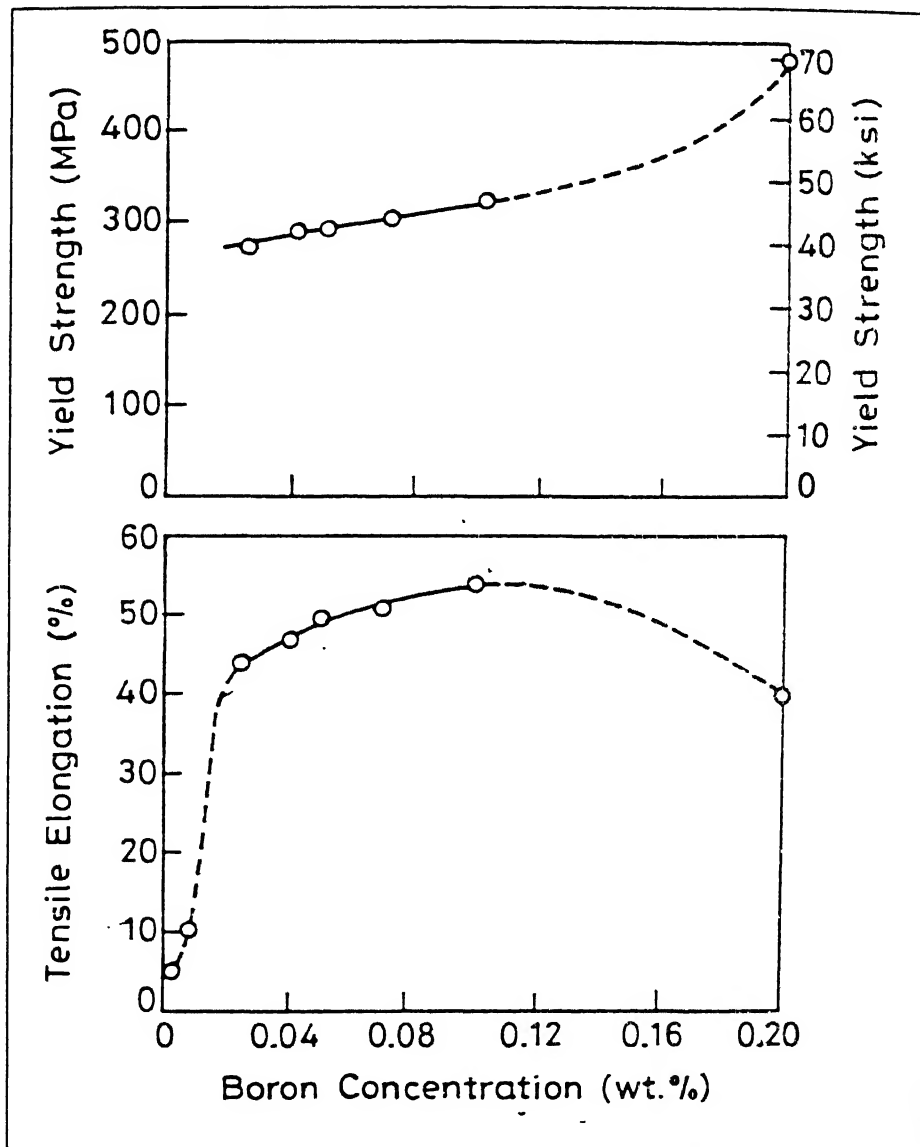


Figure 2.33a Plot of room temperature tensile properties as a function of boron concentration for  $\text{Ni}_3\text{Al}$  (24 at.% Al) [2]

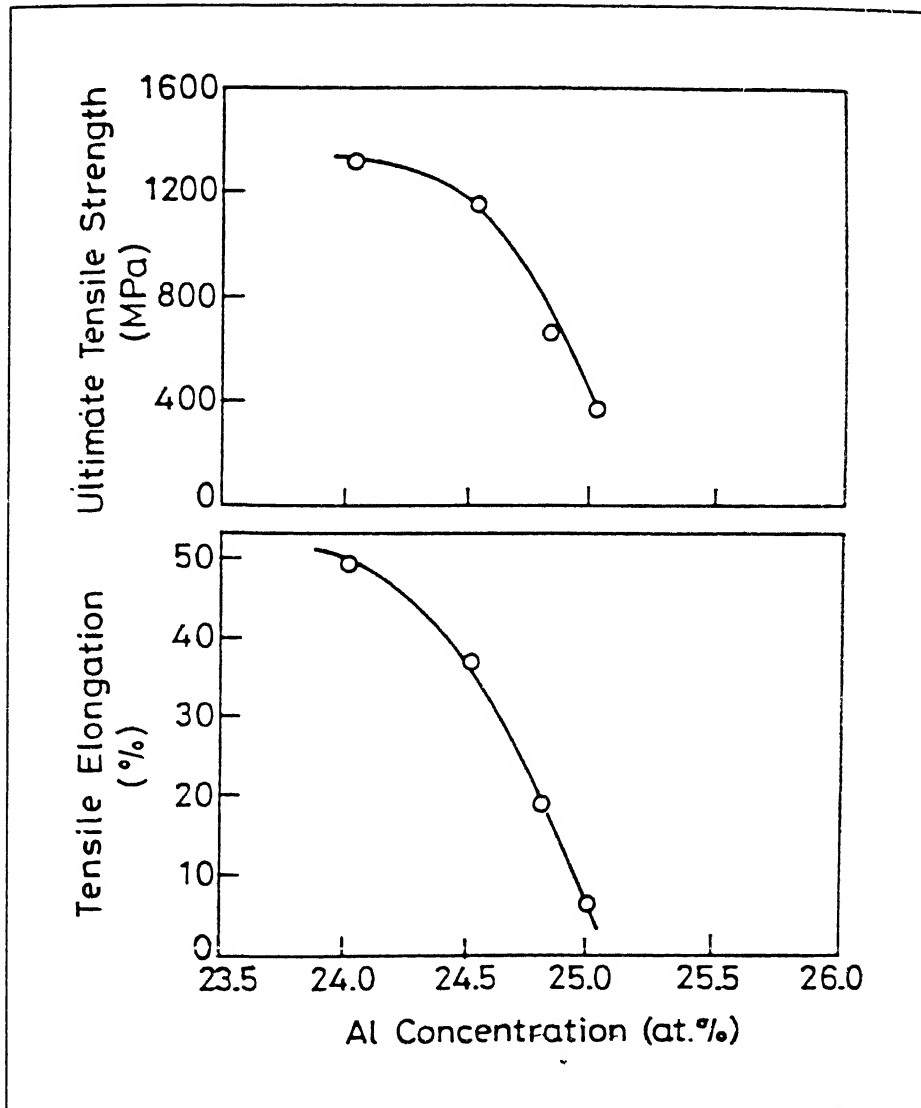


Figure 2.33b Plot of room temperature tensile properties as a function of aluminium concentration [2]

Downloaded from

Downloaded from

17/11/20

noticed that the elements like boron which segregate to grain boundary and not to cavity surfaces (free surface) lowers the grain boundary energy  $\gamma_g$  and enhances the cohesion.

Schulson *et al* [85] also observed the grain boundary strengthening effect of boron addition. According to them, boron facilitates dislocation movement across the grain boundary. Frost [86] considered the various ordering configurations at the grain boundary, and suggested that boron can lower the difference in energy between different ordering configurations, thereby lowering the drag on boundary dislocations. In a hypostoichiometric alloy, majority of Ni atoms at the grain boundary region will enhance this effect. Thus a moving dislocation will experience a lower drag, and slip will be easily accommodated.

Baker and Schulson [87] observed a continuous, locally disordered region at the grain boundaries of boron doped  $\text{Ni}_3\text{Al}$ . They concluded that the local disorder might be a prerequisite in order to maintain dislocation mobility and easy transmission of slip across the grain boundary, thereby enhancing the ductility of the material.

Yan *et al* [88] found the presence of extended dislocations in the boron free alloy only, whereas no stacking fault was observed in boron doped samples. The extension of the planar faults increased with increase in the aluminium content of the alloy. They concluded that boron inhibited the formation of  $\frac{1}{6} \langle 112 \rangle$  partials, and the absence of SISF made the situation easy for the gliding of  $\langle 110 \rangle$  dislocations. Once the mobility of the  $\langle 110 \rangle$  dislocation is ensured, the material gains sufficient ductility.

Chaki [89] also emphasized on the point of local disordering. According to him, Ni-B bonds and antisite Ni defects reduce the directionality of bonding, even at the grain interior. As a result, the ionic character of the bonds is suppressed, enhancing the metallic character, which ultimately improves the ductility in the interior of grains so that deformation can be easily transmitted from one grain to another. He also theoretically estimated the optimum boron concentration required for effective ductilization to be 3900 ppm, which is in fair agreement with the experimental value of optimum concentration of 4700 ppm or 0.1 wt%.

**II. Alloying with Substitutional Solutes :** It appears that the principal condition for ductilization is the modification of grain boundary chemistry, so as to facilitate dislocation glide motion across the grain boundaries. Effect of the addition of substitutional solutes has also been considered in this regard. Takasugi *et al* [76] introduced the concept of valency difference between the element at the substitution site and the third element which substitutes it. They concluded that when the valency difference is positive, e.g. in case of Fe, Mn which substitute for Al atoms, the ductility increases significantly. Other solutes found to ductilize  $\text{Ni}_3\text{Al}$  are Pd, Cu, Co, Au, Pt, Ag.

George *et al* [90] reported that Zr has a strong effect on the ductility of  $\text{Ni}_3\text{Al}$ . Gu *et al* [91], in a recent work, have found that the addition of zirconium to a hypostoichiometric  $\text{Ni}_{76}\text{Al}_{24}$  alloy (boron free) upto 0.7 atomic percent substantially enhanced the tensile properties. The elongation to fracture was increased from 1.1% to 13.2%, while the final yield strength (321 MPa) and ultimate tensile strength (649 MPa) were found to be more than twice and thrice the respective initial magnitudes. They have concluded that Zr essentially segregates to the grain boundaries, and the main role of Zr is to increase the grain boundary cohesion in  $\text{Ni}_3\text{Al}$  alloy.

Chiba *et al* [92] suggested that the lowering of ordering energy is responsible for ductilization of  $\text{Ni}_3\text{Al}$ . They found that the addition of  $\gamma$  former, such as Pt, Cu, Co and Pd, which degrade the ordering energy was effective in improving the ductility of  $\text{Ni}_3\text{Al}$ .

**III. Thermomechanical Treatment :** Ductility of boron doped  $\text{Ni}_3\text{Al}$  can be improved by controlling grain size through adequate thermo-mechanical treatments.  $\text{Ni}_3\text{Al}$ , with a grain size of a few microns, can show a very high ductility [93], even at superplastic range. Addition of other elements like Cr and Zr, as in case of IC50 and IC218, is extremely beneficial in developing superplastic property [74, 94, 95]. Aoki and Izumi [71] obtained nearly 15% tensile elongation when they used a boron free polycrystalline  $\text{Ni}_3\text{Al}$  specimen.

obtained by cold rolling and annealing of a single crystal.

## 2.7 Diffusion in $\text{Ni}_3\text{Al}$

Diffusion in ordered materials is much more complicated as compared to that in disordered alloys. The displacement of an atom in a lattice is extremely dependent on the crystal structure as well as on the surrounding neighbours. Therefore, it is quite important to have an idea of the diffusion in ordered structures in order to develop an understanding about their high temperature properties.

Diffusion basically refers to the spontaneous movement of atoms to new sites within a material. The atomic movement is always dependent on temperature and composition. Thermal energy and chemical potential act as driving forces for the diffusion process. It is easy to understand that atomic movement in an ordered structure results in the creation of local disordered regions, thereby violating thermodynamic equilibrium. Thus, the ordering energy is another important governing factor that controls diffusion in ordered structures. In order to minimize the system energy, atomic migration should take place in such a way as to maintain the equilibrium ordering which is often a complicated process. As a result, diffusion is eventually slower in ordered structures, theoretically upto the critical temperature for order-disorder transformation. This is supposed to be the major cause for the structural stability of ordered alloys.

Hancock [96] and Bronfin *et al* [97] worked on diffusion of Ni in  $\text{Ni}_3\text{Al}$  in the range of 920° - 1200°C. The diffusivity of Ni was found to be independent of composition and the activation energy was insensitive to aluminium content. These results have been attributed to the presence of constitutional vacancies; but Aoki and Izumi [98] reported that  $\text{Ni}_3\text{Al}$  has only substitutional antisite defects and no constitutional vacancy on either side of stoichiometry.

Hoshino *et al* [99] reported that the diffusivity of  $^{63}\text{Ni}$  in  $\text{Ni}_3\text{Al}$  was independent of Al content at above 1000°C. However, a minimum<sup>hm</sup> was observed at stoichiometric composition at

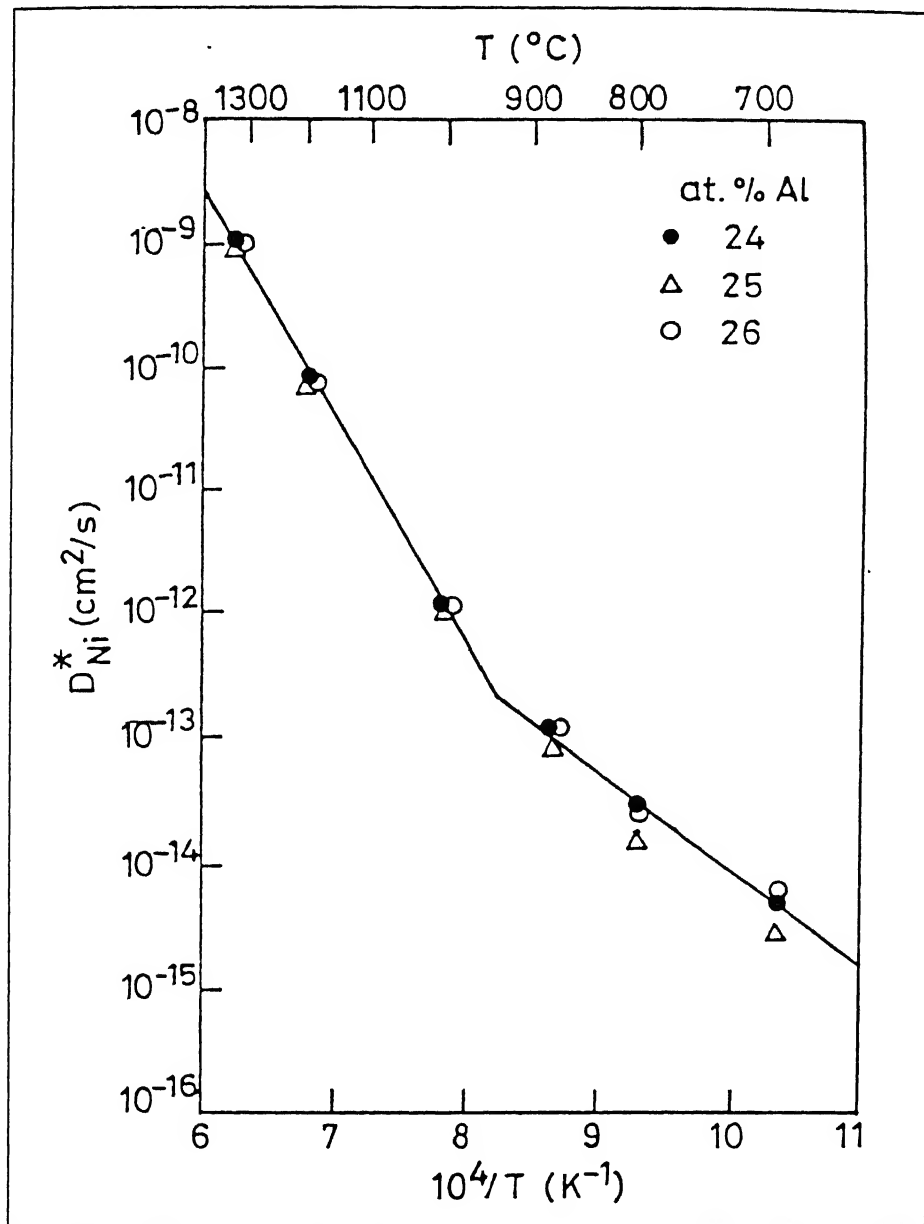
temperatures below 1000°C. They also observed the enhancement of diffusivity of Ni as an effect of boron addition in all the compositions at 1200°C, and in the stoichiometric alloy at all temperatures. Figure 2.34 shows a plot of the diffusivity of Ni in binary Ni<sub>3</sub>Al [99]. The activation energy for volume diffusion of Ni and Al in Ni<sub>3</sub>Al are listed in Table 2.5.

**Table 2.5** Activation energies and frequency factors  
of diffusion of Ni and Al in Ni<sub>3</sub>Al

Element	$D_0(m^2/s)$	$Q(kJ/mole)$	$C(at.\% Al)$	$T(K)$	Reference
Ni	$4.41 \times 10^{-4}$	309	23.8	1190-1471	96
	$1.00 \times 10^{-4}$	303	25.3	1187-1513	96
	$3.11 \times 10^{-4}$	300	26.8	1190-1557	96
	$1.00 \times 10^{-4}$	287	25.3	1187-1513	97
	$1.32 \times 10^{-2}$	345	24.0	1200-1623	99
	$1.46 \times 10^{-2}$	347	25.0	1200-1623	99
	$1.05 \times 10^{-2}$	342	26.0	1200-1623	99
	$1.00 \times 10^{-11}$	135	24.0	965-1273	99
	$1.10 \times 10^{-11}$	141	25.0	965-1273	99
	$2.00 \times 10^{-12}$	122	26.0	965-1273	99
Al	$6.60 \times 10^{-8}$	185	25.0	1273-1473	100

Sun and Lin [101] considered the antisite defects in order to explain the lower diffusivity of Ni in stoichiometric and off-stoichiometric Ni<sub>3</sub>Al. They concluded, that since antisite defects exist on both sides of stoichiometry, diffusivity is likely to increase with higher concentration of antisite defects in off-stoichiometric Ni<sub>3</sub>Al. However, the concentration of antisite defects in stoichiometric alloy is a function of temperature only, which means that the diffusivity of Ni in Ni<sub>3</sub>Al will be independent of bulk composition above a definite temperature. Hancock [96] suggested that diffusion in Ni<sub>3</sub>Al involves more complicated processes than the simple exchange of vacancies. Chou and Chou [102] measured the grain boundary diffusivities in the temperature range 955°C - 1124°C using Ni/Ni<sub>3</sub>Al+B diffusion couples. They found that the grain boundary diffusivity of Ni was much greater than the volume diffusivity, but the activation energy for grain boundary diffusion was found higher than that for volume diffusion. Watanabe and his co-workers [103, 104] carried out electron microscopic study



Figure 2.34 Temperature dependence of  $D_{Ni}^*$  in pure  $\text{Ni}_3\text{Al}$  [99]

of Ni/Ni<sub>3</sub>Al diffusion couple interfaces. They observed the formation of a coherent  $\gamma$  (disordered) phase at the interface. By measuring the diffusivity values, they concluded that interdiffusivities in the  $\gamma$  phase had been higher than those in the  $\gamma'$  phase. They also found that the interdiffusivities in the  $\gamma'$  phase were higher than the self diffusivity values of Ni in Ni<sub>3</sub>Al as obtained in other reports [96, 97, 99].

## 2.8 Annealing of Cold Worked Ni<sub>3</sub>Al : Recovery and Recrystallization

Processing of intermetallics may involve cold working followed by suitable thermal treatments. It is therefore important to consider the phenomena of recovery and recrystallization which occur during annealing of the cold worked material.

Recovery is basically the removal of work hardening effects, without motion of large angle grain boundaries. The next stage is recrystallization which consists in the formation of new strain free grains in the cold worked matrix. Since both recovery and recrystallization are diffusion controlled processes, the kinetics of recovery and recrystallization are sluggish in ordered structure as compared to disordered materials. It is also quite likely that cold working and annealing will be accompanied by changes in long range order.

The effect of cold work on the ordering behaviour of Ni<sub>3</sub>Al has been discussed earlier in section 2.3. It is known that vigorous cold work, by ball milling, filing or cold rolling, can lead to lowering of the order parameter or even total disordering [18, 19, 21-26]. The change of the order parameter of boron doped Ni<sub>3</sub>Al with large strain cold rolling has been studied by Ball and Gottstein [24] and Ghosh Chowdhury *et al* [25]. In both the cases, the microstructural development was characterized by the formation of heavy shear bands. Ball and Gottstein [24], during TEM study of the longitudinal sections, observed microband clusters with non-cellular dislocation arrangements; while Ghosh Chowdhury *et al* [50] observed twin bands in the rolling plane sections. The latter attributed the twinning phenomenon to a structural

transformation from  $L1_2$  to  $DO_{22}$  ordered phase. All these effects are expected to be reversed during the annealing treatment. The recrystallization behaviour of a few alloys with the  $L1_2$  structure, including  $Ni_3Al$ , is discussed below.

**$Ni_3Fe$  :** Vidoz *et al* [105] examined this sluggishly ordering  $L1_2$  alloy, with  $T_c = 500^\circ C$ . They found that ordering phenomenon was followed by recrystallization below  $T_c$ , and that reduced the elastic strains in the cold worked alloy. The reordering also hindered the recrystallization. They also observed a significant strain age hardening effect for the stoichiometric alloy; however the off-stoichiometric alloys gradually softened during annealing.

**$Co_3Ti$  :** Takasugi and Izumi [106] investigated the recrystallization and grain growth behaviour of  $Co_3Ti$ , which is usually ordered upto its melting point. The recrystallization behaviour was observed to be very sluggish. The hardness results indicated that recovery preceded recrystallization.

**$Zr_3Al$  :** Gagné and Schulson [107] reported that recrystallization behaviour of this alloy was normal as it was not prevented by ordering. The short term hardness maxima which appeared during annealing of the cold rolled alloy was due to the transient increase in faulting. However, Gialanella *et al* [22] found that  $Zr_3Al$  also could be disordered by ball milling. Therefore, it is quite obvious that reordering effect also plays a key role in the recrystallization of deformed  $Zr_3Al$ .

**$(Co_{78}Fe_{22})_3V$  :** The order disorder transformation temperature of this alloy is nearly  $950^\circ C$ . Cahn *et al* [108] found that recovery preceded recrystallization, and the recrystallization behaviour was also sluggish. An abrupt change at  $T_c$  was noticed (Figure 2.35), where the time for 50% recrystallization discontinuously increased to a higher magnitude. It indicates that ordering impedes the grain boundary mobility to a great extent.

**Cu<sub>3</sub>Au** : The transformation temperature of this alloy is around 390°C. It can also be disordered by cold working [20, 26, 109]. Roessler *et al* [109], while studying the annealing behaviour of 63% cold rolled Cu<sub>3</sub>Au at temperatures below  $T_c$ , observed the strain-age hardening effect. The order parameter regained its value at the peak hardness. According to Stoloff and Davies [110], the hardness at a constant degree of order varies with domain size and reaches a maximum for a critical domain size.

Feller-Kniepmeier and Rückert [111] studied the recovery and ordering kinetics at low (10%) and high (90%) strain levels in Cu<sub>3</sub>Au. They concluded that at low strain, the excess vacancy concentration was low and the ordering was sluggish enough to allow some recovery. However, the driving force for ordering was much higher for the heavily strained sample, and the ordering was so quick that recovery and recrystallization almost stopped below  $T_c$ .

Hutchinson *et al* [112] studied the recrystallization kinetics in 90% cold rolled Cu<sub>3</sub>Au. Conventional sigmoidal curves for the progress of recrystallization were obtained at temperatures both above and below  $T_c$  (shown in Figure 2.36), but the kinetics was extremely slow in presence of order. They concluded that the mechanism of recrystallization involved only the migration of low angle boundaries, whereas the migration of high angle boundaries would lead to an increase of the activation energy because of the greater extent of misorientation across the grain boundary. A strong retardation of grain boundary movement has also been observed in several other intermetallic systems [113]. Schematic Arrhenius plots for the temperature dependence of the time for 50% recovery and recrystallization and schematic plots of migration rates for grain boundaries in the ordered and disordered states have been shown in Figures 2.37a and 2.37b respectively.

**Ni<sub>3</sub>Al** : Ni<sub>3</sub>Al is ordered nearly upto its melting point. Baker *et al* [23] observed the partial disordering of Ni<sub>3</sub>Al as an effect of cold rolling. By measuring the hardness (shown in Figure 2.38) they showed that recrystallization occurred after recovery stage. Gottstein *et al* [114]

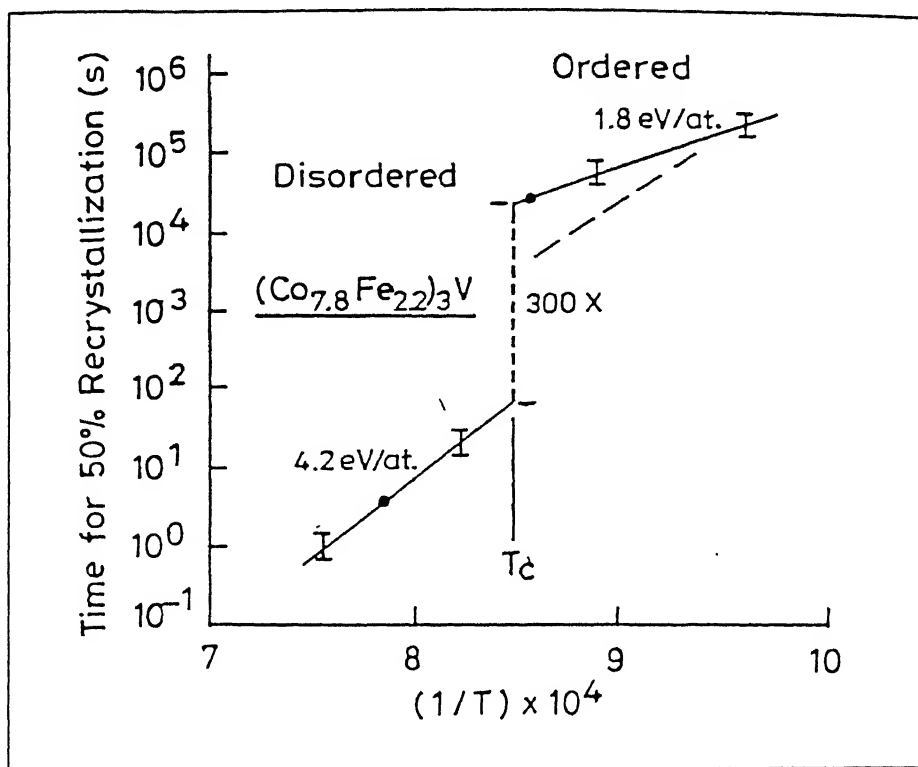


Figure 2.35 Time for 50% recrystallized volume fraction of 50% cold rolled  $(\text{Co}_{7.8}\text{Fe}_{22})_3\text{V}$  annealed above and below  $T_c$  [108]

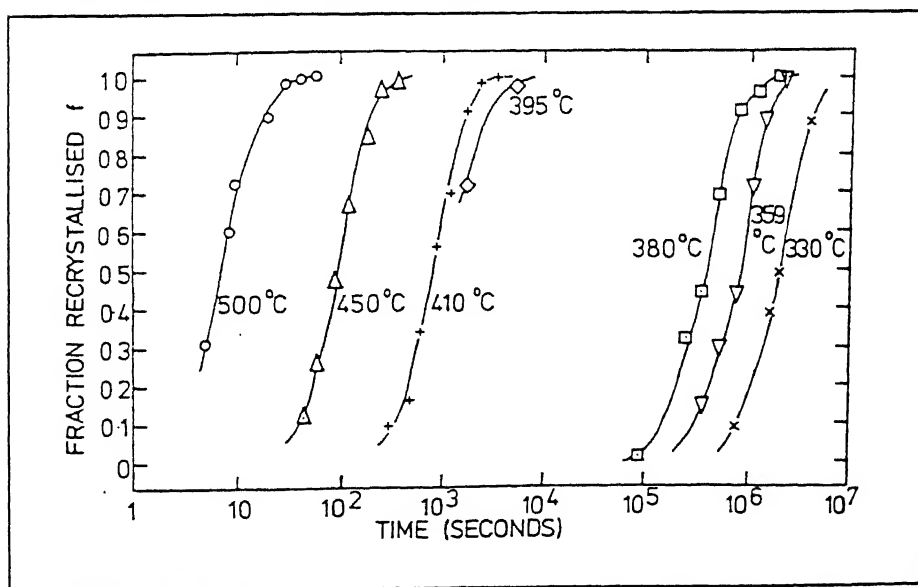


Figure 2.36 The fraction recrystallized versus annealing time for 90% cold rolled  $\text{Cu}_3\text{Au}$  [112]

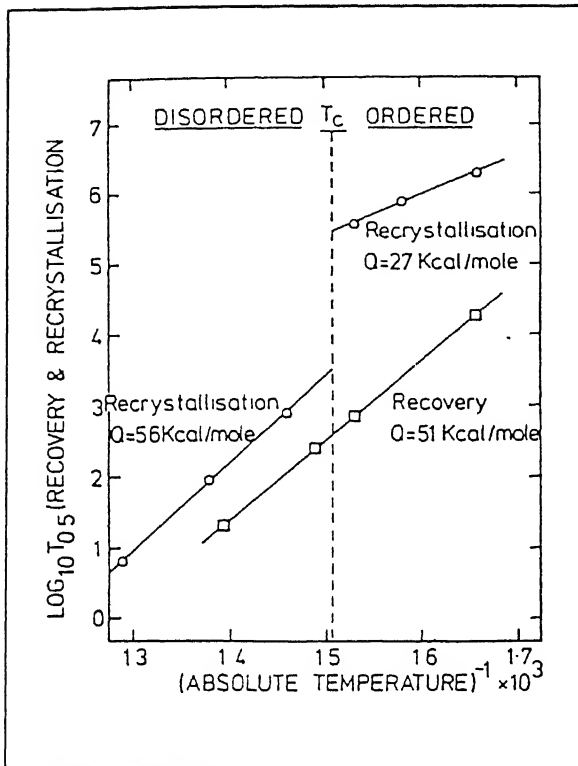


Figure 2.37a Arrhenius plots showing temperature dependence of the time for 50% recovery and recrystallization [112]

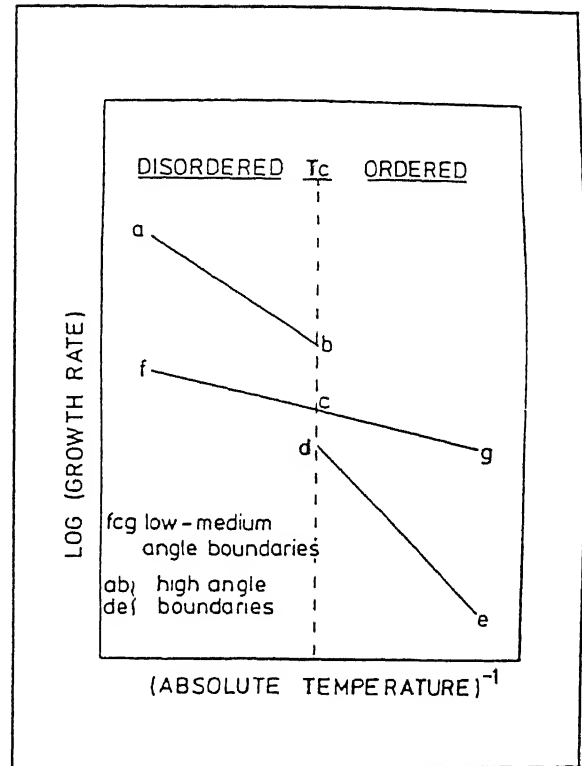


Figure 2.37b Schematic Arrhenius plots of migration rates for grain boundaries in the ordered and disordered states [112]

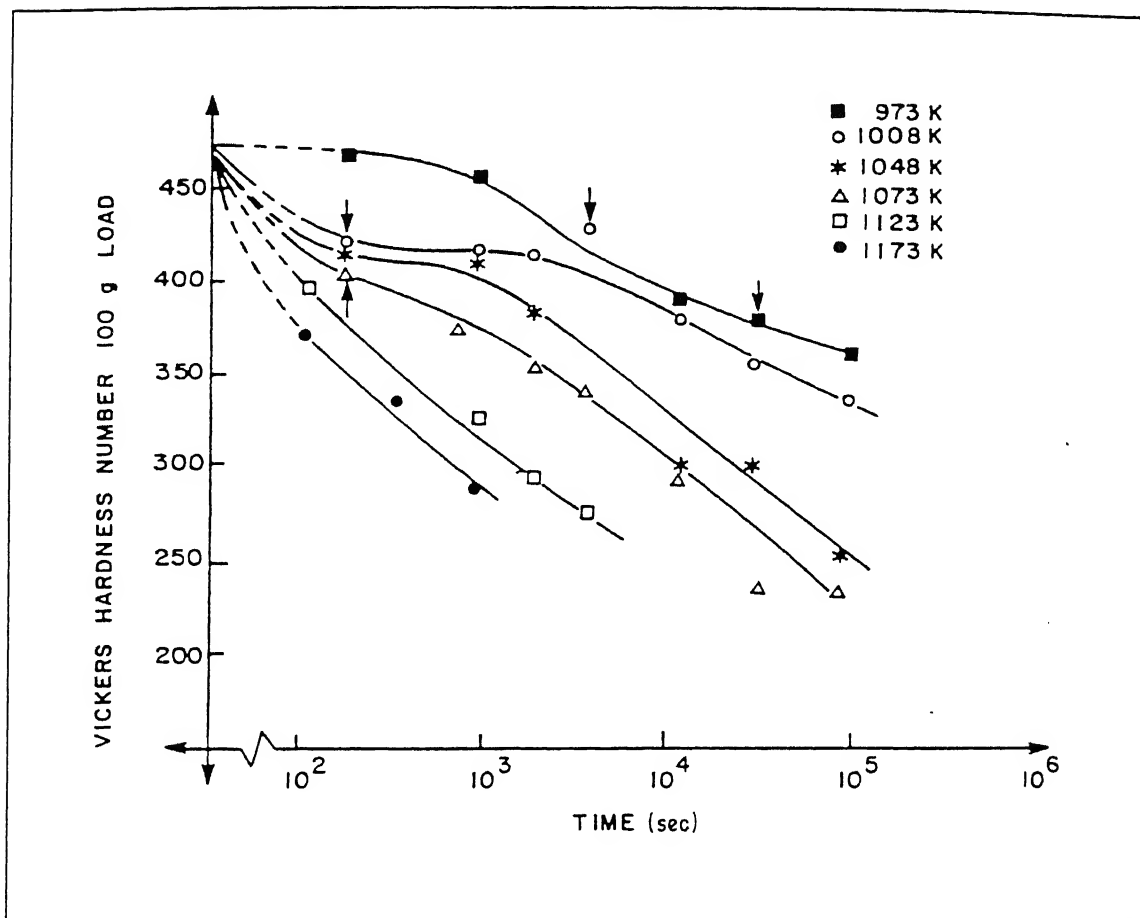


Figure 2.38 Hardness of cold deformed  $\text{Ni}_3\text{Al}$  as a function of annealing time at various temperatures. Arrows denote the starting of recrystallization [23]

found that the recrystallization kinetics followed conventional Avrami equation but the rate was quite sluggish. For 80% cold worked  $\text{Ni}_3\text{Al}$  sample, the recrystallization temperature was observed to be about  $0.55 T_m$ . For large deformations, the stored energy for deformation was also high. So, the slower kinetics of recrystallization was attributed to the poor mobility of high angle grain boundaries in the long range ordered materials. According to them, strain induced boundary migration (*SIBM*) dominated recrystallization after lower degree of cold working. Jena *et al* [115] observed extensive recovery in case of 35% rolled hypostoichiometric  $\text{Ni}_3\text{Al(B)}$ . They also found that nucleation started by strain induced boundary migration, at the deformation bands as well as at the grain boundary regions.

Ball and Gottstein [116] found differential recrystallization kinetics at localized regions. They observed a high nucleation rate in shear bands, which is followed by a low grain boundary mobility. This will produce a very small grain size in the final recrystallized material. Zhou *et al* [117] found very little effect of boron on activation energy for recrystallization. Gottstein and Kim [118] also reported that  $\text{Ni}_3\text{Al}$  did undergo dynamic recrystallization during high temperature deformation.

If ordered  $\text{Ni}_3\text{Al}$  undergoes any structural transformation during cold deformation [25], the restoration of  $\text{L1}_2$  structure could be expected during the annealing stage. Ghosh Chowdhury *et al* [119], from the study of process energetics, confirmed the existence of three phenomena, namely, recovery, reversion of  $\text{DO}_{22}$  structure to  $\text{L1}_2$  and recrystallization during annealing of a heavily cold rolled  $\text{Ni}_3\text{Al(B)}$  alloy. They also reported that the  $\text{L1}_2$  structure was restored in two stages. Process kinetics was fast in the first stage (within  $200^\circ - 400^\circ\text{C}$ ), whereas it was a slower one in the next stage ( $500^\circ - 800^\circ\text{C}$ ). The different recrystallization parameters observed by many workers are listed in Table 2.6.



**Table 2.6** Parameters of the recrystallization kinetics of  $\text{Ni}_3\text{Al}$ 

Deformation (%)	Temperature range ( $^{\circ}\text{C}$ )	$Q$ (kJ/mole)	$n$	Reference
16.7%(comp)	850 - 1000	487.7	—	117
22%CR	925 - 975	189.3	1.69	115
25%CR	850 - 900	172.6	1.74	115
30%CR	850 - 925	118 - 146	2.26	115
40%CR	850 - 1000	301	1.0	117
59%CR*	750 - 900	331	—	23
80%CR	650	120	2.3	114
	675	120	2.1	
85%CR	800 - 950	151( $X < 0.6$ )	2.2-0.71	119
		100( $X > 0.6$ )	3	

CR : cold rolled; comp : compression; \* : single crystal

## 2.9 Development of Texture During Processing

The constituent grains in a polycrystalline material generally assume preferred crystallographic orientations during cold rolling as well as after subsequent annealing treatments, leading to well defined textures [120]. It is an important phenomenon since textures are directly related to the anisotropy of the mechanical, electrical, and magnetic properties of a material. In a rolled material, the texture is normally expressed as  $\{hkl\} \langle uvw \rangle$ , which means that the  $\{hkl\}$  planes of the constituent grains are parallel to the rolling plane of the sheet, while the  $\langle uvw \rangle$  directions of those grains are aligned in the rolling direction. If there are more than one texture component, they are represented as  $\{h_1k_1l_1\} \langle u_1v_1w_1 \rangle$ ,  $\{h_2k_2l_2\} \langle u_2v_2w_2 \rangle$ , .... etc.

### 2.9.1 Deformation Texture in FCC Metals

The deformation textures developed in pure metals as well as alloys with FCC crystal structure are usually of two types – *pure metal* or *copper* type and *alloy* or  $\alpha$ -*brass* type. The copper type texture has four major components, namely Cu  $\{112\} \langle 111 \rangle$ , Bs  $\{011\} \langle 211 \rangle$ , S  $\{123\} \langle 634 \rangle$  and Goss  $\{011\} \langle 100 \rangle$ . In alloy type texture, there are mainly two

components, a very strong Bs and a relatively weak Goss component. Standard (111) pole figures representing these two types of deformation textures are shown in Figure 2.39 [121].

The deformation texture is very much controlled by the deformation mechanism. For the materials with higher stacking fault energy values, the widths of the stacking faults are very low, and therefore these can be easily constricted. In that situation, cross slip becomes easier and the material undergoes mainly slip deformation. When the deformation is governed by the slip mode, the rolling texture of FCC metals and alloys is generally of copper type. For lower SFE materials, the stacking fault width is much greater, which makes it difficult to create any constriction within the stacking fault region and therefore cross slip becomes difficult. In these circumstances, the plastic deformation is mainly governed by twinning. Wassermann [26] has shown that if mechanical twinning occurs as an additional mode of deformation other than slip, the Cu  $\{112\} \langle 111 \rangle$  component will be transformed to  $\{552\} \langle 115 \rangle$  by twinning. Further deformation of the twin orientation will then take place on the favourable slip systems which will rotate the twin orientation into the Goss position  $\{011\} \langle 100 \rangle$  and finally into the Bs position  $\{011\} \langle 211 \rangle$  by further rotation.

Temperature also plays an important role in determining the rolling texture. Hirsch *et al* [122] have experimentally shown that pure copper which on rolling at room temperature gives very sharp *copper* type texture exhibits predominantly  $\alpha$  – *brass* type texture when it is rolled at liquid nitrogen temperature.

### 2.9.2 Cold Rolling Texture in Ni<sub>3</sub>Al

A very limited amount of work has been done on the deformation texture of L1<sub>2</sub> ordered materials such as Ni<sub>3</sub>Al. Hutchinson *et al* [112] observed mainly copper type texture after 90% cold rolling of Cu<sub>3</sub>Au. They described the texture as a string of orientations extending from  $\{112\} \langle 111 \rangle$  through  $\{123\} \langle 412 \rangle$  and  $\{011\} \langle 211 \rangle$  to  $\{011\} \langle 100 \rangle$ . The stacking fault energy of Ni<sub>3</sub>Al ( $\sim 130$  mJ/m<sup>2</sup>) is quite comparable to that of pure Ni

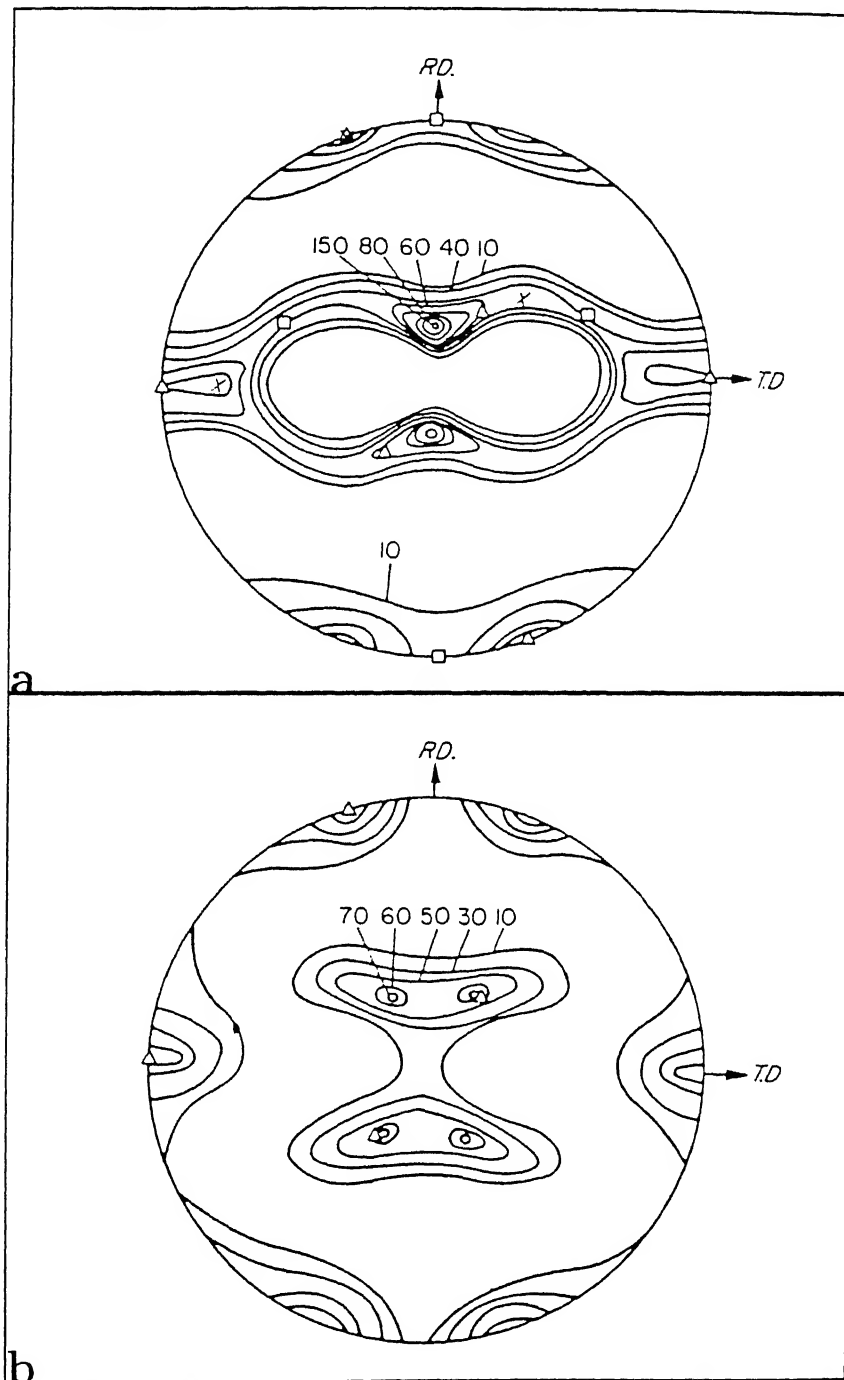


Figure 2.39 Standard  $\{111\}$  pole figures showing  
(a) copper type texture and (b)  $\alpha$ -brass type texture [121]

( $\sim 150 \text{ mJ/m}^2$ ). Therefore, apparently a pure metal type texture can be expected for  $\text{Ni}_3\text{Al}$ , as in case of pure nickel. However, Gottstein et al [114] found mainly Bs  $\{011\} \langle 211 \rangle$  and Goss  $\{011\} \langle 100 \rangle$  components in the rolling texture of boron doped  $\text{Ni}_3\text{Al}$ . They concluded that the origin of this  $\alpha$ -brass type texture was within the shear bands, generated by heavy deformation. Ball and Gottstein [24], from their TEM work, also observed microband clusters and shear bands on the longitudinal sections of 70% cold rolled  $\text{Ni}_3\text{Al(B)}$  samples.

Ghosh Chowdhury *et al* [50] studied the textural changes with cold rolling in samples of  $\text{Ni}_3\text{Al(B)}$ . They observed the development of pure metal type texture at the initial stages of cold rolling (as expected for FCC materials with high SFE), but gradually the texture transformed to alloy type with heavier deformation. The textural transition took place within 45% and 65% cold reduction levels. Electron microscopic study revealed a transition in deformation mode from slip to twinning, at the same strain level. They also detected a structural transformation from  $\text{L1}_2$  to  $\text{DO}_{22}$  at this stage and correlated the texture transition with the structural transformation.

### 2.9.3 Annealing Texture of FCC Materials

When heavily cold worked materials such as pure Cu, Ni etc. are annealed, a strong cube texture  $\{100\} \langle 001 \rangle$  is generally produced [123]. Aluminium is an exception, where the rolling texture is dominated by the S  $\{123\} \langle 634 \rangle$  component, and on recrystallization, along with the cube, 'R'  $\{123\} \langle 412 \rangle$  component (retained rolling texture) is obtained which is very close to the S. In a series of Ni-Co alloys [124], it has been observed that the compositions having higher magnitudes of SFE yield mainly the cube texture on recrystallization, while the compositions with lower SFE values do not show any cube component.

### 2.9.4 Annealing Texture of $\text{Ni}_3\text{Al}$

Hutchinson *et al* [112] reported that annealing of deformed  $\text{Cu}_3\text{Au}$  above  $T_c$  gave rise to a weak texture while a comparatively stronger texture was obtained below  $T_c$ . The main

components above  $T_c$  were cube  $\{100\} \langle 001 \rangle$ , its twin and the retained Cu  $\{112\} \langle 111 \rangle$ . Below  $T_c$ , the texture consisted of all the major deformation texture components.

Gottstein *et al* [114] reported a rather weak annealing texture in recrystallized  $\text{Ni}_3\text{Al(B)}$ . They observed a few components namely,  $\{310\} \langle 135 \rangle$  and  $\{211\} \langle 135 \rangle$  at  $650^\circ\text{C}$  and  $\{310\} \langle 135 \rangle$  at  $700^\circ\text{C}$ , but could not observe the cube component. Ball and Gottstein [116] also observed a very weak recrystallization texture on annealing  $\text{Ni}_3\text{Al(B)}$ , which consisted of the components  $\{025\} \langle 100 \rangle$  (rotated cube) and  $\{011\} \langle 100 \rangle$  (Goss). Ball *et al* [125] observed the S  $\{123\} \langle 634 \rangle$  orientation along with weak rotated cube components in an annealed two phase  $\text{Ni}_3\text{Al(B,Zr,Fe)}$  alloy.

Ghosh Chowdhury *et al* [119] also observed a weak annealing texture in  $\text{Ni}_3\text{Al(B)}$ . Figure 2.40 which shows the recrystallization texture of 85% cold rolled  $\text{Ni}_3\text{Al(B)}$ , after annealing at  $950^\circ\text{C}$  for 1 hr. depicts a nearly random texture. The maximum intensity was found to be  $\sim 1.5R$  which was much weaker compared to the intensity of the rolling texture ( $\sim 5R$ ). The main components here were weak rotated cube  $\{025\} \langle 100 \rangle$  with a weak Goss  $\{011\} \langle 100 \rangle$ . They concluded that the textural changes mainly took place during the recovery stage, which was accompanied by the reordering and structural restoration from  $\text{DO}_{22}$  to  $\text{L}_{12}$  crystal structure. No perceptible sharpening of the texture was noticed subsequently; however, after prolonged annealing treatment, the overall texture intensity improved a bit, with the enhancement of the Goss component.

## 2.10 Two Phase $\text{Ni}_3\text{Al}$ Alloys

A number of multiphase  $\text{Ni}_3\text{Al}$  based alloys have been developed recently, among which the following are highly promising: IC50, IC218, IC218LZr, IC221, IC357, IC396M etc. [126]. Suitable alloying additions impart attractive mechanical properties to these multiphase alloys. Cold workability of IC50 is excellent due to its  $\gamma' + \gamma$  two phase structure. Although not much work has been done in this alloy, it is expected that recrystallization in this material

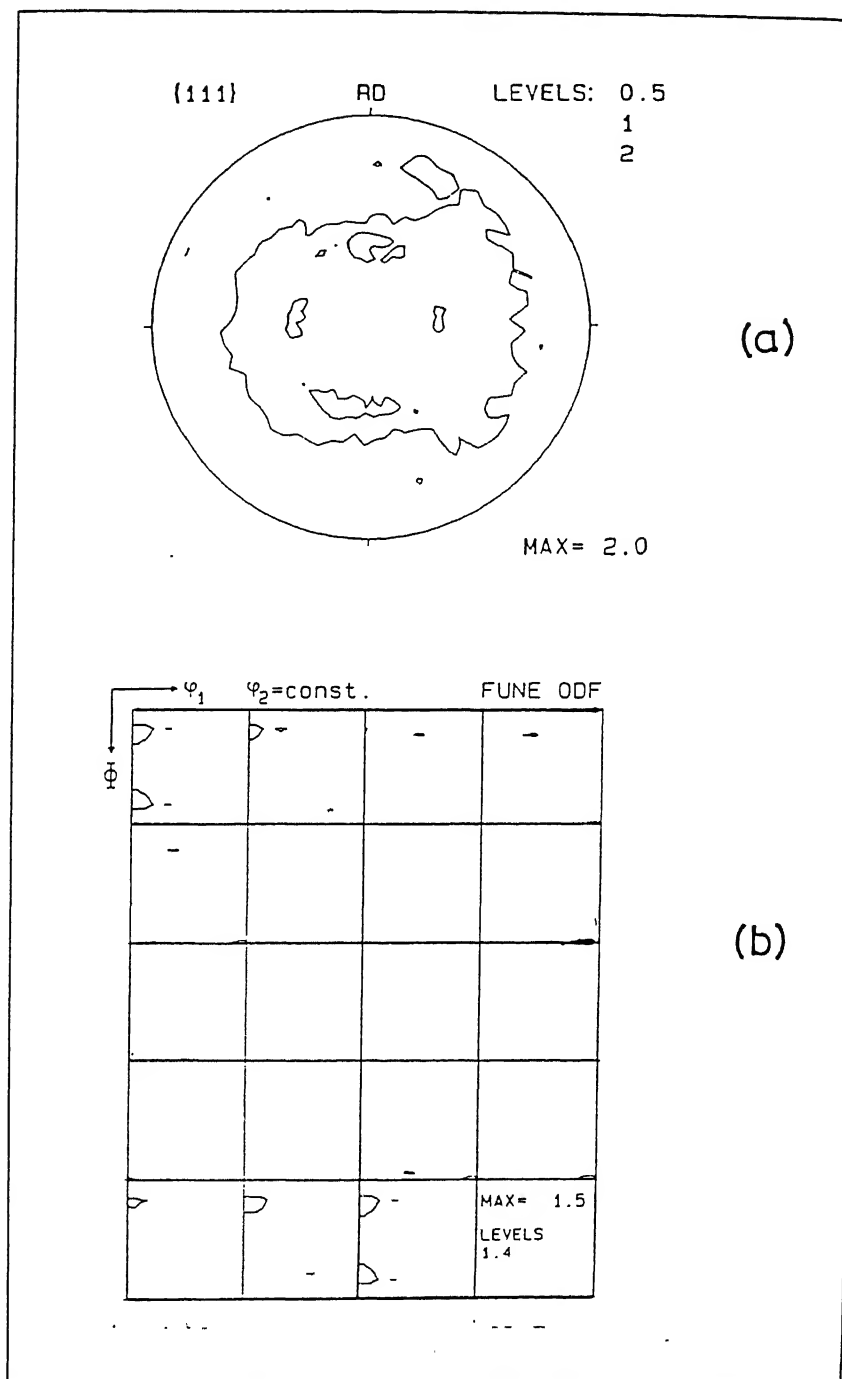


Figure 2.40 Texture of cold rolled  $\text{Ni}_3\text{Al(B)}$  after annealing at  $950^\circ\text{C}$  for 1hr [119];

(a)  $\{111\}$  pole figure, (b) corresponding ODF

could be a sluggish process, slower than that in single phase  $\text{Ni}_3\text{Al}$ . Due to the presence of zirconium, as well as the two phase structure, the grain growth could be effectively controlled, thereby producing a fine grain structure after annealing. This material has very good hot corrosion resistance also. The solid solution strengthening effect of Zr is depicted in the diagram shown in Figure 2.41. Ball *et al* [127] studied the softening behaviours of IC15 (single phase  $\text{Ni}_3\text{Al}$ ) and two-phase IC50  $\text{Ni}_3\text{Al}$  (B,Zr,Fe) on the basis of microhardness data taken after isochronal annealing. They observed a limiting plateau level in the softening curve of IC50, whereas IC15 continued to soften with increasing temperature (as shown in Figure 2.42). That the two phase boron doped  $\text{Ni}_3\text{Al}$  can be used as a superplastic material has also been reported [74, 94, 95].

## 2.11 Scope of the Present Investigation

Although enormous amount of research work has already been conducted on the development of optimum mechanical properties in  $\text{Ni}_3\text{Al}$  and related alloys, many ambiguities still remain in respect of their deformation and yielding behaviour, annealing characteristics, ordering and texture development during processing. Very little work has been done till date to study systematically the structure-property relationship of two phase  $\text{Ni}_3\text{Al}$  base materials, which appear to be more prospective as compared to the single phase  $\text{Ni}_3\text{Al}$ . So far as the development of textures during processing of  $\text{Ni}_3\text{Al}$  and related alloys is concerned, very little information is available in the literature.

According to Sikka [128], the nickel aluminide alloy designing technology developed by Oak Ridge National Laboratory (ORNL) is now being transferred to various industries for the commercialization of the  $\text{Ni}_3\text{Al}$  base materials. The ORNL is now producing a wide spectra of  $\text{Ni}_3\text{Al}$  alloys (as mentioned in the previous section) in order to meet different industrial requirements. The base composition developed in ORNL is IC50, which is used as the master alloy from which the other compositions are derived by suitable and proportionate

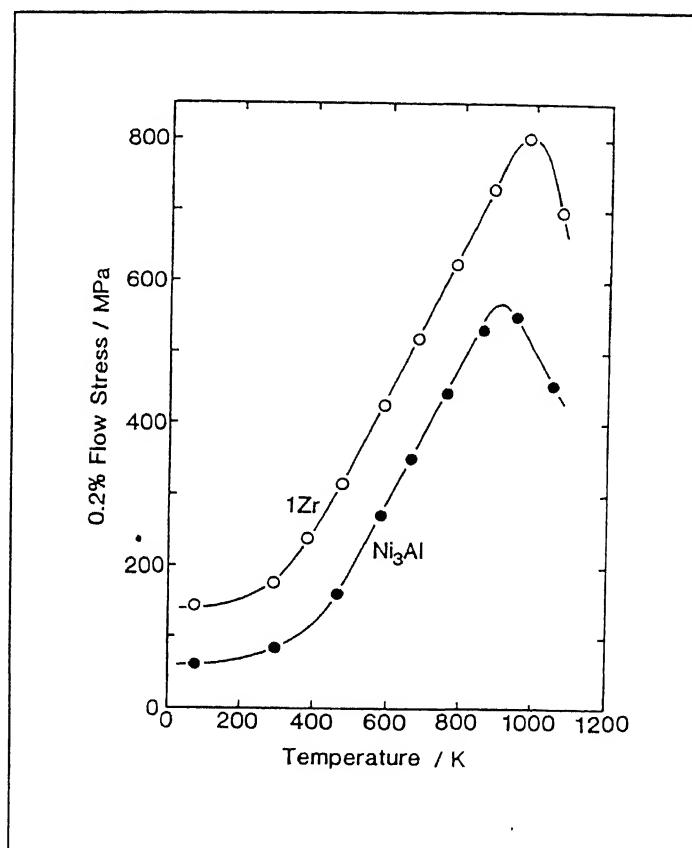


Figure 2.41 Solid solution strengthening of  $\text{Ni}_3\text{Al}$  by the addition of Zr [60]



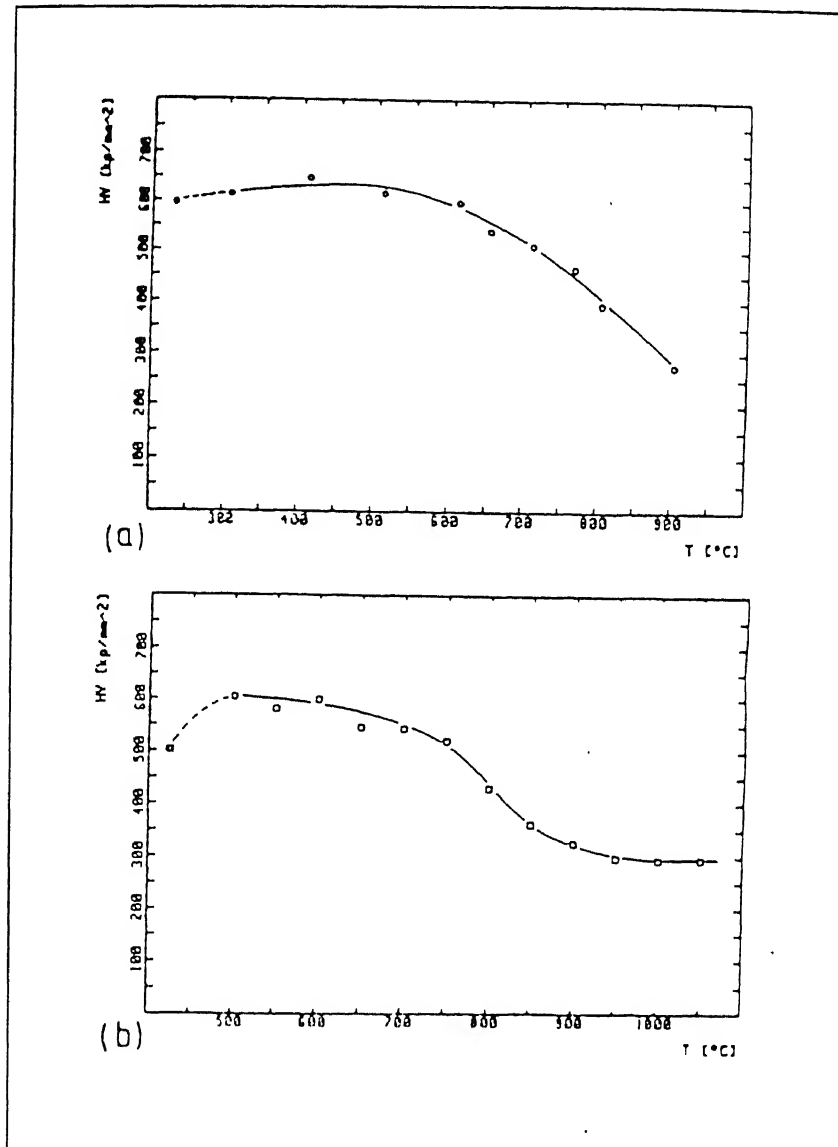


Figure 2.42 Microhardness versus temperature for isochronal annealing of 85% cold rolled  
(a) IC15 and (b) IC50 [127]

alloying additions. Therefore, it appears to be the right moment to carry out a comprehensive study on the cold rolling and annealing behaviour of IC50, the key composition for all the specialized  $\text{Ni}_3\text{Al}$  alloys. With this view, the present investigation has been aimed at studying the textural and microstructural changes, as well as changes in order during cold rolling and subsequent annealing. Attempts have also been made to study the recrystallization kinetics and the energy release during annealing. Finally, the results obtained from various experimental observations have been correlated and discussed.

# CHAPTER 3

## EXPERIMENTAL

## ● *Experimental*

### 3.1 Alloy Preparation

A hypostoichiometric alloy was selected for the present investigation. The composition of the alloy was Ni-21.8Al-0.1B-0.34Zr (in atomic percent). The Oak Ridge National Laboratory, USA designated this composition as IC50 [128].

The alloy melt was prepared by arc melting with non-consumable tungsten electrode. It was then directly cast into sheet form of initial thickness 0.97 mm (average). The cast sheet was then cut into small plates of nearly 10 mm width and 50 mm length, and subsequently sealed in quartz capsules in high vacuum ( $\sim 10^{-4}$  Pa). The encapsulated plates were then subjected to homogenization annealing at 1150°C for 24 hrs to produce a two phase microstructure in which the  $\gamma$  (disordered Ni-base FCC phase) islands were randomly distributed over the  $\gamma'$  (ordered L1<sub>2</sub> phase) grains. The initial grain size was 40 - 45  $\mu\text{m}$  and the volume fraction of second phase was about 25%. This homogenized alloy was the starting material for the subsequent cold rolling and annealing experiments.

### 3.2 Cold Rolling

The edges of the homogenized plates were smoothened by grinding. These plates were then subjected to cold rolling at room temperature in a two-high laboratory rolling mill. The diameter of the rolls was 150 mm and the thickness reduction was 2 - 3% at each pass. No edge cracking was detected upto nearly 55% reduction. Although cracks started appearing after 60% reduction, these were not very significant even upto 73% reduction. After 73%

reduction, the material was so thin ( $< 0.27$  mm), that no further effective deformation could be given. A few other sheets were rolled to different degrees of reduction, namely, 15%, 25%, 35%, 45%, 55% and 65%. Thus a range of rolling reductions from 15% to 73% was obtained. In order to reduce friction, lubricating oil was used during cold rolling.

### **3.3 Annealing**

The 73% rolled material was chosen for the study of recrystallization characteristics and kinetics. For this purpose, small pieces of rolled sheets, with average dimensions 5mm x 8mm, were vacuum sealed ( $\sim 10^{-4}$  Pa) for environmental protection and subjected to heat treatment in a horizontal tube furnace. The temperature controller attached to the furnace was capable of maintaining the temperature within a range of  $\pm 2^\circ\text{C}$ .

#### **3.3.1 Isochronal Annealing**

Initially, one set of 73% rolled samples was subjected to isochronal annealing for 1 hr at temperatures ranging from  $500^\circ$  to  $1200^\circ\text{C}$ , with an interval of  $100^\circ\text{C}$ . X-ray diffraction (XRD) and optical microscopic characterizations were carried out on these specimens in order to have an overall idea on the annealing behaviour of the deformed alloy as a function of annealing temperature.

#### **3.3.2 Isothermal Annealing**

In the next stage, a number of 73% rolled samples were given isothermal recrystallization anneal for time durations ranging from 1 min to 150 hr (depending on the annealing temperature). Temperatures selected for this purpose were  $800^\circ$ ,  $900^\circ$ ,  $1000^\circ$ ,  $1100^\circ$  and  $1200^\circ\text{C}$ .

## 3.4 Microstructural Characterization

After cold rolling and annealing treatments, the microstructures of the experimental specimens were characterized using optical microscopy, scanning electron microscopy (SEM) and transmission electron microscopy (TEM).

### 3.4.1 Optical Microscopy

All the samples, namely, cast, homogenized, cold rolled and annealed specimens (both isochronally and isothermally annealed) were cold mounted, with the aim to study their longitudinal surfaces. These were then subjected to metallographic polishing followed by chemical etching. The etching reagent used was alcoholic ferric chloride with the following composition:

<i>Anhydrous Ferric Chloride</i>	-	5 gm
<i>Concentrated HCl</i>	-	2 ml
<i>Ethanol</i>	-	96 ml

Microstructures of the etched samples were observed in a LEITZ Optical Microscope with camera attachment and photographs were taken from the surfaces of all the samples. To study the recrystallization kinetics, a number of photomicrographs were taken randomly from each of the isothermally recrystallized specimens. The recrystallized volume fractions were measured by two dimensional systematic point counting. About 20 - 25 areas were examined for each sample using a 21 x 21 square grid.

### 3.4.2 Scanning Electron Microscopy (SEM)

The mounted samples used for optical microscopy were also studied in a SEM. The chemical etching in this case was made a little darker. The instrument used was a JSM 840A JEOL SEM with EDAX facility for elemental analysis. The acceleration voltage used for observing the microstructures was 15 kV. EDAX analysis was done at a few selected spots on a few specimens, using a working distance of 37 mm and acceleration voltage of 12 kV.

### 3.4.3 Transmission Electron Microscopy (TEM)

A number of rolled and annealed samples were selected for TEM study. For this purpose, specimens of dimensions approximately 13 mm x 7 mm were first mechanically thinned down to 0.05 mm by manual grinding on emery papers. Discs of 3 mm diameter were punched out of the thin sheets which were then electrolytically thinned in a FISHIONE Twin Jet Polisher. The conditions used were

---

<i>Electrolyte</i>	-	10% Perchloric acid in 90% butanol (by volume)
<i>Temperature</i>	-	+10° to +12°C
<i>Voltage</i>	-	50 V.

---

TEM studies were carried out on the rolling plane sections at 160 kV (acceleration voltage) in a JEM 2000FXII JEOL Transmission Electron Microscope.

### 3.5 Microhardness Measurements

Hardness measurement was carried out on the longitudinal sections of the specimens. i.e., on the same sections from which optical micrographs were also taken. It was not possible to measure the bulk hardness due to the extremely small area of the longitudinal sections of the samples. Therefore, microhardness values were measured on all the mounted and etched samples using a LEITZ Microhardness tester. The dimensions of the indentations (i.e. the diagonals of the square shaped indentations) were directly measured using a micron scale attached to the microscope, and the corresponding Vicker's Hardness values were readily obtained from the standard tables. The microhardness values were recorded randomly from the longitudinal surface of each of the samples, without considering any particular phase. At least 20 - 25 indentations were recorded for each sample in order to determine the average microhardness of that sample.

### 3.6 X-ray Diffraction Study

X-ray diffraction was carried out on each of the deformed as well as annealed samples for

- eliciting structural information,
- measuring the long range order parameter and
- measuring the strain parameter.

X-ray diffraction patterns were taken from the polished and thoroughly cleaned rolling surface of each specimen.

All the XRD patterns were taken in a SEIFERT ISO-DEBYEFLEX 2002 X-ray Diffractometer with copper target. The diffraction intensity profiles were recorded on a strip chart recorder. At the beginning, a few samples were subjected to rapid scanning within a range of  $20^\circ - 150^\circ$ . After the peak positions were located, slow scanning was made for all the samples to measure correctly the  $2\theta$  values for the corresponding peaks. The conditions used were as follows:

<i>Rapid Scanning</i>	Voltage	30 kV
	Current	20mA
	Scanning Speed	$1.2^\circ/\text{min}$ (in $2\theta$ )
	Chart Speed	1.2 cm/min
	Time Constant	10 sec
	Counts per min	10 K
<i>Slow Scanning</i>	Voltage	30 kV
	Current	20mA
	Scanning Speed	$0.3^\circ/\text{min}$ (in $2\theta$ )
	Chart Speed	0.6 cm/min
	Time Constant	10 sec
	Counts per min	Varied according to the peak heights

In order to avoid the instrumental error, the machine was initially calibrated with a standard silicon single crystal specimen. Finally, the corrected values of  $2\theta$  were taken for the precise lattice parameter measurements using the *Nelson - Riley* extrapolation technique.



### 3.6.1 Long Range Order Parameter (S)

The long range order parameter (S) was measured from the integrated intensity ratios of the (100)/(200) and (110)/(220) pairs of reflections. The following relationship was used for the calculation of S [16]:

$$S^2 = \frac{I_s}{I_f} \cdot 16 \cdot \frac{(X_{Al}f_{Al} + X_{Ni}f_{Ni})^2}{(f_{Ni} - f_{Al})^2} \cdot \frac{(L_p)_f}{(L_p)_s} \cdot \frac{(e^{-2M})_f}{(e^{-2M})_s} \quad (3.1)$$

where,

$I$  is the measured integrated intensity,

$X_{Al}$  and  $X_{Ni}$  are the atomic fractions of Al and Ni respectively,

$f_{Al}$  and  $f_{Ni}$  are the atomic scattering factors for Al and Ni respectively

$L_p$  is the Lorentz-Polarization factor

$e^{-2M}$  is the Debye-Waller temperature factor,

and the subscripts s and f refer to the superlattice and fundamental peaks respectively.

Among all the parameters mentioned above, atomic fractions of Ni and Al for the experimental alloy were already known. The *atomic scattering factors* and *Lorentz polarization factors* for corresponding peak angles were readily obtained from the standard charts available in literature [129]. The *Debye-Waller temperature factor* practically was of little significance because all the diffraction runs were taken at room temperature. The integrated intensity values were directly obtained from the X-ray intensity profiles by measuring the areas under the peaks with the aid of 1 mm square grid tracing paper.

### 3.6.2 Strain Parameter

When a polycrystalline material is subjected to deformation, a broadening effect in the X-ray diffraction peaks can readily be observed [7]. Since the strain induced in the material is responsible for this effect, the changes in peak width dimensions can provide a quantitative

estimation of the strain in the material. The amount of strain can be estimated from a strain parameter which can be defined as a ratio,  $B_r/B_o$ , where  $B_r$  is the half intensity width of an XRD line in case of the deformed material and  $B_o$  is the width of the same line for the undeformed (initial) material. The half intensity width values were taken from two specific XRD lines, namely, the (111) and the (200).

In case of an annealed sample, the strain parameter can be defined as a ratio,  $B/B_r$ , where  $B$  is the half intensity width of a particular X-ray peak in the annealed material and  $B_r$  is the half intensity width of the same peak in the initial deformed condition. For the annealed materials, the half intensity widths were measured only from the respective (111) peaks.

### 3.7 Measurement and Representation of Texture

It has already been mentioned earlier (in section 2.9 of chapter 2) that the crystallographic texture of a rolled polycrystalline sheet metal can be represented as being of the type  $\{hkl\} <uvw>$ , where  $\{hkl\}$  set of planes of the crystals are parallel to the rolling plane and  $<uvw>$  set of directions are along the rolling direction. Usually the texture of a particular specimen may consist of a number of components. Texture data from a specimen are generally represented with the help of pole figures [130]. A pole figure actually contains all the information regarding the texture components of a particular material. However, the information given by pole figures is qualitative or at best semiquantitative in nature. A much more comprehensive and quantitative description of texture can be given with the aid of *Orientation Distribution Function* (ODF) technique.

An ODF actually describes the frequency of occurrence of orientations in the three dimensional (*Euler*) orientation space. The *Euler space* can be defined by three *Euler angles*  $\phi_1$ ,  $\phi$  and  $\phi_2$ . These angles constitute a set of three consecutive rotations which transform the sample frame S to crystallite frame C, as shown in the Figure 3.1 [131]. From the Figure, it

is readily understood that a particular texture component  $\{hkl\} \langle uvw \rangle$  can be completely represented by a point  $(\phi_1, \phi, \phi_2)$  in the *Euler space*. Quite naturally, each component of texture has a distinct position in the orientation space. As a result, a quantitative analysis of texture is possible with a much better resolution. Figure 3.2 shows the schematic diagram of the *Euler space* [132]. Mathematical methods are available for calculating ODF from several experimentally determined pole figures. The most widely accepted methods are those proposed independently by Bunge [133] and Roe [134], who used generalized spherical harmonic functions to represent the orientation distributions. A thorough mathematical treatment of the ODF can be found in the texts by Bunge [135, 136]. The *Bunge notation* [133] is the more common and this has been used throughout in the present investigation. For the cubic crystal symmetry, the orientation space is defined by three orthogonal axes  $\phi_1$ ,  $\phi$  and  $\phi_2$ , each ranging from  $0^\circ$  to  $90^\circ$ . This total volume is divided into three basic ranges in which each orientation appears only once. The value of the orientation density at each point is the intensity of that orientation in multiples of the random.

The maxima of the pole density variations can be described as single peaks or fibres [137]. In case of peak type texture, the maxima can be described by assuming a crystallographic plane  $(hkl)$  perpendicular to the normal direction ND and a crystallographic zone axis  $[uvw]$  parallel to the rolling direction RD. The fibre types are defined by an orientation rotated around a given axis with the intensity along the fibre being constant. In FCC materials, there are three important fibres [138] which run through almost all the important rolling texture components. Figure 3.3 illustrates the positions of main rolling texture components of FCC materials in *Euler space*, and Figure 3.4 indicates their positions in the corresponding  $\phi_2$  sections [138]. Any change in intensity or the peak positions can be readily detected in a quantitative manner, when the intensity variations are plotted as a function of orientation angle in two dimensional coordinates.

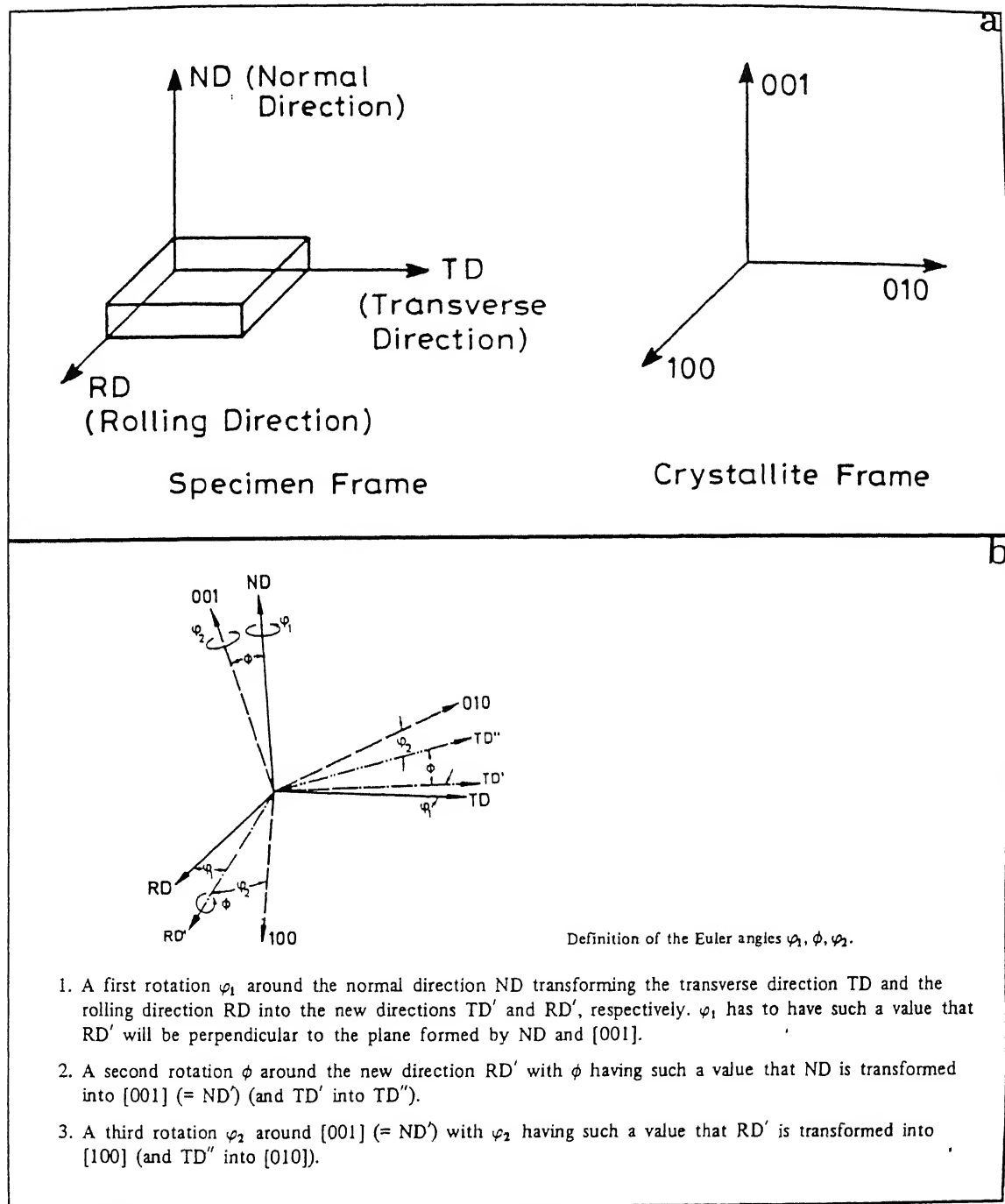


**Figure 3.1** Schematic representation of three Euler angles  $\phi_1$ ,  $\phi$ ,  $\phi_2$ ; (a) sample frame *S* and crystallite frame *C*, (b) Transformation of sample frame into crystallite frame [131]

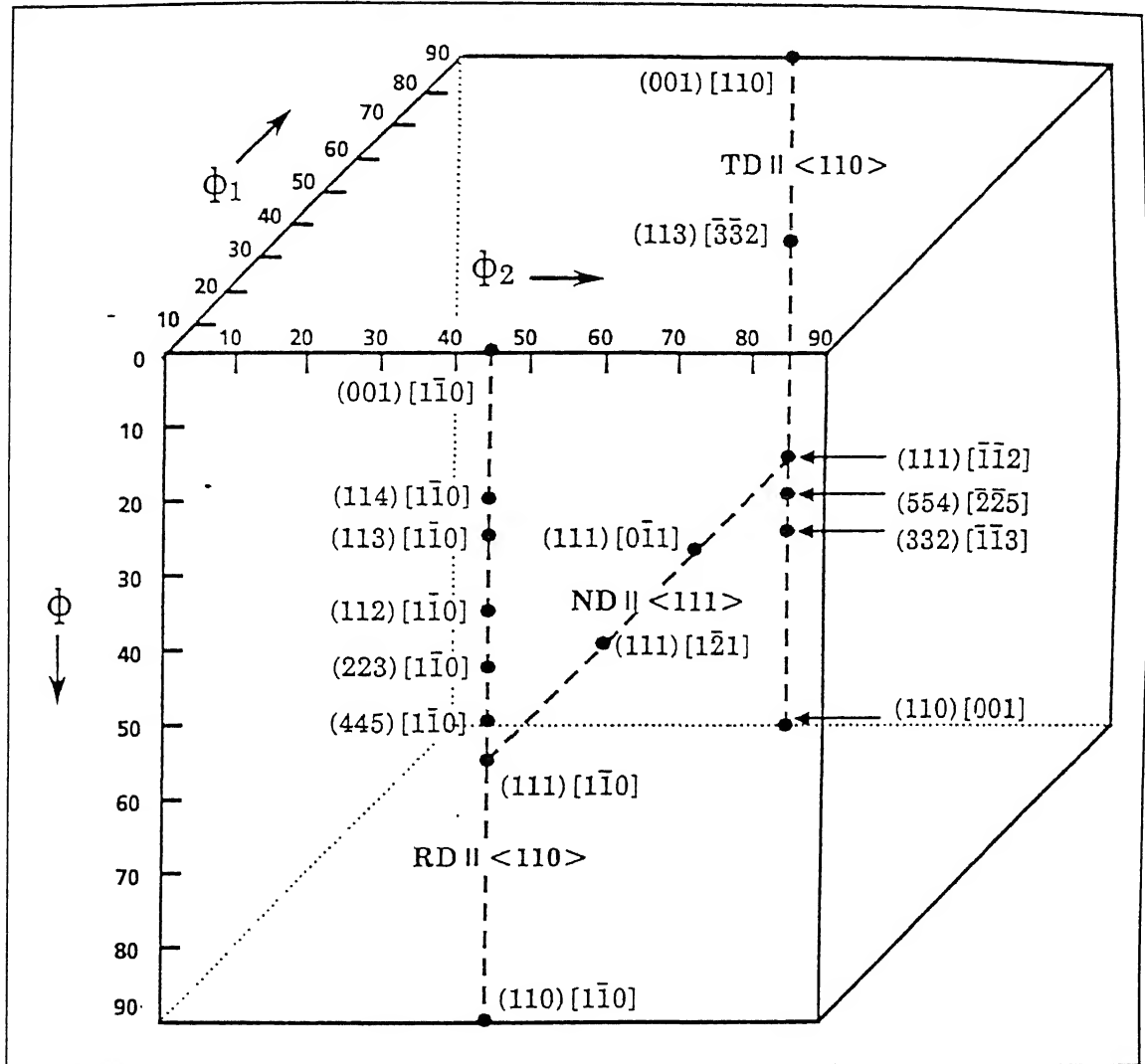


Figure 3.2 Schematic presentation of Euler space [131]

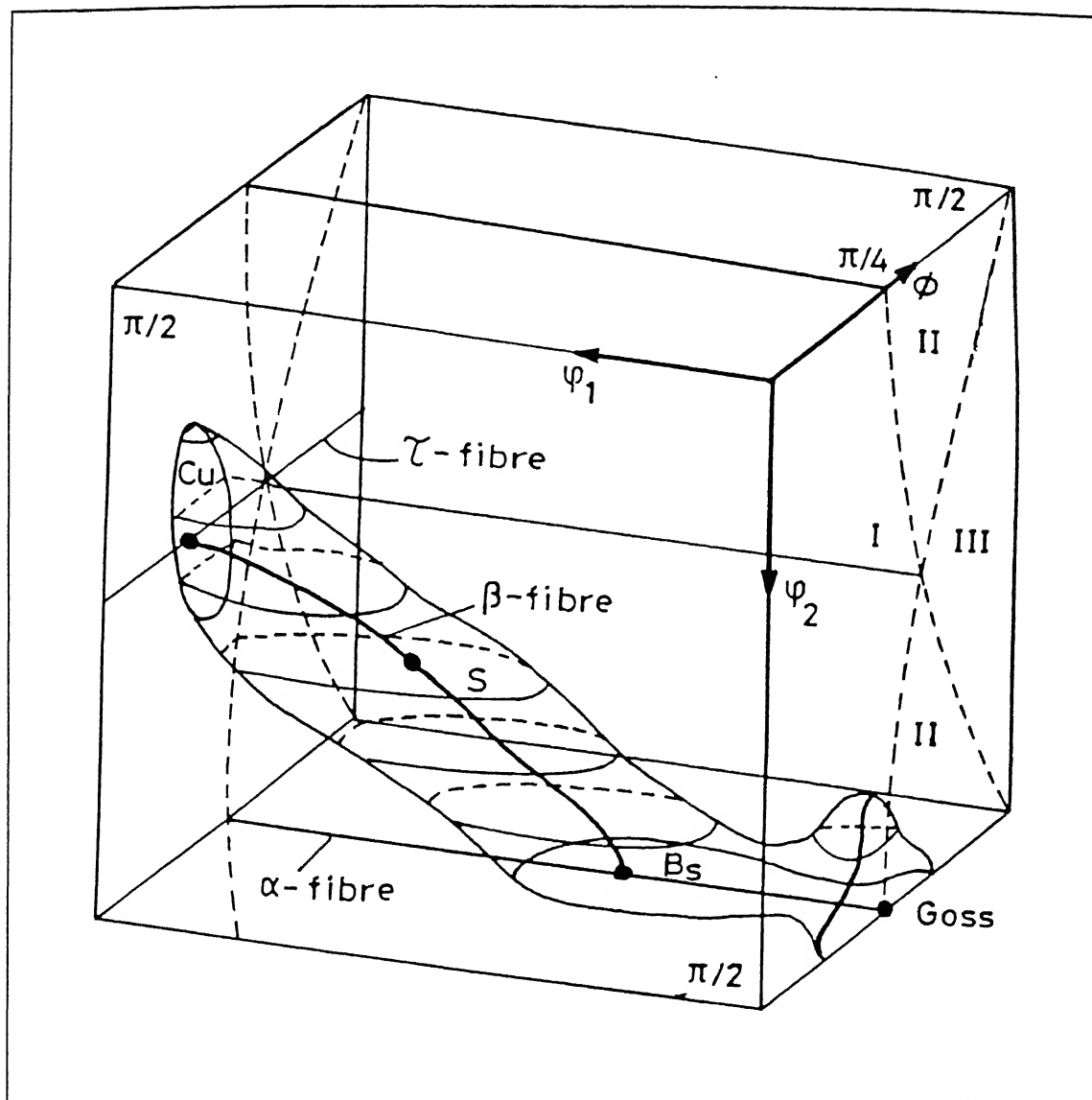


Figure 3.3 Schematic presentation of the FCC rolling texture in the first subspace of three dimensional Euler angle space [138]

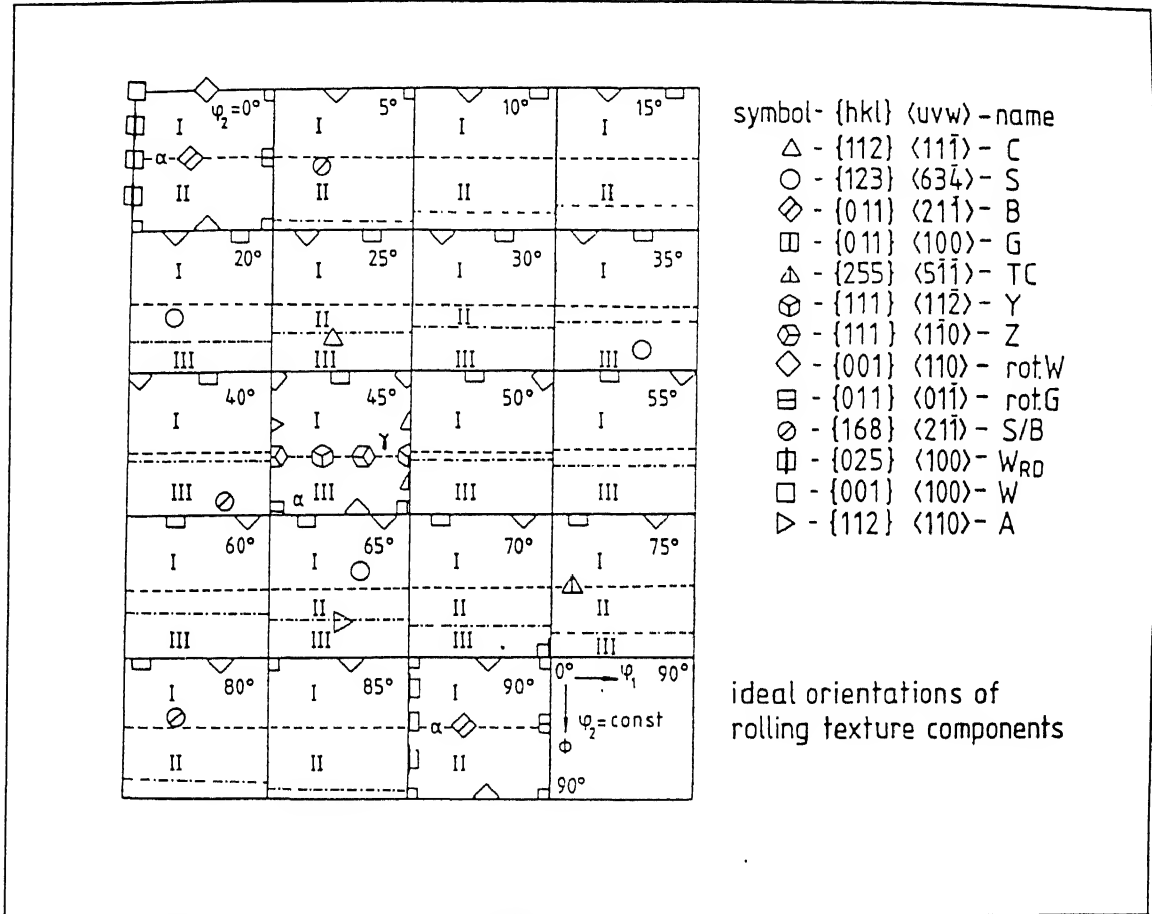


Figure 3.4 Main FCC rolling texture components

schematically shown in two dimensional  $\phi_2$  sections of Euler space [138]

In the present investigation, all the cold rolled samples and a few selected annealed samples were used for texture analysis. For this purpose, 10 mm x 18 mm rectangular specimens were prepared by carefully polishing a surface at a depth of one quarter thickness from any of the free surfaces. These samples were then subjected to X-ray diffraction using  $\text{Cu}_{K\alpha}$  radiation in a fully computerized texture analysing equipment. An advanced software package analysed the diffracted intensity and generated the pole figures as well as the three dimensional ODF plots. Intensity variations of the texture fibres were directly obtained from the numerical data charts, which were then used to draw the line diagrams of different fibres.

### **3.8 Differential Scanning Calorimetry (DSC)**

The amount of heat energy released during annealing of cold deformed samples was measured by using a Differential Scanning Calorimeter (DSC). When a specimen and a reference material are heated in a DSC at a known heating rate, the heat inputs to the specimen and the reference remain almost the same unless a heat related transformation takes place in the specimen. The rate of heat input to the specimen relative to the reference is directly related to the amount of transformation in the specimen.

In the present case, the reference used was well annealed platinum (i.e. a material which is not supposed to undergo any transformation when heated). The weights of the rolled experimental samples were chosen in such a manner that the heat capacities could be approximately the same for all the samples. The DSC operation was carried out in a STANTON REDCROFT 1500 DSC equipment. Same thermal environment was maintained for the reference as well as the specimen. High purity argon gas was passed through the DSC cell to prevent oxidation of the material. For all the rolled samples, a heating rate  $20^{\circ}\text{C}/\text{min}$  was used. The output, heat evolution per unit time ( $\text{mcal}/\text{sec}$ ), was recorded as a function of temperature.



# CHAPTER 4

## DEFORMATION BEHAVIOUR

## ● *Deformation Behaviour*

### 4.1 Microstructure

#### 4.1.1 Starting Material

The starting material, as stated earlier, was a piece of continuously cast sheet of about 1 mm thickness. This was then cut into small pieces and sealed into quartz capsules in high vacuum ( $\sim 10^{-4}$  Pa). The encapsulated pieces were subjected to homogenization annealing at 1160°C for 24 hrs. Figure 4.1a shows the microstructure of the cast material taken from the flat sheet surface. Figure 4.1b shows the micrograph of an area on the longitudinal surface of the cast sheet, indicating typical dendritic characteristics of the cast structure.

Homogenization annealing led to the development of well delineated grains; almost every one of them shows the presence of a second phase inside (Figure 4.2a). A magnified micrograph (Figure 4.2b) clearly shows the dispersion of second phase islands within large grains. The existence of a second phase is supported by the Nickel-Aluminium binary phase diagram [6], as the particular composition used in this study lies within the  $\gamma' + \gamma$  two phase region. The compositions of the two phases, as given by EDAX analysis, are indicated in Table 4.1.

---

**Table 4.1** Compositions of the Two Phases (atomic percent)

<i>Phases</i>	<i>Al</i>	<i>Ni</i>	<i>Zr</i>
Matrix Phase	23.7	75.48	0.83
Second Phase	16.49	83.22	0.29

\* Boron content was not determined

---

The above table shows that the matrix phase can be described as the ordered  $\text{Ni}_3\text{Al}$  ( $\gamma'$ )



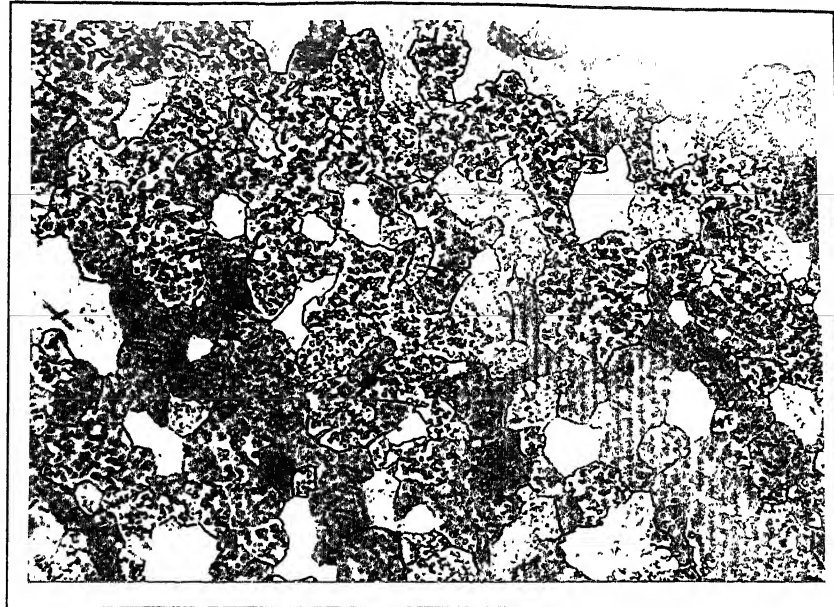
200 μm

Figure 4.1a Optical micrograph of cast Ni<sub>3</sub>Al(B,Zr) (flat sheet surface)



20 μm

Figure 4.1b Optical micrograph of cast Ni<sub>3</sub>Al(B,Zr) (longitudinal surface)



200 $\mu$ m

Figure 4.2a Optical micrograph of homogenized  $\text{Ni}_3\text{Al}(\text{B},\text{Zr})$  alloy (sheet plane)



20 $\mu$ m

Figure 4.2b Optical micrograph of homogenized  $\text{Ni}_3\text{Al}(\text{B},\text{Zr})$  alloy (longitudinal plane)

while the second phase is basically a disordered Ni-rich solid solution ( $\gamma$ ). The Zr preferentially partitioned into the  $\gamma'$  phase. The average size of the  $\gamma'$  grains is 40 - 50  $\mu\text{m}$  and the volume fraction of the  $\gamma$  phase is around 25%.

Transmission electron microscopy of the thin foils made from the homogenized material, sometimes showed fine particles inside what could presumably be the  $\gamma$  regions. The SAD pattern taken from such regions invariably showed the presence of weak superlattice spots along with the fundamental reflections – typical of an ordered structure (Figure 4.3). It therefore appears quite likely that the particles inside the  $\gamma$  islands are of  $\gamma'$ . These observations agree well with those of Ball et al [125].

## 4.1.2 Cold Rolled Material

### 4.1.2.1 Optical and Scanning Electron Micrographs

Gradual changes in microstructure were observed when the homogenized alloy was cold rolled at stages to a maximum level of 73% (Figures 4.4a to 4.4h). The material could not be rolled further due to the sheet becoming extremely thin which could not be reduced further in the rolling mill. All the optical and scanning electron micrographs were taken from the longitudinal section.

No significant changes from the homogenized microstructure could be observed after 15% rolling (Figure 4.4a); however, after 25% deformation (Figure 4.4b) many of the  $\gamma$  islands appeared to be somewhat elongated along the rolling direction. At the same time, these were found to be arranged in a number of parallel rows (possibly deformation bands) which were inclined to the rolling direction at an angle of nearly  $60^\circ$ . A few regions could also be seen where the second phase islands were still showing a random arrangement. This trend was more prominently visible after 35% deformation (Figure 4.4c). The  $\gamma$  being the softer of the two phases, it is likely to deform more easily, elongating itself along the rolling direction.

After 45% cold reduction, the microstructure showed a drastic change (Figure 4.4d). The



Figure 4.3 SAD pattern taken from the thin foil of homogenized alloy shows superlattice spots along with the fundamental spots

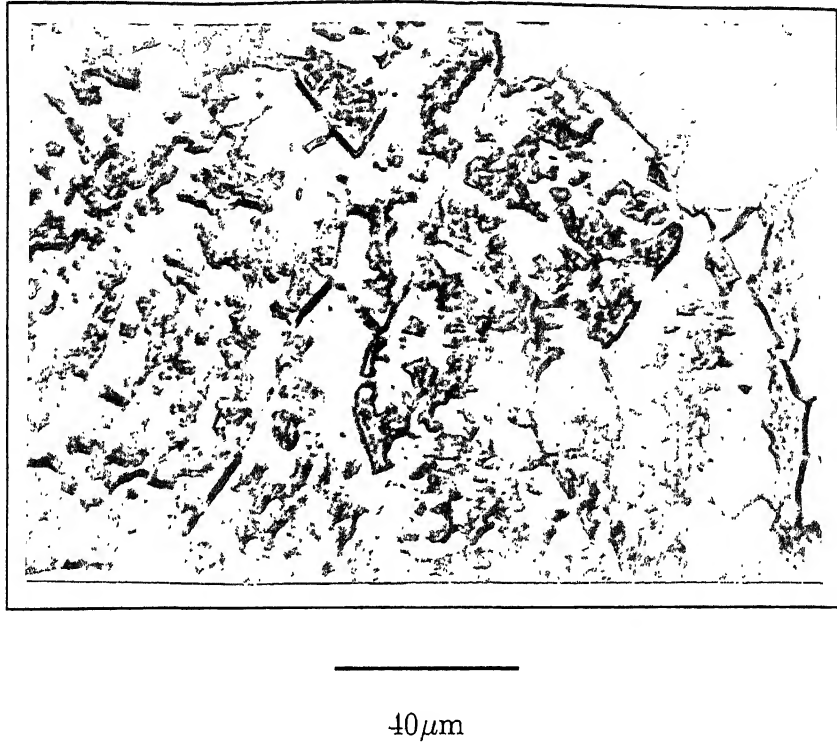


Figure 4.4a Optical micrograph of 15% cold rolled material

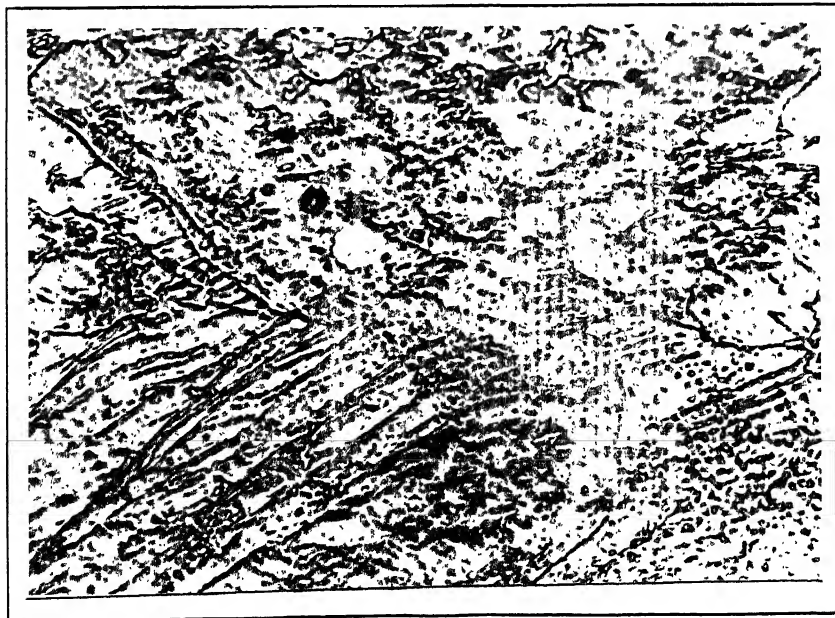


Figure 4.4b Optical micrograph of 25% cold rolled material



40 $\mu$ m

Figure 4.4c Optical micrograph of 35% cold rolled material



40 $\mu$ m

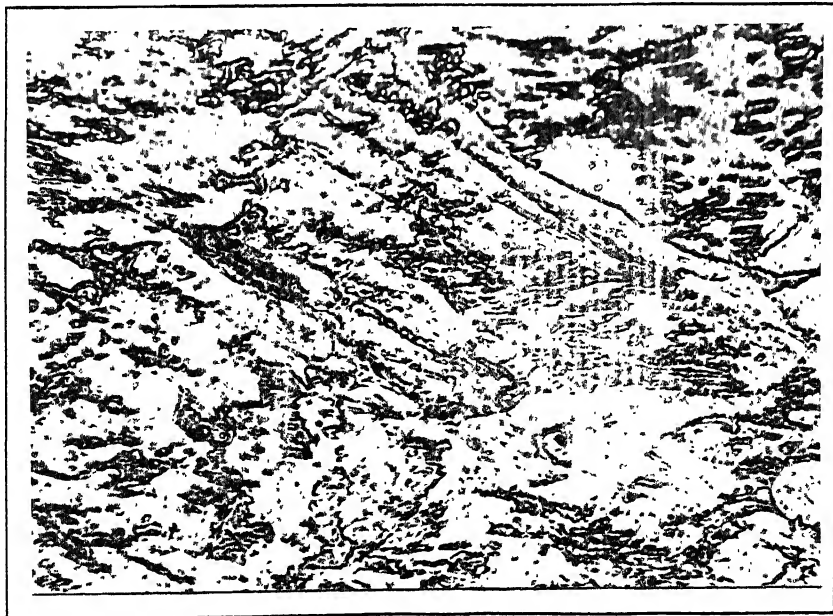
Figure 4.4d Optical micrograph of 45% cold rolled material





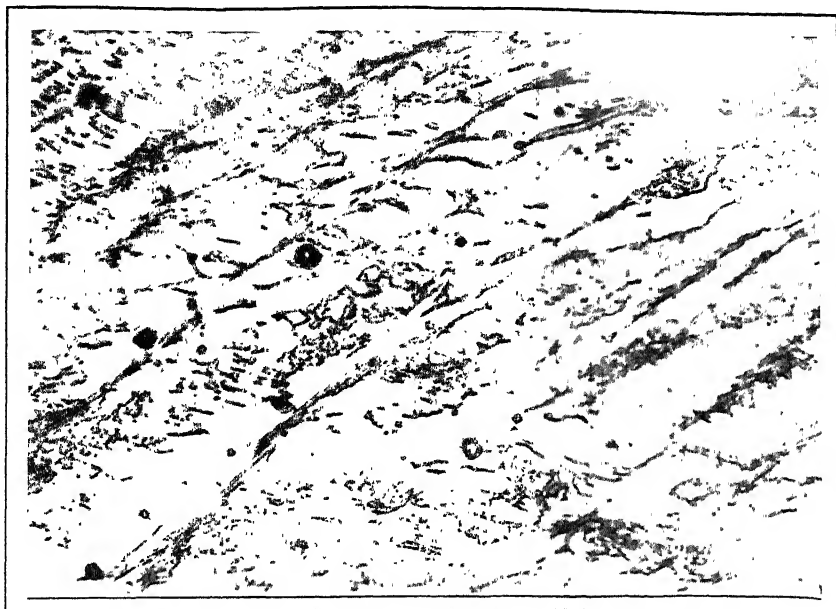
100 $\mu$ m

Figure 4.4e Optical micrograph of 45% cold rolled material (at lower magnification)



40 $\mu$ m

Figure 4.4f Optical micrograph of 55% cold rolled material



40 $\mu$ m

Figure 4.4g Optical micrograph of 65% cold rolled material



40 $\mu$ m

Figure 4.4h Optical micrograph of 73% cold rolled material

arrangement of  $\gamma$  phase islands in rows elongated along the rolling direction was no longer discernible, rather they appeared to be distributed in a more or less random fashion in the  $\gamma'$  matrix. This could possibly be due to the formation of a large number of shear bands at this stage, as shown in a low magnification micrograph of the same sample (Figure 4.4e). The density of shear bands steadily increased with increasing rolling reductions (Figures 4.4f to 4.4h). The  $\gamma$  phase islands were observed to gradually realign themselves within the shear bands. Well developed shear bands at this stage were observed to be inclined to the rolling direction at an angle of nearly  $30^\circ$  -  $35^\circ$ . Although in the initial stages of cold rolling the distribution of the  $\gamma$  islands in  $\gamma'$  could be clearly identified in optical micrographs, it became quite difficult at later stages because of the incidence of a high density of shear bands. A much clearer idea about the  $\gamma$  distribution pattern could be had from the scanning electron micrographs (SEM) presented in Figures 4.5a to 4.5d.

#### **4.1.2.2 Transmission Electron Micrographs**

In order to obtain more detailed structural information from the cold rolled alloy, thin foils from a number of selected samples were examined using a transmission electron microscope. The examination was conducted on the rolling plane sections.

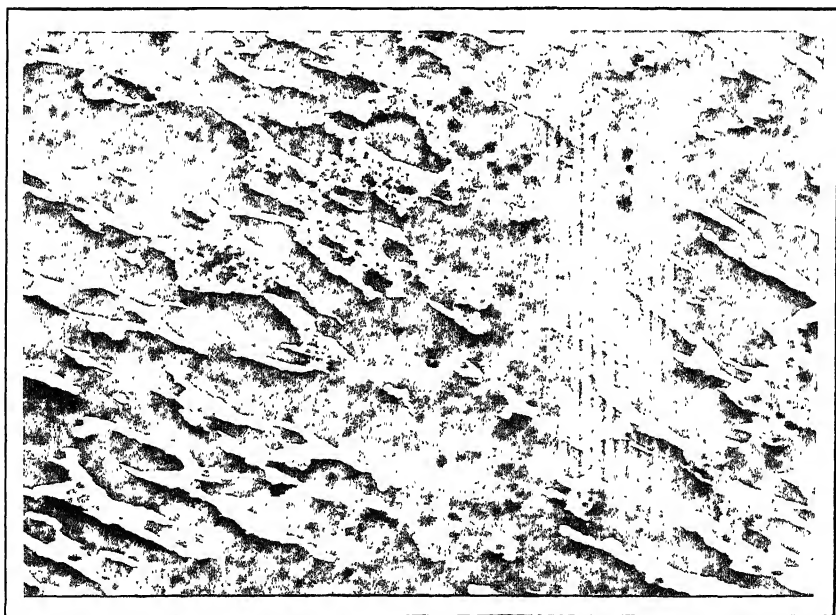
TEM micrographs of the deformed samples exhibit the usual cell structure at lower reduction levels. This is shown typically in Figure 4.6a for the 35% rolled sample. The SAD pattern from this area and corresponding indexed spots are shown in Figures 4.6b and 4.6c respectively. These indicate an ordered FCC ( $L1_2$ ) crystal structure, featuring both the  $\{100\}$  and  $\{110\}$  superlattice reflections. Sometimes, specially near the  $\gamma'$  grain boundaries, twin traces could also be observed (Figure 4.7a). Another such twinned region is shown in Figure 4.7b.

Cellular microstructure was also observed from the 45% cold rolled material (Figure 4.8a); its SAD indicating again a fully ordered  $L1_2$   $\gamma'$  phase (Figure 4.8b). At this stage, features



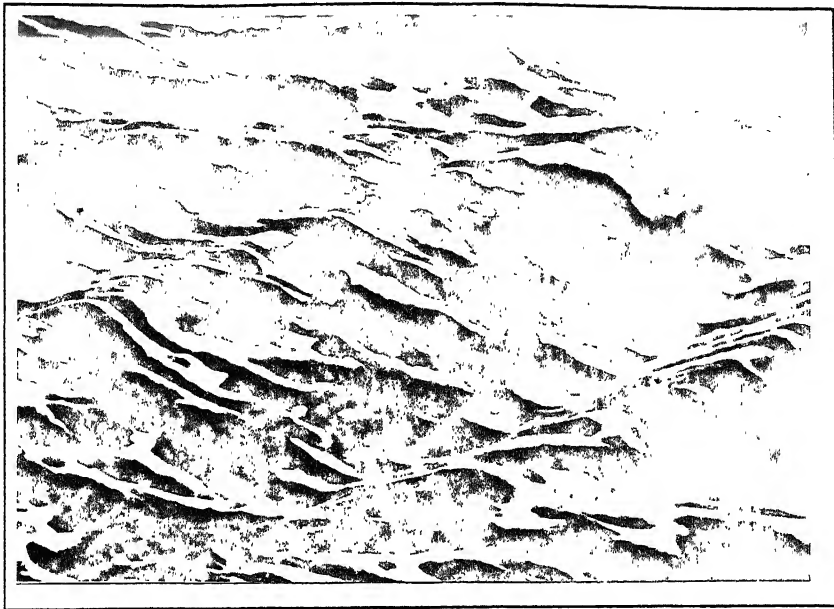
20 $\mu$ m

Figure 4.5a SEM micrograph of homogenized material



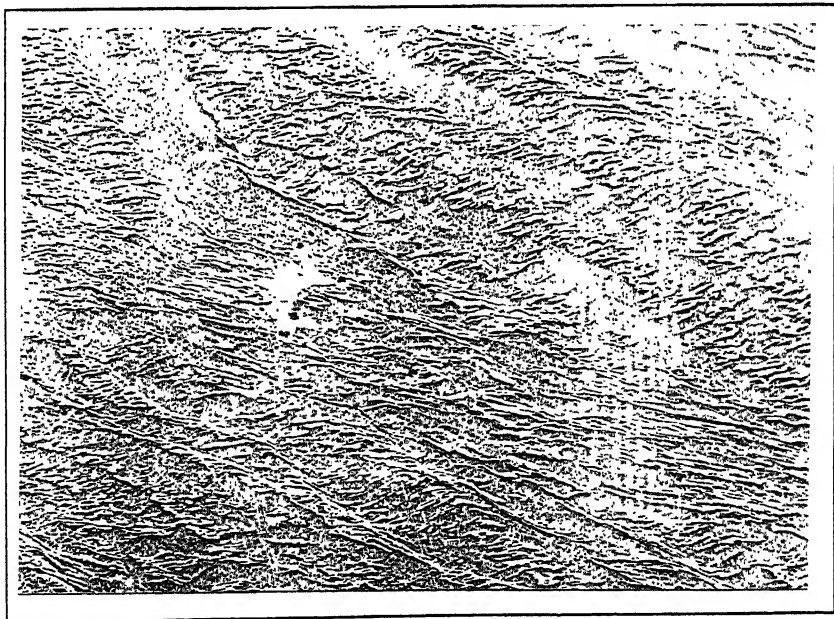
10 $\mu$ m

Figure 4.5b SEM micrograph of 45% rolled material



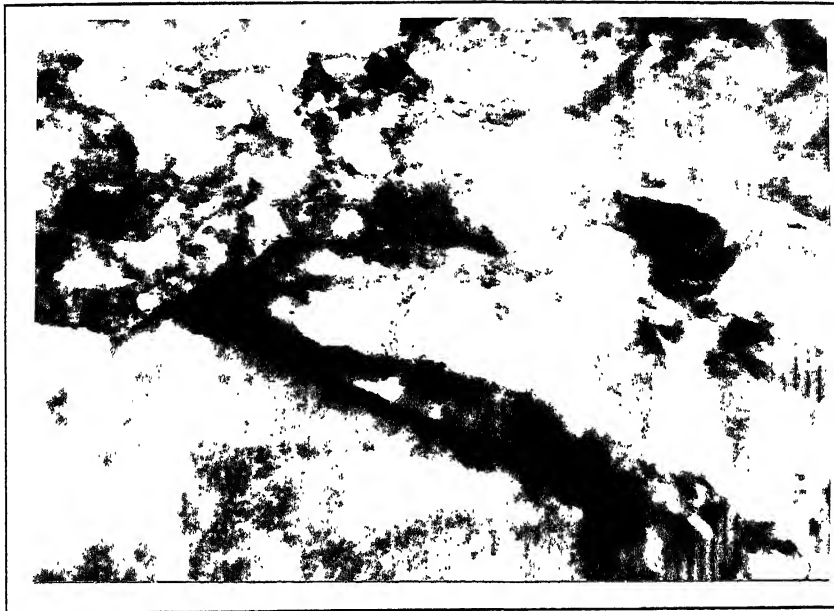
10 $\mu$ m

Figure 4.5c SEM micrograph of 65% rolled material



40 $\mu$ m

Figure 4.5d SEM micrograph of 73% rolled material



$2\mu\text{m}$

Figure 4.6a TEM micrograph of 35% rolled material



Figure 4.6b SAD pattern of the thin foil area shown in Figure 4.6a

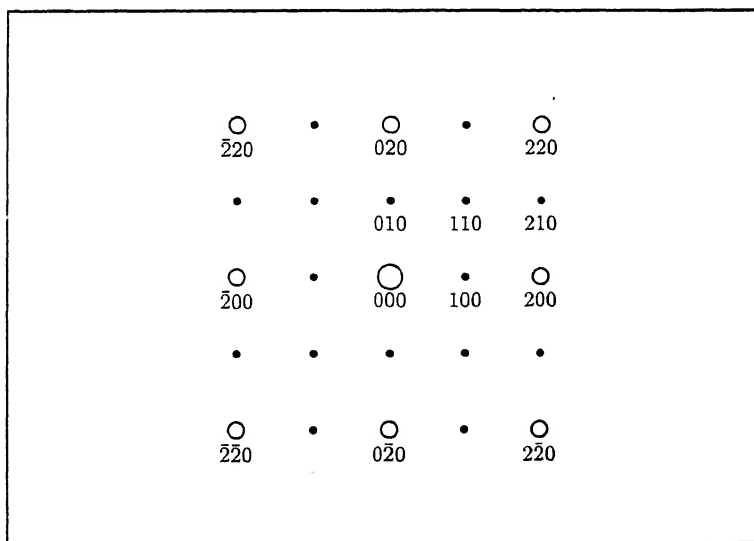


Figure 4.6c Indexing of the SAD pattern shown in Figure 4.6b



5 $\mu$ m

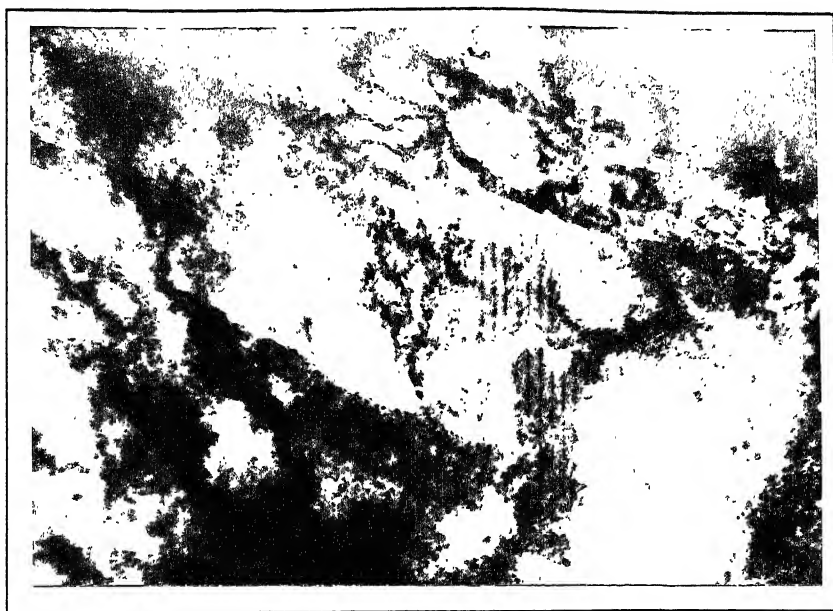
Figure 4.7a TEM micrograph of the 35% rolled material showing the twin bands



2 $\mu$ m

Figure 4.7b Twin bands in the same material as shown above





1 $\mu$ m

Figure 4.8a TEM micrograph of 45% rolled material

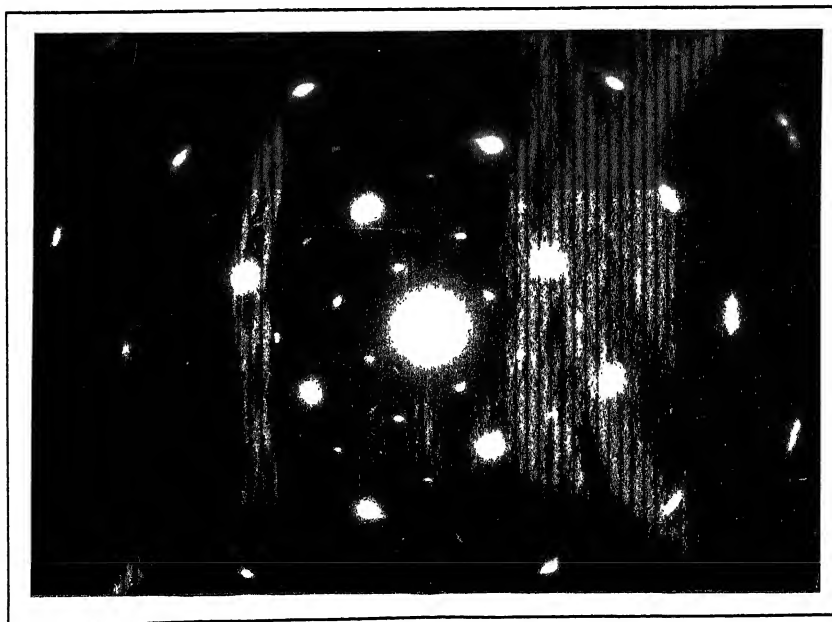


Figure 4.8b Corresponding SAD pattern of the above area  
indicating ordered  $L1_2$  structure



5 $\mu$ m

Figure 4.9a Microbands in thin foil of 45% rolled material



2 $\mu$ m

Figure 4.9b Twin bands in thin foil of 45% rolled material



2 $\mu$ m

Figure 4.9c Shear bands in thin foil of 45% rolled material

showing microbands (Figure 4.9a), twins (Figure 4.9b) and shear bands (Figure 4.9c) could also be seen.

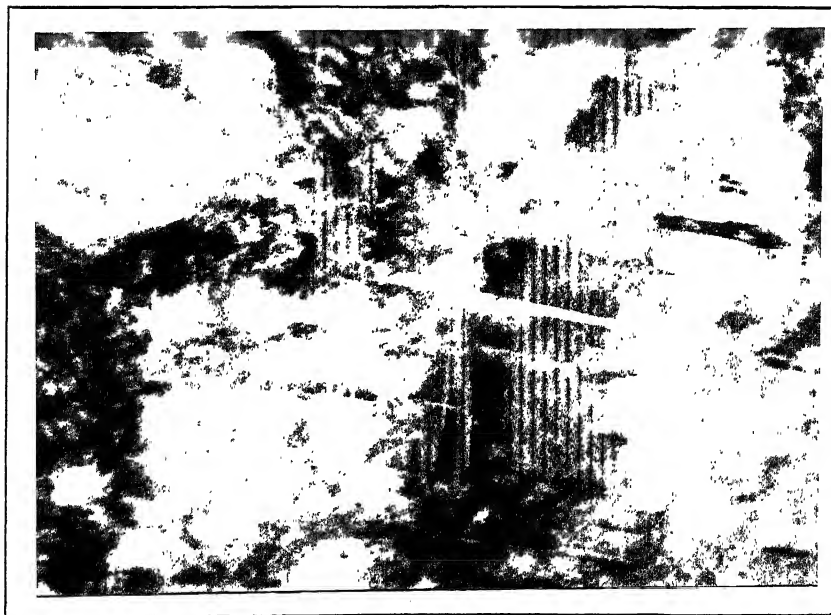
The density of twins increased as the amount of cold deformation increased. This is shown clearly in the TEM microstructures of the 65% and 73% rolled materials (Figures 4.10a and 4.10b). The SAD pattern from the area in Figure 4.10b and the corresponding indexed spots are presented in Figures 4.10c and 4.10d respectively. The presence of extra reflection spots (other than the fundamental and superlattice spots) with fractional indices indicates that these are twin spots [139]. The twin plane here has been identified as  $(111)_{L1_2}$ . Pashley and Stowell [140] also noticed in their work on gold film the presence of weak  $\frac{1}{3}\{4\bar{2}2\}$  twin reflections which generally arise from the boundaries between the two twin orientations.

Although thin foils from the 73% deformed samples were found to contain twins in most places, isolated untwinned regions could also be observed in them. An example is shown in Figure 4.11a which features a cellular substructure. The superlattice spots were practically absent in the corresponding SAD pattern (Figure 4.11b). This indicates that this could probably be a disordered  $\gamma$  region. Similar cell-like regions were also found close to the heavily twinned regions after 65% deformation (Figure 4.12a). The SAD pattern taken from the central untwinned region *A* shows only faint superlattice spots (Figure 4.12b). On the other hand, the superlattice spots are relatively more intense in the SAD taken from a twinned region *B* (Figure 4.12c). Presumably, region *A* is most probably  $\gamma$  with some  $\gamma'$  dispersed in it. Probable  $\gamma$  regions could also be observed in the 35% rolled material. Figure 4.13a shows a highly dislocated area in the material whose SAD pattern practically does not show any superlattice spot (Figure 4.13b). The indexed spots in the pattern (Figure 4.13c) indicate that the beam direction is  $[310]$ .



2 $\mu$ m

Figure 4.10a Twin bands in thin foil of 65% rolled material



2 $\mu$ m

Figure 4.10b Twin bands in thin foil of 73% rolled material

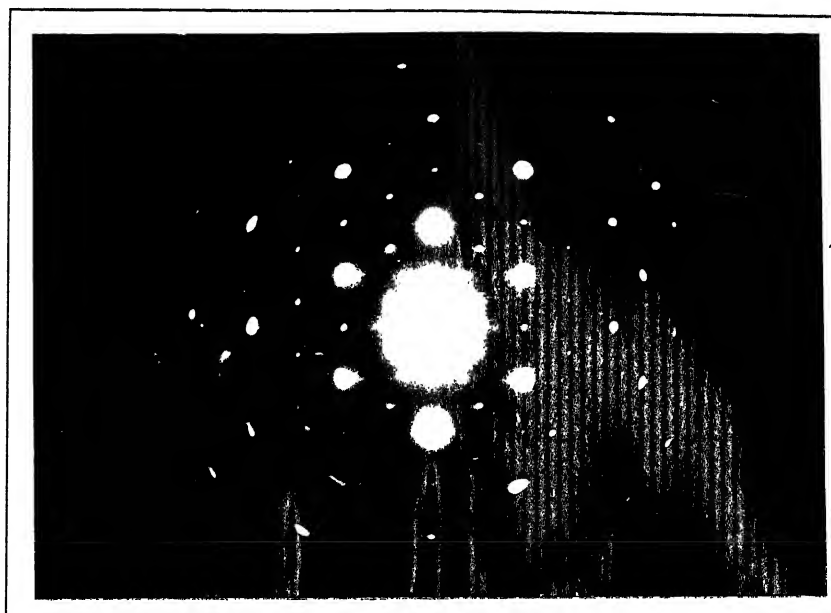


Figure 4.10c SAD pattern of the area shown in Figure 4.10b

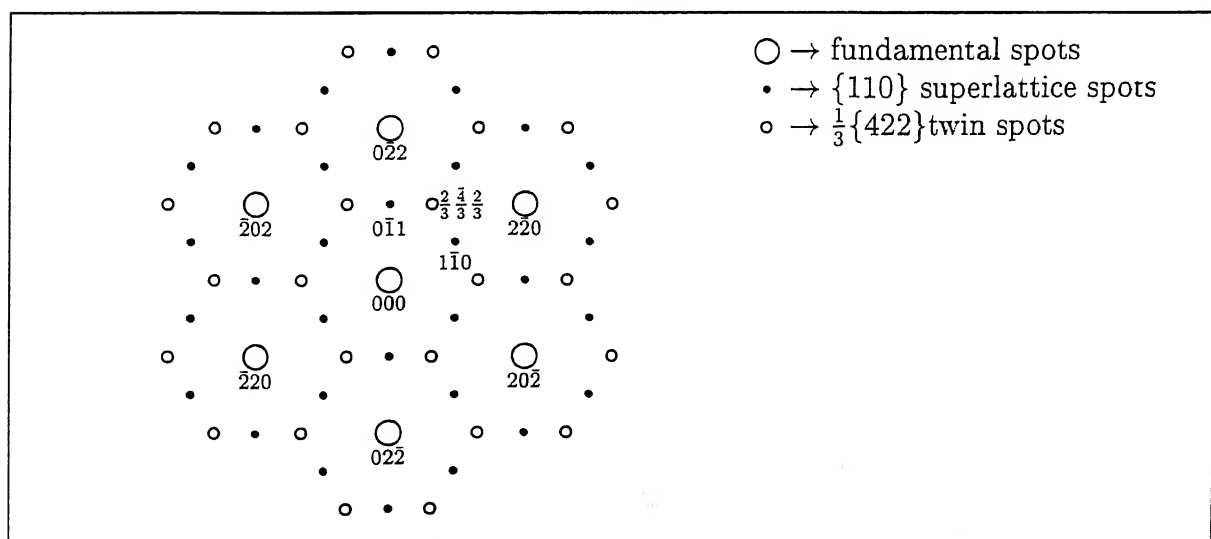
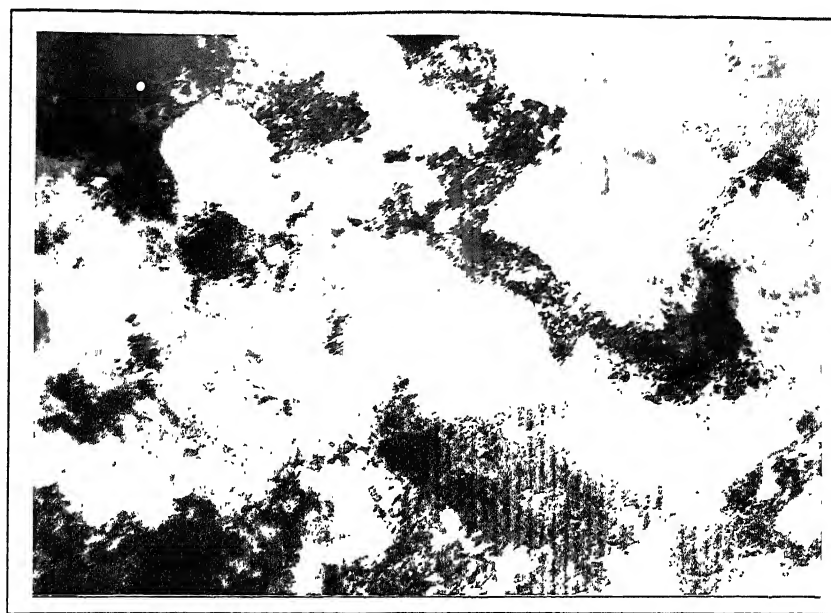


Figure 4.10d Indexing of the SAD pattern shown in Figure 4.10c



0.5 $\mu$ m

Figure 4.11a Cellular substructure in thin foil of 73% rolled material

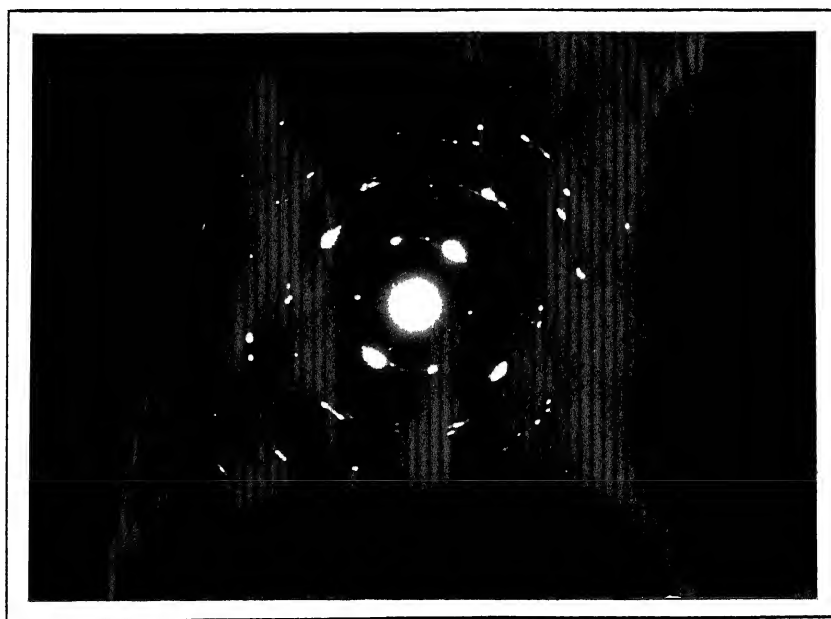


Figure 4.11b Corresponding SAD pattern of the area shown above



2 $\mu$ m

**Figure 4.12a** TEM micrograph of 65% rolled material showing a combination of twinned and untwinned regions





Figure 4.12b SAD pattern taken from the region *A* in Figure 4.12a

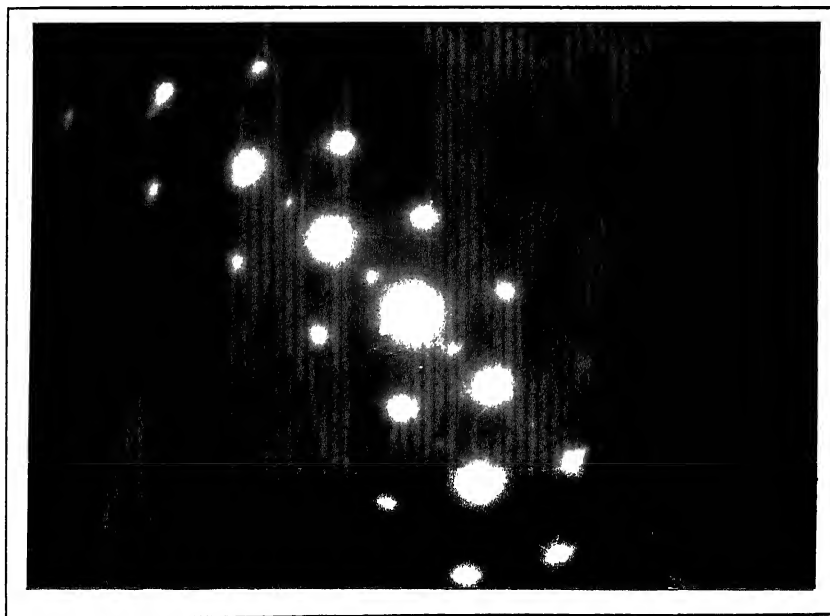
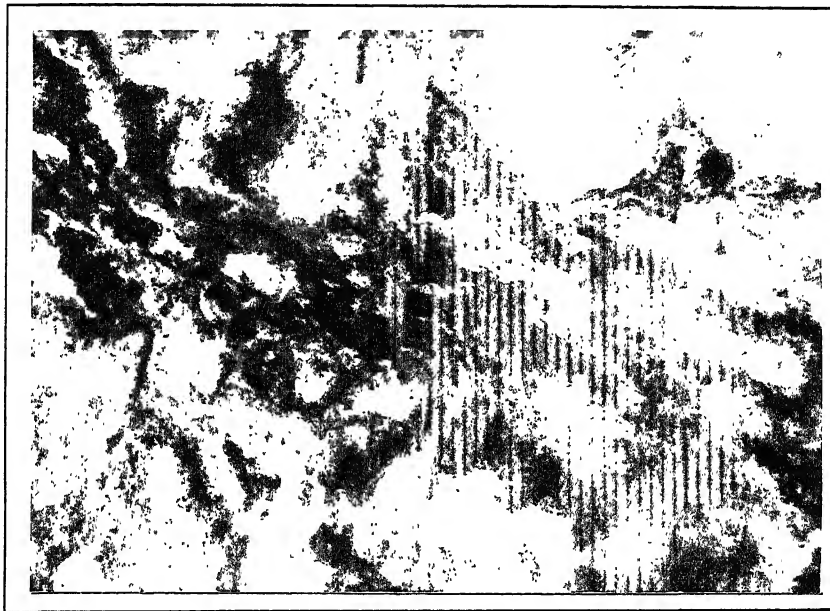


Figure 4.12c SAD pattern taken from the region *B* in Figure 4.12a



2 $\mu$ m

Figure 4.13a TEM micrograph of 35% rolled material



Figure 4.13b SAD pattern of the area shown in Figure 4.13a

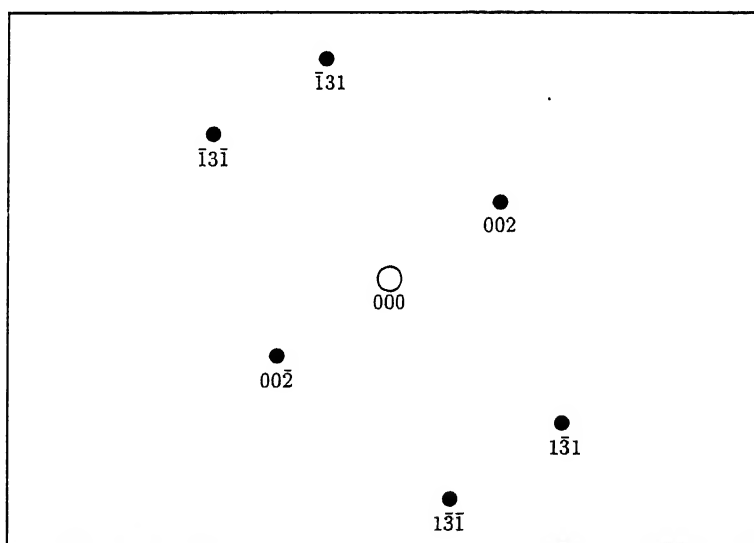


Figure 4.13c Indexing of the SAD pattern shown in Figure 4.13b

## 4.2 X-ray Diffraction Analyses

### 4.2.1 X-ray Line Profiles

#### 4.2.1.1 Starting Material

Figure 4.14 displays the X-ray diffraction profiles for the initial material in the as cast as well as different heat treated conditions. The diffraction pattern for the cast material shows, amongst the fundamental lines, just traces of (111) and (220) while the (200) peak is present with a strong intensity. Among the superlattice peaks, (100) and (102) can be distinguished whereas the (110) peak is totally absent.

The XRD profile for the homogenized material shows the usual FCC peaks in their normal positions, but their relative intensities deviate widely from the ideal values. The two fundamental peaks (111) and (220) have much smaller intensities while the (200) peak assumes an unusually high intensity value. Among the superlattice peaks, (100) is considerably strengthened as compared to that in the cast material. The (102) peak is also present in this profile, whereas the (110) is still absent.

The X-ray diffraction pattern taken from filed powder of the homogenized sample clearly shows the fundamental peaks having relative intensities comparable to a normal FCC material with the highest intensity for the (111) peak. All the superlattice peaks are totally absent in this XRD profile.

The filed powder was vacuum sealed and annealed at 1150°C for 15 min. The XRD profile of the annealed powder again shows traces of (100), (110) and (102) superlattice peaks, along with the well developed fundamental lines.

Figure 4.15 shows a few selected peaks from the X-ray line profiles of the homogenized material, obtained by slow scanning. The existence of the  $\gamma$  phase along with the  $\gamma'$  can be clearly seen from the splitting of the fundamental lines, especially at higher  $2\theta$  values. The entire spectra of the XRD profiles were utilized to correctly measure the values of the lattice parameters of the two phases. The exact peak positions of the two phases along with their

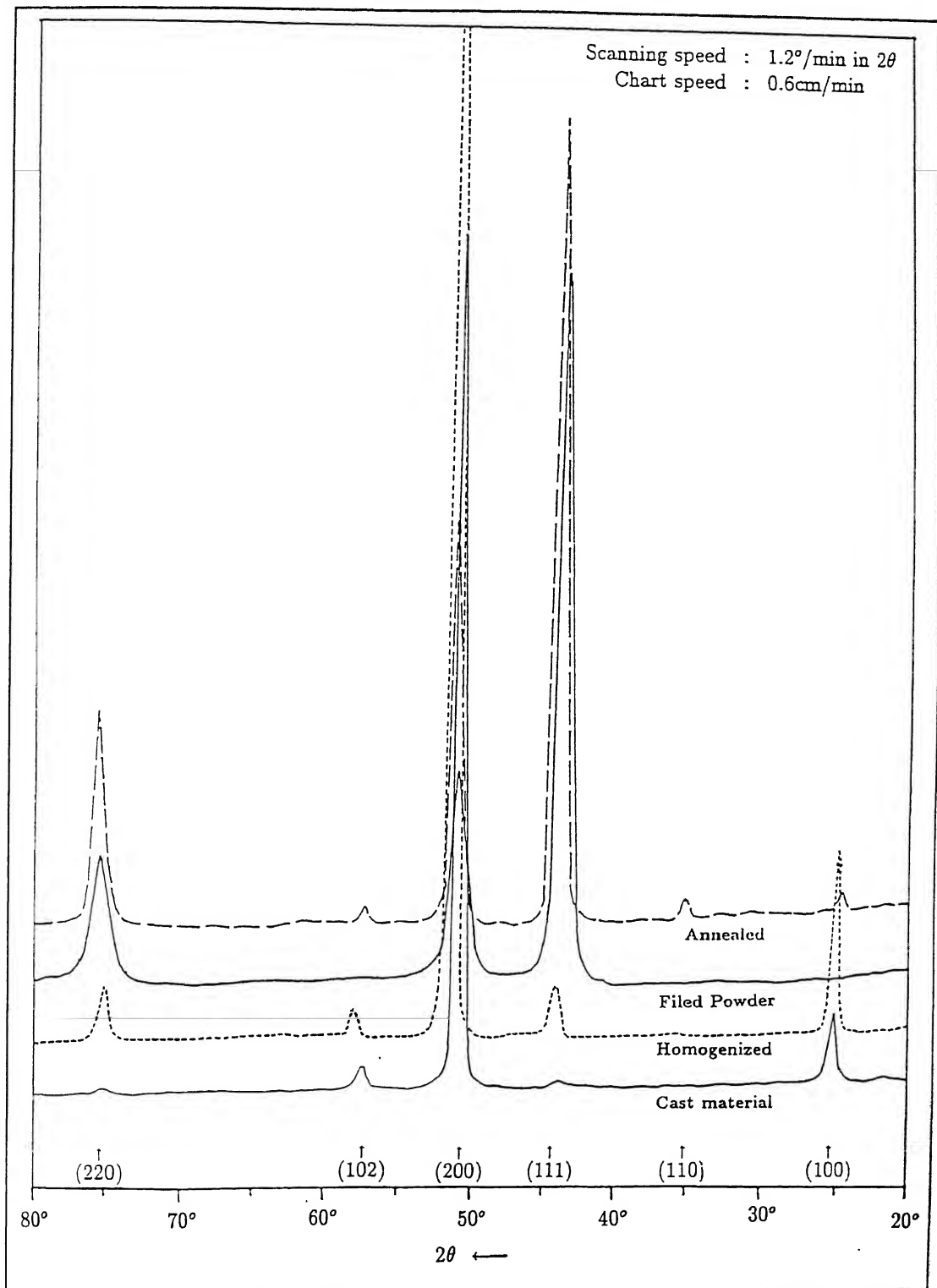


Figure 4.14 X-ray diffraction profiles of the initial material in different conditions

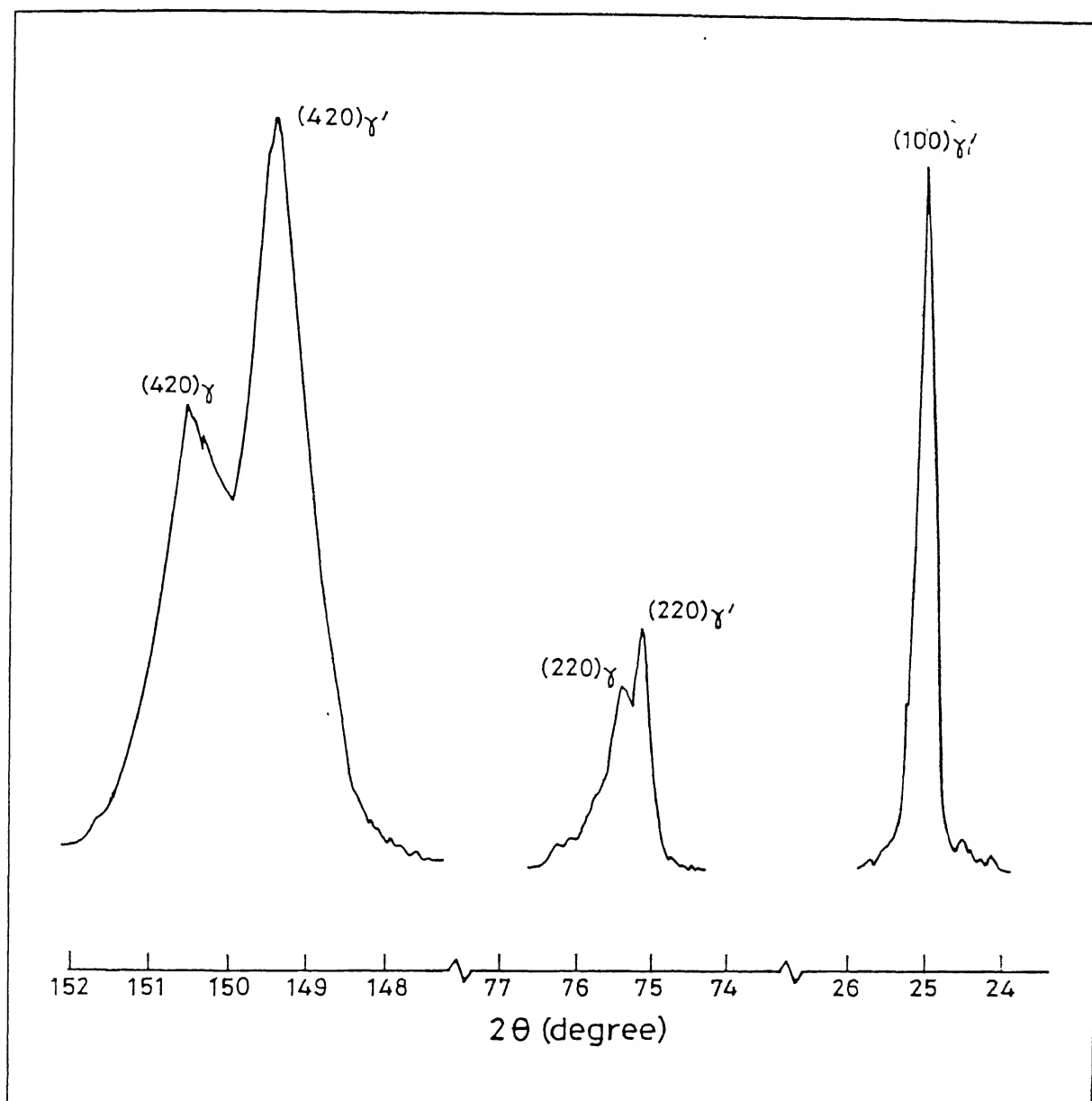


Figure 4.15 A few selected peaks from the X-ray line profiles of the homogenized alloy

lattice parameter values are given in Table 4.2.

**Table 4.2** Peak positions and lattice parameters of  $\gamma'$  and  $\gamma$  phases

XRD line profiles	Ordered $\gamma'$ ( $\text{Ni}_3\text{Al}$ )				Disordered $\gamma$			
	$2\theta$ (degree)	$d$ (Å)	$I/I_{\max}$ (obsvd.)	$I/I_{\max}$ (theo.*)	$2\theta$ (degree)	$d$ (Å)	$I/I_{\max}$ (obsvd.)	$I/I_{\max}$ (theo.*)
100	24.95	3.569	9	40	–	–	–	–
110	–	–	–	40	–	–	–	–
111	43.9	2.062	2	100	44.15	2.051	2.5	100
200	51.2	1.784	100	70	51.39	1.778	100	42
210	57.7	1.598	1.2	40	–	–	–	–
211	–	–	–	20	–	–	–	–
220	75.14	1.264	2.2	60	75.38	1.261	3.3	21
311	91.32	1.078	15	60	91.64	1.075	17	20
222	–	–	–	40	–	–	–	7
400	119.28	0.893	7	20	119.74	0.891	7	4
331	–	–	–	70	–	–	–	14
420	149.38	0.799	7.5	70	150.52	0.797	8.5	15
L.P.	0.3574 nm				0.3565 nm			

\* From ASTM index cards; L.P. – Lattice Parameter

#### 4.2.1.2 Cold Rolled Material

X-ray line intensities recorded for all the cold rolled specimens are shown in Figure 4.16. The XRD profile for the 25% rolled material shows all the lines as are present in the profile of the homogenized material. However, amongst the fundamental peaks, the (111) is much stronger and the (200) weaker in the former as compared to the latter. The (220) peak intensity increases and it shifts a little towards higher  $2\theta$ . Among the superlattice peaks, the (100) intensity decreases considerably and it also drifts towards lower  $2\theta$ : the (102) line becomes marginally weaker.

After 35% rolling, the (100) peak disappears completely, whereas a tiny kink can be observed at the (110) location. This indicates the early stage of appearance of the (110) peak. The (220) peak gets substantially strengthened at this level, whereas the (200) peak

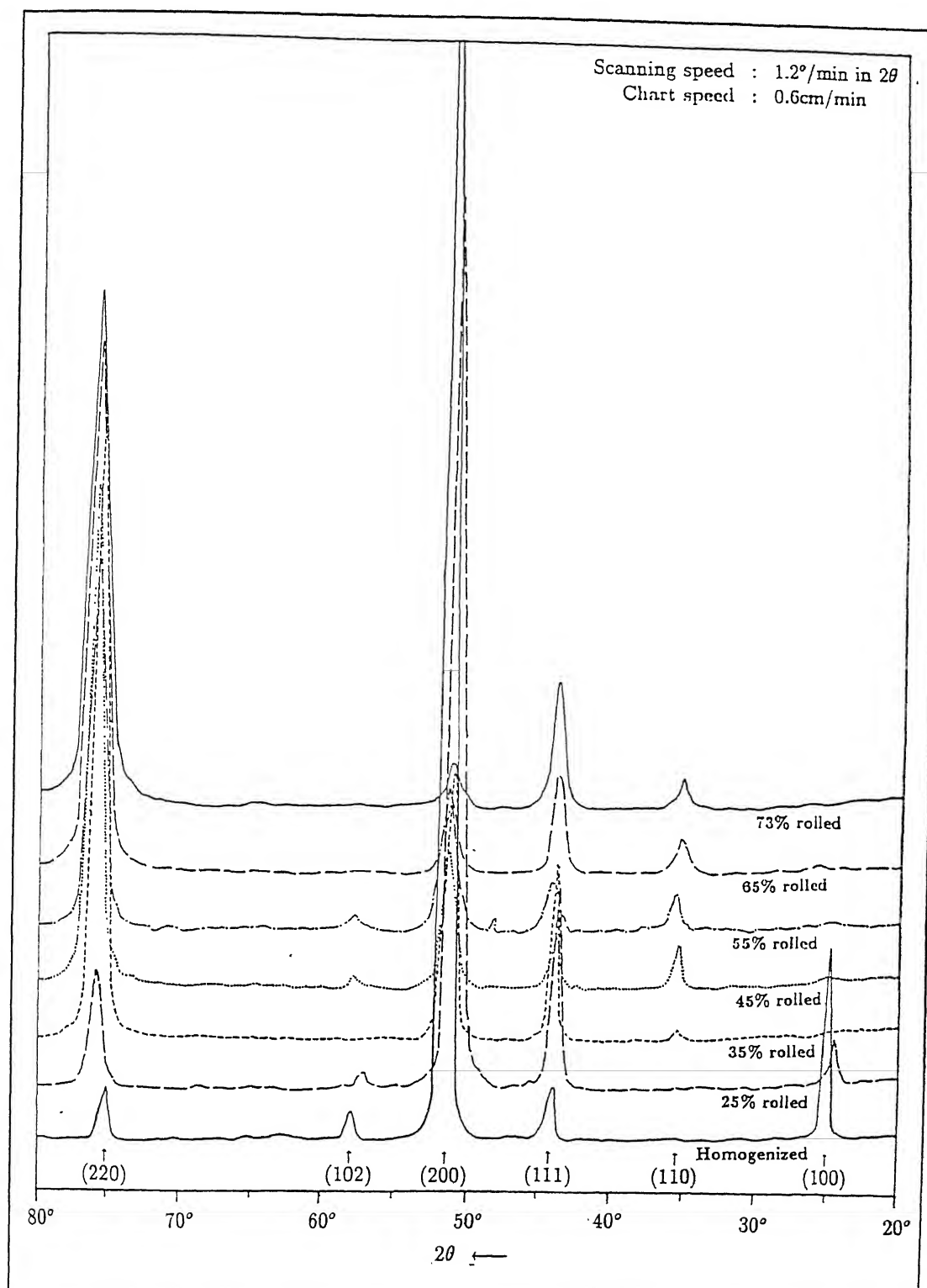


Figure 4.16 X-ray diffraction profiles of the  $\text{Ni}_3\text{Al}(\text{B},\text{Zr})$  alloy  
rolled at different strain levels



intensity declines perceptibly. The intensity of the (111) peak is maintained at nearly the previous level.

The XRD profile from the 45% rolled sample, can be characterized by a distinct (110) and a highly intense (220) peak. The intensities of the other lines are maintained at nearly the previous level. This trend is maintained in all the subsequent XRD profiles for samples rolled upto the 73% level. The salient features of the XRD profiles can be summarized as follows:

- Initially the (100) and (200) peaks have exceptionally high intensity values, but the (200) intensity is reduced significantly whereas the (100) peak completely disappears after only 35% rolling reduction.
- Initially there is no (110) peak and the (220) peak is also considerably weak. The (110) appears only after 45% rolling reduction and the (220) peak gradually intensifies with increase in the deformation level.
- The (111) peak is very weak in the homogenized sample, but it intensifies to some extent after deformation.
- The whole set of the XRD profiles clearly indicates that the (100)/(200) reflection pair dominates in the homogenized material as well as in the very early stages of deformation. By contrast, the (110)/(220) pair becomes stronger at later stages. This significant changeover takes place at around 35% deformation level.

#### **4.2.2 Order Parameter**

Cold rolling usually gives rise to strong textural effects which may alter the relative intensities of the X-ray diffraction lines. Considering this point, all the order parameter measurements were carried out from the two sets of parallel reflections, (100)/(200) and (110)/(220). Since

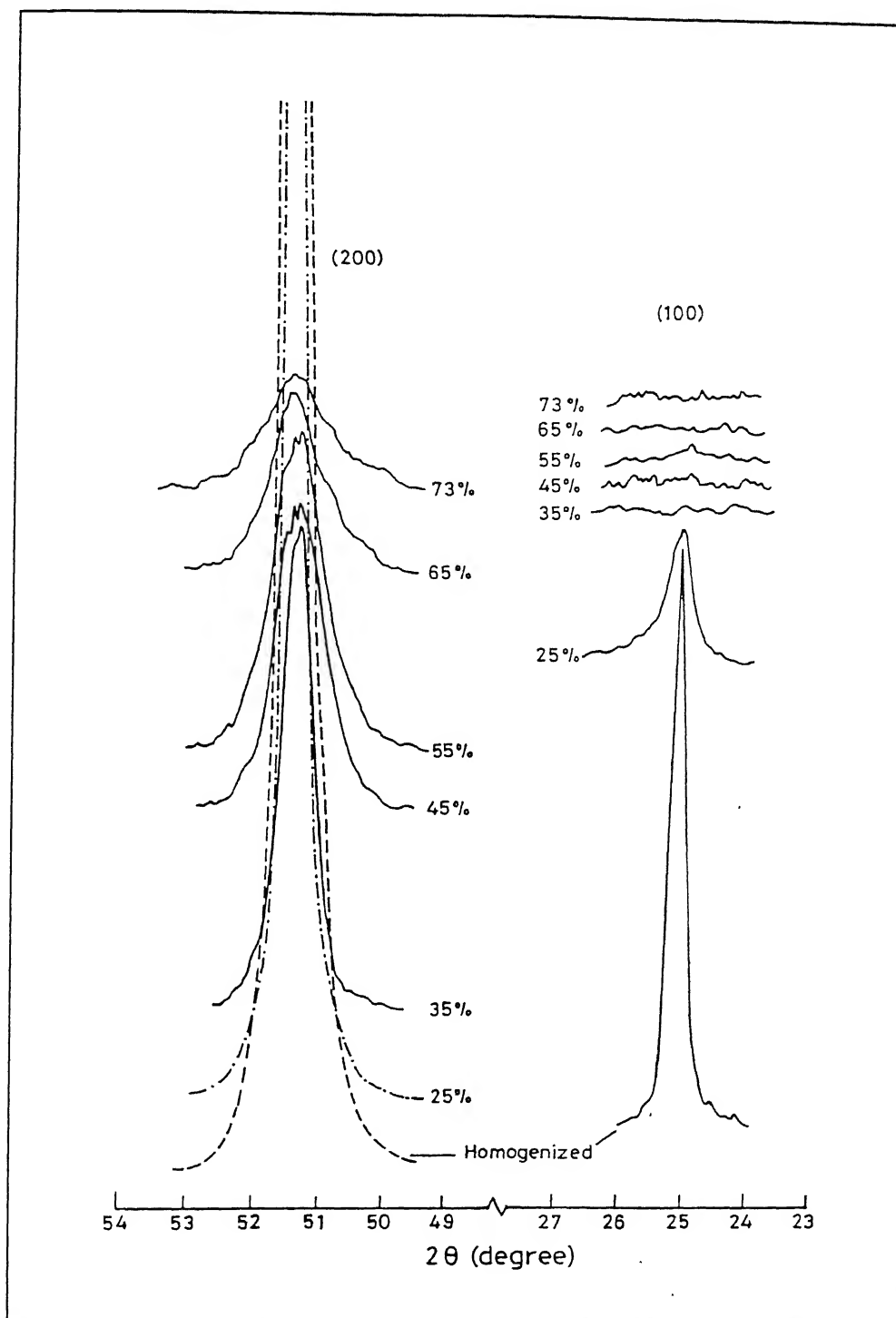


Figure 4.17 XRD line profiles at different degrees of cold reduction showing (100) and (200) reflections

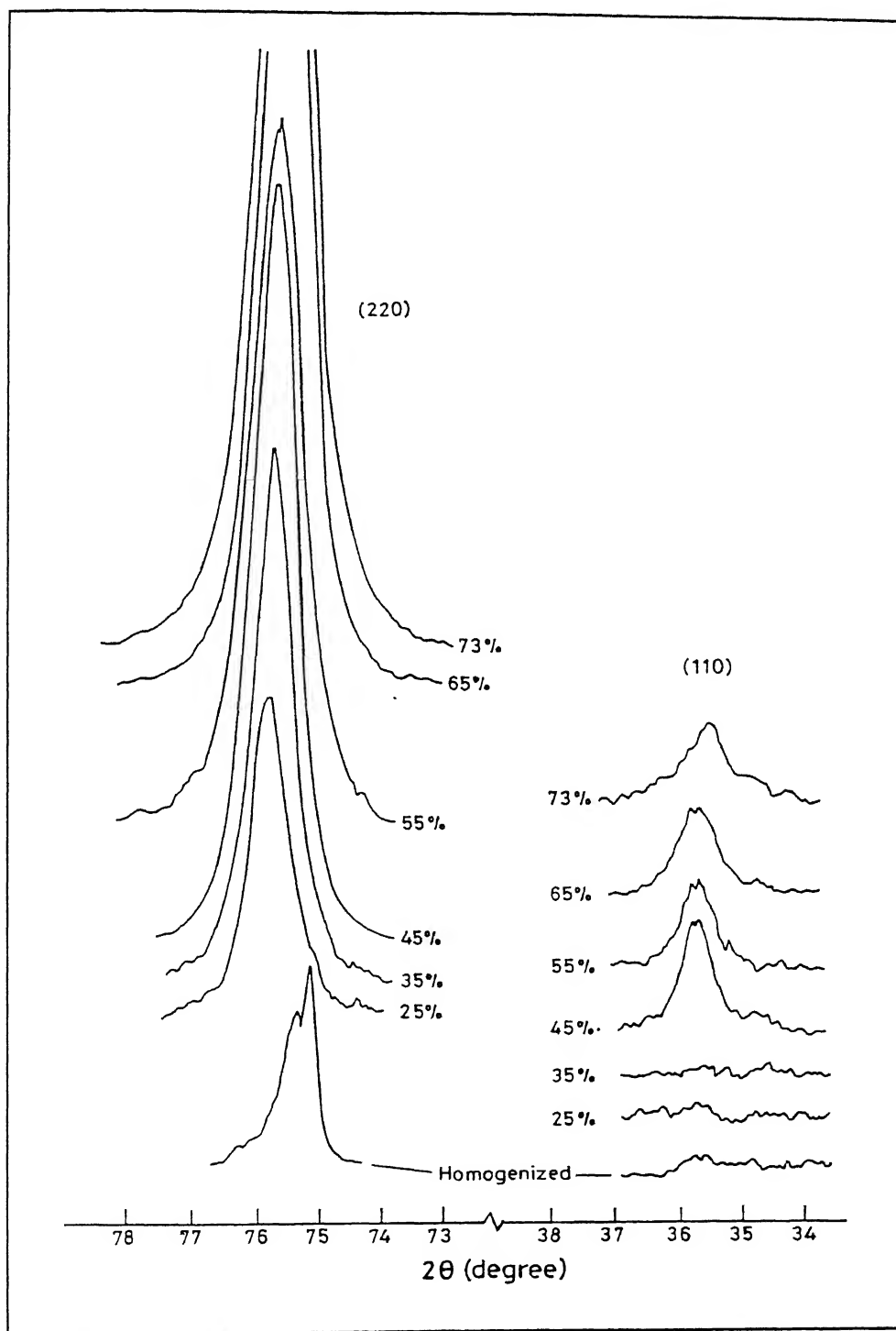


Figure 4.18 XRD line profiles at different degrees of cold reduction showing (110) and (220) reflections

the textural effects will be the same on both the planes of the two pairs, measurements of the order parameters from them are expected to be independent of texture.

The (100)/(200) and (110)/(220) reflection pairs from the homogenized and the cold rolled samples have been shown in Figures 4.17 and 4.18, respectively. For better clarity, these peaks were recorded by slow scanning (i.e.  $0.3^\circ/\text{min}$  in  $2\theta$ ). Even then the peaks became significantly broadened owing to deformation and therefore it was extremely difficult to correctly identify the peaks of the two different phases such as  $\gamma'$  and  $\gamma$ . The calculation of the order parameter value for the  $\gamma'$  phase was not an easy task because of this.

As stated earlier, the order parameter calculation based on the (100)/(200) and (110)/(220) reflection pairs involved the determination of integrated intensities of the relevant peaks, specially of the  $\gamma'$  phase. However, in practice, this was not so easy, specially in case of the (220) peak. The reason is that the  $(220)_{\gamma'}$  peak was found to shift to higher  $2\theta$  values, thereby eclipsing the  $(220)_{\gamma}$  peak, making it difficult to distinguish the respective peaks for the two phases.

In order to minimize the possible error as far as practicable, the integrated area of a  $\gamma'$  peak was taken as  $2A$ , where  $A$  is the area of the line profile between the  $2\theta$  value corresponding to the peak height and the cut-off on the lower angle side (Figure 4.19). Although it may not be the best method of carrying out the measurements, it is practical and can be used with advantage, particularly for those situations where the two close peaks of  $\gamma'$  and  $\gamma$  are at least distinctly identifiable. It is admitted though that it may not be always possible to avoid the  $(220)_{\gamma}$  peak completely while measuring the integrated intensity of  $(220)_{\gamma'}$ . In addition to the closeness of the  $\gamma'/\gamma$  peaks, the situation is made all the more difficult due to the pronounced line broadening effect of cold rolling.

The plot of order parameter ( $S$ ) as function of rolling reduction is presented in Figure 4.20. It is clear from this diagram that on the basis of the (100)/(200) line pair the value of  $S$  is  $\sim 0.6$  for the homogenized material. The value of  $S$  decreases to some extent after 25%

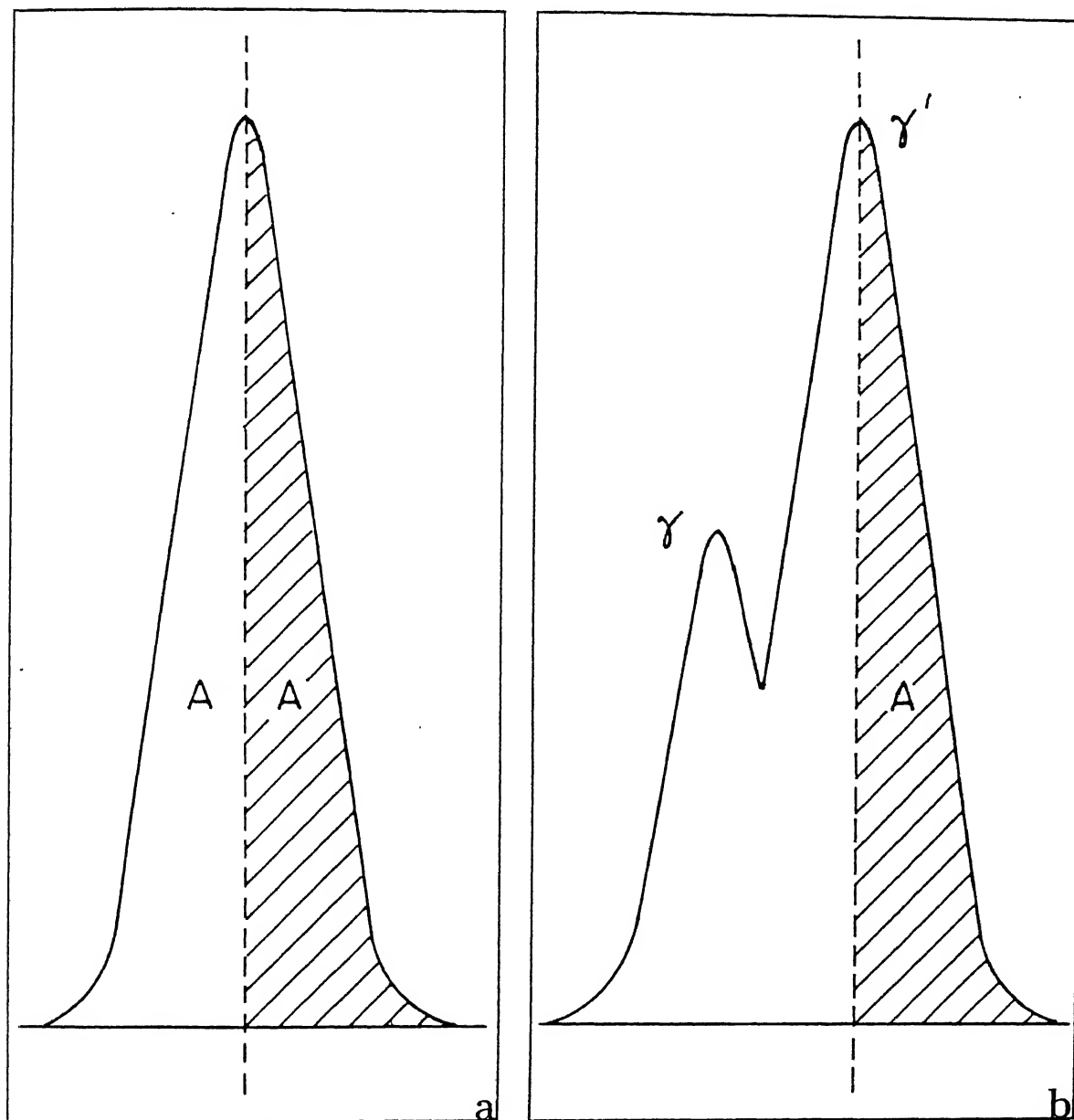


**Figure 4.19** Scheme for determination of the integrated intensity of a  $\gamma'$  XRD peak;  
(a) an isolated peak. (b) determination of  $2A$  from  $\gamma/\gamma'$  combination

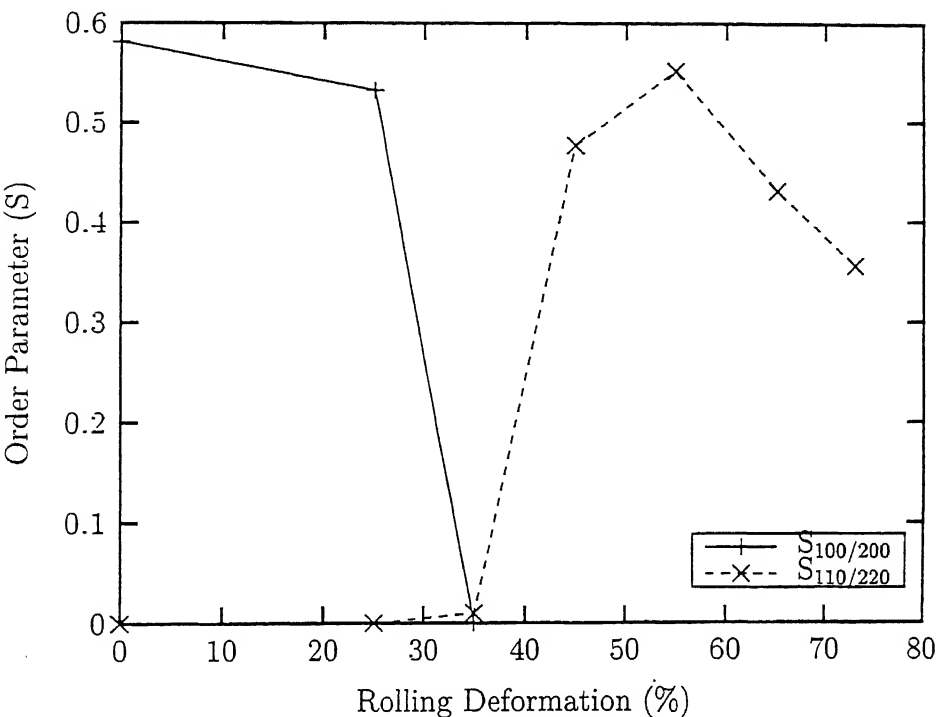


Figure 4.20 Variation of order parameter as a function of rolling deformation

deformation and becomes practically zero after 35% deformation. This is quite expected as the (100) X-ray line disappears completely at this deformation level. Beyond 35% rolling, the XRD patterns start showing the (110) superlattice line. The value of  $S$  calculated on the basis of the (110)/(220) pair is also plotted for higher rolling reductions in the same diagram. It is clear that  $S$  increases sharply and reaches a maximum value of  $\sim 0.55$  after 55% deformation and then decreases with further rolling reduction.

### 4.2.3 Strain Parameter and Microhardness

Figure 4.21 represents the strain parameter values measured from the (111) and (200) line profiles for all the deformed samples. As depicted in the Figure, the two plots show a sharp increase in the strain parameter values after 25% deformation. However, they then decrease to significantly lower levels after 35% deformation, followed by increase with increase in the deformation level. After 45% reduction, the slopes of the two plots decrease and remain almost constant upto 73% cold rolling. Apparently, both the plots exhibit more or less the same trend.

The microhardness values for all the cold rolled samples along with that for the homogenized material are shown in Figure 4.22. It is clear that the microhardness values shown here follow a trend similar to the strain parameter plots (figure 4.21), showing an initial rise, followed by a drop of hardness after around 45% rolling reduction.

## 4.3 Cold Rolling Texture

The {111} pole figure of the initial (homogenized) material is shown in Figure 4.23a. Although the maximum pole density is above the random value, no significant clustering of poles can be observed in the pole figure. The  $\phi_2$  sections of the corresponding ODF plot (Figure 4.23b) also do not indicate the presence of any prominent texture component in the material; however, rotated cube components can be seen in the section  $\phi_2 = 0^\circ$ .

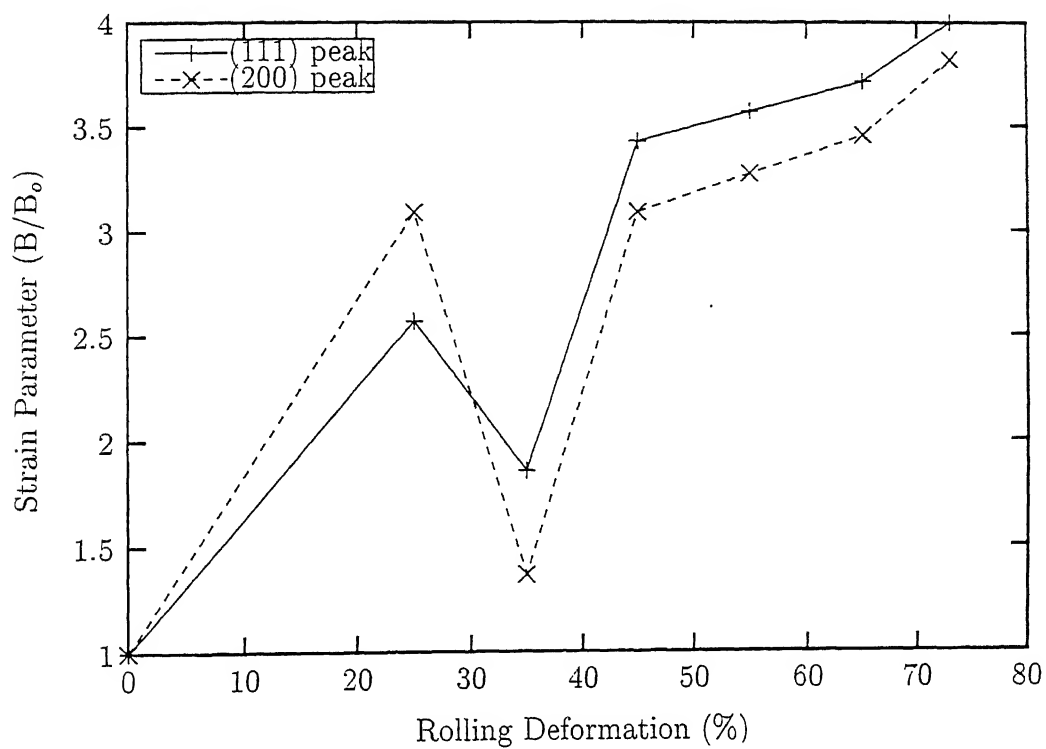


Figure 4.21 Variation of strain parameter as a function of rolling deformation



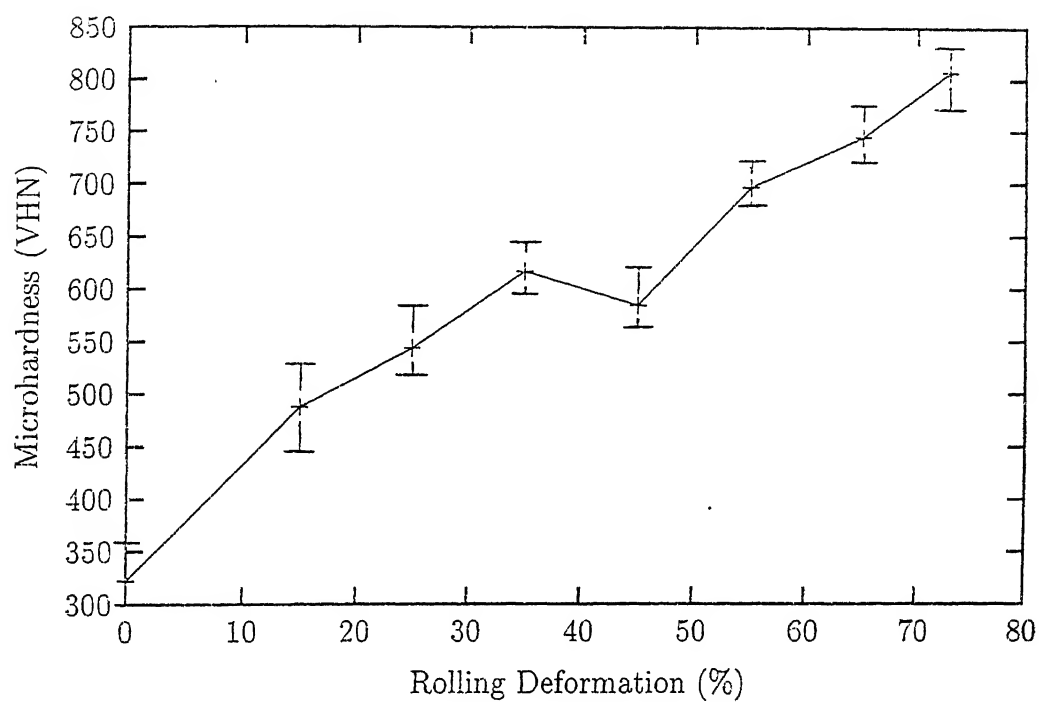


Figure 4.22 Variation of microhardness as a function of rolling deformation

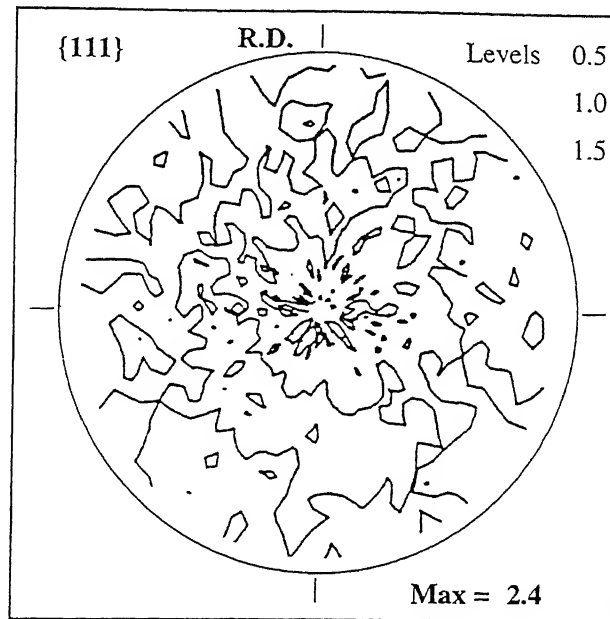
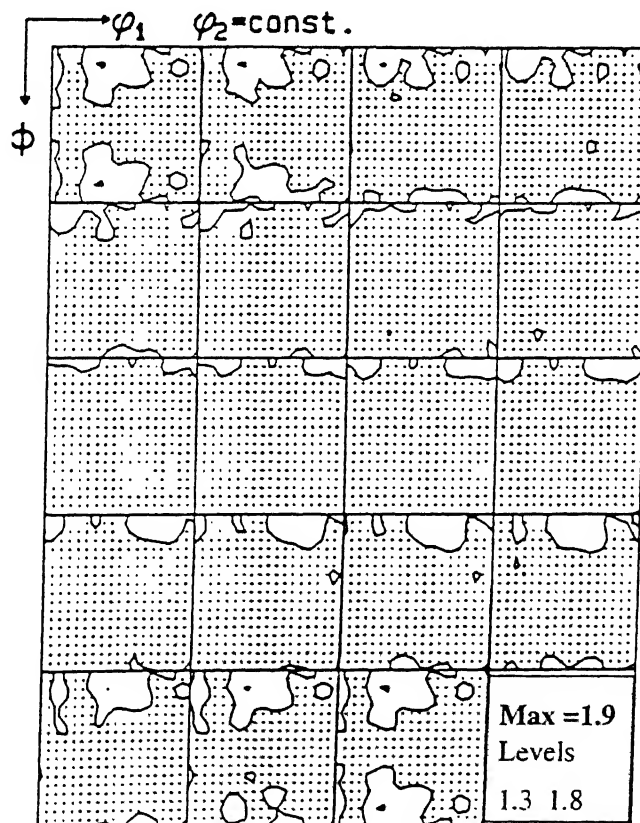
Figure 4.23a  $\{111\}$  pole figure of the homogenized material

Figure 4.23b Corresponding ODF of the homogenized material

The  $\{111\}$  pole figures of all the deformed materials are presented in Figures 4.24a to 4.24f. The pole figure of the 25% rolled material shows the initial stages of the formation of pure metal or *copper-type* rolling texture. The pole figure becomes quite unsymmetrical after 35% cold rolling and its nature remains unchanged after 45% rolling. Although the pole densities of the 35% and 45% rolled samples show enhanced values compared to that for the 25% rolled material, it is difficult to identify the prominent poles except the  $\{011\}\langle 100 \rangle$ . The pole figure becomes symmetrical again after 55% rolling and remains similar after 65% deformation. However, the pole densities here are lower than in the previous case (i.e. 45% rolling). Once again, the most prominent poles are the Goss  $\{011\}\langle 100 \rangle$  and also the Bs  $\{011\}\langle 211 \rangle$  component. Both these components appear to intensify after 73% cold rolling. The pole figure at this stage looks quite unsymmetrical once again.

In order to have a much clearer idea of the development of deformation texture in this alloy as function of the amount of cold rolling, orientation distribution functions (ODF) were calculated from the pole figure data in a manner outlined in section 3.7 of chapter 3 and these plots ( $\phi_2$  sections) are presented in Figures 4.25a to 4.25f. In the ODF of the 25% rolled material (Figure 4.25a), the components Bs  $\{011\}\langle 211 \rangle$ , Cu  $\{112\}\langle 111 \rangle$ , Goss  $\{011\}\langle 100 \rangle$  and S  $\{123\}\langle 634 \rangle$  can be easily identified, indicating that a weak *pure-metal* or *copper* type rolling texture has already developed at this stage.

After 35% cold rolling (Figure 4.25b) the ODF becomes nearly twice as sharp as the one from the 25% rolled material. In addition to a sharp Bs component, a prominent maxima appears a few degrees away from the Bs. The Cu and the Goss components are rather weak. Although the basic characteristics of the texture do not change, the general sharpness of the texture declines after 45% cold rolling, as evidenced from Figure 4.25c.

The ODF obtained from the 55% rolled material (Figure 4.25d) is found to be significantly weaker compared to the previous one and looks very similar to the ODF of the 25% rolled material in both nature and intensity. Beyond this stage, the overall texture sharpens

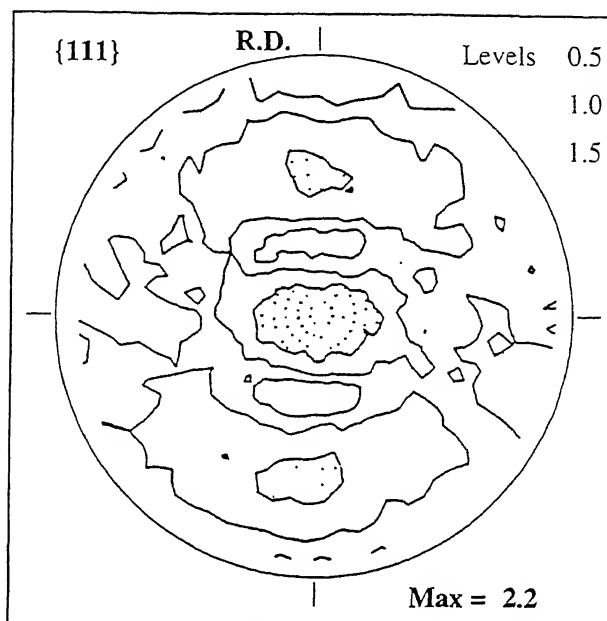


Figure 4.24a {111} pole figure of the 25% rolled material

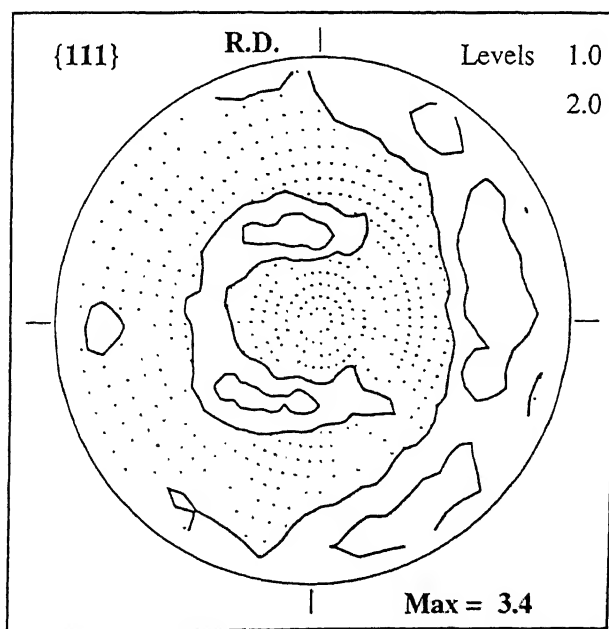


Figure 4.24b {111} pole figure of the 35% rolled material

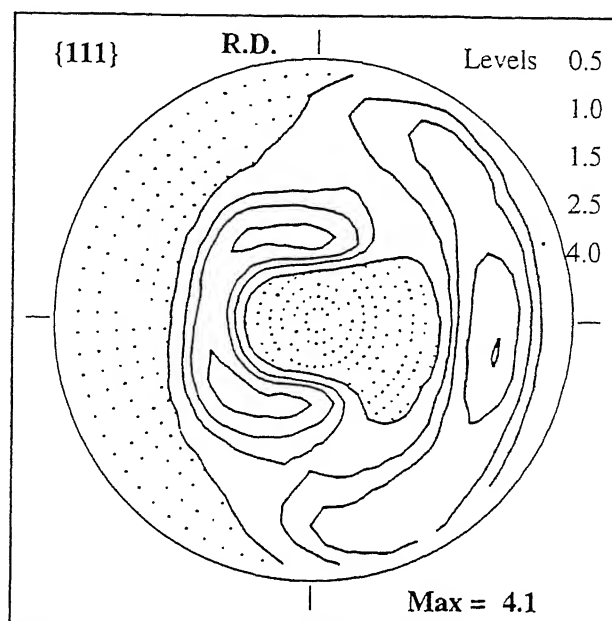


Figure 4.24c {111} pole figure of the 45% rolled material

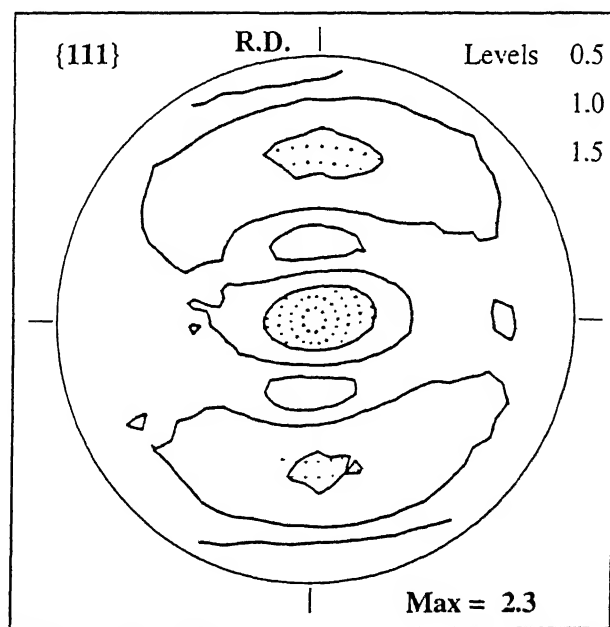


Figure 4.24d {111} pole figure of the 55% rolled material

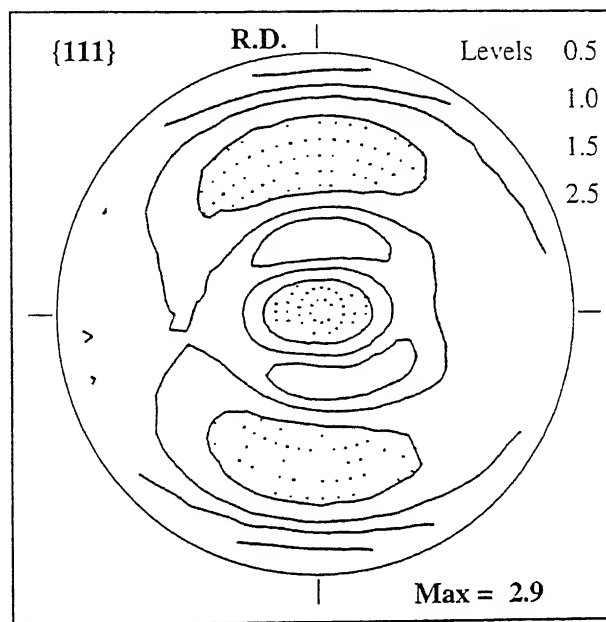


Figure 4.24e {111} pole figure of the 65% rolled material

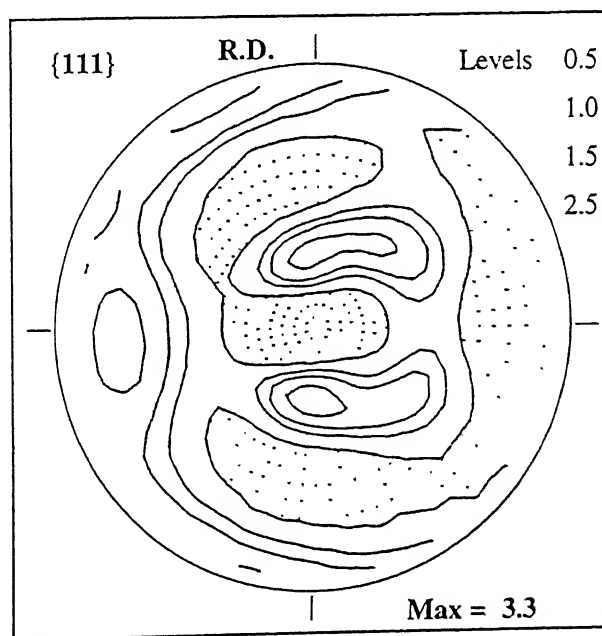


Figure 4.24f {111} pole figure of the 73% rolled material

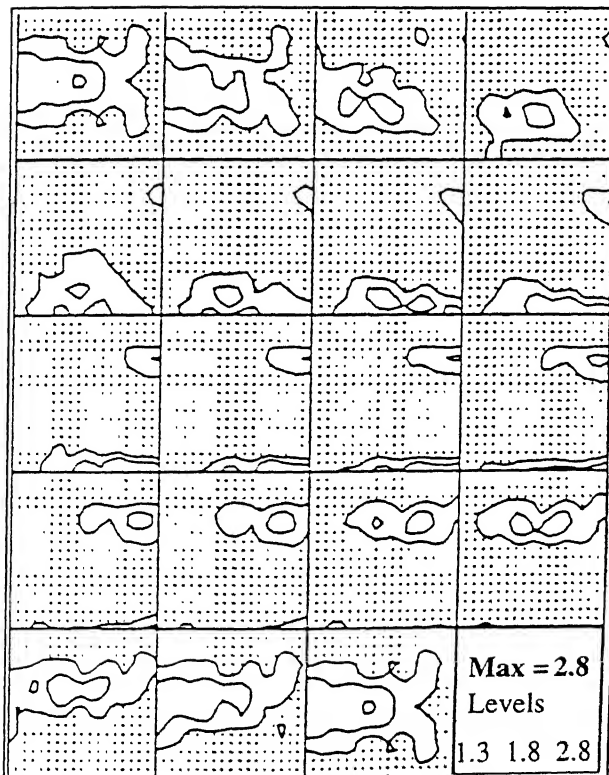
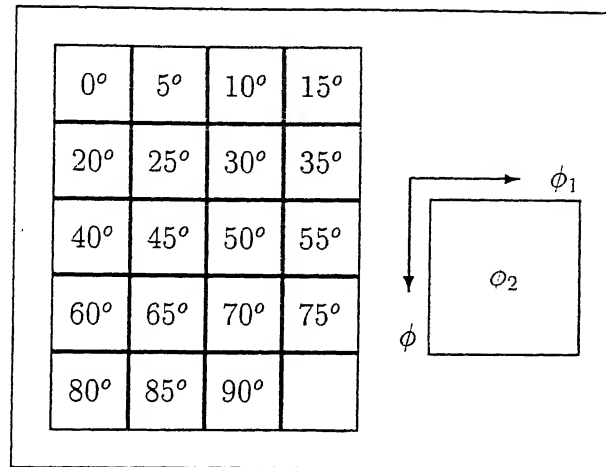


Figure 4.25a ODF of 25% rolled material

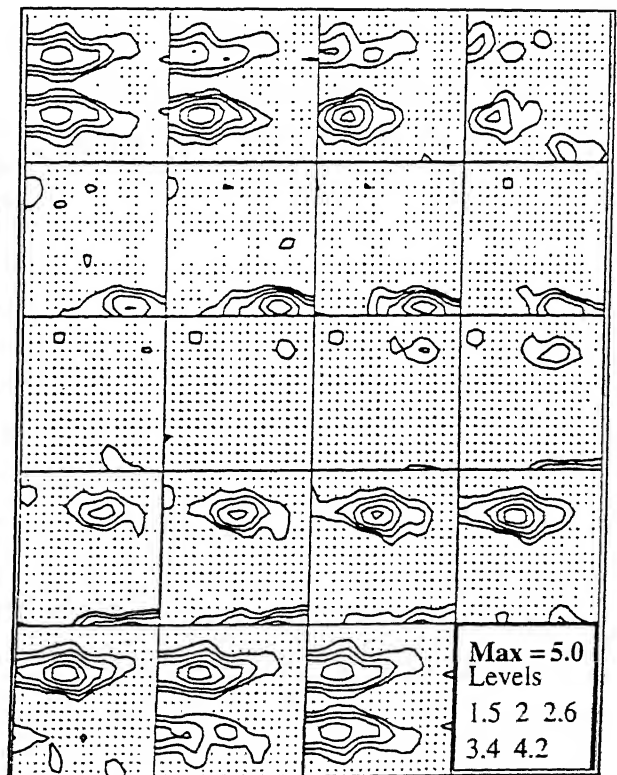


Figure 4.25b ODF of 35% rolled material

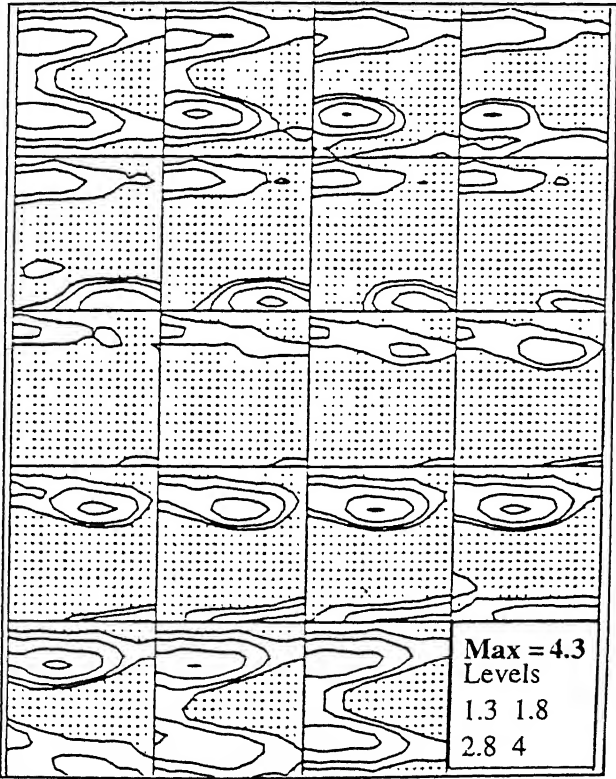
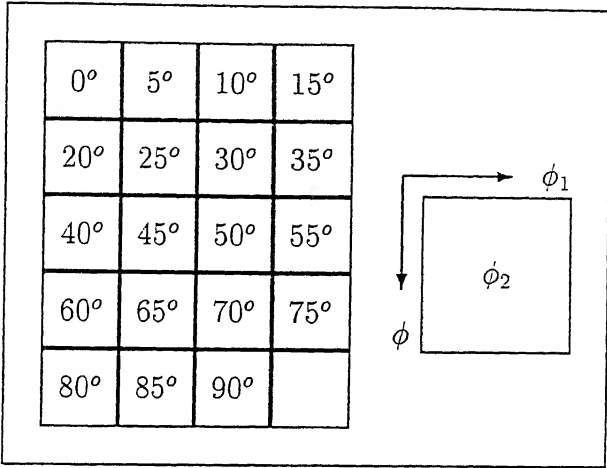


Figure 4.25c ODF of 45% rolled material

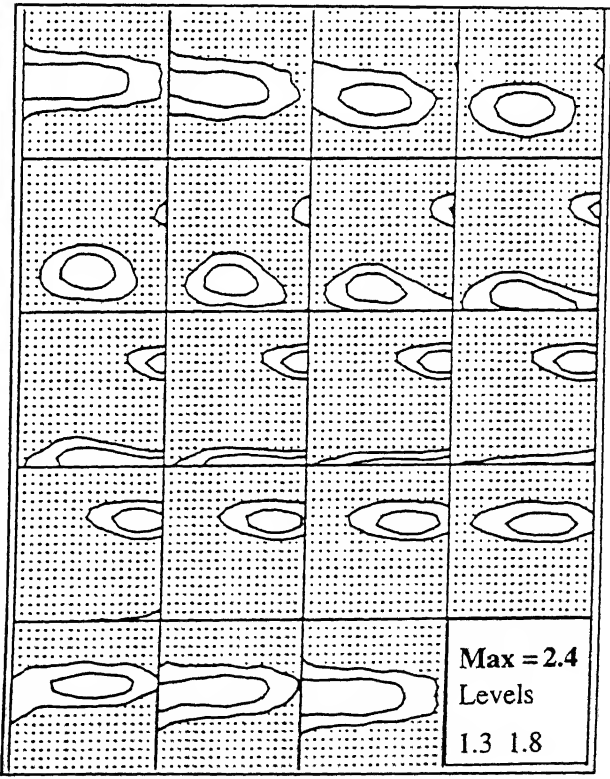


Figure 4.25d ODF of 55% rolled material



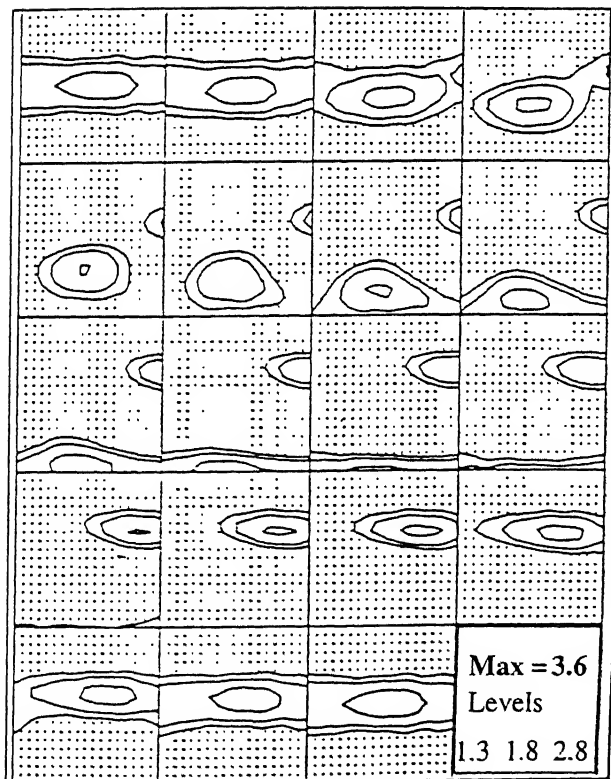
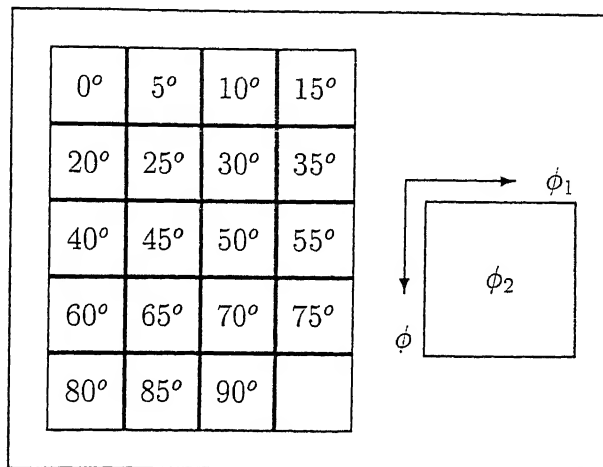


Figure 4.25e ODF of 65% rolled material

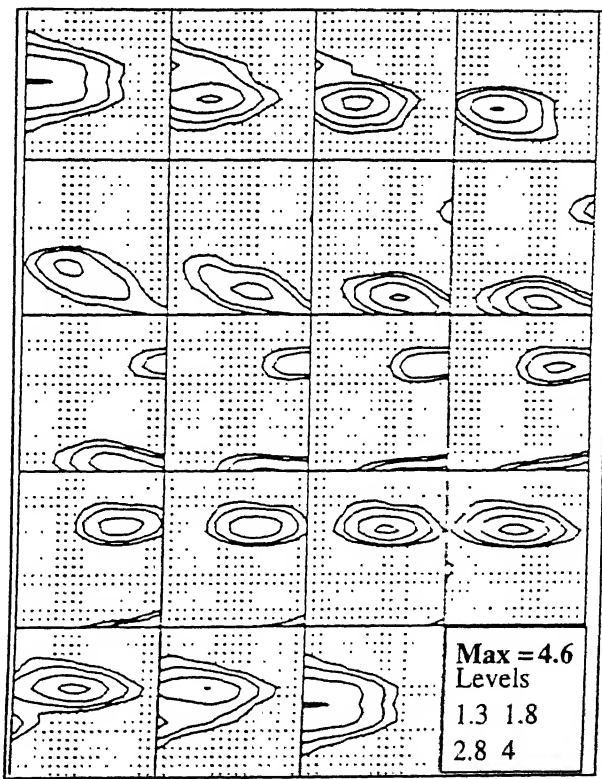


Figure 4.25f ODF of 73% rolled material

continuously with increasing deformation (Figures 4.25e and 4.25f), with the Bs component, becoming the most prominent one.

As has already been discussed earlier in Chapter 3 (section 3.7), the principal deformation texture components of FCC materials appear along certain fibres in the orientation space, namely, the  $\alpha$ ,  $\beta$  and  $\tau$  fibres [138]. In order to understand the development of these fibres with rolling deformation in a more quantitative manner, a useful exercise will be to study the intensity variations along the fibres. The plots of the magnitude of the orientation density  $f(g)$  along these fibres are presented in Figures 4.26 – 4.29. The salient features of these fibres are described as follows.

**$\beta$ -fibre :** The  $\beta$ -fibre starts from the Cu  $\{112\} < 111 >$  position, passes through the S  $\{123\} < 634 >$  orientation and finally terminates at the Bs  $\{011\} < 211 >$  location. Figure 4.26 shows the  $\beta$ -fibre plots for all the cold rolled samples which were drawn by plotting the maximum orientation density at each  $\phi_2$  section against the corresponding value of  $\phi_2$ .

The general intensity levels of the  $\beta$ -fibre at different rolling reductions closely follow the general sharpness of the corresponding ODFs. It is clear that the fibres do not develop continuously with increasing rolling deformation. A well developed  $\beta$ -fibre forms after 35% deformation. The intensity remains almost constant till upto 45% deformation, followed by a decrement of the fibre intensity with deformation upto 55%. With further rolling upto 65% the  $\beta$ -fibre intensity generally improves again and strengthens considerably after 73% rolling. These results corroborate the qualitative findings made from a study of the ODFs themselves. Although the final texture shows a reasonably strong intensity in the Bs position, the maximum value of the  $\beta$ -fibre occurs at a location between the Bs and the S, which is usually known as the Bs/S position  $\{168\} < 211 >$ .

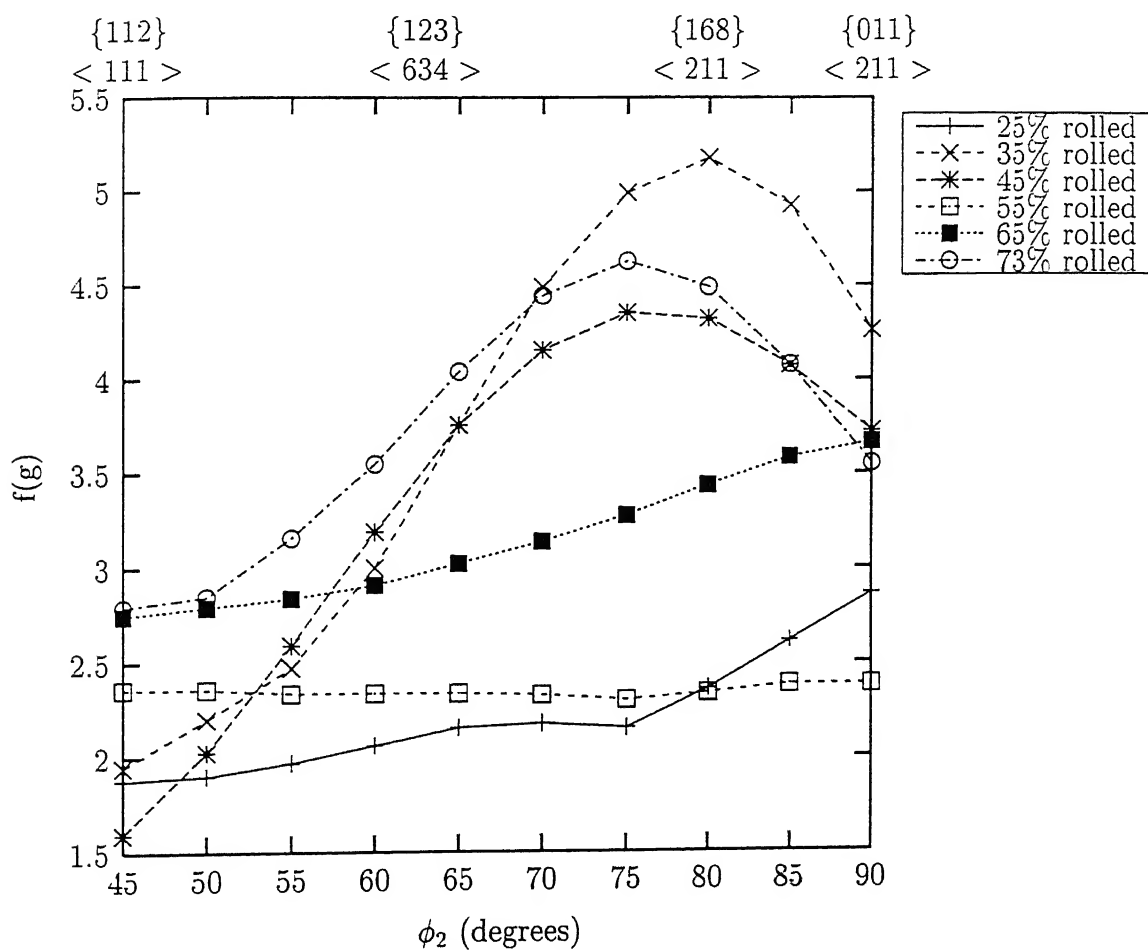
The exact course of the  $\beta$ -fibre through the orientation space, as function of the degree of deformation, is shown in Figure 4.27 where the  $\phi_1$  and  $\phi$  values for each orientation maxima

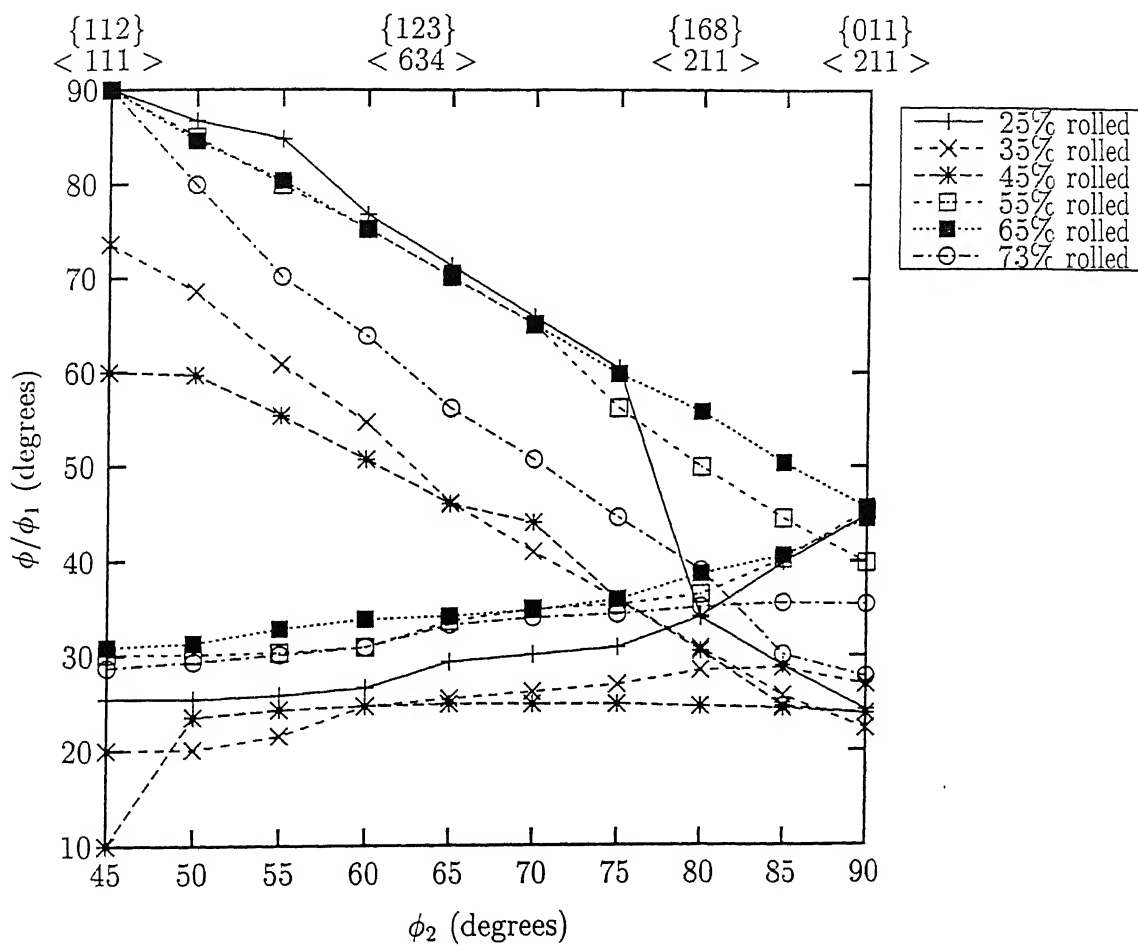
occurring in different  $\phi_2$  sections have been plotted against  $\phi_2 = 45^\circ - 90^\circ$ . It is interesting to note that the course of the  $\beta$ -fibre (Figure 4.27) also changes just as the general level of intensity of the fibre changes as a function of the amount of rolling deformation. After 35% deformation, the fibre shifts to lower  $\phi_1$  and lower  $\phi$  values, and this nature was maintained upto 45% deformation. Beyond this level, however, the fibre starts shifting to higher values of  $\phi_1$  and  $\phi$ . Then again, after 73% reduction the fibre changes to lower  $\phi_1$  values.

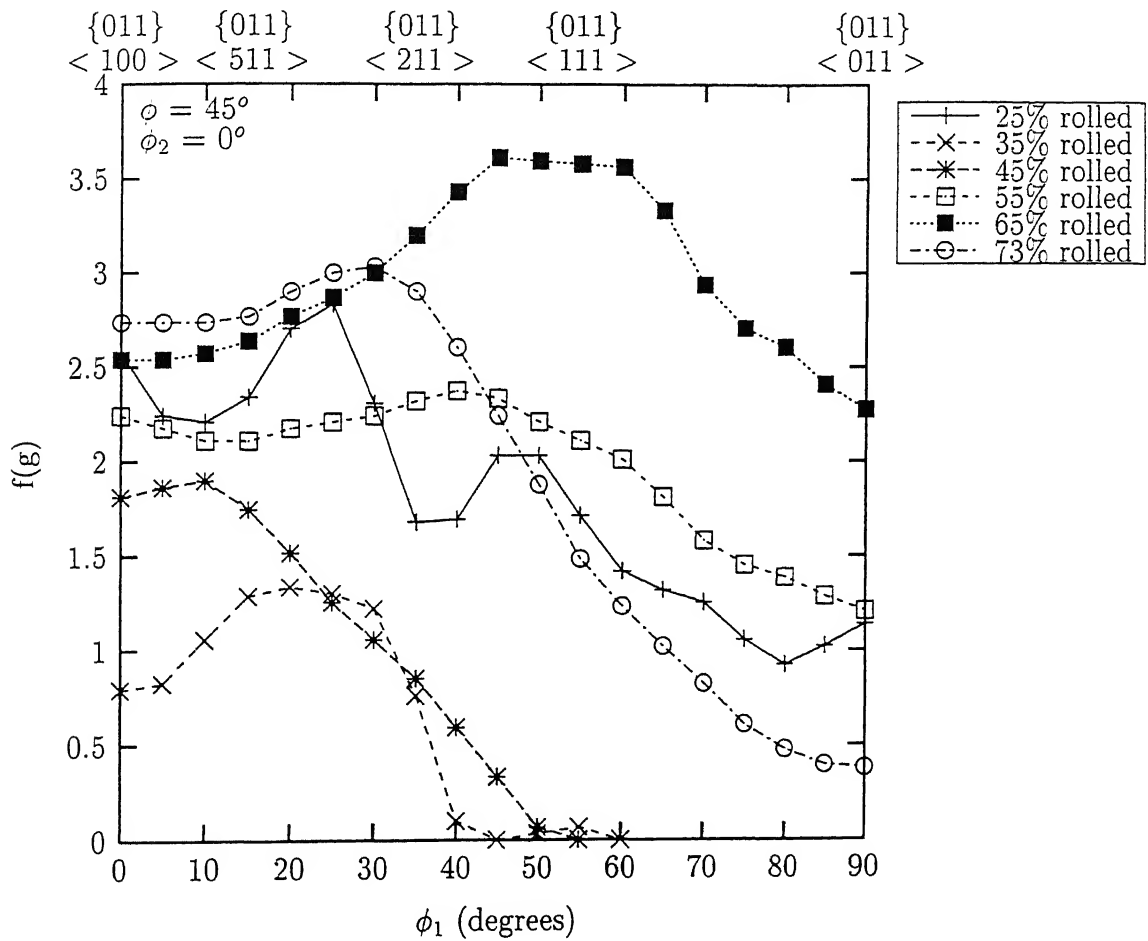
**$\alpha$ -fibre :** The  $\alpha$ -fibre runs from the Goss  $\{011\} \langle 100 \rangle$  location through the Bs  $\{011\} \langle 211 \rangle$  and terminates at the rotated Goss  $\{011\} \langle 011 \rangle$  position. The  $\beta$ -fibre actually meets the  $\alpha$ -fibre at the Bs position in the orientation space. The  $\alpha$ -fibre is drawn by plotting the orientation density values  $f(g)$  against  $\phi_1$  in the  $\phi_2 = 0^\circ$  section when  $\phi = 45^\circ$ . The  $\alpha$ -fibre plots for all the rolled materials are shown in Figure 4.28. The variations of the intensities of the Goss  $\{011\} \langle 100 \rangle$ , Bs/Goss  $\{011\} \langle 511 \rangle$ , Bs  $\{011\} \langle 211 \rangle$  and rotated Goss  $\{011\} \langle 011 \rangle$  orientations with degree of rolling deformations are obtained from this set of plots. The  $\alpha$ -fibre for the 25% cold rolled material clearly indicates the presence of the Goss  $\{011\} \langle 100 \rangle$  component, and the peak appears near about the Bs/Goss  $\{011\} \langle 511 \rangle$  position. After 35% rolling, the Goss component weakens significantly. After 45% rolling, the Goss component reappears and gradually becomes intensified till 73% rolling. The rotated Goss  $\{011\} \langle 011 \rangle$  component is reasonably sharp after 65% rolling but then it drastically weakens after 73% reduction. The  $\{011\} \langle 111 \rangle$  component emerges as the most prominent one for the 45% as well as the 65% rolled specimens, whereas the peak of  $\alpha$ -fibre for the 73% rolled material appears somewhere between the Bs/Goss and Bs location.

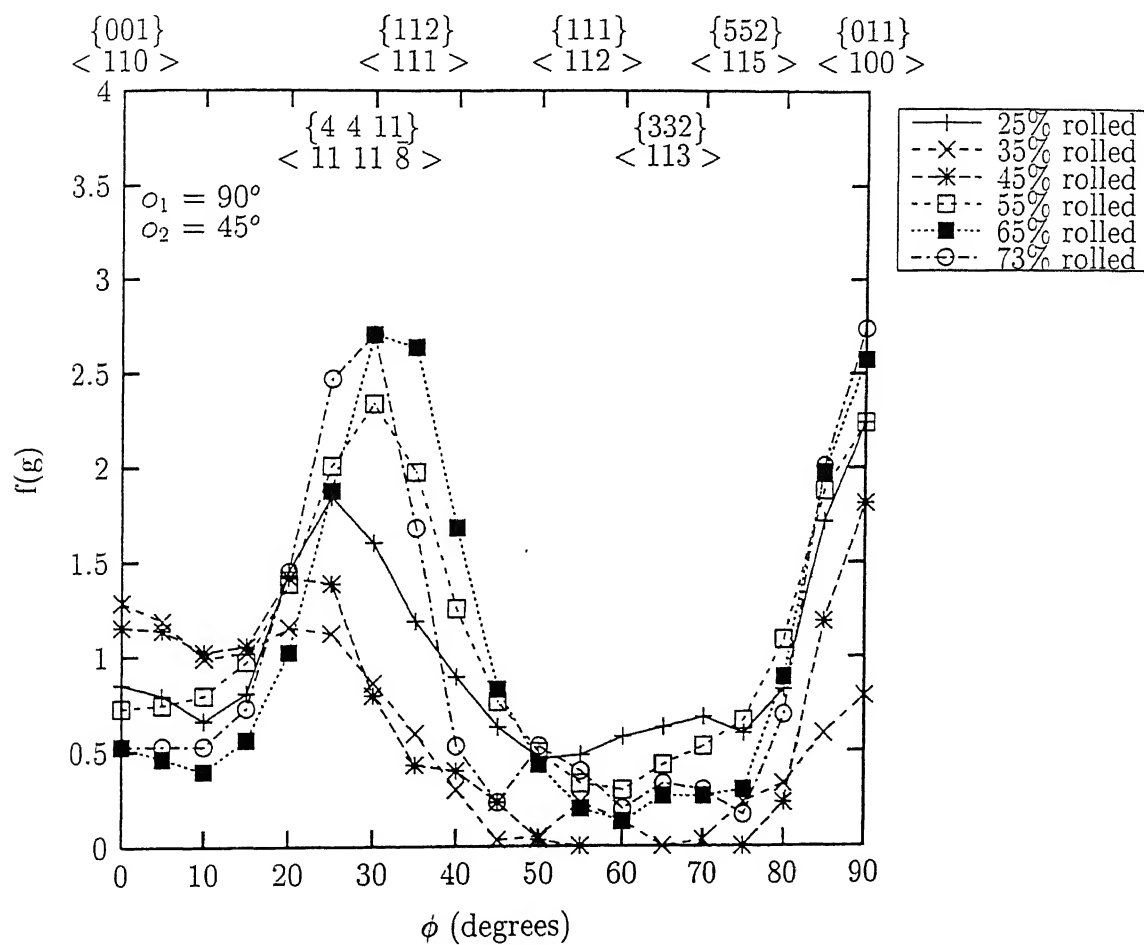
**$\tau$ -fibre :** Starting from the  $\{001\} \langle 110 \rangle$ , the  $\tau$ -fibre runs through the Cu  $\{112\} \langle 111 \rangle$  position and extends upto the Goss  $\{011\} \langle 100 \rangle$  position. The  $\alpha$  and  $\beta$  fibres meet the  $\tau$ -fibre at the Goss  $\{011\} \langle 100 \rangle$  and the Cu  $\{112\} \langle 111 \rangle$  positions respectively. In order to draw the  $\tau$ -fibre, the orientation density values  $f(g)$  are plotted against  $\phi$  when  $\phi_2 = 45^\circ$

and  $\phi_1 = 90^\circ$ . The  $\tau$ -fibre plots for all the cold rolled materials are shown in Figure 4.29. The orientation maxima in all the plots are found to be located at the Cu (or more correctly, the *Taylor*  $\{4\ 4\ 11\} \langle 11\ 11\ \bar{8} \rangle$ ) and the Goss position. The  $\{001\} \langle 110 \rangle$  component has little significance for all the materials, except for the ones which are deformed by 35% and 45% rolling reductions respectively. The 25% rolled specimen shows a peak at the Taylor position. Beyond 45% deformation, this peak appears to shift more towards the Cu side, and this continues upto 65% rolling when the peak is exactly at the Cu position. However, after 73% rolling, the peak again shifts towards the Taylor location.

Figure 4.26  $\beta$ -fibre (maximum intensity) plots of cold rolled  $\text{Ni}_3\text{Al(B.Zr)}$

Figure 4.27  $\beta$ -fibre orientation plots of cold rolled  $\text{Ni}_3\text{Al}(\text{B}, \text{Zr})$

Figure 4.28  $\alpha$ -fibre plots of cold rolled  $\text{Ni}_3\text{Al}(\text{B,Zr})$

Figure 4.29  $\tau$ -fibre plots of cold rolled  $\text{Ni}_3\text{Al}(\text{B,Zr})$



## 4.4 Discussion of Deformation Results

### 4.4.1 Changes in Order and Structure of Ni<sub>3</sub>Al with Rolling

The homogenized material consists of two phases – the ordered  $\gamma'$  (Ni<sub>3</sub>Al) and the Ni-rich disordered FCC  $\gamma$  phase. There has been a partition of Zr among these two phases – Zr has preferentially gone into solution in the  $\gamma'$  phase (Table 4.1). A comparison of the XRD line intensities for both the  $\gamma'$  and  $\gamma$  phases with the corresponding line intensities for Ni<sub>3</sub>Al and pure Ni respectively, as per the ASTM index files (Table 4.2), shows very significant and substantial differences. This can be explained as due to the presence of a strong solidification texture in both the  $\gamma'$  and  $\gamma$  phases.

It is known that in FCC materials, during solidification, the dendritic arms are expected to grow preferentially in the  $\langle 100 \rangle$  direction, the fastest growth direction [141]. Since for a continuously cast sheet material the direction of heat abstraction will be mainly along the perpendicular to the sheet plane, quite naturally, the  $\{200\}$  and other parallel planes will be arranged parallel to the sheet surface. This is going to produce a strong intensity for the (200) line in the X-ray pattern, which appears to be the case for both  $\gamma'$  (ordered FCC) and  $\gamma$  (disordered FCC) in the experimental material. Since the cast material was homogenized without any prior deformation, the high (200) intensity was retained after homogenization also.

A fully ordered Ni<sub>3</sub>Al ( $\gamma'$ ) phase is known to have the L1<sub>2</sub> structure, showing equal intensities of superlattice lines at both the (100) and (110) positions. Although the (220) line is present in the X-ray diffraction pattern of the homogenized material, its intensity is extremely low compared to that in the perfectly ordered Ni<sub>3</sub>Al, but the (110) line is practically absent. Again, the intensity of the (111) line, the strongest in ordered  $\gamma'$ , is also quite low in the X-ray pattern of the experimental material. Similar differences are found to exist between the X-ray line profiles of the pure  $\gamma$  (Ni) phase and the corresponding phase in the experimental material. All these facts point to the strong possibility that the starting

homogenized material is highly textured.

The X-ray diffraction profile from the filed powder, taken from the homogenized material, corresponds very well to that from FCC Ni (Figure 4.14 and Table 4.2). This pattern, therefore, essentially corresponds to that of a completely disordered FCC  $\gamma$  phase, which also does not show any trace of texture. A heavy deformation, as is possible by filing, is known to destroy the order in  $\text{Ni}_3\text{Al}$  intermetallics completely [18, 19]. Annealing of the filed powder seems to restore the order in  $\gamma'$  phase (Figure 4.14). However, the significantly low intensities of the (100) and (110) superlattice lines indicate that full order has not yet been restored and this possibly needs a longer annealing treatment.

The pattern of ordering in the experimental material (Figure 4.16) seems to undergo a drastic change upon cold rolling. After 35% rolling, the (100) superlattice line disappears while a small peak at the (110) superlattice position makes its first appearance. But for this small (110) peak, the X-ray pattern appears to correspond more or less with that of a disordered  $\gamma$  phase. The (110) line becomes more intense after 45% deformation and it maintains its intensity till about 73% deformation. Thus a rolling reduction of 35% marks a sudden change in the nature of order in the  $\gamma'$  phase. Not only does the order parameter  $S_{100/200}$  become zero at this stage (Figure 4.20), the values of the strain parameter and the hardness also exhibit a perceptible decrease (Figures 4.21 and 4.22). Transmission electron microstructures start showing the incidence of twinning after 35% rolling (Figure 4.7a), indicating that twins also become an important mode of deformation at this stage, in addition to slip.

None of the above changes can be attributed to any change occurring in the  $\gamma$  phase. The  $\gamma$  is not an ordered phase, hence no question of change in order in the  $\gamma$  phase arises. Moreover, disordered  $\gamma$  (Ni) is known to deform by octahedral slip only during rolling. Hence, most of the changes noticed after 35% rolling must be related to changes occurring in the  $\gamma'$  phase.

Ordered  $\text{Ni}_3\text{Al}$  with the  $\text{L1}_2$  structure is known to deform by slip only without any twinning. The observation of twinning in the microstructure after such a low level of deformation of 35% could point to the possibility of a change from  $\text{L1}_2$  to some other structure of  $\gamma'$  where twinning may be a possible additional mode of deformation. Ramesh *et al* [16] observed that the  $\text{L1}_2$  structure of  $\text{Ni}_3\text{Al}$  may not be very stable at high temperatures. They found that annealing of filed powders of a  $\text{Ni}_{76}\text{Al}_{24}$  alloy produced changes in the relative intensities of the  $\{200\}$  and  $\{220\}$  peaks as a function of the temperature of annealing. They observed splitting of the  $\{200\}$  peaks in their well annealed samples, from which they concluded that above  $1000^\circ\text{C}$  the  $\text{L1}_2$  structure of  $\text{Ni}_3\text{Al}$  transformed to  $\text{DO}_{22}$  with a  $c/a$  ratio of 2.015.

The possibility of obtaining the  $\text{DO}_{22}$  structure from the  $\text{L1}_2$  was considered by several researchers. It has been suggested by Sato and Toth [142], Beattie [143] and Yamaguchi *et al* [17] that the  $\text{DO}_{22}$  structure can be derived from the  $\text{L1}_2$  by introducing  $\frac{1}{2}[110]$  APB on every  $\{001\}$  plane of  $\text{L1}_2$ . Unlike  $\text{L1}_2$ , the  $\text{DO}_{22}$  phase deforms by twinning instead of slip [144, 145]. The formation of twins in the experimental material after 35% rolling and the gradual increment of the twin density as deformation progresses may be indicative of the transformation of  $\text{L1}_2$  structure to  $\text{DO}_{22}$  followed by the growth of the latter phase. The sharp decrease of the strain parameter at this stage could indicate release of strain energy to accommodate the transformation (Figure 4.21). Again the drop in hardness indicates softening which could be induced by some phase transformation (Figure 4.22).

Ball and Gottstein [24] were the first to report the effect of cold rolling on the structural and textural changes in a polycrystalline  $\text{Ni}_3\text{Al(B)}$  single-phase alloy. They did not observe any twins in their TEM microstructures taken from thin foils of the 70% cold rolled material. On the other hand, Ghosh Chowdhury *et al* [50] observed copious twins when a similar alloy was cold rolled to 85%. They attributed this twinning phenomenon to a structural transformation from  $\text{L1}_2$  to  $\text{DO}_{22}$  in  $\text{Ni}_3\text{Al(B)}$  between 45% and 65% cold rolling. They also pointed out that if an ordered tetragonal structure ( $\text{DO}_{22}$ ) (Figure 4.30) is assumed for

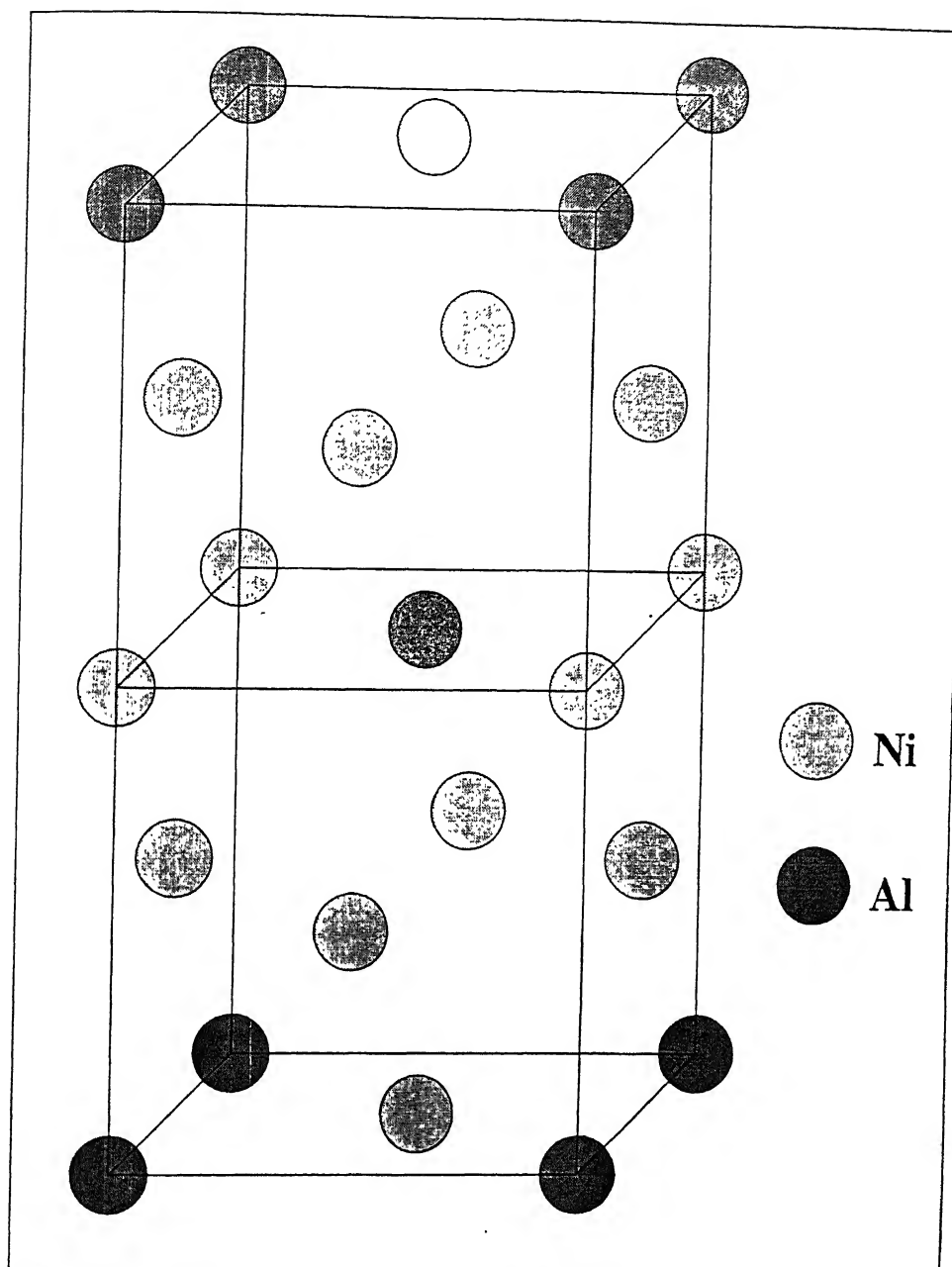


Figure 4.30 DO<sub>22</sub> (ordered tetragonal) structure of Ni<sub>3</sub>Al

Ni<sub>3</sub>Al, the respective atom positions will be:

$$\text{Al: } 000, \frac{1}{2}\frac{1}{2}\frac{1}{2};$$

$$\text{Ni: } \frac{1}{2}0\frac{1}{4}, \frac{1}{2}0\frac{3}{4}, \frac{1}{2}\frac{1}{2}0, 0\frac{1}{2}\frac{1}{4}, 0\frac{1}{2}\frac{3}{4}, 00\frac{1}{2}.$$

Therefore, the structure factor F will be given by:

$$F = f_{\text{Al}}[1 + e^{\pi i(h+k+l)}] + f_{\text{Ni}}[e^{\pi i(h+\frac{1}{2}l)} + e^{\pi i(h+\frac{3}{2}l)} + e^{\pi i(h+k)} + e^{\pi i(k+\frac{1}{2}l)} + e^{\pi i(k+\frac{3}{2}l)} + e^{\pi il}] \quad (4.1)$$

By putting appropriate values of  $hkl$  in the above expression, it can be easily seen that for (100) plane the value of F will be zero, indicating that the (100) line will be totally absent in the XRD pattern for this structure. On the other hand F will have a finite value for (110).

Figure 2.11 depicts the effect of the degree of cold work on the order parameter (S) for the single phase Ni<sub>3</sub>Al(B) alloy studied by Ghosh Chowdhury *et al* [25]. It can be seen here that  $S_{100/200}$  progressively decreases with cold work and becomes zero after 65% deformation. On the other hand,  $S_{110/220}$  value is observed to decrease gradually and it attains a value of 0.4 after 65% cold rolling; this remains nearly constant till after 90% cold rolling. On the basis of the above, Ghosh Chowdhury *et al* [25] strongly suggested a structural transformation in their Ni<sub>3</sub>Al(B) taking place between 45% and 65% cold rolling.

A direct comparison between the results obtained by Ghosh Chowdhury *et al* [25] and the results of the present investigation is not possible because of the following factors:

- The alloy used by Ghosh Chowdhury *et al*, was single phase Ni<sub>3</sub>Al(B) whereas the present experimental alloy contains both the Ni<sub>3</sub>Al(B)  $\gamma'$  as well as the disordered Ni-base  $\gamma$  solid solution.
- The starting material used by Ghosh Chowdhury *et al* was a cold forged and subsequently homogenized material, which was more or less texture-free. By contrast, the experimental material in the present investigation has an initial texture. Thus the starting material for Ghosh Chowdhury *et al* was having a reasonably perfect L1<sub>2</sub>

structure showing both the (100) and (110) superlattice peaks, whereas the present experimental material, right from the beginning, has a texture and does not show the (110) superlattice line at all. These differences will be quite evident from Figure 4.31.

It is felt that the disappearance of the (100) superlattice line from the XRD pattern cannot be the only significant condition to conclude about a possible structural transformation from  $L1_2$  to  $DO_{22}$ . The following Table (Table 4.3) shows a comparison of the theoretical relative intensities of the first few lines for the  $L1_2$ ,  $DO_{22}$  and disordered FCC structures which were calculated [146] by using the appropriate *multiplicity factor* ( $p$ ), *Lorentz-polarization factor* ( $L_p$ ) and *structure factors* ( $F$ ). It is clear from this Table that even if there is a structural transformation from  $L1_2$  to  $DO_{22}$  the (002) line of the  $DO_{22}$  should appear quite close to the position of the (100) line in the  $L1_2$  structure. In fact, Ramesh *et al* [16], from their annealing experiments on powdered  $Ni_3Al$  clearly observed a splitting of the (100) $_{L1_2}$  peak, indicating the coexistence of the (002) $_{DO_{22}}$  peak that suggested the beginning of such a transformation. In their work, Ghosh Chowdhury *et al* [25] did not elaborate on this point. Neither could the (002) $_{DO_{22}}$  peak be observed in the usual XRD patterns in the present case. It must be pointed out, however, that it could be quite difficult to identify such a weak line from XRD patterns taken from sheet samples with strong textures present.

**Table 4.3** Theoretical relative intensities of the XRD lines of  $L1_2$ ,  $DO_{22}$  and  $\gamma$  phases

$2\theta$ (degree)	$L1_2$		$DO_{22}$		$FCC$	
	$hkl$	$I/I_{max}$	$hkl$	$I/I_{max}$	$hkl$	$I/I_{max}$
$\sim 24^\circ$	100	16	002	3	100	0
$\sim 35^\circ$	110	16	110,102	7.5*	110	0
$\sim 43^\circ$	111	100	112	100	111	100
$\sim 51^\circ$	200	90	004,200	48*	200	50
$\sim 75^\circ$	220	55	220,204	27*	220	25

\* Total of the combined  $I/I_{max}$  values from the two sets of planes

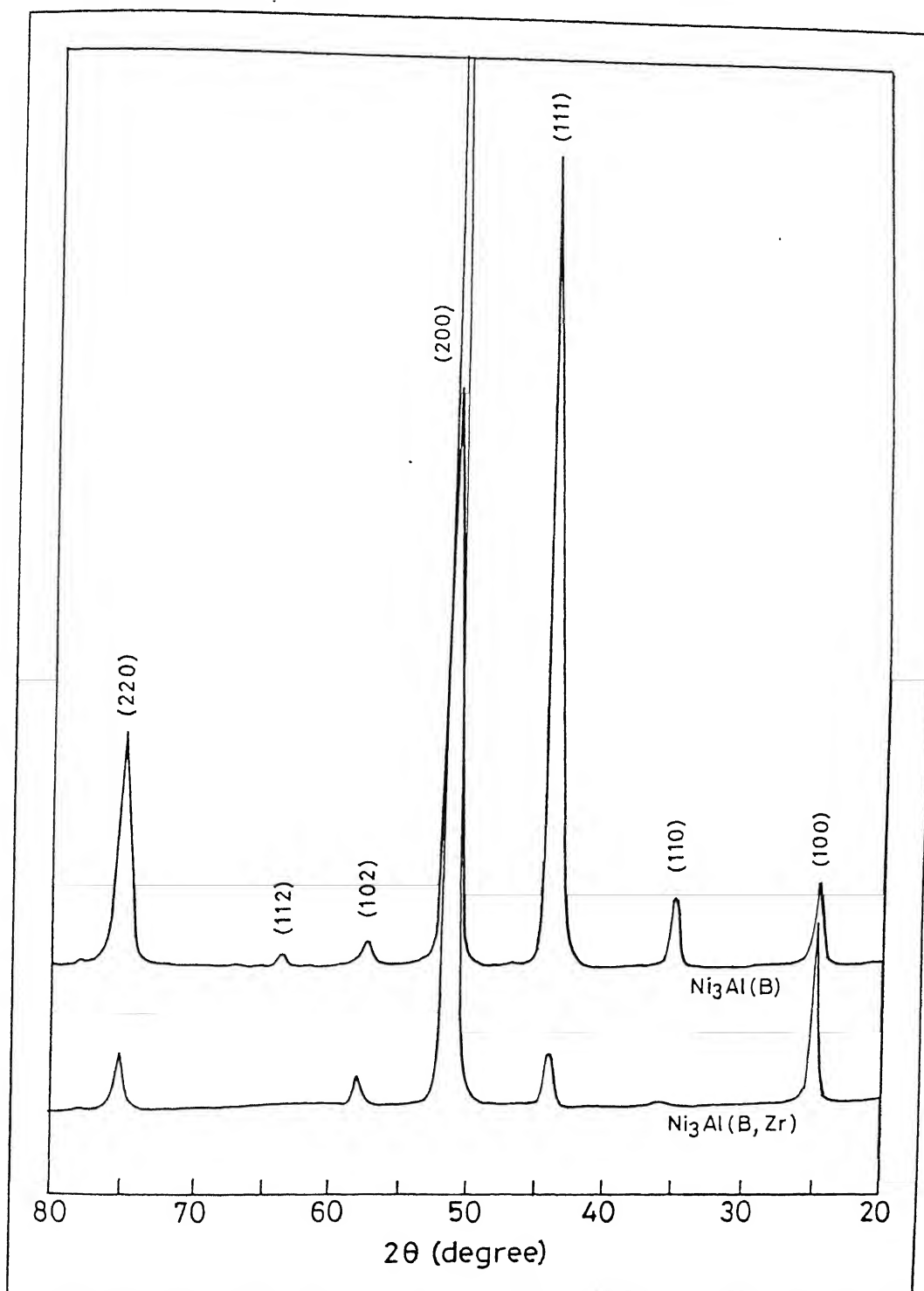


Figure 4.31 Comparison of the XRD profiles of the two homogenized alloys,  $\text{Ni}_3\text{Al}(\text{B})$  [25] and  $\text{Ni}_3\text{Al}(\text{B}, \text{Zr})$

Nevertheless, an attempt was made to investigate this aspect a little further. Using a slow scanning speed of  $0.3^\circ/\text{min}$  in  $2\theta$ , the (110), (111), (200) and (220) XRD line profiles were measured from the 35%, 45% and 55% rolled samples. These are shown in Figure 4.32, where the split peaks have been properly identified and indicated. It is clearly observed in this diagram that upto 35% rolling reduction the fundamental peaks of the  $\gamma'$  phase do not show any splitting. The splitting effect was observed from 45% rolling onwards and was more clearly visible after 55% rolling. Beyond 55% deformation, pronounced line broadening effect made it difficult to detect any splitting of the XRD lines. As an illustration, the relative X-ray intensities of the different lines for the 45% cold rolled sample as well as the theoretical intensities of the corresponding lines of the  $\text{DO}_{22}$  structure are given in Table 4.4 below and the two sets of data compared.

**Table 4.4** X-ray intensities of the different lines for 45% cold rolled sample

$2\theta$ (degree)	<i>hkl</i> planes in $L1_2$	Equivalent <i>hkl</i> in $\text{DO}_{22}$	Theoretical $I/I_{\text{max}}$	Experimental $I/I_{\text{max}}$	Peak shape
$\sim 35^\circ$	110	011	2.5	10	split
$\sim 43^\circ$	111	112	100	12	split
$\sim 51^\circ$	200	004	16	30	split
$\sim 75^\circ$	220	204	18	100	Broadened, no splitting

The perceptible splitting of the XRD lines for the  $\gamma'$  phase indicates the possibility of another structure coexisting with the  $L1_2$ . On the basis of the identified extra peak positions, other than those for the  $\gamma'$  and the  $\gamma$ , a new tetragonal structure could be visualized with a  $c/a$  ratio of 2.004. This value is quite close to the  $c/a$  ratios of 2.015 and 2.01 calculated by Ramesh *et al* [16] and Ghosh Chowdhury *et al* [25] respectively for their transformed  $\text{DO}_{22}$  structures. The discrepancy of the experimental  $I/I_{\text{max}}$  values with the corresponding theoretical  $I/I_{\text{max}}$  values of the  $\text{DO}_{22}$  structure (Table 4.4) could be attributed to the strong crystallographic texture present in the rolled material.



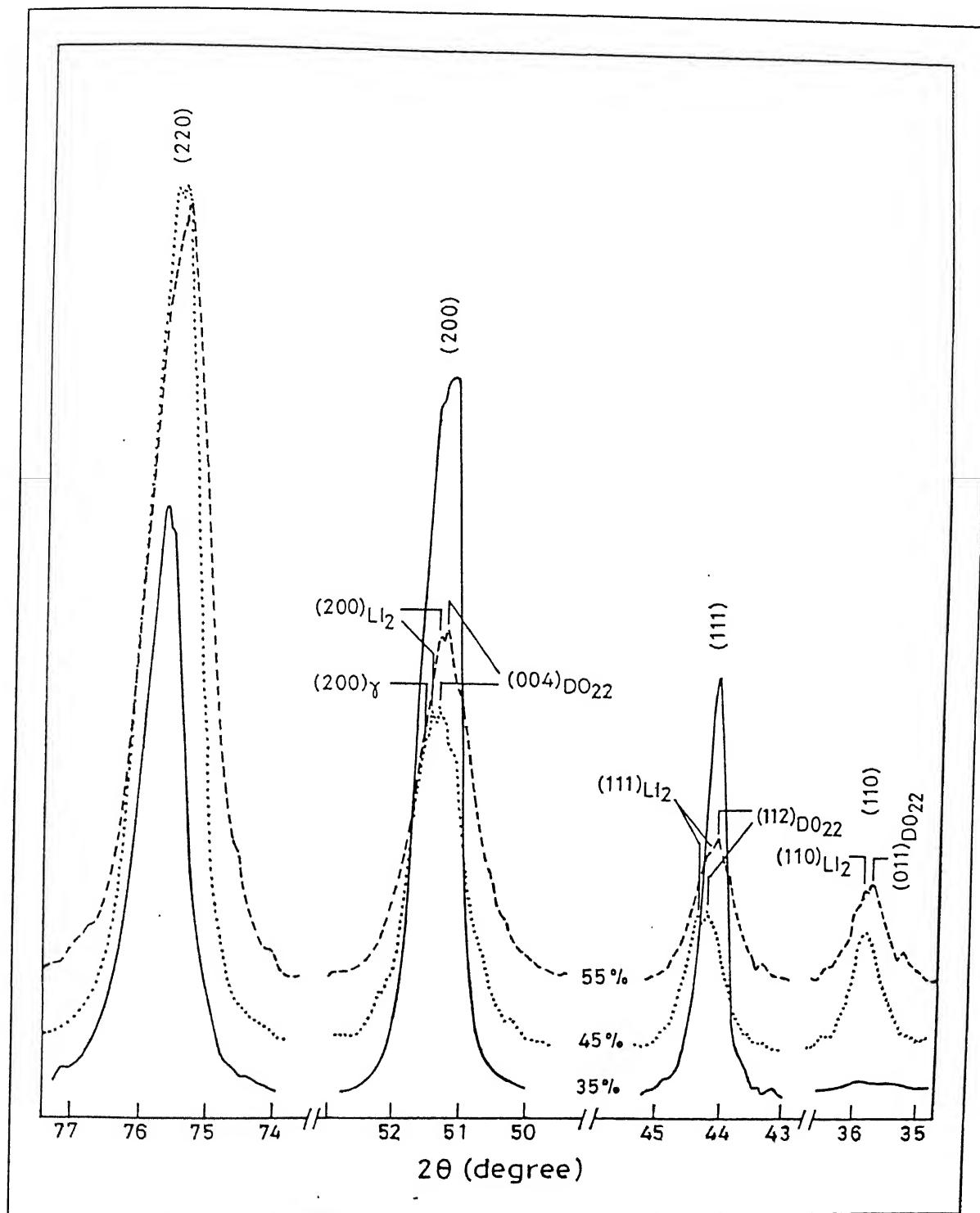
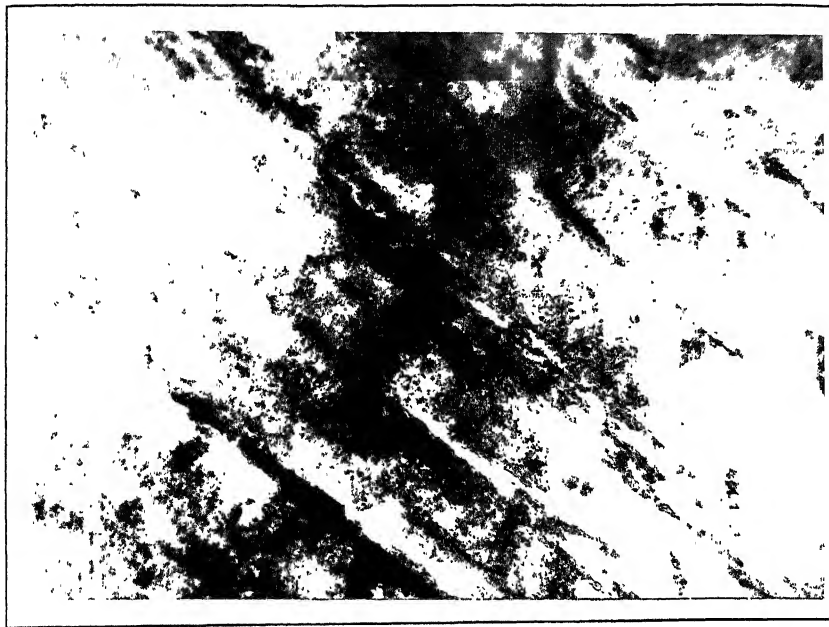


Figure 4.32 XRD line profiles of 35%, 45% and 55% cold rolled materials



1 $\mu$ m

Figure 4.33a Twin bands in thin foil of 73% cold rolled material

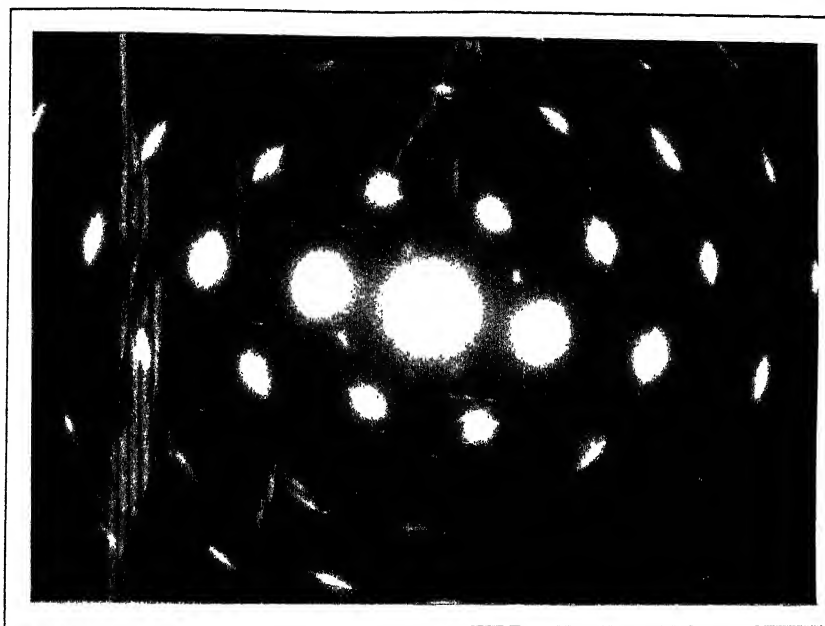


Figure 4.33b SAD pattern of the area shown in Figure 4.33a

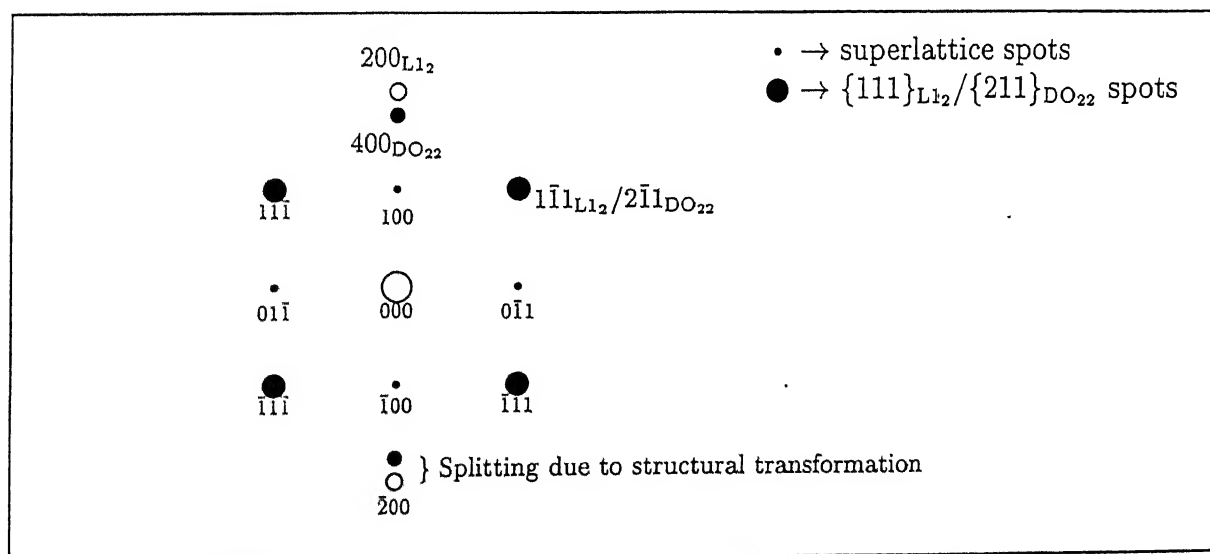


Figure 4.33c Indexing of the SAD pattern indicates a tetragonal structure

The rather low value of the  $c/a$  ratio of the proposed  $DO_{22}$  structure and the pronounced textural effect leading to substantial broadening of the X-ray diffraction lines make it extremely difficult to identify the  $DO_{22}$  phase without any ambiguity. However, the presence of twins in the material, cold worked 35% and more, gives an indirect proof of the existence of the  $DO_{22}$  phase, which usually deforms by twinning. The twinning plane in  $DO_{22}$  is (112) which is equivalent to the (111) plane in the  $L1_2$  structure. The twin plane in Figure 4.10c could be identified as the (111) plane of  $L1_2$ , no splitting of the SAD spots could be obtained presumably due to the low  $c/a$  ratio of the  $DO_{22}$  phase. Figure 4.33a features a heavily twinned region in a thin foil of the 73% rolled material, while Figure 4.33b displays the SAD pattern taken from the same area. The indexed SAD pattern, given in Figure 4.33c, shows the expected splitting of spots due to the coexistence of  $DO_{22}$  phase along with the  $L1_2$ .

On the basis of what has been stated above it is quite reasonable to conclude therefore that cold rolling of the experimental alloy leads to a gradual transformation of the  $L1_2$  crystal structure of  $\gamma'$  to the  $DO_{22}$ .

#### 4.4.2 Textural Changes

The point has already been made that one of the main reasons which makes the structural transformation during cold rolling very difficult to identify and elucidate from X-ray diffraction studies, is the presence of strong deformation textures in the material. The problem has been made more complicated by the presence of two phases –  $\gamma'$  and  $\gamma$  which have ordered FCC and disordered FCC crystal structures respectively. Moreover, their lattice parameters are very close (0.3574 nm for  $\gamma'$  and 0.3565 nm for  $\gamma$ ) which is the reason why it is quite difficult to separate their fundamental X-ray peaks. As a result, it has not been possible to obtain the textures of the two phases separately at any stage during the investigation. The cold rolling textures of the two phases are therefore essentially superimposed and this

makes an understanding of the development of the deformation texture in this material quite difficult.

It is known that heavily cold rolled FCC metals and alloys with medium to high stacking fault energies usually exhibit a pure metal type texture, characterized by the Cu  $\{112\} < 111 >$ , the Bs  $\{011\} < 211 >$ , the S  $\{123\} < 634 >$  and the Goss  $\{011\} < 100 >$  components. By contrast, FCC metals and alloys of low stacking fault energies show an alloy type texture, characterized mainly by a strong Bs and a weak Goss component [147].

Again, in FCC materials, the dominance of dislocation glide or deformation twinning basically determines the type of rolling texture that develops at high strain levels. It has been suggested [148] that just as a critical shear stress exists for slip ( $\tau_s$ ), there is also a critical shear stress for twinning ( $\tau_t$ ). Texture transition from pure metal to alloy type will depend on the magnitude of the ratio  $\tau_t/\tau_s$  ( $= m$ ) [149]. Deformation by slip will be promoted for values of  $m > 1$ , whereas  $m < 1$  should promote deformation by twinning. The texture produced will be pure metal type in the former case, whereas in the latter case texture developed will be of alloy type.

According to Wassermann [26], if mechanical twinning is an available mode of deformation, in addition to normal crystallographic slip, the Cu component will get transformed to  $\{552\} < 115 >$  by twinning. Further deformation of the twin orientation will take place on the favourable slip systems which will rotate it to the Goss position  $\{011\} < 100 >$  and finally to the Bs position  $\{011\} < 211 >$  by further rotation. The Bs component is considered to be a stable one and is normally not affected by twinning during deformation.

The development of the rolling texture in the experimental alloy will now be discussed in the light of the above facts. Since the crystal structure ( $L1_2$ ) of the  $\gamma'$  phase can be considered basically as ordered FCC, the formation of rolling texture in this material is expected to be similar to that in pure FCC metals or alloys of comparable stacking fault energies (SFE).

The SFE of  $\text{Ni}_3\text{Al}$  is expected to be similar to that of pure Ni [114, 146]. Pure Ni possesses an SFE of  $\sim 130 \text{ mJ/m}^2$  [114]. At low levels of deformation, therefore, the texture of  $\gamma'$  is expected to be similar to that of pure Ni, deforming by slip alone. At levels of deformation of 35% and more, however, twinning becomes an important mode of deformation in  $\gamma'$  due to structural transformation from  $\text{L1}_2$  to  $\text{DO}_{22}$ . The formation of pure metal type texture in the initial stages is therefore expected to be modified by the formation of alloy type texture at the later stages of deformation.

Texture development in an FCC material, as a function of cold rolling, can normally be followed from the  $\beta$ -fibre intensity plots. Such plots for the experimental alloy have been presented in Figure 4.26 earlier. For comparison purposes, the  $\beta$ -fibre plots for pure Ni ( $\gamma$ ) and for pure  $\text{Ni}_3\text{Al}$  ( $\gamma'$ ) are presented here in Figures 4.34 [150] and 4.35 [50] respectively. In general, the textural intensities are found to be rather low for the intermetallics such as  $\text{Ni}_3\text{Al}$  as compared to those for pure FCC metals [24, 50]. For pure Ni, the texture develops continuously with increasing rolling deformation (Figure 4.34). The final texture formed after heavy deformation consists of nearly equally strong Cu and S components and a comparatively weak Bs component. The  $\gamma$  phase in the experimental alloy is expected to have cold rolling texture similar to this. Strictly speaking though this may not be fully true. It may be mentioned that very often SAD patterns taken from  $\gamma$  regions show faint superlattice reflections in addition to the strong FCC fundamental spots (Figure 4.12b). Therefore the  $\gamma$  phase regions everywhere may not be pure  $\gamma$  and may contain fine  $\gamma'$  particles inside. This has also been confirmed by other workers [95, 125]. The deformation behaviour of the  $\gamma$  regions in this alloy may, therefore, be a little bit different from the behaviour of pure  $\gamma$  and would be expected to be similar to that of superalloys where particles of  $\gamma'$  are dispersed in a  $\gamma$  matrix. However, since the  $\gamma$  regions comprise only about 25% volume fraction of the entire alloy, the overall texture of the alloy should be predominantly determined by the texture of the  $\gamma'$  phase. The texture of the  $\gamma'$  phase is also bound to be affected by the

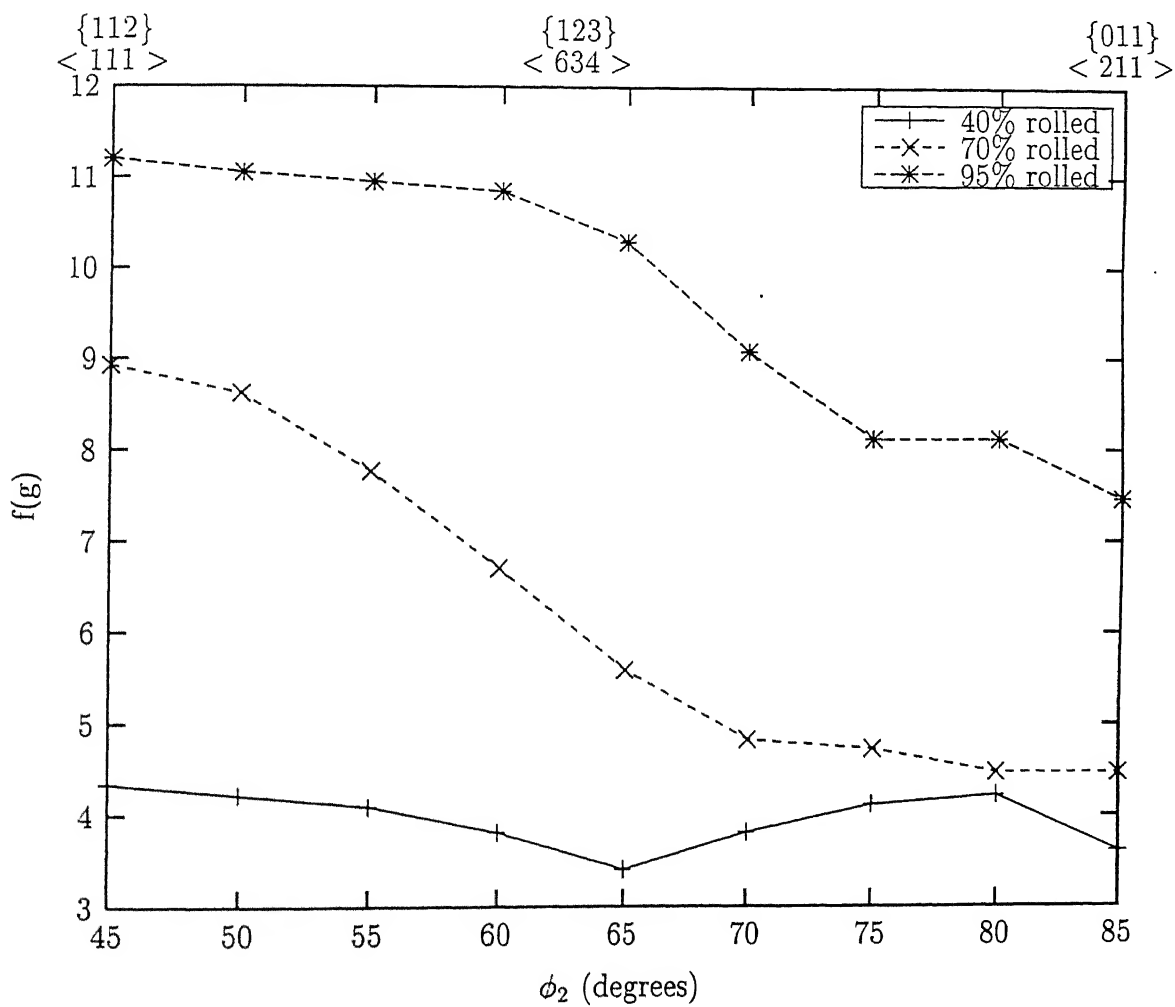


Figure 4.34  $\beta$ -fibre plots of pure Ni at different levels of cold rolling [150]

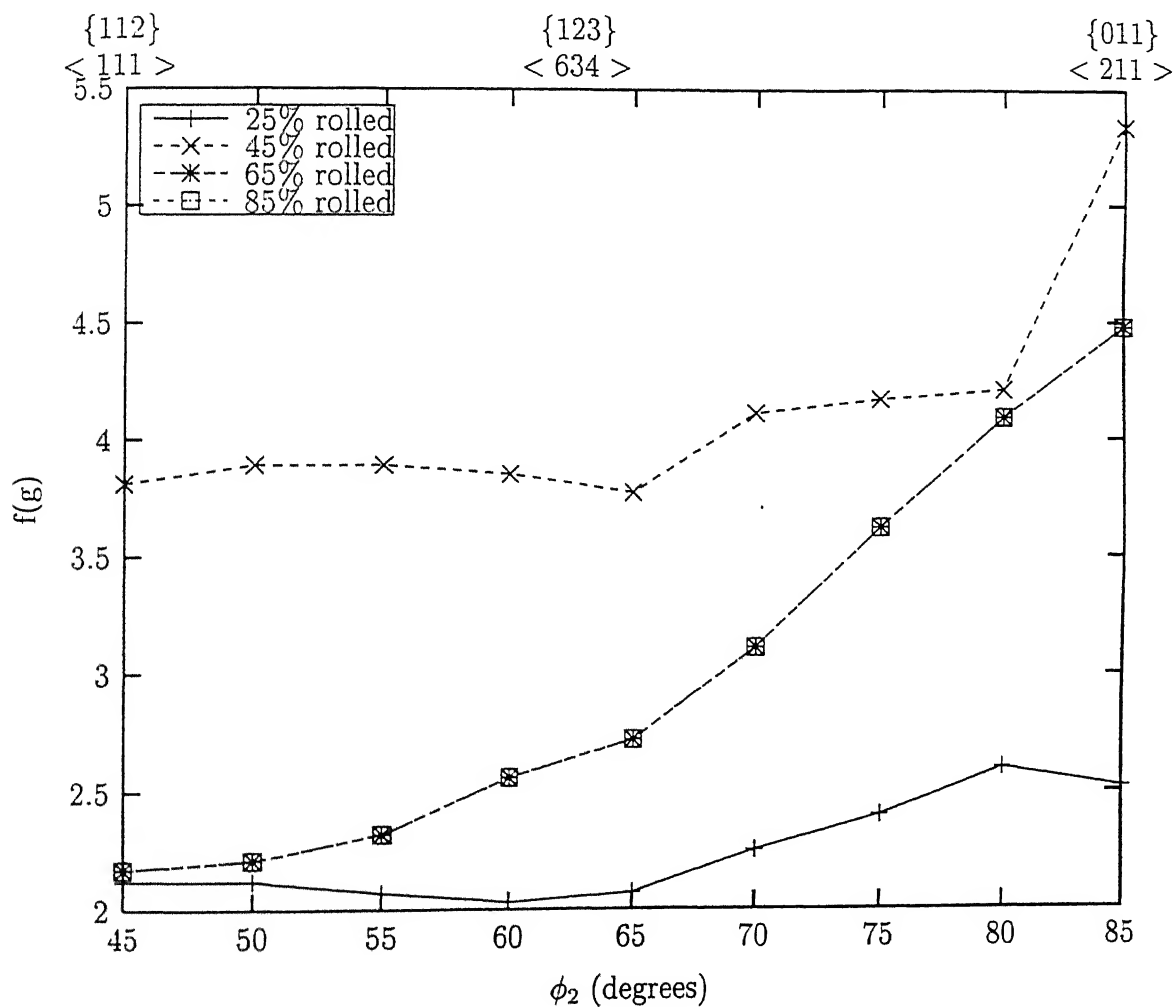


Figure 4.35  $\beta$ -fibre plots of single phase  $\text{Ni}_3\text{Al(B)}$  at different levels of cold rolling [50]



dispersion of  $\gamma/\gamma'$  regions within the matrix.

The cold rolling texture of the experimental material (containing both  $\gamma'$  and  $\gamma$ ) is expected to combine the essential characteristics of the textures of both  $\gamma'$  and  $\gamma$ , as stated above. However, the state of order in the  $\gamma'$  of the experimental alloy has been found to be quite different from that of pure  $\gamma'$  at comparable stages of rolling deformation (Figures 4.26 and 4.35) This, coupled with the fact that the starting material here was somewhat textured unlike the textureless initial material studied by Ghosh Chowdhury *et al* [50] is expected to cause major differences in the deformation texture development in the two cases.

A study of the  $\beta$ -fibre plots (Figure 4.26) for the experimental material shows normal pure metal type texture development after 25% cold rolling, with the Bs component slightly stronger than the other components, such as the Cu and the S. After 35% deformation the  $\beta$ -fibre intensity shoots up to an unusually high level, with the highest intensity near the Bs/S  $\{168\} < 211 >$  location and substantially high intensity at the Bs location. This very much resembles the characteristics of an alloy type texture. A high density of twins has been found in the microstructure at this stage (Figure 4.7b) presumably as a result of the  $L1_2 \rightarrow DO_{22}$  transformation. The changeover from pure metal to alloy type has probably been brought about by twinning, in a manner suggested by Wassermann [26], as mentioned earlier. In the earlier work on pure  $\gamma'$  [50] incidence of twinning on a large scale was observed only after about 65% deformation and this was found to cause a similar texture transition. While investigating the cause of twinning (as a result of  $L1_2 \rightarrow DO_{22}$  transformation) at a much earlier stage of deformation in the experimental alloy, as compared to the pure  $\gamma'$ , it was often noticed that heavily twinned regions were invariably obtained in the close vicinity of the deformed  $\gamma$  regions (Figure 4.36). In fact, the twins were found to be much denser near the  $\gamma/\gamma'$  interface than in regions away from these interfaces. This observation suggests that during deformation, the localized strain at the  $\gamma/\gamma'$  interface may reach a critical value much earlier than in other regions and this may trigger the  $L1_2 \rightarrow DO_{22}$  transformation and



2 $\mu$ m

Figure 4.36 TEM micrograph of 73% rolled  $\text{Ni}_3\text{Al}(\text{B},\text{Zr})$  shows high density of twin bands nearby the  $\gamma$  regions

the consequent formation of twins. Li and Wahi [151], from their work on  $\gamma/\gamma'$  boundaries in two phase superalloys, concluded that the  $\gamma/\gamma'$  lattice mismatch and the presence of misfit dislocation arrays may cause straining at localized regions. Bonnet and Ati [152], who conducted a comprehensive investigation on dislocation interactions at  $\gamma/\gamma'$  interfaces in two phase superalloys, sometimes observed a ribbon of APB in the  $\gamma'$  phase which was limited on one side by the  $\gamma/\gamma'$  interface and on the other side by a Shockley dislocation connected to a *Superlattice Intrinsic Stacking Fault* (SISF). Thus it appears that it may not be easy for the dislocations produced by deformation in the  $\gamma'$  phase to cross the  $\gamma'/\gamma$  interface, and this essentially means reasonable chances of strain accumulation in the  $\gamma'/\gamma$  interface. This may account for the much earlier occurrence of the  $L1_2 \rightarrow DO_{22}$  transformation and the consequent formation of twins in the experimental alloy, as compared to pure  $Ni_3Al$  ( $\gamma'$ ).

The high intensity of the S component of the  $\beta$ -fibre (more specifically near the Bs/S location,  $\{168\} < 211 >$ ) after 35% deformation was quite unusual. Although the Cu component of the  $\beta$ -fibre is known to reduce substantially due to twinning, Hirsch *et al* [122] suggested that the orientation  $(123)[\bar{4}\bar{1}2]$  near S produces its symmetrically equivalent variant  $(123)[41\bar{2}]$  after twinning. Thus the intensity of the S component is supposed to be unaffected by twinning. Although the deformation of  $\gamma$  regions is expected to contribute both to Cu and S components during deformation, their magnitude will be small and therefore cannot account for the high intensity of the  $\beta$ -fibre at Bs/S location. Mao *et al* [153] investigated the influence of the cube starting texture on rolling and recrystallization texture development in high purity Al. They observed the formation of a component  $\{124\} < 211 >$  ( $\phi_1 = 57^\circ$ ,  $\phi = 29^\circ$  and  $\phi_2 = 63^\circ$ ) from the cube at high rolling reductions. This component, named by them as *cube/S* component is not far from the S location ( $\phi_1 = 59^\circ$ ,  $\phi = 37^\circ$  and  $\phi_2 = 63^\circ$ ). It may be mentioned here that the XRD pattern of the starting material in the present investigation shows a strong (200) reflection and the corresponding ODF showed, not the exact cube, but rotated cube orientations (Figure 4.23b). Some of these orientations,

after deformation, could provide some intensity near the Bs/S location.

After 45% cold work the experimental material showed the first appearance of shear bands in the microstructure (Figure 4.4e) but their numbers were few. At this stage, there is already a high density of twins present in the material. Thus, the deformation behaviour at this stage will somewhat resemble that of a low SFE material with packages of twin/matrix lamellae. The resulting shear bands will therefore be of *Brass type* [122] which are broad bands usually extending over many grains, as has been found out experimentally also (Figure 4.4e). The crystallites present within these shear bands have a certain preference for Goss  $\{011\} < 100 > [154]$  and that could explain the sharpening of this component after 45% deformation from the previous level (Figure 4.28). The density of the shear bands has been found to increase continuously with increase in rolling reduction (Figures 4.4f to 4.4h). This explains the continuous sharpening of the Goss component till the final reduction of 73%. The  $\beta$ -fibre after 45% deformation appears similar to that after 35% deformation, but its overall intensity was found to weaken a little bit. A slight increase in the intensity of the Cu component and decrease in the intensity in the Bs component at this stage could be due to the contribution from deformed  $\gamma$  regions.

The density of shear bands was found to increase dramatically after 55% deformation (Figure 4.4g). The ODF intensity got drastically reduced and the  $\beta$ -fibre appeared similar to what was obtained after only 25% deformation. The overall weakening of the texture at this stage indicates the formation of a large background comprising of a host of weak components. This could be due to very inhomogeneous deformation at this stage, with the matrix/twin lamellae cut by the shear bands, leading to considerable fragmentation of the grains and a resultant weak crystallographic texture (Figure 4.25d). Similar weakening of texture and formation of a large background component was observed by Hirsch *et al* [138] in 70/30 brass deformed in the medium strain range (50 - 85%).

The overall texture intensity was found to increase after 65% deformation with perceptible

sharpening of all the important components – Cu, S and Bs, the sharpening of the last component being the most remarkable. Most of the shear bands were found aligned at this stage, in a particular direction making an angle of  $30^\circ$  -  $35^\circ$  with the rolling plane (Figure 4.4g). The twin density also increased significantly at this stage. The sharpening of the Cu and S components in the overall texture at this stage (Figure 4.26) could be due to the expected reasonably sharp pure metal type texture of the  $\gamma$  regions. A look at the  $\alpha$ -fibre plots of the 65% rolled material shows that maximum intensity at this stage is obtained not at the exact Bs location, but at the  $\{011\} \langle 111 \rangle$  position which is  $20^\circ$  away from the Bs. In addition to that, reasonably high intensity is also obtained at the rotated Goss orientation. This could be possible if the deformation mechanism changes again from twinning and shear banding to homogeneous slip which will rotate the fine equiaxed grains of the shear banded structure into the stable Bs orientation [122]. Some of the material in the Bs location could possibly be transferred along the  $\alpha$ -fibre to the rotated Goss  $\{011\} \langle 011 \rangle$  position by shear banding.

The alloy type texture sharpens after 73% rolling. Although the texture intensity at the Bs location does not change from the previous value, there has been a sharp increase near the Bs/S location and a drastic decrease in the rotated Goss position. The  $\beta$ -fibre at this stage again looks similar to the one obtained after 35% and 45% deformation.

# CHAPTER 5

## ANNEALING BEHAVIOUR

## ● *Annealing Behaviour*

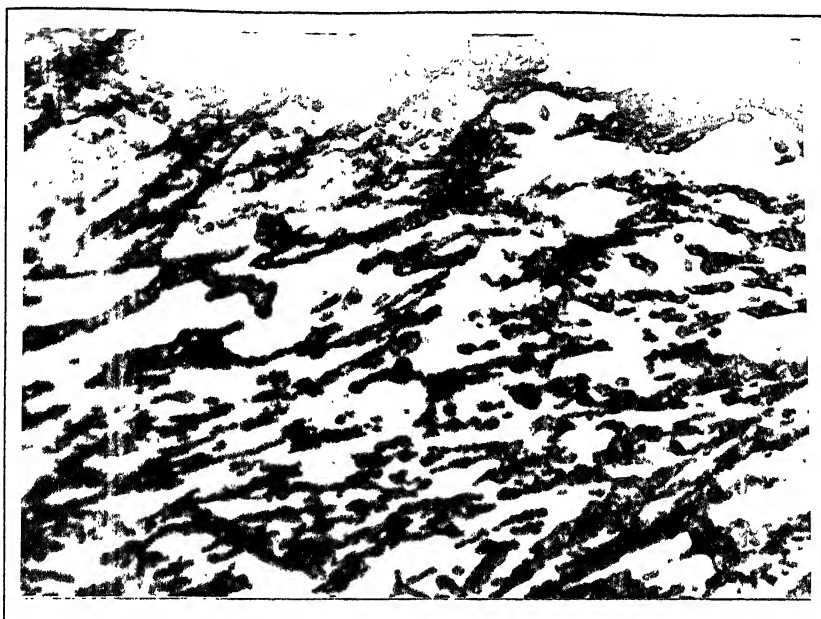
The annealing behaviour of the alloy was investigated by subjecting the 73% cold rolled material to recrystallization anneal at a number of temperatures for various lengths of time.

### 5.1 Isochronal Annealing

#### 5.1.1 Optical Microstructures

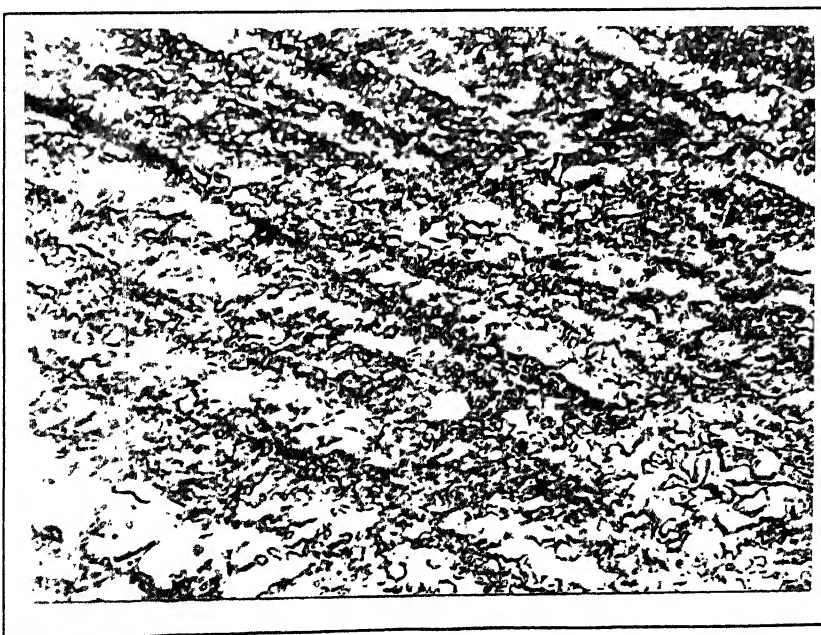
In order to evaluate the effect of annealing temperature on the recovery and recrystallization behaviour, the 73% cold rolled alloy was subjected to isochronal annealing for 1 hr at several temperatures ranging from 500° to 1200°C, at intervals of 100°C. It was observed that the microstructure of the deformed sample remained unaltered upto 600°C. Figures 5.1a to 5.1f show the optical micrographs of the samples annealed for 1 hr at temperatures ranging from 700° to 1200°C.

After annealing at 700°C (Figure 5.1a), numerous deformed second phase islands arranged within shear bands were still found to be present in the deformed  $\gamma'$  matrix. Early stages of recrystallization were noticed after annealing at 800°C (Figure 5.1b). The recrystallized volume fraction increased gradually after annealing at higher temperatures (Figures 5.1c and 5.1d), and a fully recrystallized structure was obtained after 1 hr annealing at 1100°C (Figure 5.1e). An aggregate of both large and fine grains was observed at this stage. After annealing at 1200°C (Figure 5.1f), a more or less equiaxed grain structure was obtained. The average grain size at this stage was about 6 - 8  $\mu\text{m}$ .



40 $\mu$ m

Figure 5.1a Optical micrograph after isochronal annealing at 700°C



40 $\mu$ m

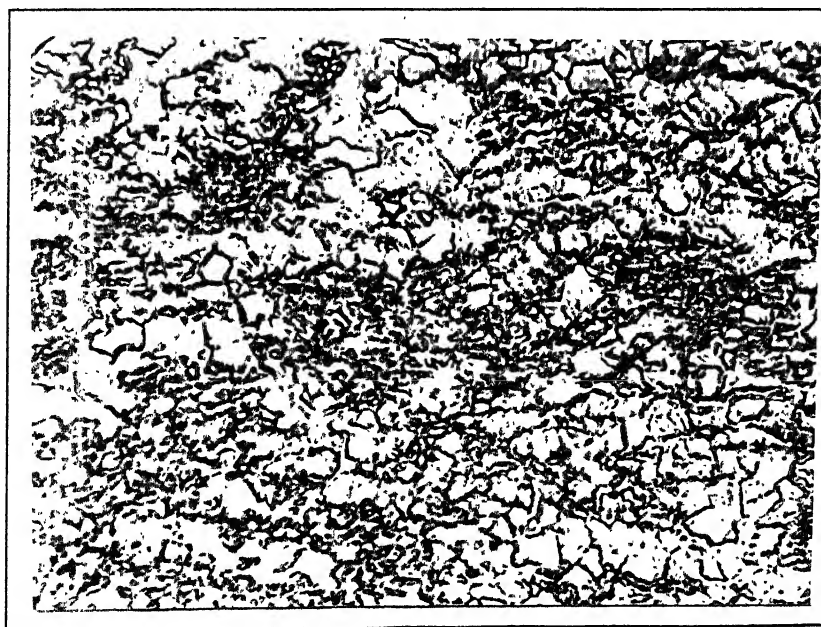
Figure 5.1b Optical micrograph after isochronal annealing at 800°C





40  $\mu$ m

Figure 5.1c Optical micrograph after isochronal annealing at 900°C



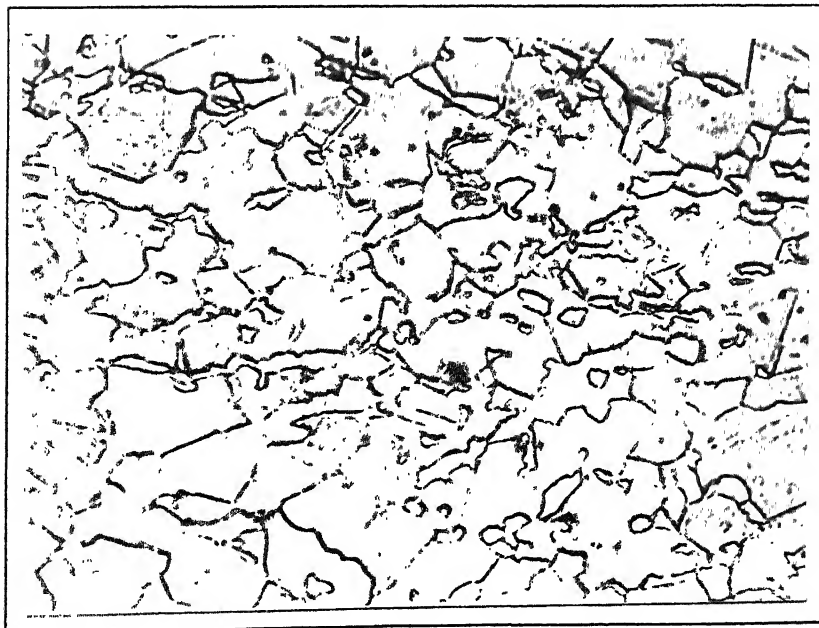
40  $\mu$ m

Figure 5.1d Optical micrograph after isochronal annealing at 1000°C



40 $\mu$ m

Figure 5.1e Optical micrograph after isochronal annealing at 1100°C



40 $\mu$ m

Figure 5.1f Optical micrograph after isochronal annealing at 1200°C

### 5.1.2 XRD Line Profiles

The XRD profiles recorded for all the isochronally annealed samples are presented in Figure 5.2. The (100) superlattice peak which was absent in the profile of the 73% rolled material, reappeared after 1 hr annealing at 600°C. It intensified somewhat with higher annealing temperatures, but the general pattern of the profile remained unchanged till after the highest temperature of isochronal annealing.

The XRD peaks from a few selected samples measured at a slower scanning speed are presented in Figure 5.3. The very closely spaced fundamental lines from the  $\gamma'$  and  $\gamma$  phases simultaneously present in the alloy can be distinguished one from the other for samples isochronally annealed at 800°C and above. The separation of the fundamental peaks (111), (200) and (220) for the two phases was more prominent after annealing at 1000°C.

### 5.1.3 Order Parameter (S)

The ordering behaviour of the 73% rolled material during isochronal annealing is shown in Figure 5.4. The (100) superlattice peak was absent in the 500°C annealed sample. Then it reappeared in the XRD profiles of the materials annealed at 600°C and above. The value of  $S_{100/200}$  which was zero upto 500°C, abruptly jumped to 0.34 at 600°C and improved further at higher annealing temperatures, reaching the maximum value of 0.67 at 1200°C.

The magnitude of the  $S_{110/220}$  value was nearly 0.33 at the initial condition (i.e. in the 73% cold deformed material). On isochronal annealing its value started rising slowly. The variation of  $S_{110/220}$  with the annealing temperature followed the same trend as the  $S_{100/200}$  and the order parameter reached a maximum value of 0.6.

### 5.1.4 Strain Parameter and Microhardness

Figure 5.5 shows a plot of the strain parameter values as function of isochronal annealing temperature. It is clearly observed in this Figure that the strain parameter decreased slowly

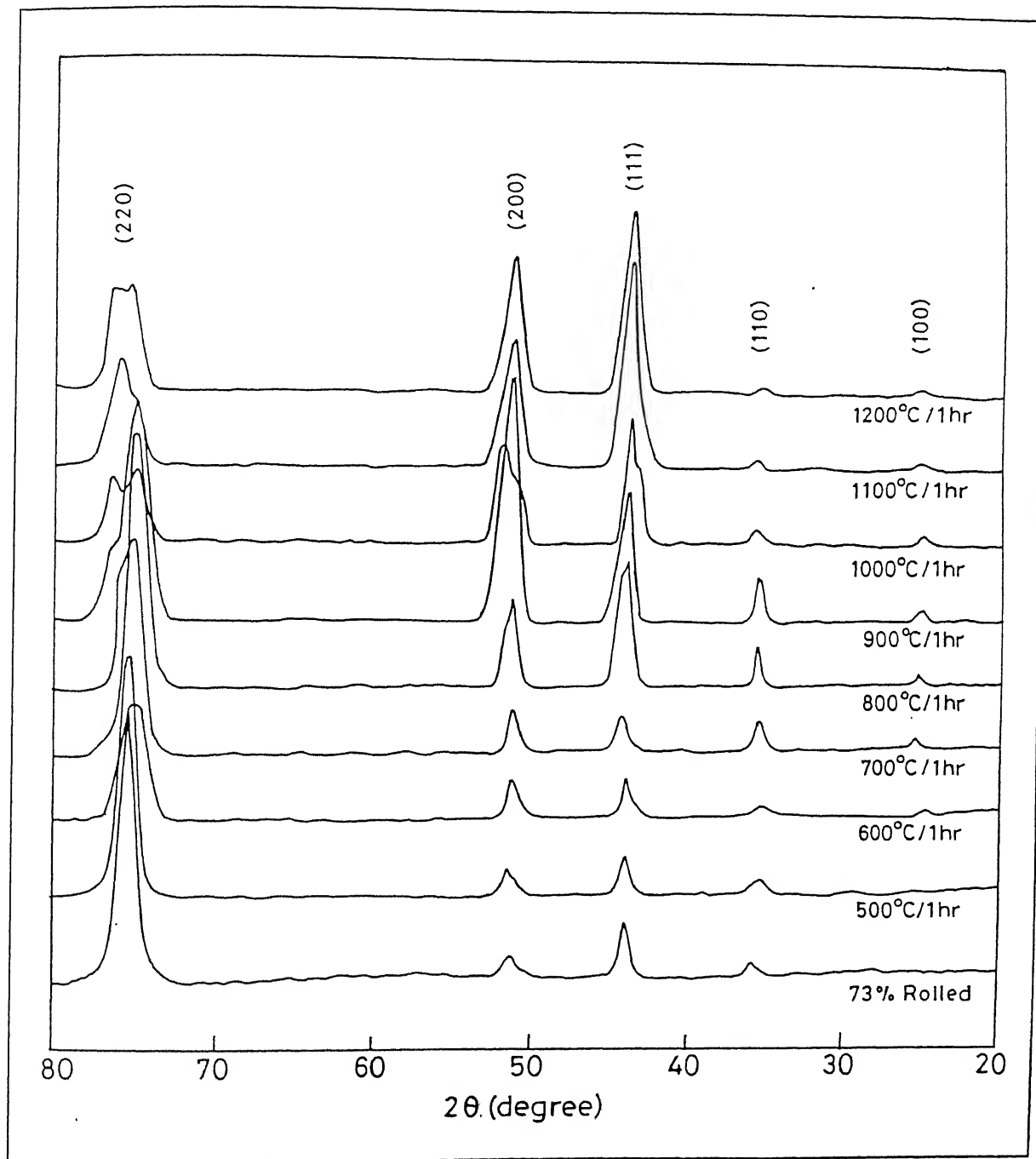


Figure 5.2 XRD line profiles of isochronally annealed samples

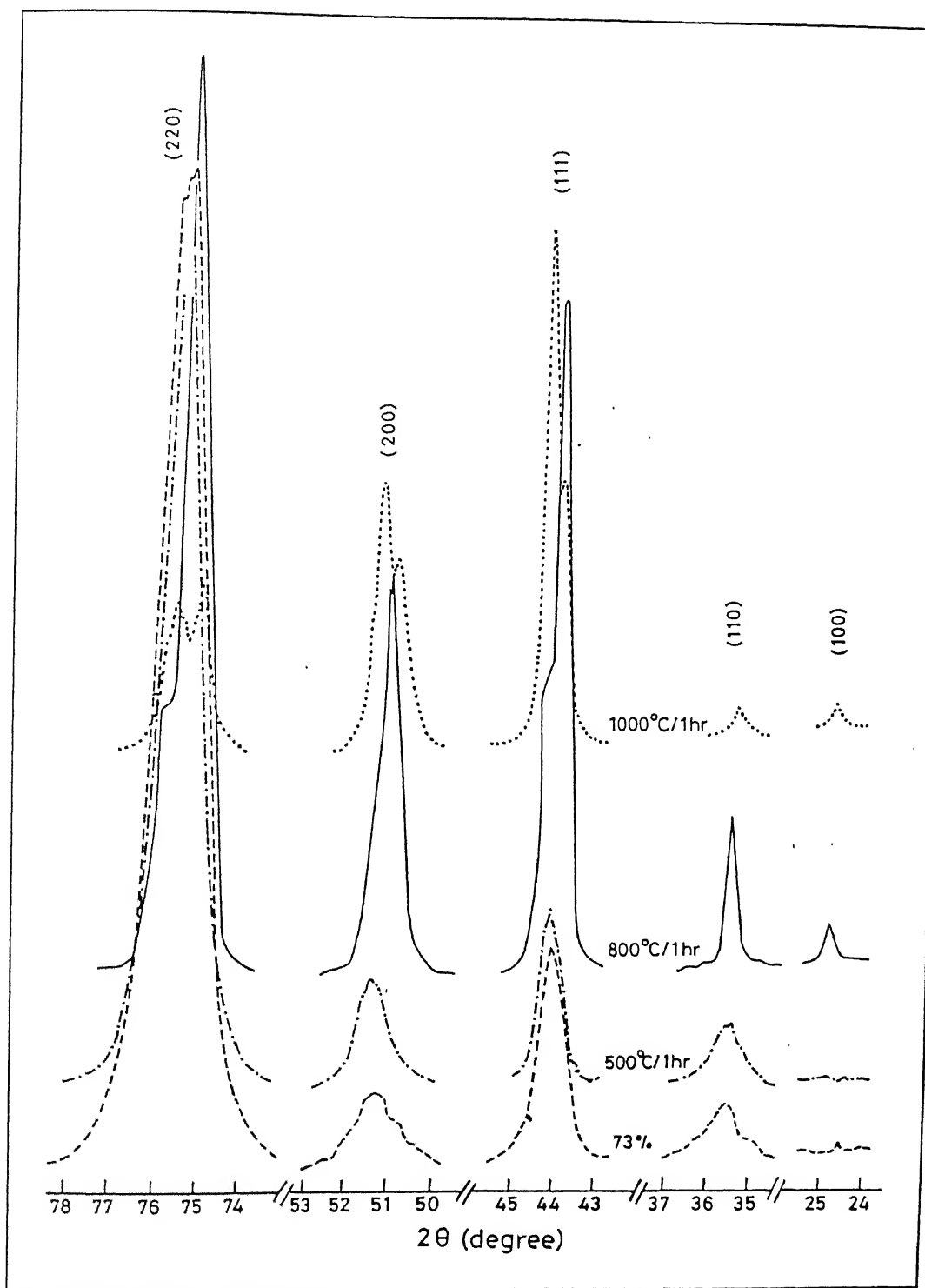


Figure 5.3 XRD line profiles of a few selected isochronally annealed samples  
(recorded at a slower scanning speed)

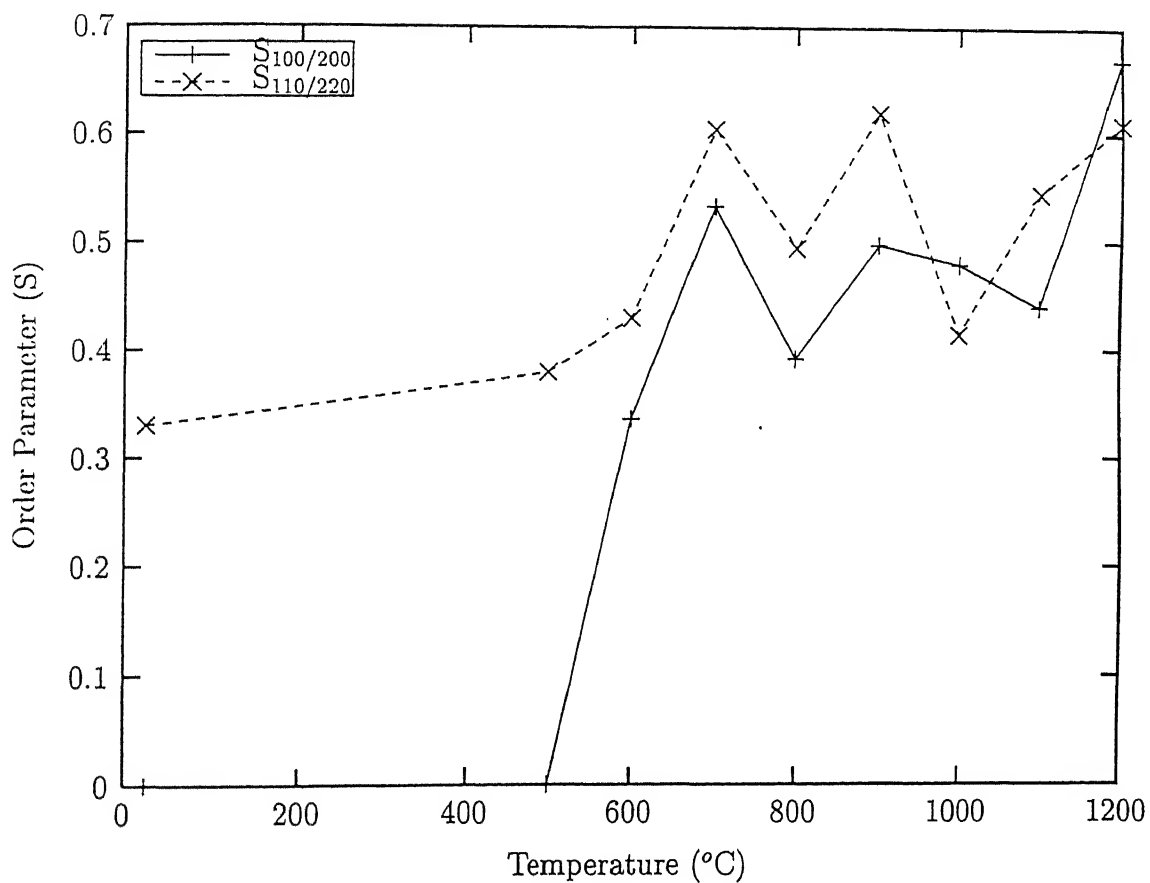


Figure 5.4 Variation of order parameter (S) with isochronal annealing

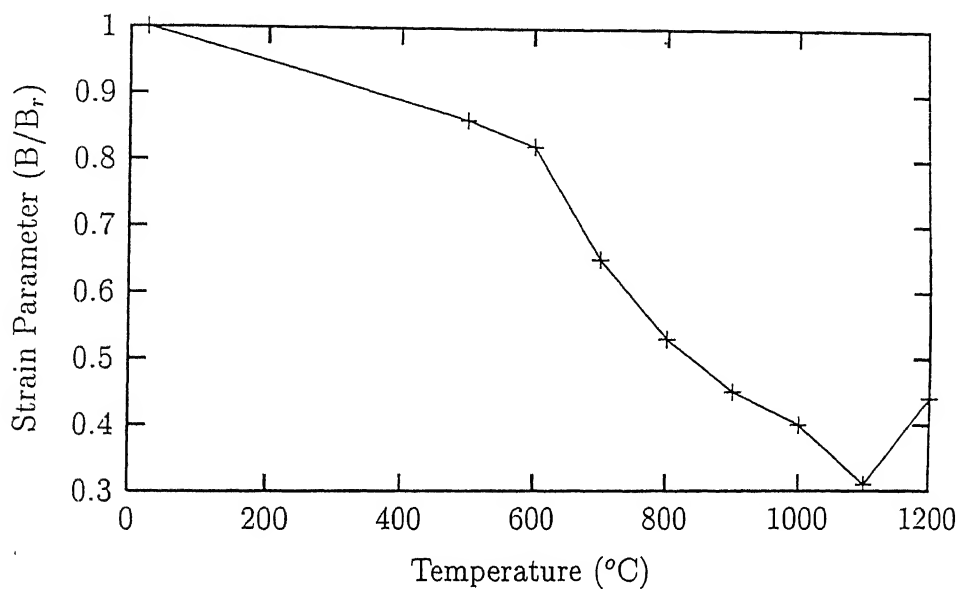


Figure 5.5 Variation of strain parameter with isochronal annealing

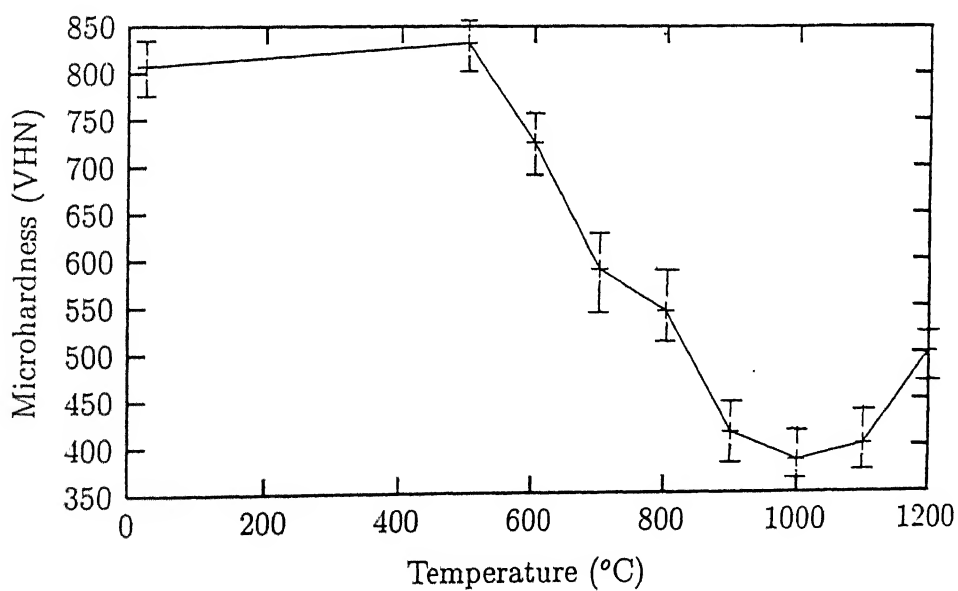


Figure 5.6 Variation of microhardness with isochronal annealing

upto the annealing temperature of 600°C and then at a much faster rate upto about 1100°C, before showing a slight increase at 1200°C.

The variation of microhardness values with isochronal annealing temperature is plotted in Figure 5.6. This plot is quite similar to the one obtained for strain parameter values in Figure 5.5. Hardly any softening of the material took place upto the annealing temperature of 500°C beyond which the hardness value dropped at a much faster rate. A plateau region was observed between 900° and 1100°C, followed by an increase in hardness at 1200°C.

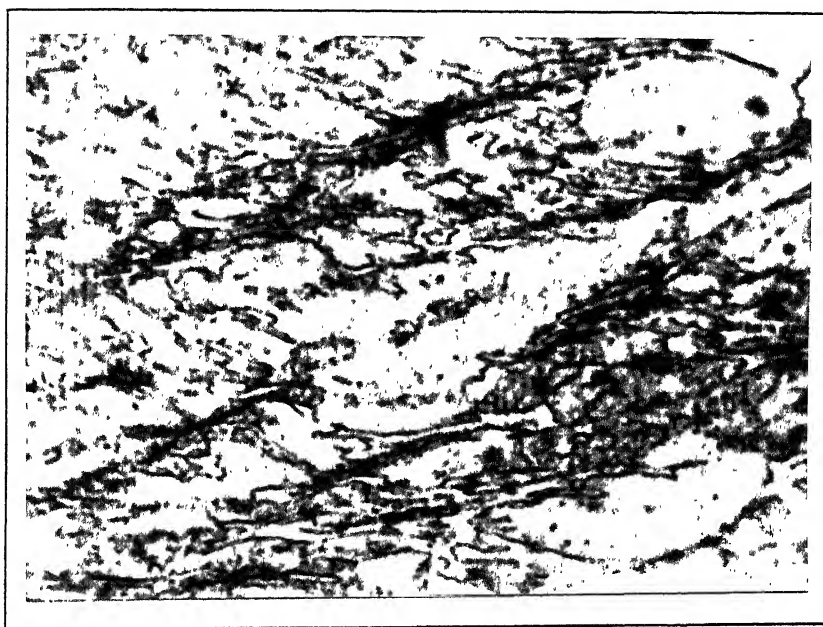
## 5.2 Isothermal Annealing

The annealing behaviour of the alloy was investigated more thoroughly by examining the microstructures and related parameters after subjecting the 73% cold rolled material to isothermal annealing at several temperatures, ranging from 800° to 1200°C, at 100° intervals, for various lengths of time.

### 5.2.1 Optical and SEM microstructures

Although isothermal annealing was not carried out at the lower temperature of 700°C, because of the sluggishness of the reaction, annealing for 16 hr at 700°C, revealed important changes in the microstructure of the  $\gamma$  regions aligned along the shear bands (Figure 5.7). Presumably, these are the preferred locations for recrystallization to start. A series of optical micrographs depicting typically the effect of isothermal annealing on the development of microstructure are shown in Figures 5.8a to 5.8d. This set of micrographs bring out the gradual changes in the microstructure as a function of time at 900°C. Starting from a very low volume fraction of recrystallized grains after 5 min annealing (Figure 5.8a), complete recrystallization was achieved at this temperature after 15 hr (Figure 5.8d). Figures 5.9a and 5.9b show the completely recrystallized microstructures obtained at higher annealing temperatures, such as 1000° and 1200°C.





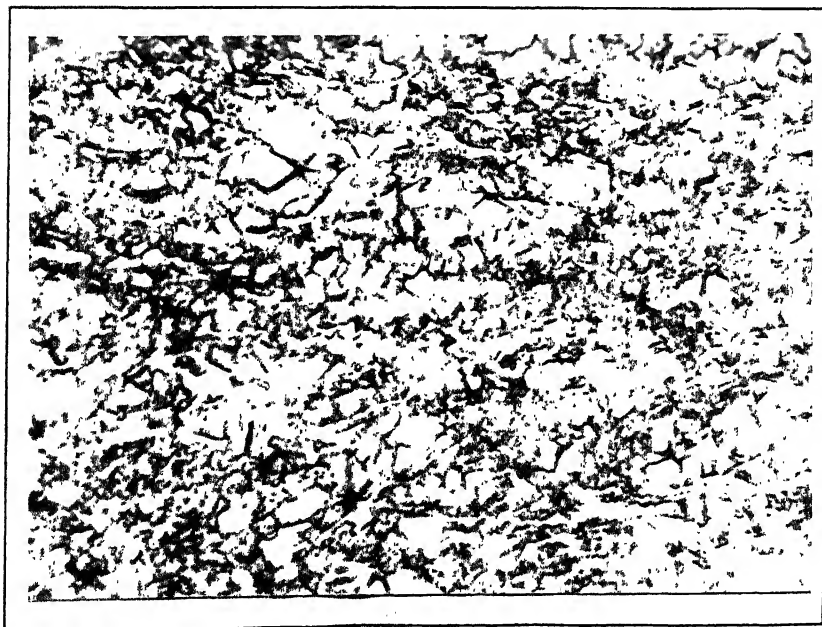
20 $\mu$ m

Figure 5.7 Optical micrograph after annealing at 700°C for 16 hr



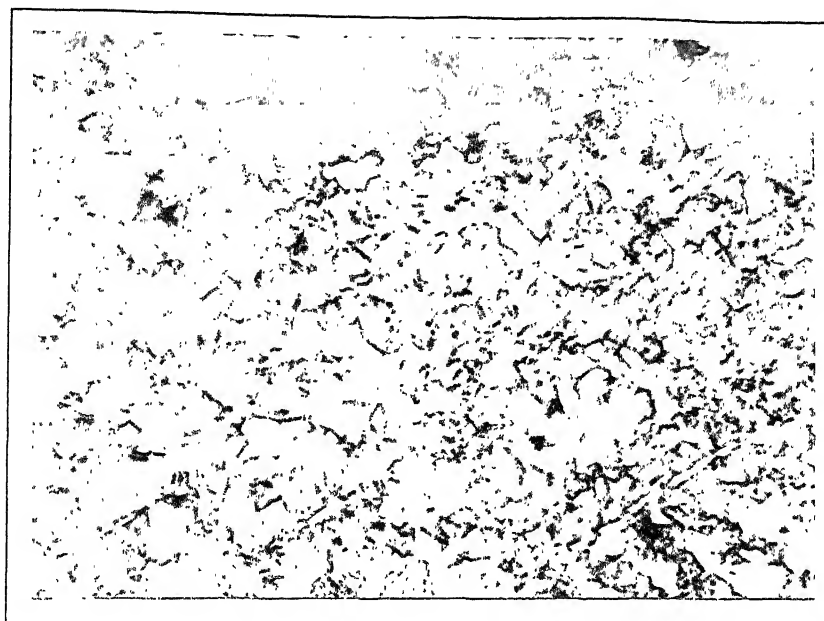
40 $\mu$ m

Figure 5.8a Microstructure after annealing at 900°C for 5 min



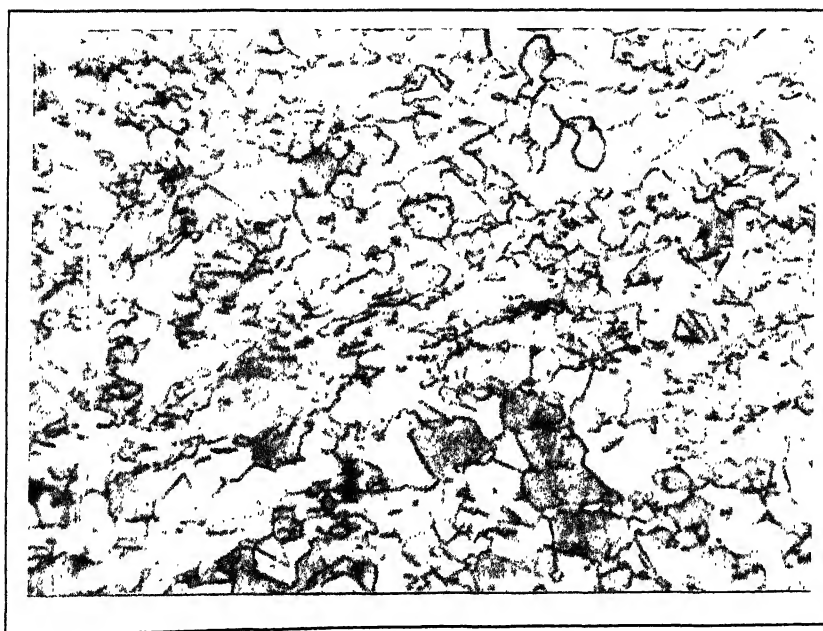
40 $\mu$ m

Figure 5.8b Microstructure after annealing at 900°C for 1.5 hr



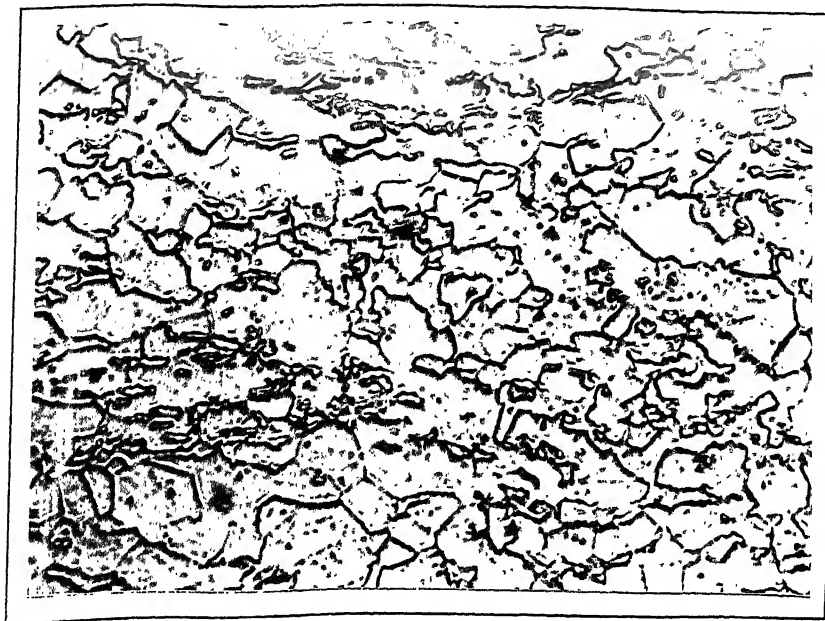
40 $\mu$ m

Figure 5.8c Microstructure after annealing at 900°C for 5 hr



40 $\mu$ m

Figure 5.8d Microstructure after annealing at 900°C for 15 hr



40 $\mu$ m

Figure 5.9a Recrystallized microstructure after annealing at 1000°C for 10 hr



40 $\mu$ m

Figure 5.9b Recrystallized microstructure after annealing at 1200°C for 1.5 hr

Figures 5.10a to 5.10f show a series of SEM photographs taken at different stages of isothermal annealing at 1100°C. Elongated second phase  $\gamma$  islands dispersed in the  $\gamma'$  matrix were clearly observed at the early stage of annealing (after 5 min), but the final microstructure (Figure 5.10f), after complete recrystallization, did not give the appearance of containing two distinct phases. This was also true of the fully recrystallized grain structure obtained at other annealing temperatures.

An attempt was made to obtain the chemical composition, by EDAX analysis, from the  $\gamma'$  and  $\gamma$  phases present in the microstructures at different stages of annealing at two representative temperatures of 800° and 1000°C. The results are given in a tabular form in Table 5.1. For any particular phase, analysis was carried out over at least ten different areas and quite comparable atomic percent values for the elements were obtained from them. The averages of these values have been finally presented in the Table.

**Table 5.1** Chemical composition of different phases during isothermal annealing (at. %)

Annealing Temperature 800°C								
Element	5.5 hr		12 hr		35 hr		100 hr	150 hr
	$\gamma'$ matrix	$\gamma$ island	$\gamma'$ matrix	$\gamma$ island	$\gamma'$ matrix	$\gamma$ island	Single phase	Single phase
Al	23.90	14.19	22.38	16.27	24.02	15.93	22.10	21.57
Ni	75.31	85.61	76.81	83.51	75.22	83.80	77.34	77.54
Zr	0.79	0.20	0.81	0.22	0.75	0.27	0.56	0.69

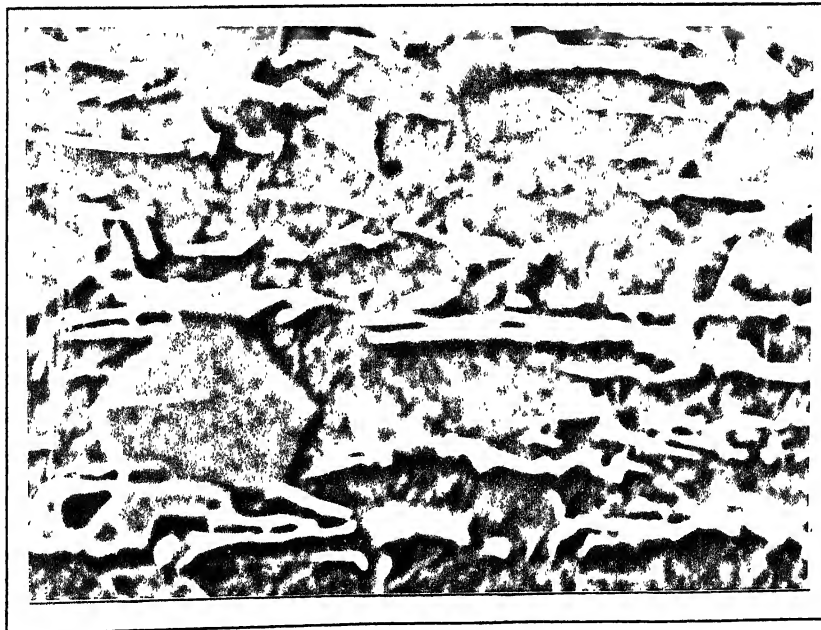
Annealing Temperature 1000°C								
Element	2 min		5 min		10 min		6 hr	10 hr
	$\gamma'$ matrix	$\gamma$ island	$\gamma'$ matrix	$\gamma$ island	$\gamma'$ matrix	$\gamma$ island	Single phase	Single phase
Al	23.91	16.85	23.69	17.29	22.35	16.01	22.19	22.00
Ni	75.24	83.01	75.44	82.37	76.83	83.63	76.89	77.31
Zr	0.95	0.14	0.87	0.34	0.81	0.36	0.92	0.69

It was also observed that after annealing for 100 hr and more at 800°C and for 6 hr and more at 1000°C, no two distinct phases could be seen in the microstructure. The alloy was



5 $\mu$ m

Figure 5.10a SEM micrograph after annealing at 1100°C for 5 min



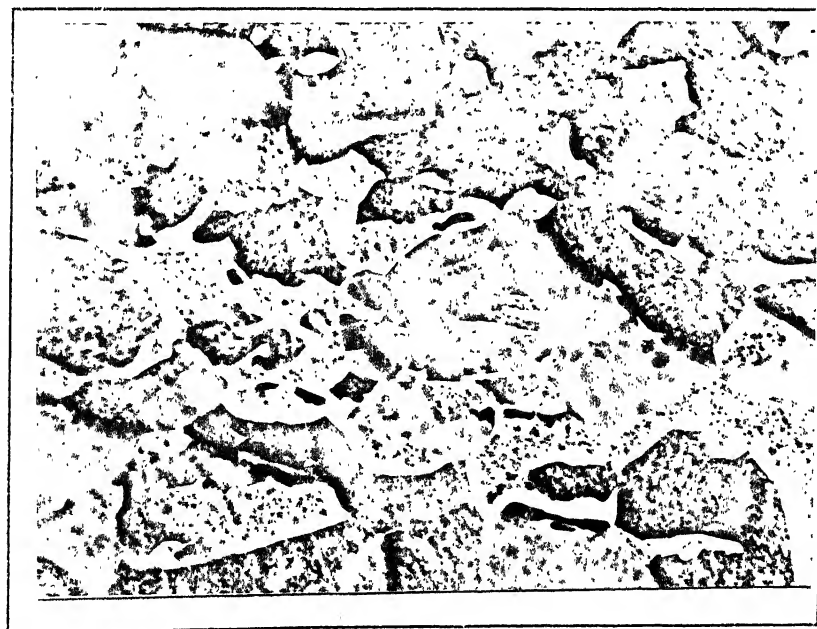
10 $\mu$ m

Figure 5.10b SEM micrograph after annealing at 1100°C for 10 min



10 $\mu$ m

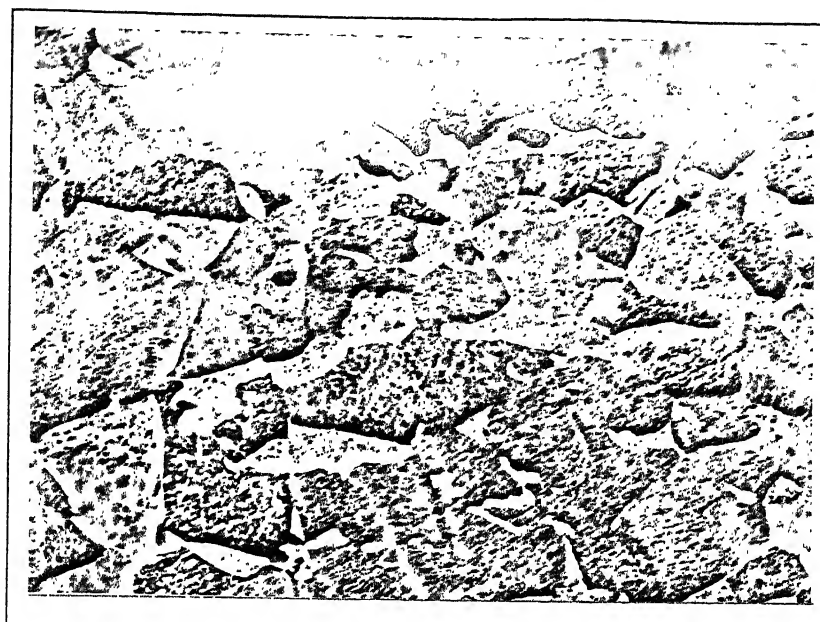
Figure 5.10c SEM micrograph after annealing at 1100°C for 20 min



10 $\mu$ m

Figure 5.10d SEM micrograph after annealing at 1100°C for 30 min





10 $\mu$ m

Figure 5.10e SEM micrograph after annealing at 1100°C for 1 hr



10 $\mu$ m

Figure 5.10f SEM micrograph after annealing at 1100°C for 2 hr



fully recrystallized in those conditions and appeared to consist of nearly equiaxed grains of a single phase. For any one of these samples EDAX analysis was carried out at random on at least ten different grains and the analysis was found to be quite comparable. The data presented in the Table is the average of the values obtained from all the ten grains.

### 5.2.2 XRD Line Profiles

The XRD line profiles of all the samples annealed at temperatures 800°C, 900°C, 1000°C, 1100°C and 1200°C are shown in Figures 5.11a to 5.11e. The most important feature in all of them is the reappearance of (100) superlattice peak after annealing for certain length of time at a particular temperature. This time shortens as the isothermal annealing temperature is increased. With prolonged annealing, the splitting of the fundamental lines showing the peak positions of the lines of the  $\gamma'$  and  $\gamma$  phases, becomes more prominent. This is displayed typically in Figures 5.12a and 5.12b for annealing temperatures of 800°C and 1000°C respectively. It can further be noticed in these Figures that as annealing progresses at a particular temperature the relative heights of the  $\gamma$  peaks increase indicating formation of larger volume fractions of the  $\gamma$  phase.

### 5.2.3 Order Parameter (S)

The order parameter (S) values were determined for all the isothermally annealed samples, from their respective XRD profiles, and these have been displayed as function of annealing time in Figures 5.13a to 5.13e. At any particular annealing temperature, order is re-established quickly after short annealing time. Higher the annealing temperature, shorter is the time required for ordering. Between 800° and 1000°C (Figures 5.13a to 5.13c), once the order is re-established (as compared to the 73% cold rolled material) the value of S does not seem to change significantly with annealing time, and the maximum value of S never exceeds 0.7. It is interesting to note that both the  $S_{100/200}$  and  $S_{110/220}$  plots run almost parallel to each other and nearly the same trend is observed in the variation of the S parameter at all

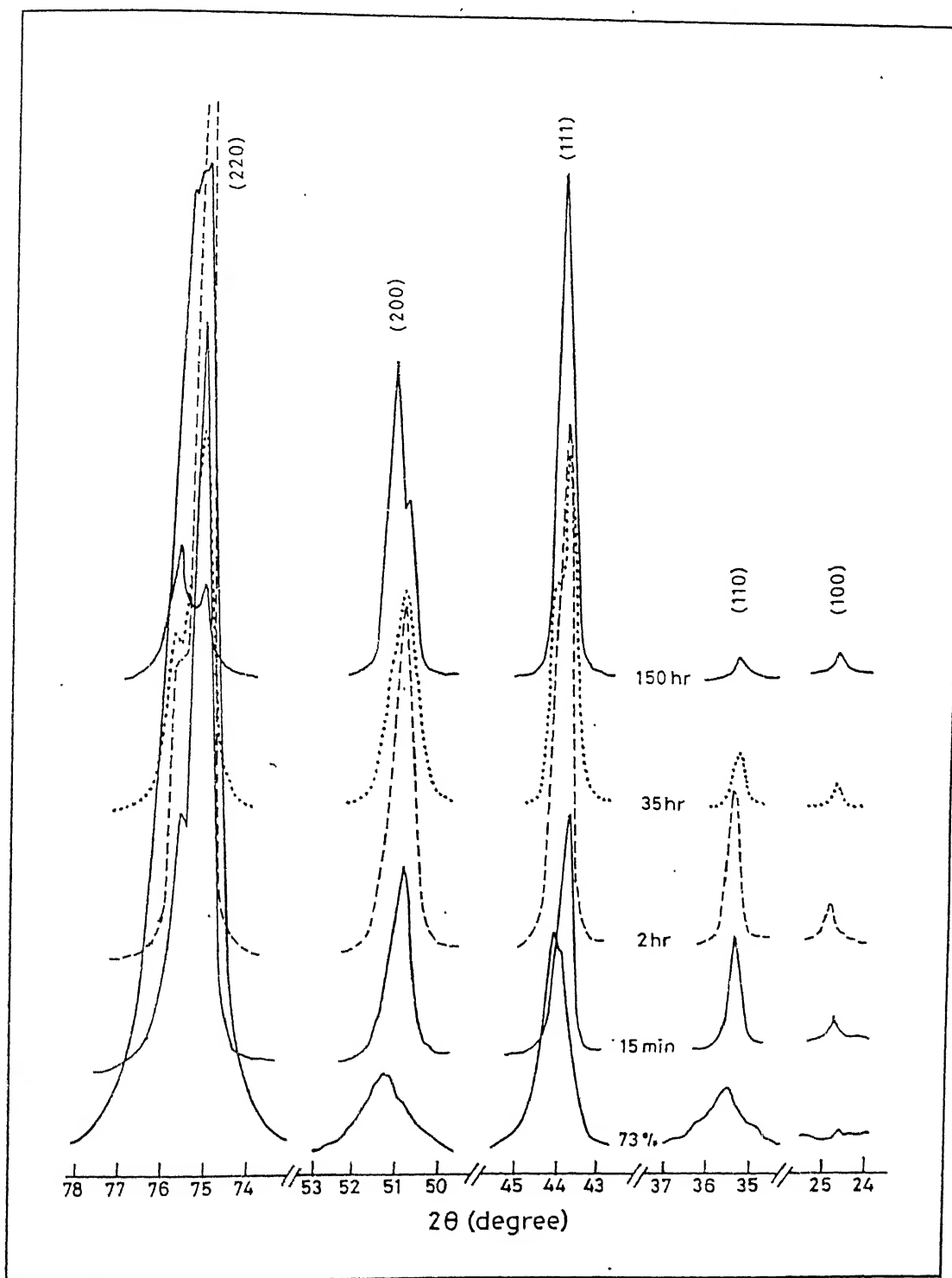


Figure 5.11a XRD line profiles of isothermally annealed samples at 800°C

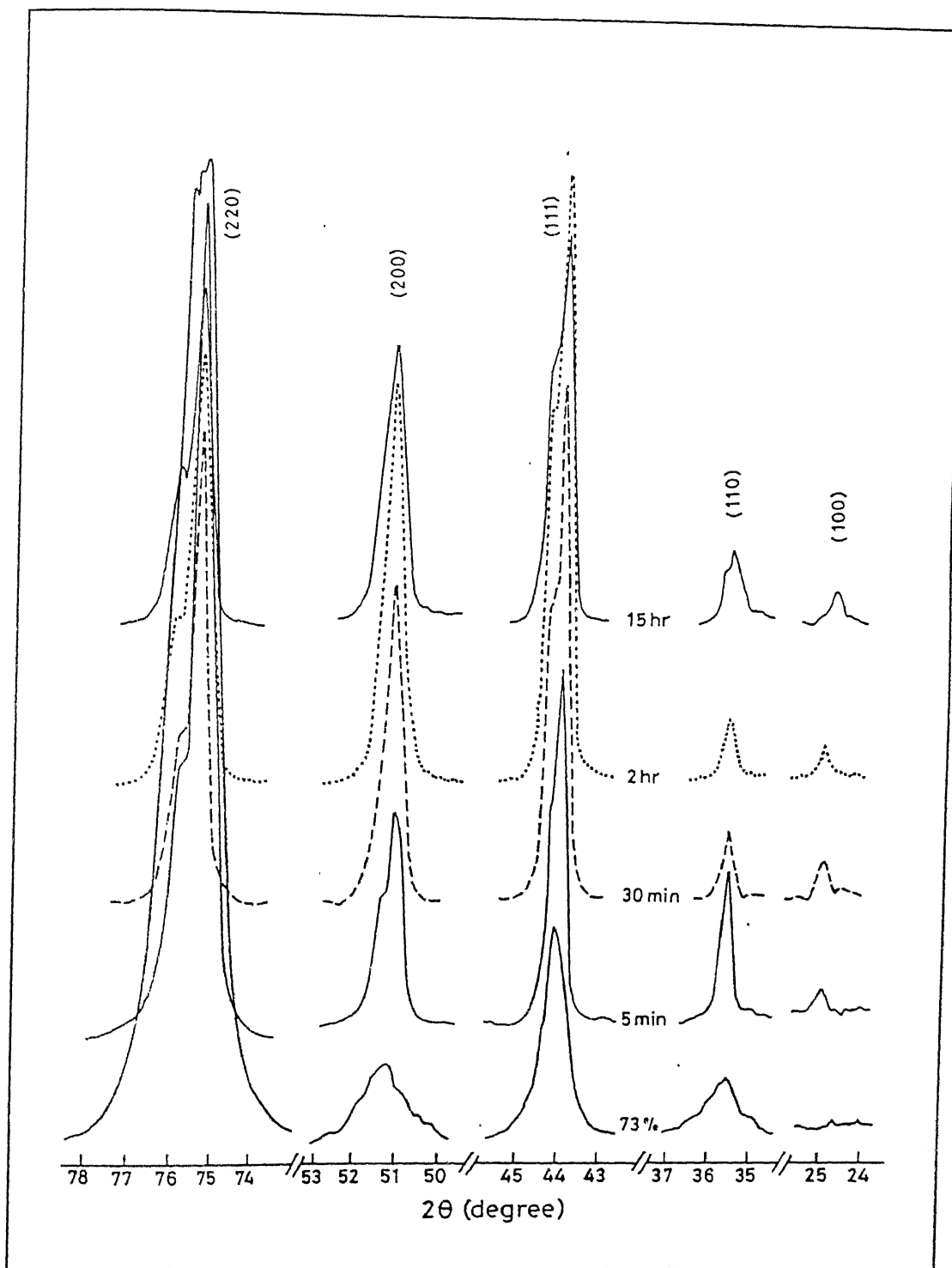


Figure 5.11b XRD line profiles of isothermally annealed samples at 900°C

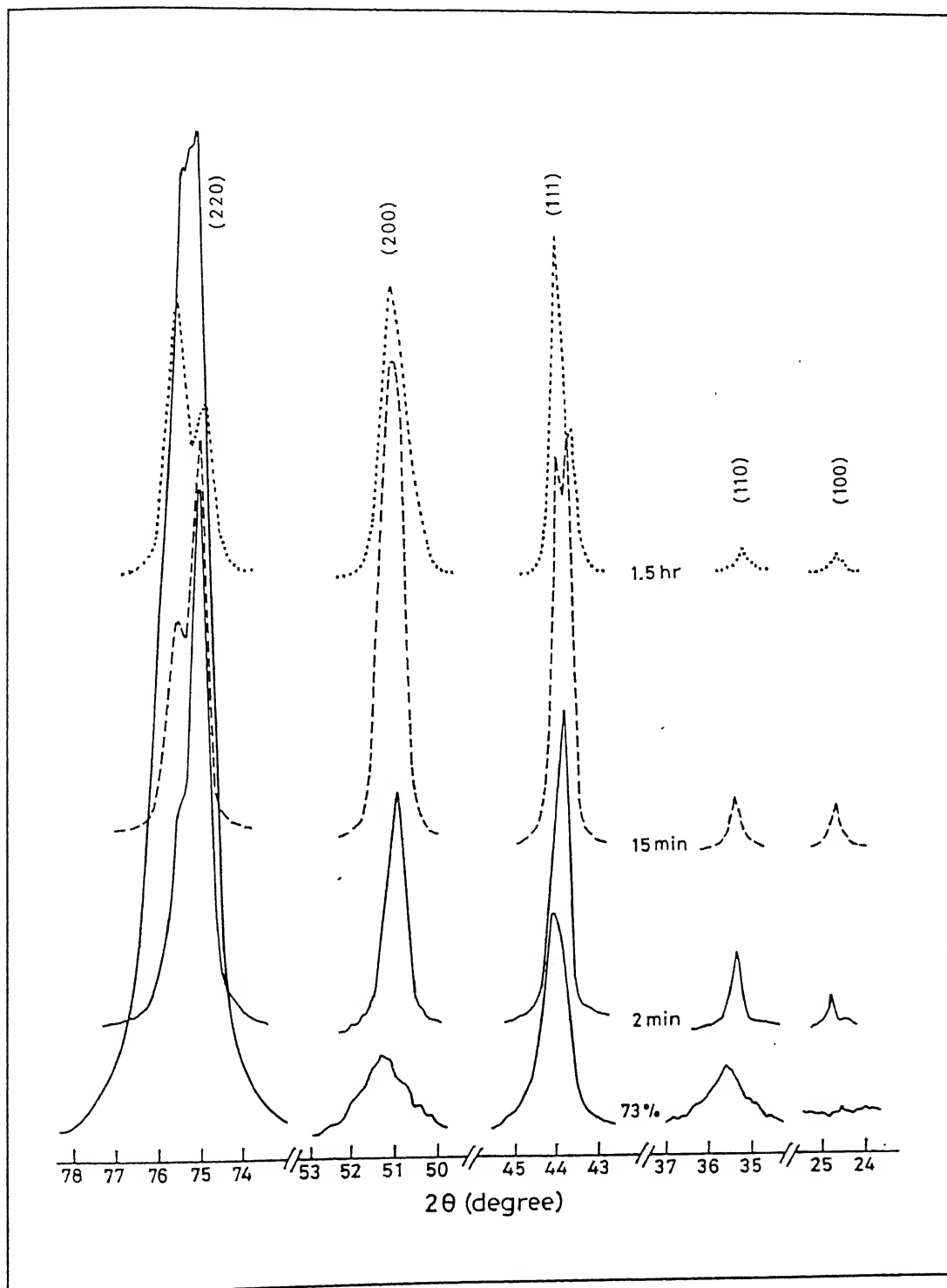


Figure 5.11c XRD line profiles of isothermally annealed samples at 1000°C

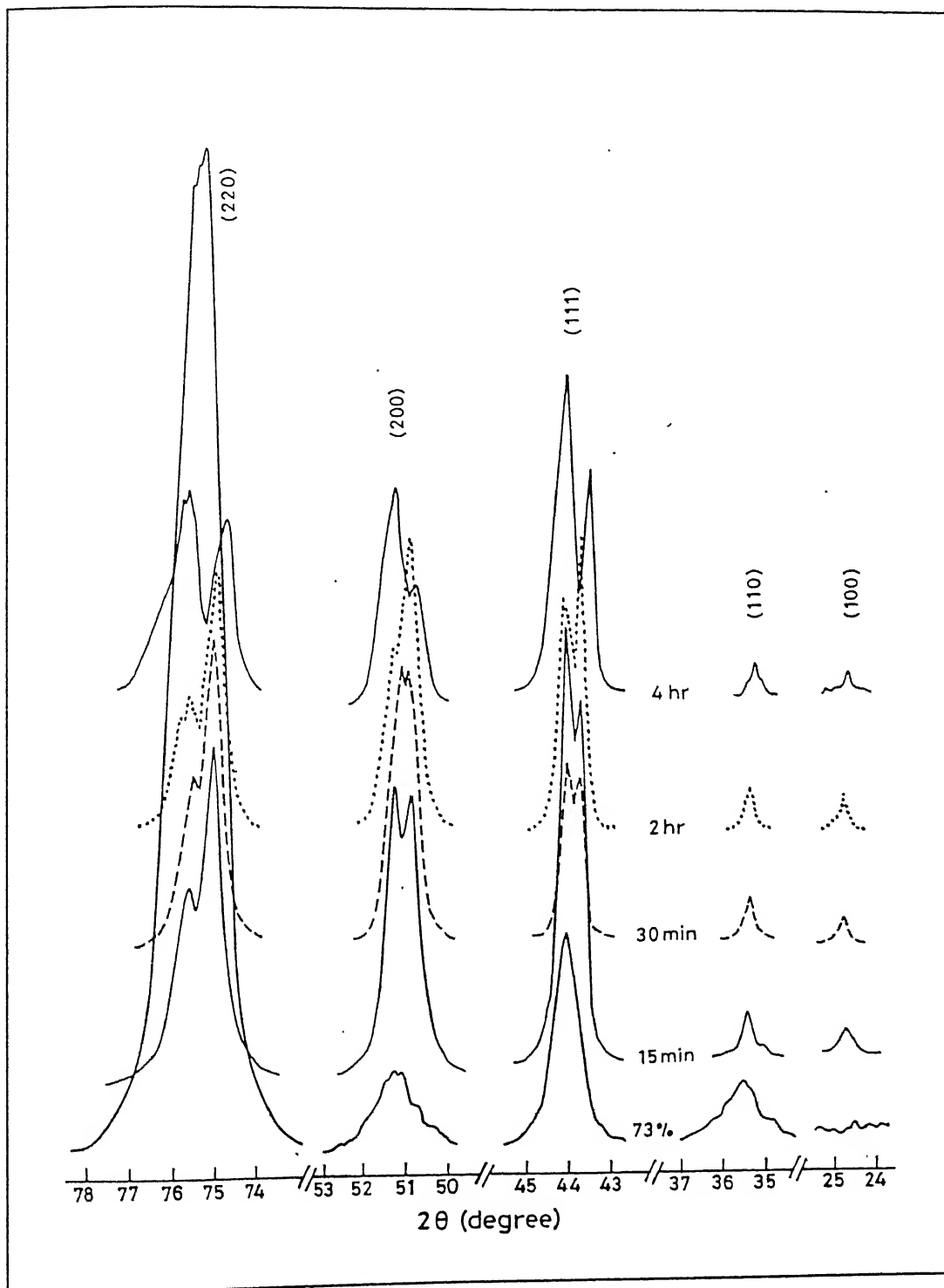


Figure 5.11d XRD line profiles of isothermally annealed samples at 1100°C

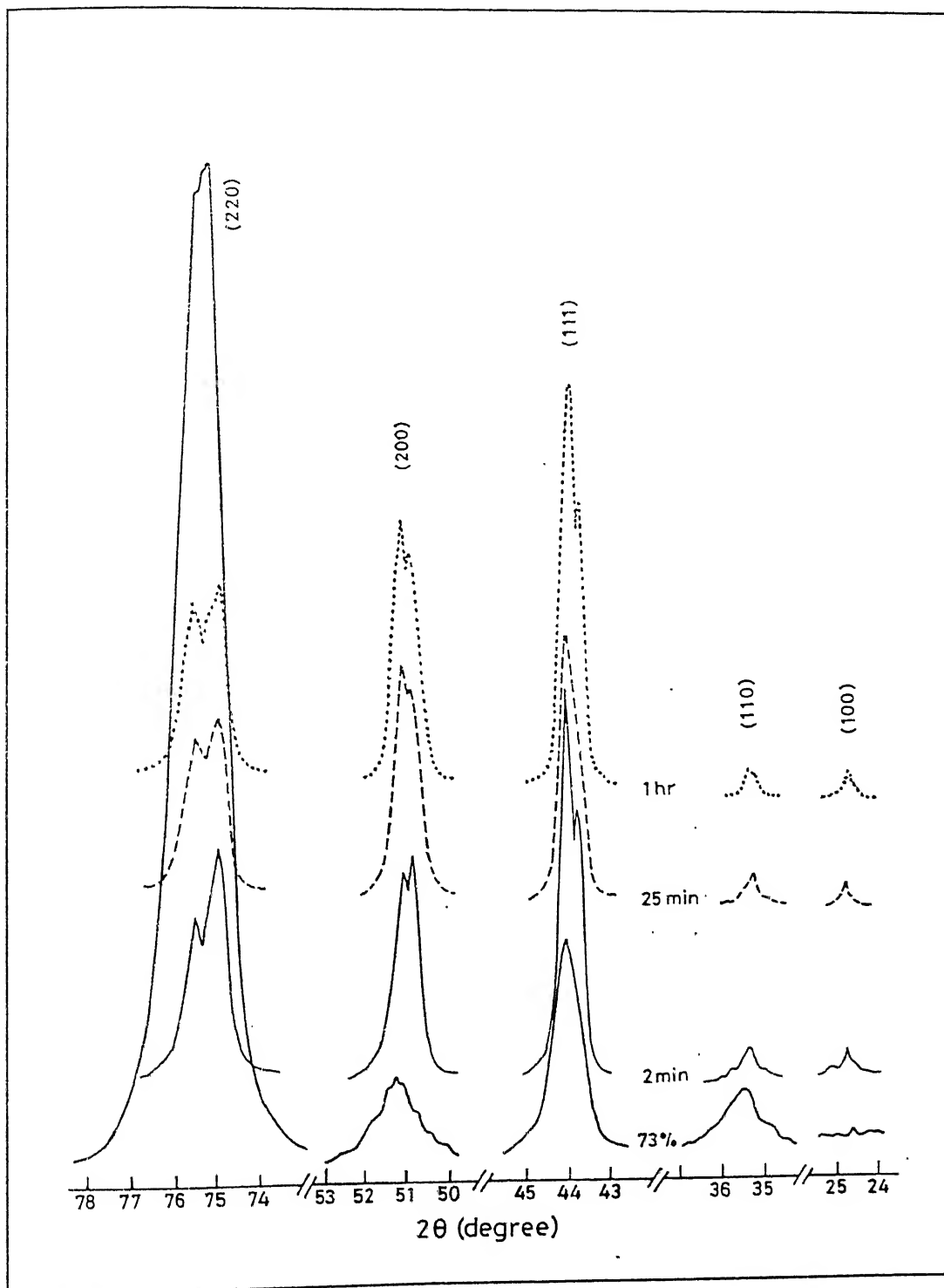


Figure 5.11e XRD line profiles of isothermally annealed samples at 1200°C

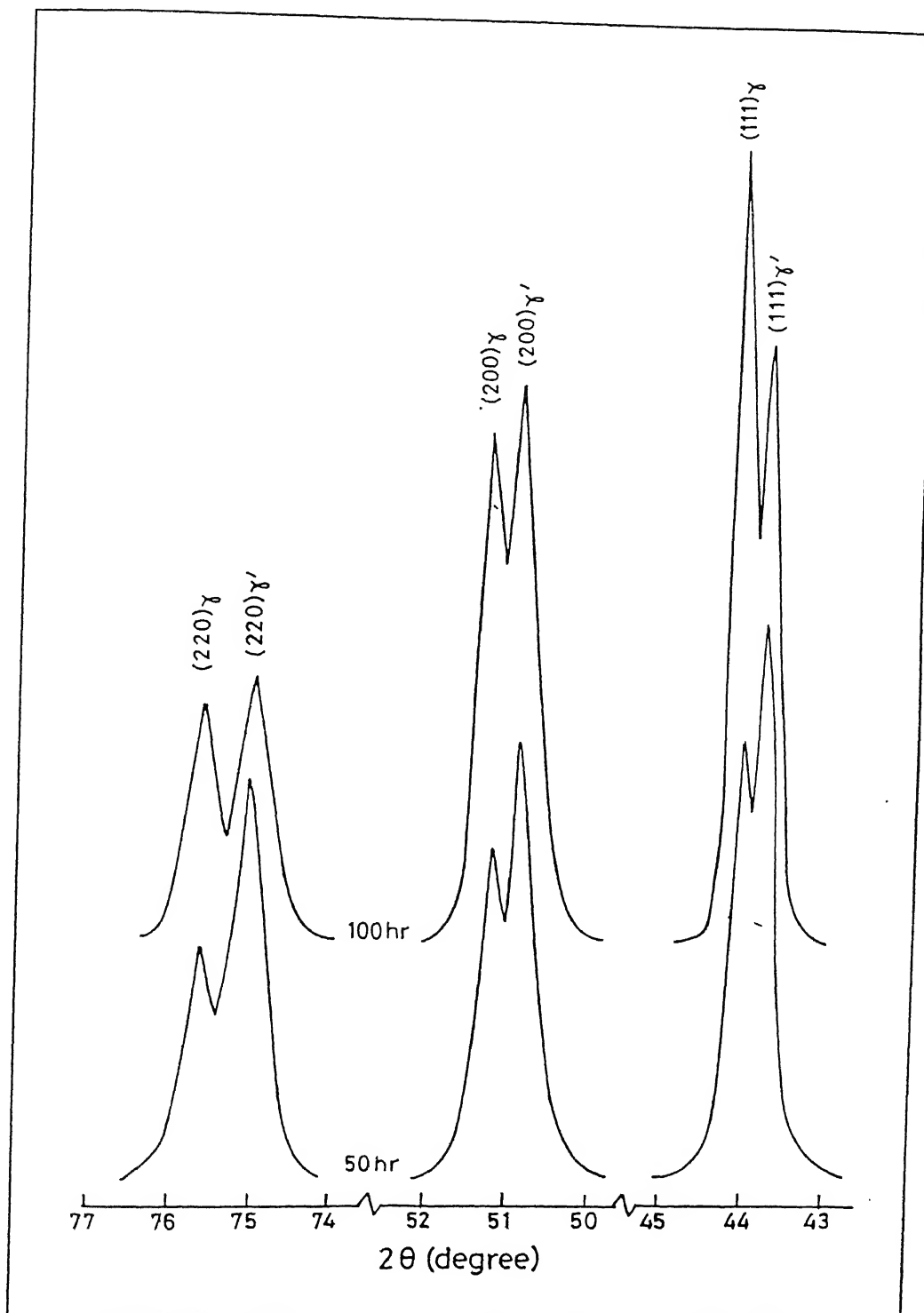


Figure 5.12a A few selected XRD peaks after annealing at 800°C

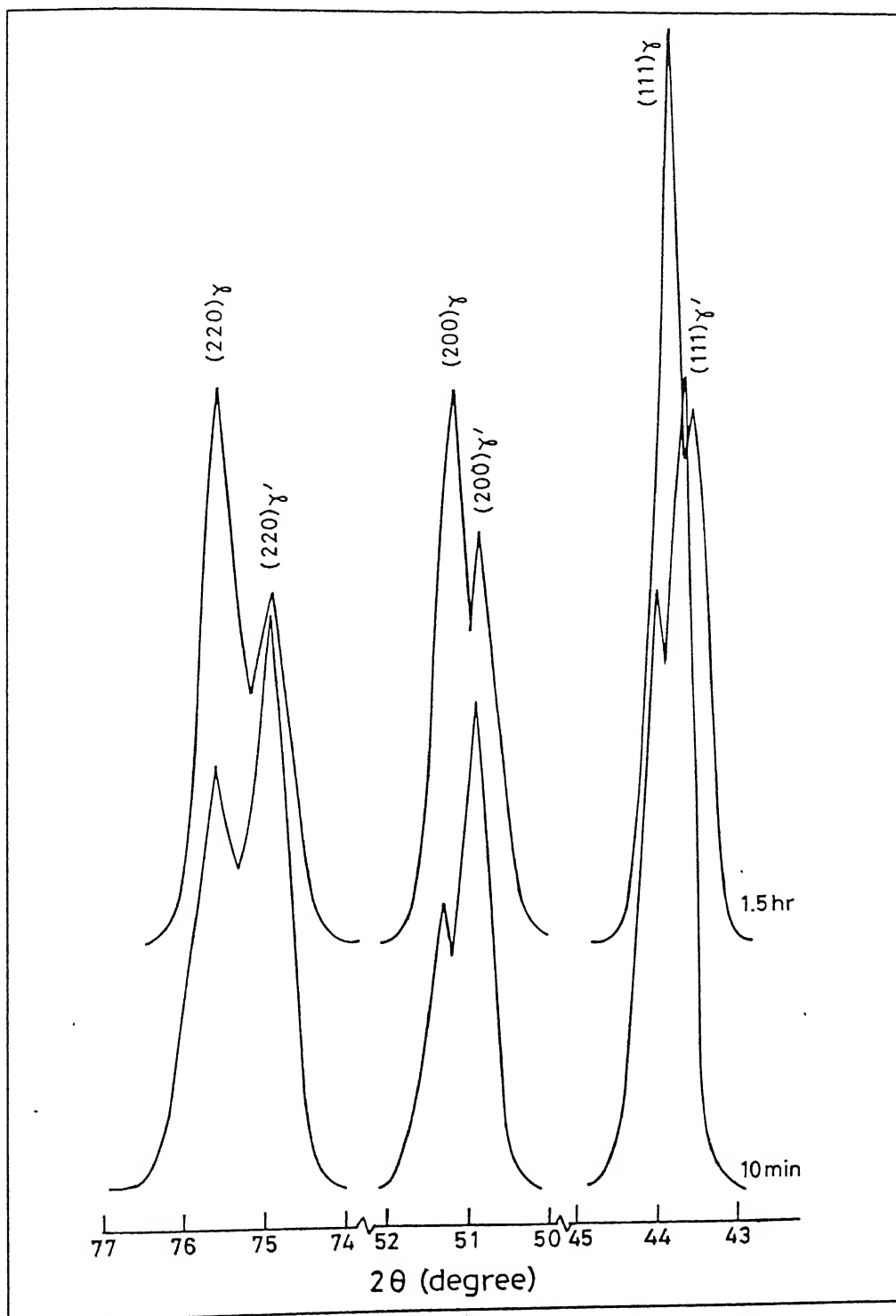


Figure 5.12b A few selected XRD peaks after annealing at 1000°C



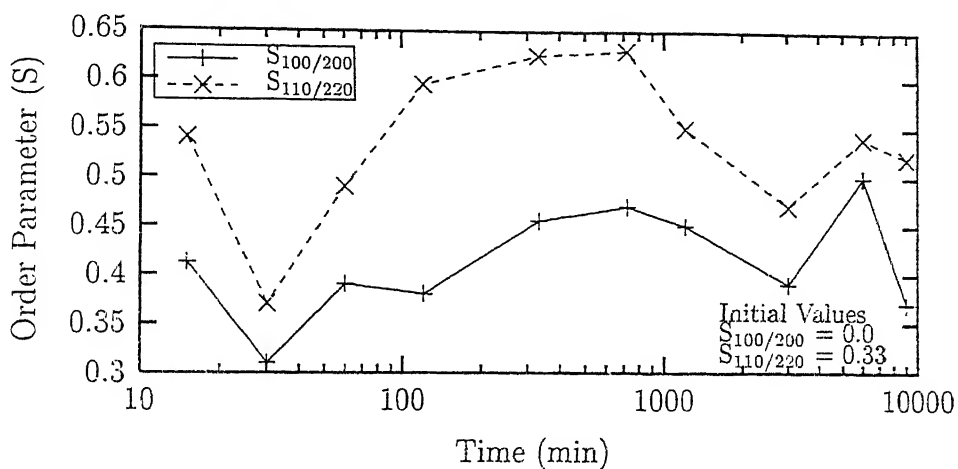


Figure 5.13a Variation of order parameter (S) with isothermal annealing at 800°C

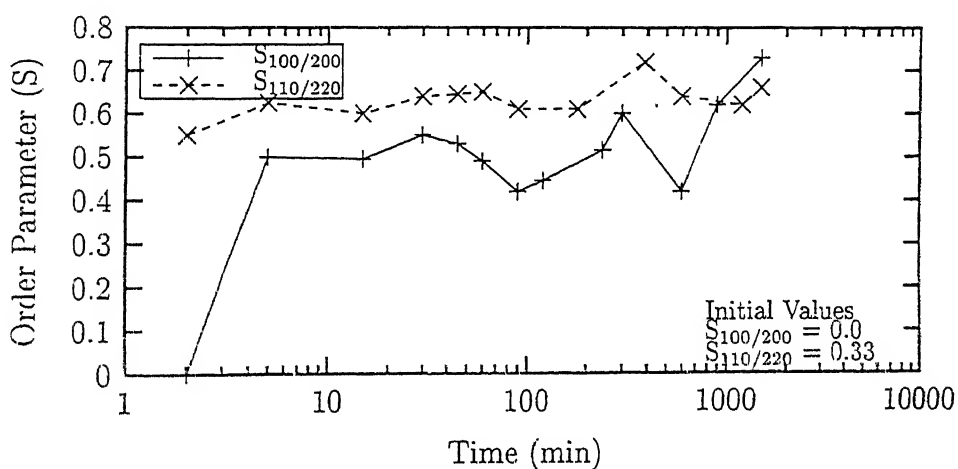


Figure 5.13b Variation of order parameter (S) with isothermal annealing at 900°C

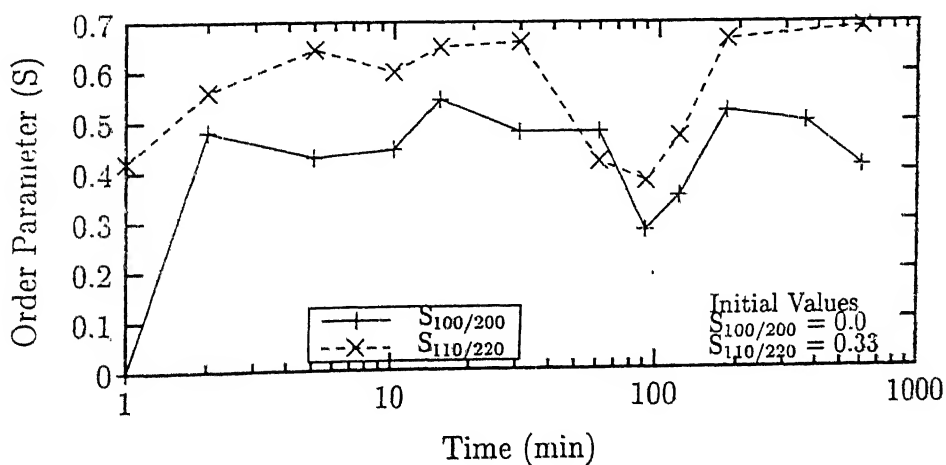


Figure 5.13c Variation of order parameter (S) with isothermal annealing at 1000°C

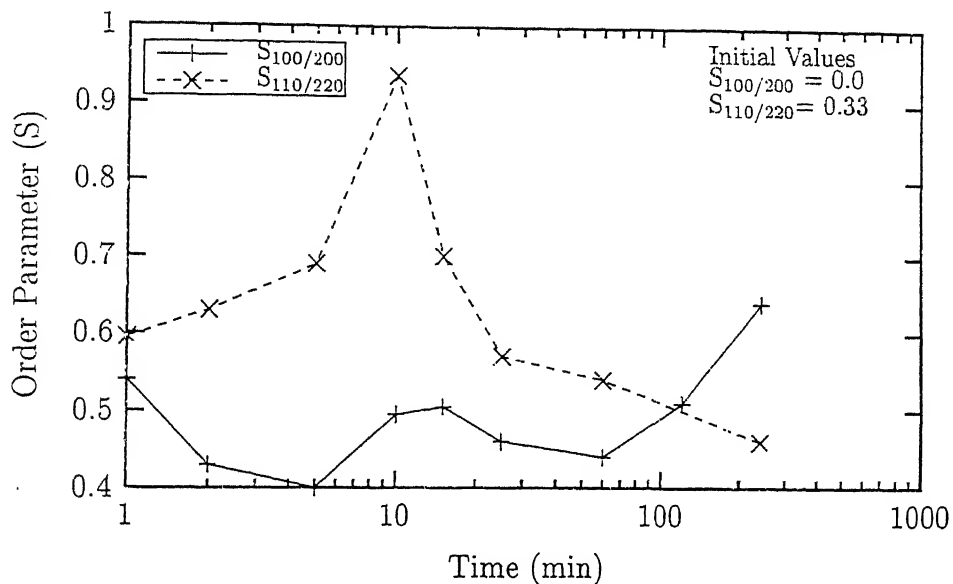


Figure 5.13d Variation of order parameter (S) with isothermal annealing at 1100°C

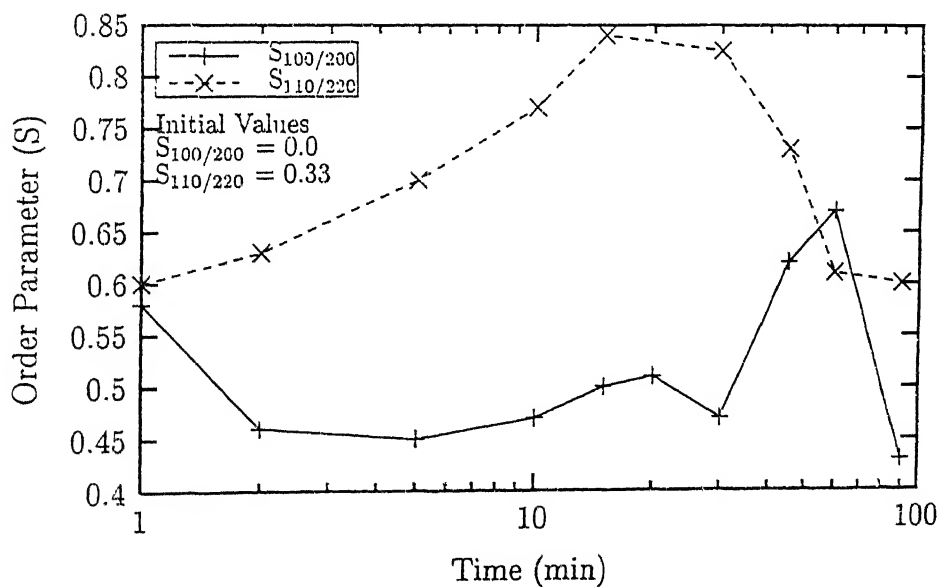


Figure 5.13e Variation of order parameter (S) with isothermal annealing at 1200°C

the temperatures between 800° and 1000°C.

A somewhat different behaviour is depicted in the Figures 5.13d and 5.13e, showing the variations of the  $S$  parameter during isothermal annealing at 1100°C and 1200°C, respectively. Here the  $S_{100/200}$  and  $S_{110/220}$  plots are found not to maintain a nearly parallel relationship as at lower temperatures. These plots also show that after about 10 min of annealing a peak value of  $S = 0.85$  to  $0.95$  is reached by  $S_{110/220}$ . This is very close to the theoretical value for a fully ordered material.

#### 5.2.4 Strain Parameter and Microhardness

The plots showing the variations of the strain parameter ( $B/B_r$ ) on isothermal annealing at different temperatures are shown in Figure 5.14. The basic nature of all the plots shown in this Figure is found to be quite similar. Each one of them shows an initial downward trend, reaching a minimum value before rising again to produce a little hump followed by a further decrease.

The plots of microhardness values against time of annealing at different temperatures are shown in Figure 5.15. These plots show a trend similar to the strain parameter diagrams (Figure 5.14). At the initial stage, a significant softening effect can be observed in all the plots, more prominently at higher temperatures. This is followed by an intermediate hardening effect before the material softens again. The hardening effect was not very clear at 800°C. It was however more prominent at higher temperatures, and a well developed peak was observed in the microhardness value in the plot for 1200°C.

### 5.3 TEM Microstructures

An attempt was made in this investigation to characterize the very early stages of recrystallization and record its progress by carefully analysing the microstructural details using a Transmission Electron Microscope (TEM). For this purpose, lot of attention was paid to

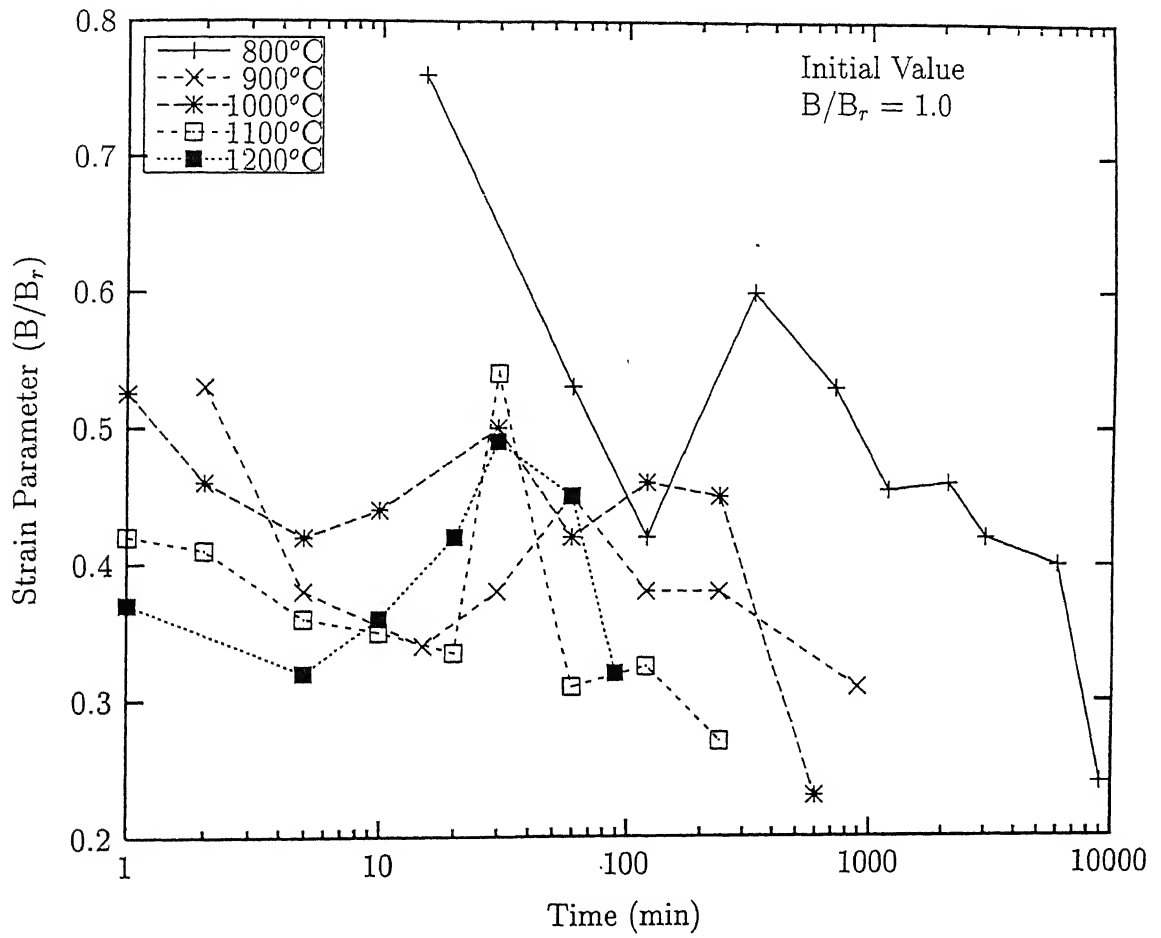


Figure 5.14 Variation of strain parameter with isothermal annealing at five temperatures

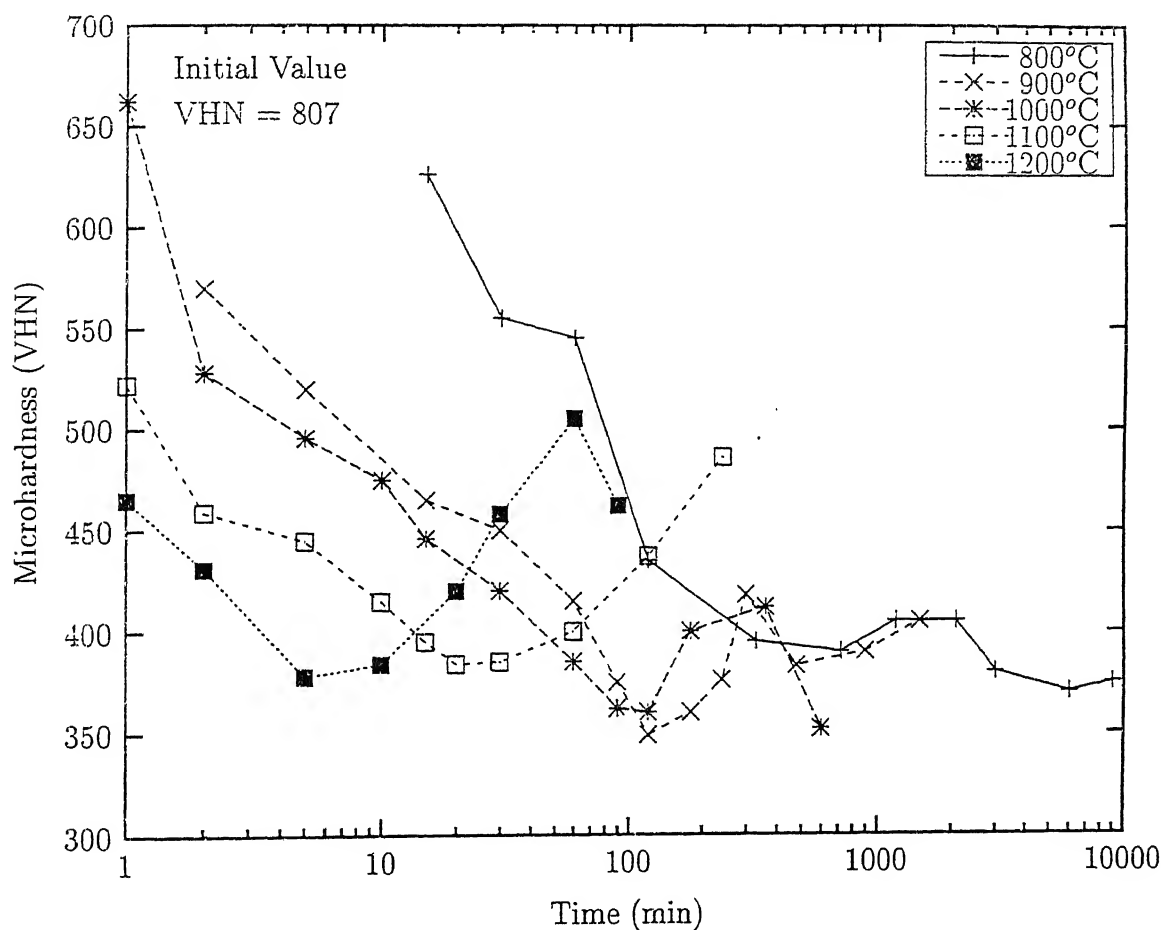


Figure 5.15 Variation of microhardness with isothermal annealing at five temperatures

(The error bars are omitted in order to maintain the clarity of the diagram)

study the partly recrystallized regions in many foils produced from materials annealed at different temperatures for various lengths of time.

Figure 5.16a shows a partly recovered area within a partially recrystallized sample, annealed at 700°C for 16 hr. Lot of dislocation activity can be seen within the elongated cells which must be a prelude to the formation of subgrains. The corresponding SAD pattern, shown in Figure 5.16b, indicates a (110) pattern, featuring the {100} superlattice spots. Dislocation activity leading to the formation of nearly clear subgrains is displayed in Figures 5.17a and 5.17b. An interesting observation at this stage was that the deformation twins, which were the major constituents of the substructure of the 73% cold rolled material, were very few in number and could be seen only rarely. Figures 5.18a and 5.18b show such regions in the sample annealed for 16 hr at 700°C, where well defined twins with sharp boundaries could still be observed. However, quite a bit of dislocation activity within the twinned regions as well as at the boundaries can be seen. In a few other regions also the twins were observed but their boundaries were not that well defined, and in fact, found to be quite diffuse (Figure 5.19a). Figure 5.19b shows another area where a high density of fine twins seems to have just disappeared on annealing.

The very early recrystallized grains found in thin foils of the alloy annealed for 16 hr at 700°C almost invariably show the presence of particles inside which look like discontinuous (cellular) precipitation (Figures 5.20a and 5.20b). Upon tilting the foil, some of the otherwise clear grains in Figure 5.20b were also found to contain these particles. SAD pattern taken from the cold rolled area to the left indicates that it is highly ordered (Figure 5.20c), the superlattice spots being quite strong. On the other hand, the SAD pattern taken from the subgrain cluster shows only weak superlattice spots (Figure 5.20d).

Figures 5.21a to 5.21c show different morphologies of the discontinuous precipitation occurring within recrystallized grains and subgrains formed from the highly deformed matrix. Figure 5.22a shows a recrystallized grain advancing into a cluster of small cells and subgrains.

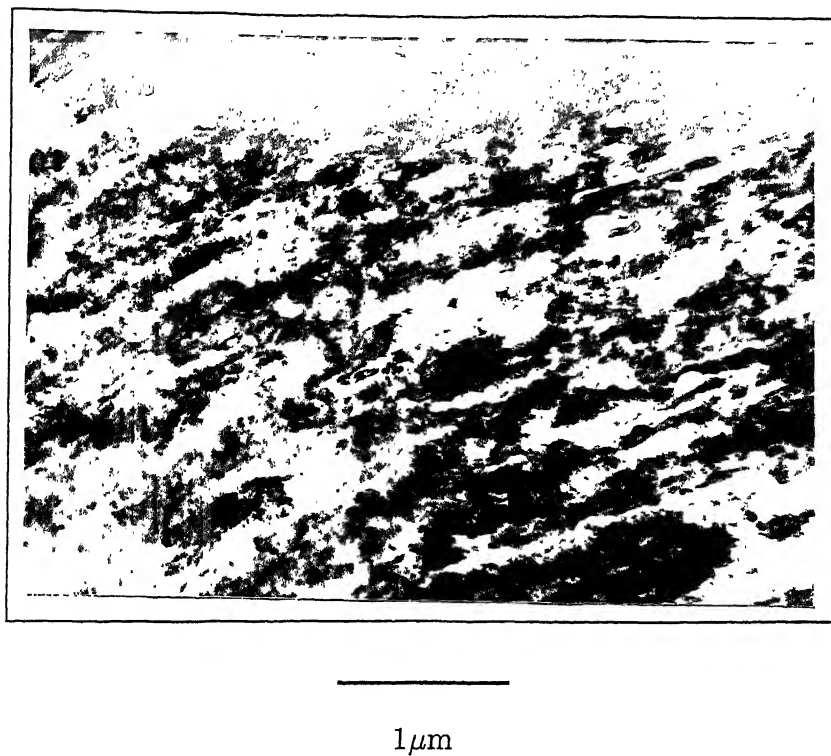


Figure 5.16a TEM micrograph showing a partly recovered area after annealing at  $700^{\circ}\text{C}$  for 16 hr

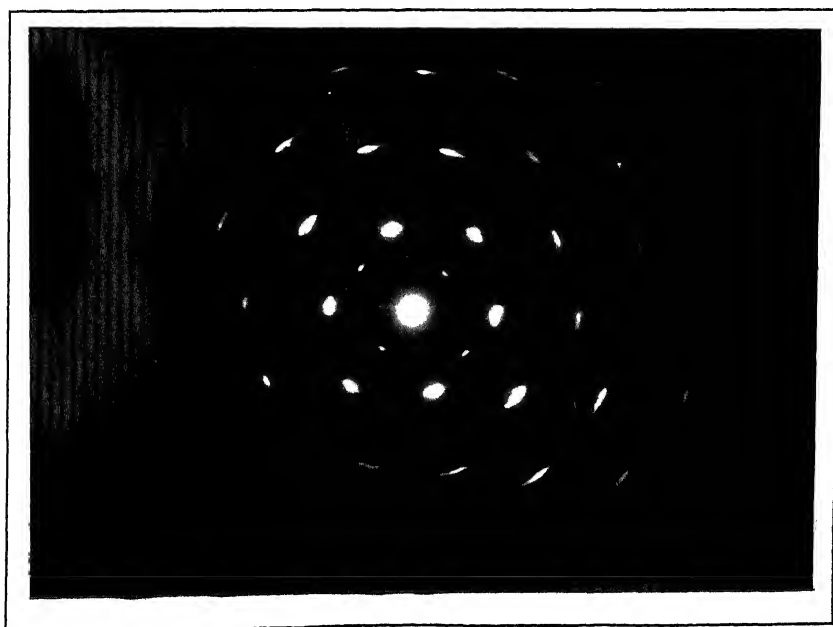
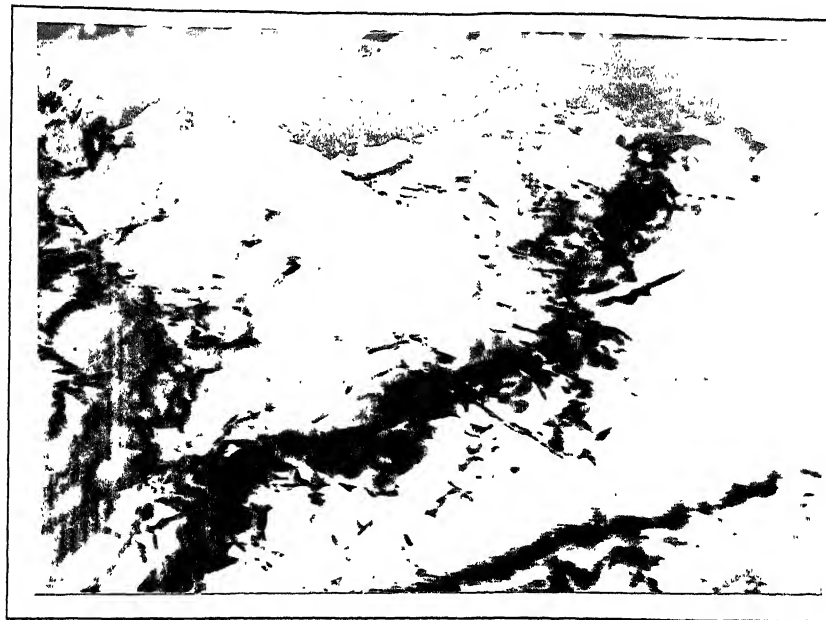


Figure 5.16b Corresponding SAD pattern of the area shown in Figure 5.16a



0.2 $\mu$ m

Figure 5.17a Recovery after annealing at 700°C for 16 hr



0.2 $\mu$ m

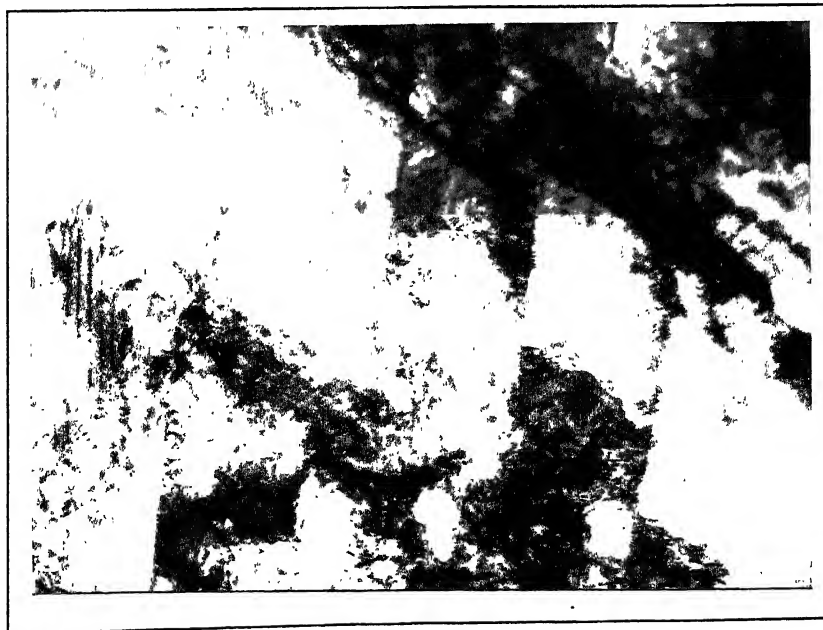
Figure 5.17b Formation of subgrain after annealing at 700 °C for 16 hr





0.5 $\mu$ m

Figure 5.18a Retained twin bands after annealing at 700°C for 16 hr



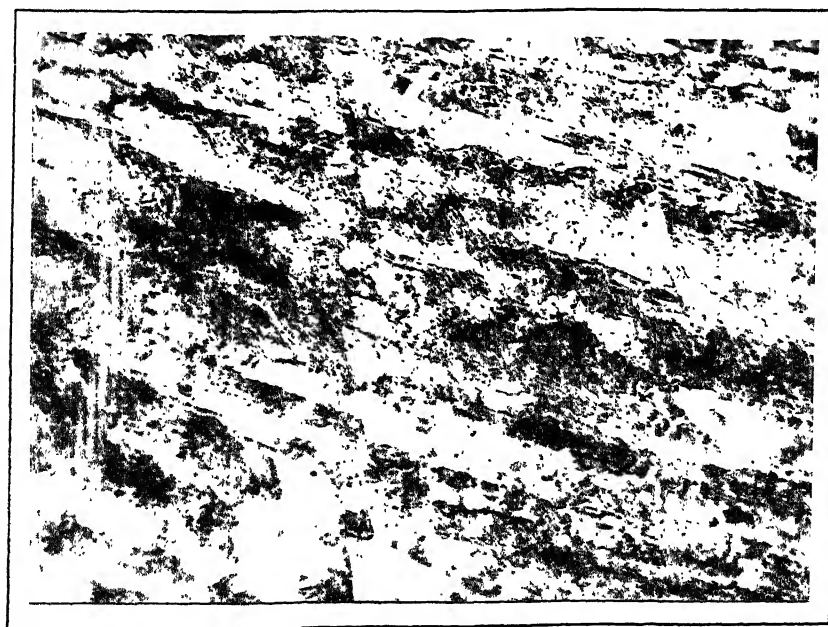
0.5 $\mu$ m

Figure 5.18b Retained twin bands after annealing at 700°C for 16 hr



2 $\mu$ m

Figure 5.19a TEM micrograph showing diffuse twin bands after annealing at 700°C for 16 hr



1 $\mu$ m

Figure 5.19b Partly recovered area showing the disappearance of fine twin bands after annealing at 700°C for 16 hr



1  $\mu\text{m}$

Figure 5.20a Cellular precipitation in the recrystallized subgrains  
(annealed at 700°C for 16 hr)



5  $\mu\text{m}$

Figure 5.20b Cluster of subgrains with cellular precipitates near  
the cold worked regions (annealed at 700°C for 16 hr)

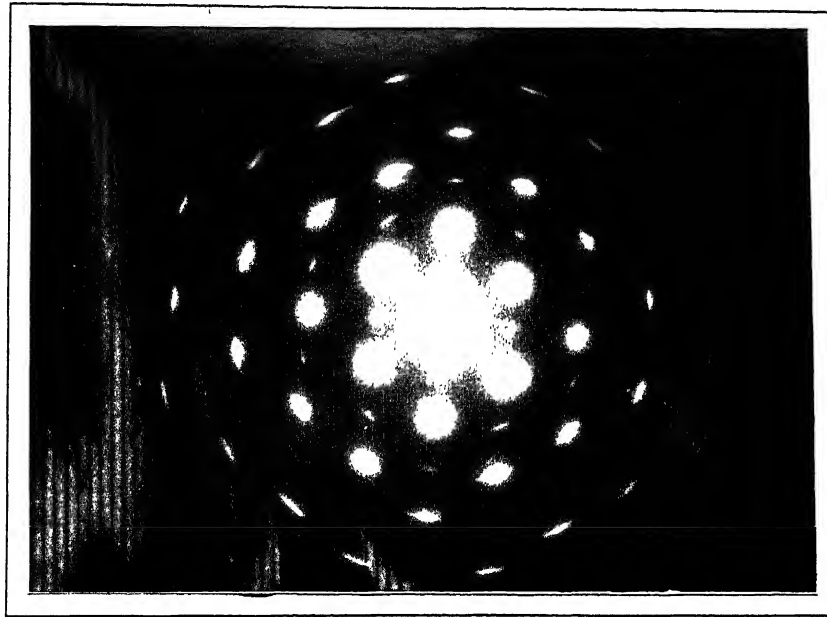
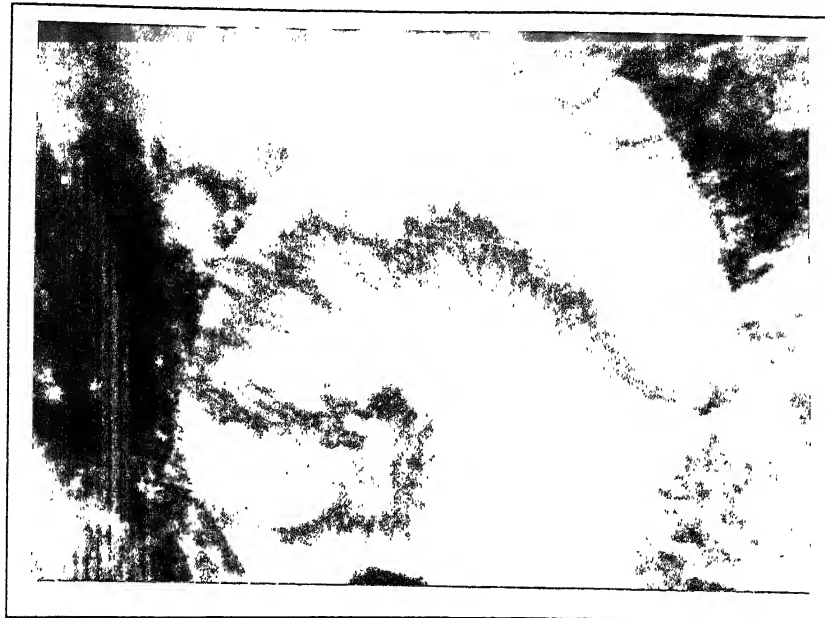


Figure 5.20c SAD pattern of the cold worked region in Figure 5.20b

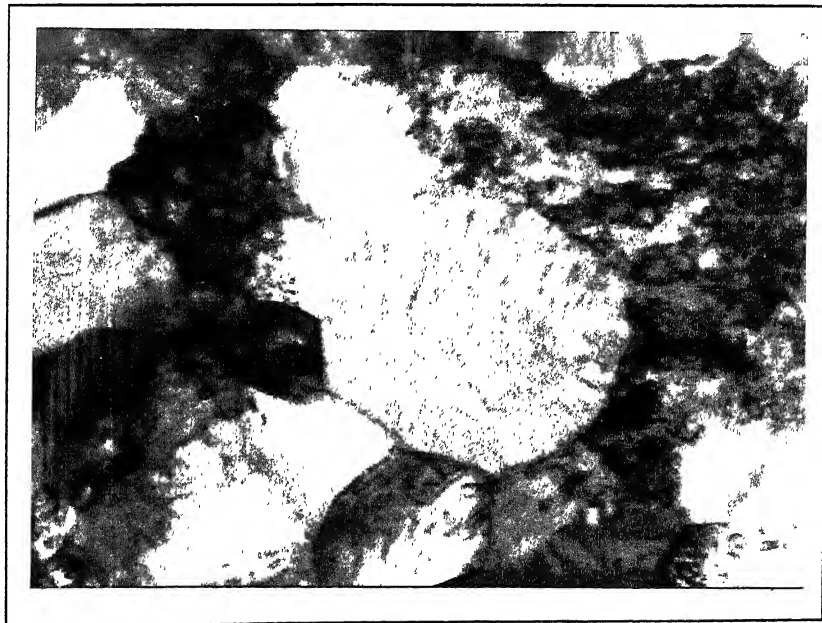


Figure 5.20d SAD pattern of the cluster of subgrains in Figure 5.20b



2 $\mu$ m

Figure 5.21a A recrystallized subgrain with cellular precipitates inside  
(annealed at 700°C for 16 hr)



2 $\mu$ m

Figure 5.21b A cluster of subgrains with cellular precipitates  
(annealed at 700°C for 16 hr)



1 μm

Figure 5.21c A subgrain with cellular precipitates grows by consuming the highly deformed matrix (*annealed at 700°C for 16 hr*)



0.5 μm

Figure 5.22a A recrystallized grain containing cellular precipitates advancing into a cluster of small cells and subgrains (*annealed at 700°C for 16 hr*)

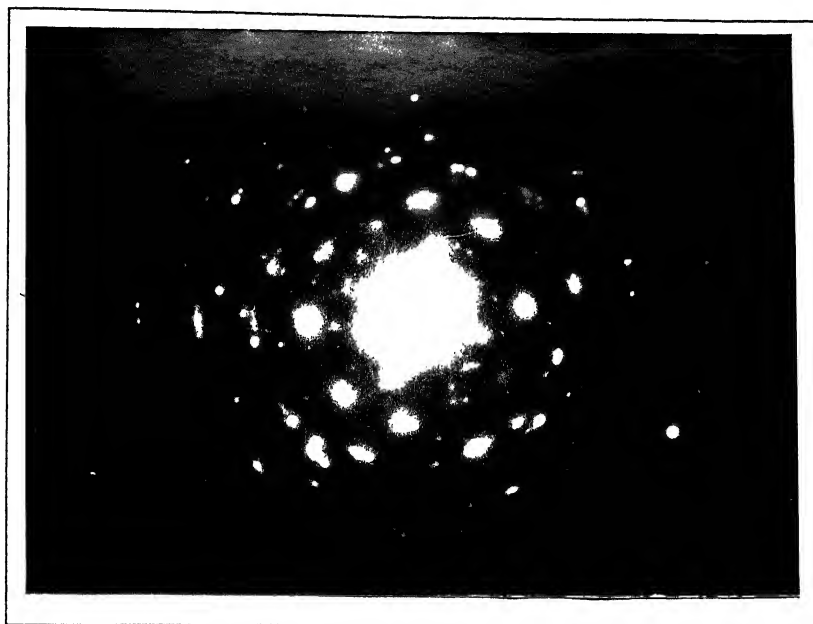


Figure 5.22b SAD pattern of the recrystallized grain in Figure 5.22a



Figure 5.22c SAD pattern of the cluster of subgrains and cells in Figure 5.22a

Inside the advancing grain, discontinuous precipitates can also be seen. SAD pattern taken from the big grain (Figure 5.22b) shows many spots making it almost impossible to index the pattern. SAD pattern taken from the cluster of subgrains and cells indicates a highly ordered region (Figure 5.22c). A high magnification micrograph showing the jagged interface between a growing recrystallized grain and the deformed matrix is presented in Figure 5.23a. This interface evidently is a reaction front involved in combined discontinuous precipitation and recrystallization. A similar microstructure is shown in Figure 5.23b which also features isolated precipitated particles along the interface between a recrystallized grain and the adjoining cold worked region. It is likely that these precipitates were the precursors for the formation of the cellular precipitates in the recrystallized grain when the combined recrystallization/precipitation front advanced into the cold worked region to the left. The morphology of the discontinuous precipitation inside a recrystallized grain is shown in Figure 5.24.

A group of two grains A and B and the adjacent cold rolled region are presented in Figure 5.25a. Discontinuous precipitates appear to grow from the interface between A and the cold worked matrix and then advance into the inside of the grain. The grain B also has some cellular precipitation inside. SAD pattern taken from the cold worked matrix, grain A and grain B are shown in Figures 5.25b, 5.25c and 5.25d respectively. All three regions appear to have an ordered  $L1_2$  structure.

Cellular precipitation has hardly been observed in recrystallized grains obtained by annealing at 900°C and above. Figure 5.26 shows a partially recrystallized region after annealing at 900°C for 5 min. A few small subgrains are featured in this micrograph, among which the one at the centre is seen to grow and consume the nearby deformed matrix. The inside of this subgrain is quite clean and no cellular precipitates could be observed even after tilting the foil. In another area of the same foil, a small recrystallized grain was observed embedded in the deformed matrix. A rod like feature was present in the grain (Figure 5.27a).





0.2  $\mu\text{m}$

Figure 5.23a Interface between a growing recrystallized grain and deformed matrix  
(annealed at 800°C for 30 min)



0.5  $\mu\text{m}$

Figure 5.23b Isolated dislocations and precipitate particles along the interface between  
a recrystallized grain and cold worked region (annealed at 800°C for 1 hr)

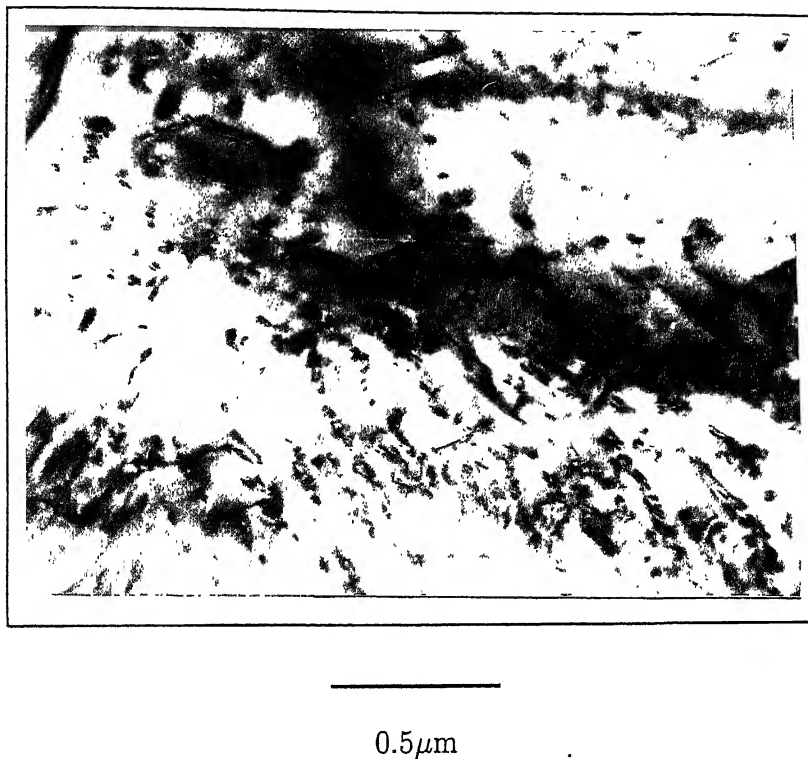
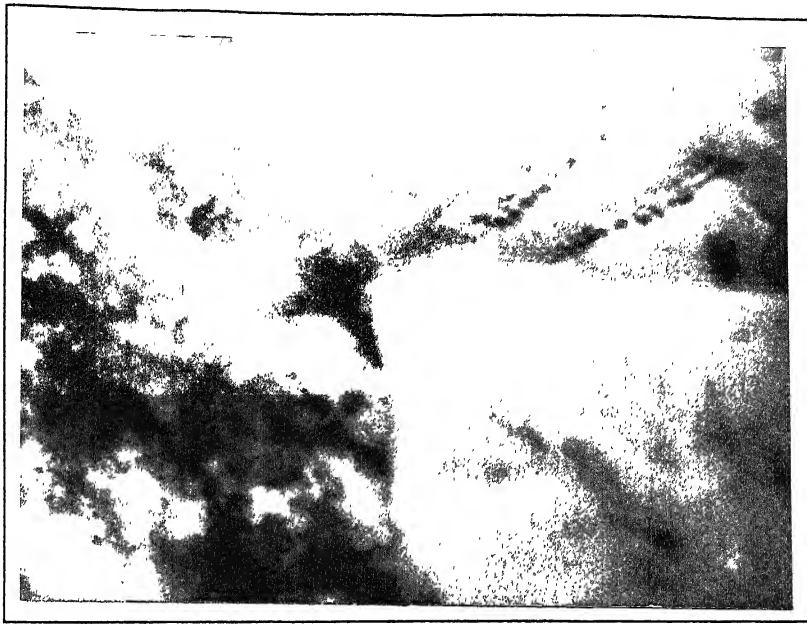


Figure 5.24 Morphology of the discontinuous precipitation inside a recrystallized grain  
(annealed at 800°C for 1 hr)



0.5  $\mu\text{m}$

Figure 5.25a Two recrystallized grains and the adjacent deformed region  
(annealed at 800°C for 30 min)

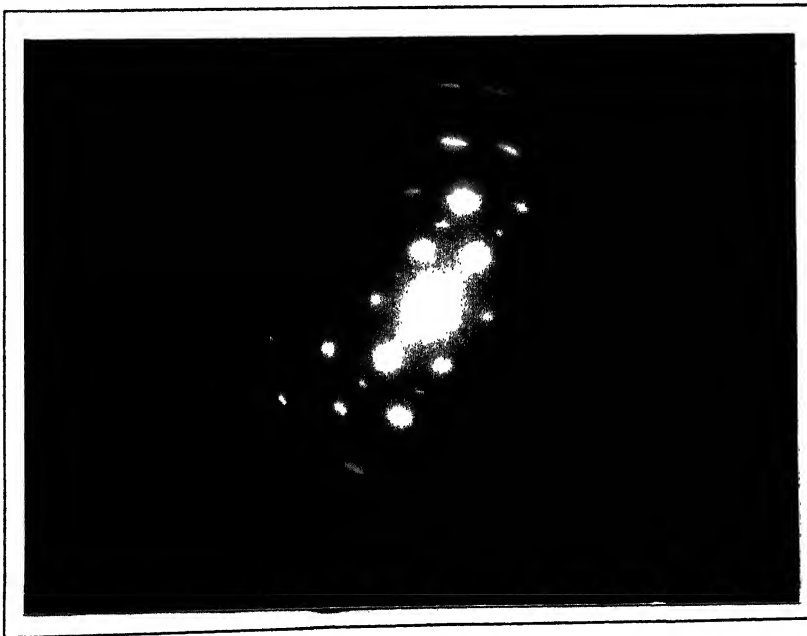


Figure 5.25b SAD pattern of the deformed region in Figure 5.25a

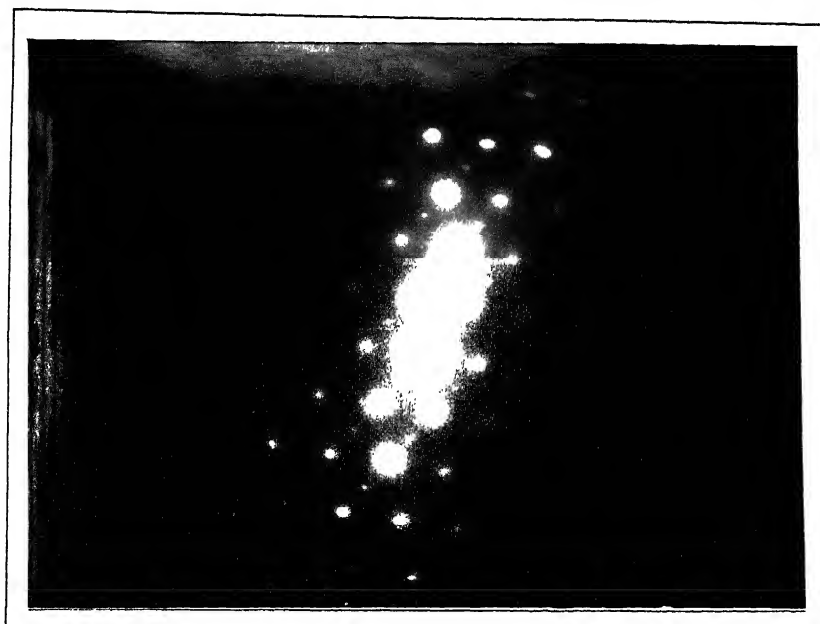


Figure 5.25c SAD pattern of the grain *A* in Figure 5.25a

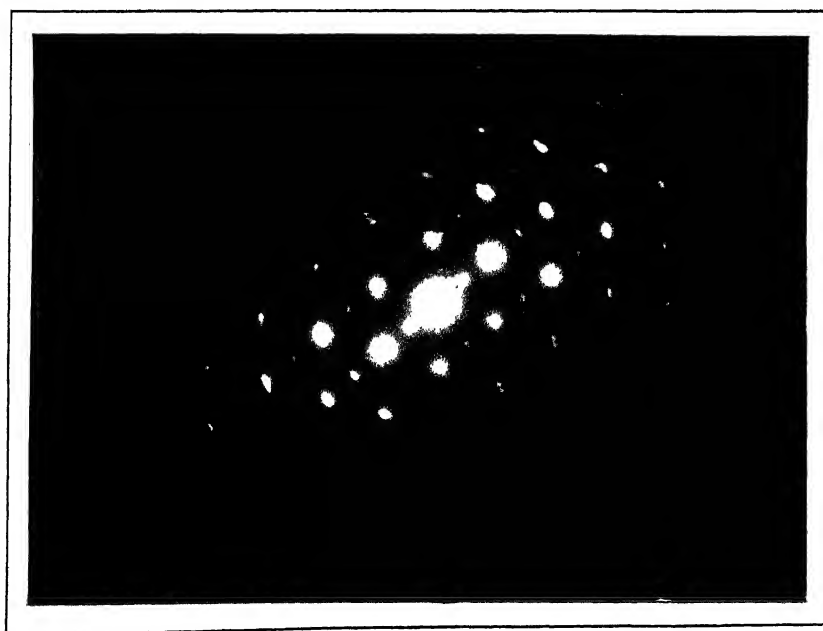


Figure 5.25d SAD pattern of the grain *B* in Figure 5.25a



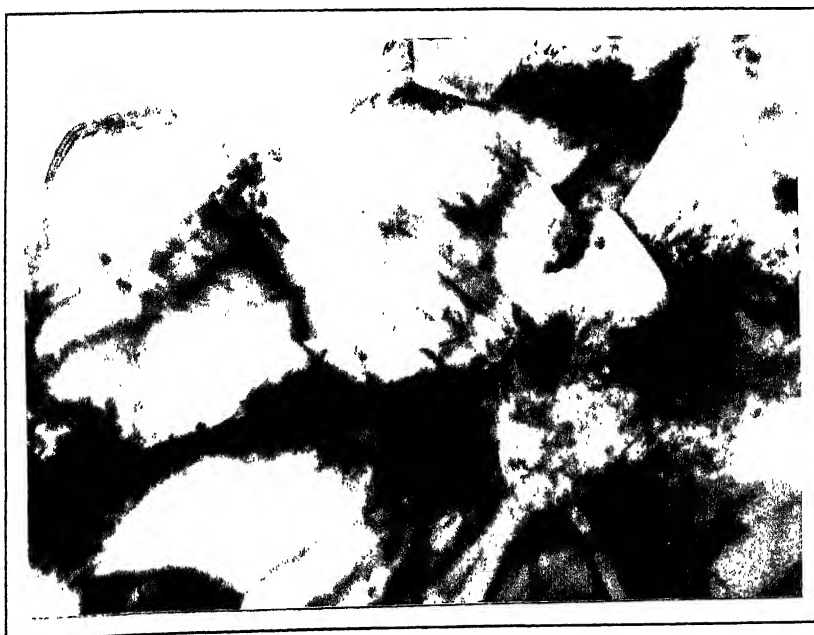
4 $\mu$ m

Figure 5.26 A partially recrystallized region after annealing at 900°C for 5 min



2 $\mu$ m

Figure 5.27a A small recrystallized grain with a rod-like feature inside  
(annealed at 900°C for 5 min)

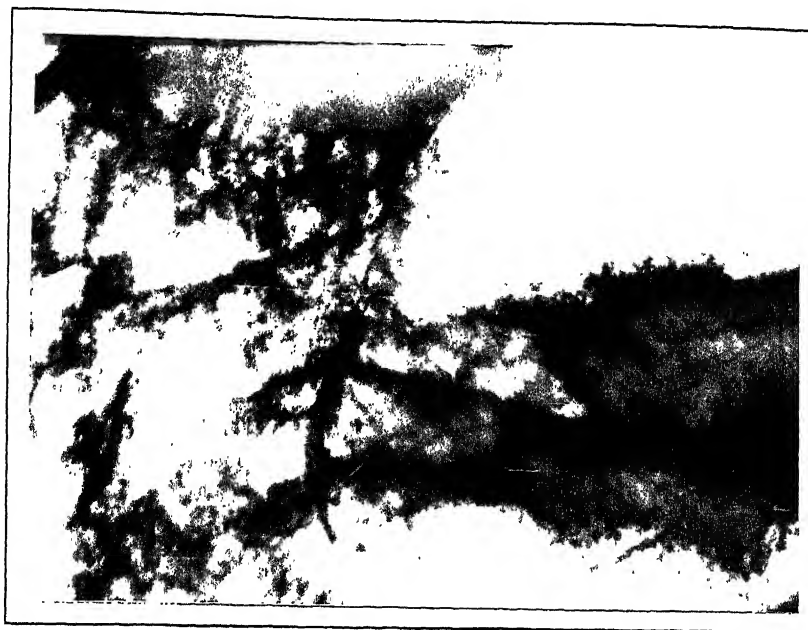


2 $\mu$ m

Figure 5.27b Recrystallized grains with fine striations  
(annealed at 900°C for 5 min)

Sometimes fine striations (faults) are found to be present in the new formed subgrains (Figure 5.27b). Some of the recrystallized grains at this stage also contain a high dislocation density (Figure 5.28a). The corresponding SAD pattern shows that this grain has an ordered  $L1_2$  structure (Figure 5.28b). Figure 5.29a also shows an ordered grain at this stage, which contains clear-cut paired dislocations inside. Some of the new formed recrystallized grains also show a high density of precipitate particles – but little evidence of any cellular precipitation (Figure 5.29b).

TEM micrographs obtained from the foils of the material annealed at 1000°C for 2 min show features similar to the ones obtained for the 900°C annealed sample. Most of the grains and subgrains appear quite clear inside and no cellular precipitation could be noticed even after tilting (Figure 5.30a). Figure 5.30b shows an area where a newly formed grain is in the process of migration in the surrounding deformed matrix. The corresponding SAD pattern (Figure 5.30c) shows that it has an ordered  $L1_2$  structure. Sometimes the recrystallized grains are found to contain a high density of faults (Figure 5.30d). High density of parallel dislocation lines are sometimes observed within the recrystallized grains (Figure 5.31a). Sometimes even the newly formed grains show distinct globular precipitation (Figure 5.31b). Some features similar to twins are also seen in this micrograph. Figure 5.32 shows a recrystallized grain with a high density of precipitate particles inside. A magnified image of another grain with precipitates is shown in Figure 5.33a. The corresponding SAD pattern (Figure 5.33b) indicates presence of an  $L1_2$  structure. Sometimes distinct Moiré fringe like features are also seen within the subgrains (Figure 5.34). Very often elongated band-like features are also noticed in the microstructure (Figure 5.35a). These have been identified as mainly  $\gamma$  regions as seen from the corresponding SAD (Figure 5.35b). A cluster of  $\gamma$  subgrains are seen in Figure 5.36a. Selected area diffraction patterns indicate that the boundaries between these subgrains are indeed low-angle boundaries. A magnified image of the subgrain A is presented in Figure 5.36b. The boundaries all around this show a lot



2 $\mu$ m

Figure 5.28a A recrystallized grain adjacent to the deformed matrix  
(annealed at 900°C for 5 min)

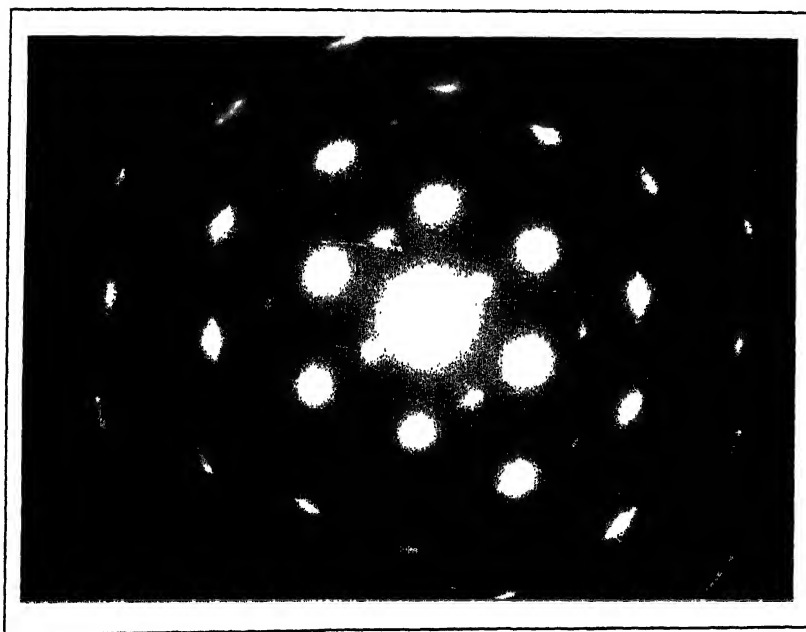


Figure 5.28b SAD pattern of the recrystallized grain in Figure 5.28a





0.5 $\mu$ m

Figure 5.29a Dislocations within a recrystallized grain  
(annealed at 900°C for 5 min)



0.5 $\mu$ m

Figure 5.29b Precipitations within a few recrystallized grains  
(annealed at 900°C for 5 min)



2 $\mu$ m

Figure 5.30a A cluster of recrystallized grains (*annealed at 1000°C for 2 min*)



4 $\mu$ m

Figure 5.30b Growth of the newly formed grains (*annealed at 1000°C for 2 min*)

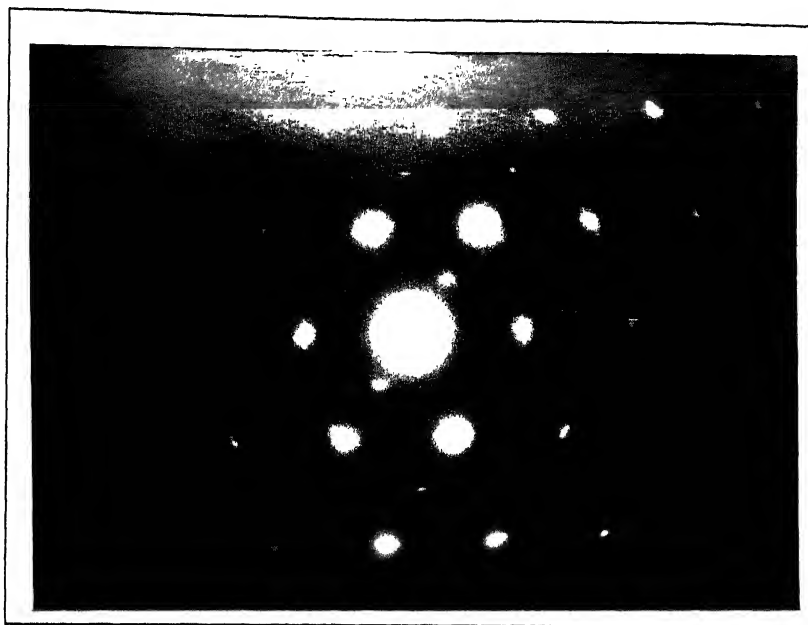
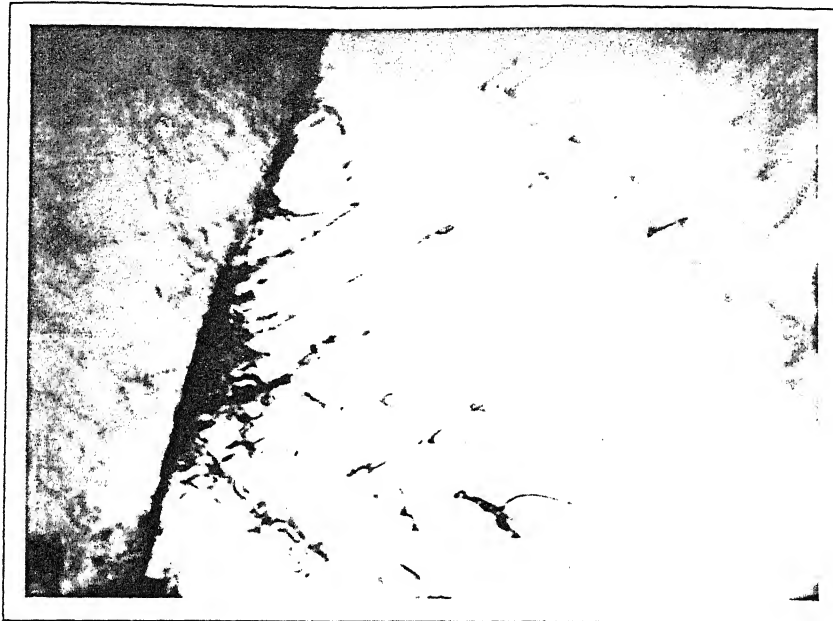


Figure 5.30c SAD pattern of the grain at the centre in Figure 5.30b



2 $\mu$ m

Figure 5.30d Faults within the recrystallized grains (annealed at 1000°C for 2 min)



1 $\mu$ m

Figure 5.31a Parallel dislocation lines within recrystallized grain  
(annealed at 1000°C for 2 min)



2 $\mu$ m

Figure 5.31b A partly recrystallized region after annealing at 1000°C for 2 min



1 $\mu$ m

Figure 5.32 A recrystallized grain with high density of globular precipitates inside  
(annealed at 1000°C for 2 min)



0.4 $\mu$ m

Figure 5.33a A grain with precipitates inside (*annealed at 1000°C for 2 min*)

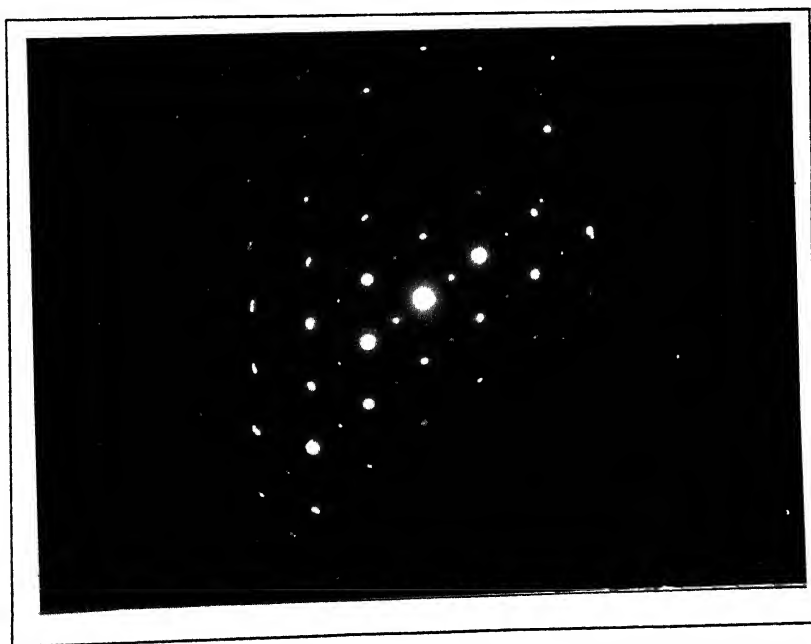
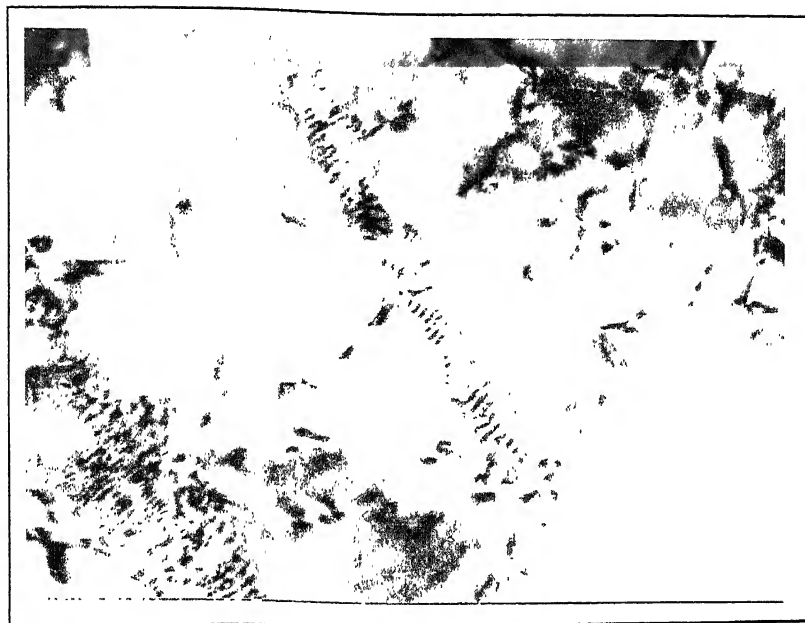
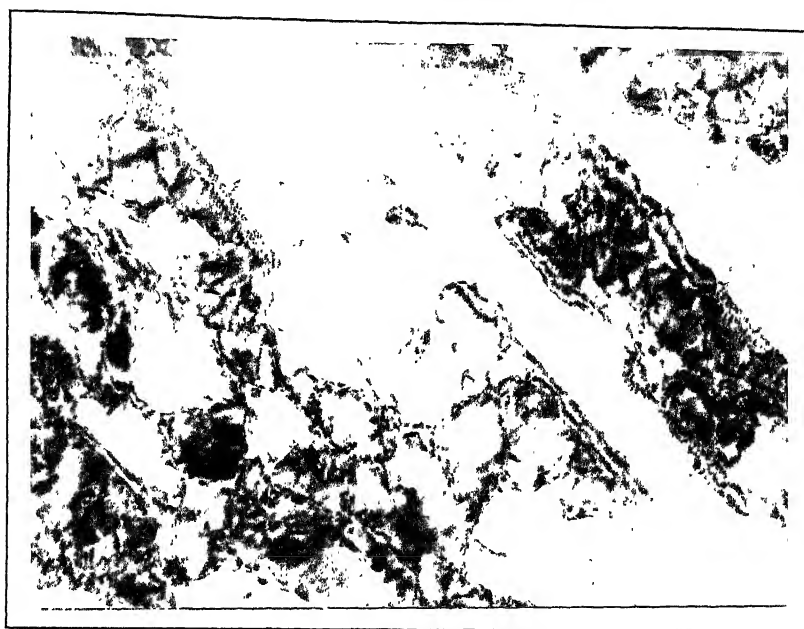


Figure 5.33b SAD pattern of the grain in Figure 5.33a



0.2 $\mu$ m

Figure 5.34 Moiré fringe like features developed during recovery  
(annealed at 1000°C for 2 min)



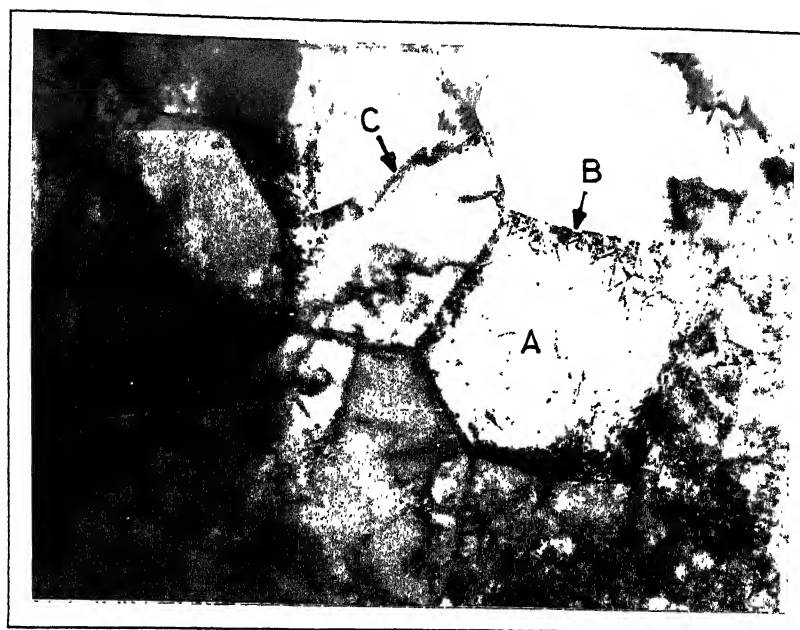
0.5  $\mu\text{m}$

Figure 5.35a Parallel bands of  $\gamma$  regions (annealed at  $1000^\circ\text{C}$  for 2 min)



Figure 5.35b SAD pattern of the thin foil area shown in Figure 5.35a





1 $\mu$ m

Figure 5.36a A cluster of  $\gamma$  subgrains (annealed at 1000°C for 2 min)



1 $\mu$ m

Figure 5.36b Magnified image of the subgrain A in Figure 5.35a



0.4 μm

Figure 5.36c Magnified image of the boundary *B* in Figure 5.35a



0.5 μm

Figure 5.36d Magnified image of the feature *C* in Figure 5.35a

of dislocation activity. A magnified image of the boundary at  $B$ , shown in Figure 5.36c, indicates that it is made up of a large number of parallel dislocation lines. A magnified image of the feature  $C$  in Figure 5.36a is presented in Figure 5.36d, which shows that it is some kind of a fault.

## 5.4 Recrystallization Kinetics

### 5.4.1 Analysis of Recrystallized Volume Fraction Data

The volume fraction of recrystallized grains with respect to time at five different annealing temperatures have been plotted in Figure 5.37. All the five plots depict a general sigmoidal behaviour. However, a careful examination reveals that above around 50% recrystallization, all the curves become much steeper. For a quantitative evaluation of the kinetics of recrystallization, all the data points in Figure 5.37 were fitted with the traditional Avrami [155] equation.

$$X = 1 - \exp[-kt^n] \quad (5.1)$$

where

$X$  is the recrystallized volume fraction,

$k$  is a temperature dependent constant, and

$n$  is the Avrami exponent.

The above equation can be expressed in the following manner also

$$1 - X = \exp[-kt^n]$$

$$\text{or, } \exp[kt^n] = \frac{1}{1 - X}$$

Taking double logarithm on both sides

$$\ln[\ln\{1/(1 - X)\}] = n \ln t + \ln k \quad (5.2)$$

Therefore, plotting the values of  $\ln[\ln\{1/(1 - X)\}]$  as a function of  $\ln t$  should produce a straight line. The slope of that straight line will directly give the value of  $n$ , the Avrami exponent, while the Y-axis intercept will give the value of  $\ln k$ . The constant  $k$  is directly related with the temperature and activation energy which can be expressed as

$$k = k_o \exp\left(-\frac{Q}{RT}\right) \quad (5.3)$$

where

$Q$  is the activation energy

$T$  is the absolute temperature of annealing

$R$  is the universal gas constant, and

$k_o$  is a constant

Taking logarithm of both sides of this equation

$$\ln k = \ln k_o - \frac{Q}{RT}$$

$$\text{or, } \ln k = -\frac{Q}{R} \cdot \frac{1}{T} + \ln k_o \quad (5.4)$$

According to this equation, plotting of  $-\ln k$  values (which are obtained using equation 5.2) as a function of  $1/T$  should produce a straight line again. The slope of that straight line will be equivalent to  $-Q/R$ , from which the activation energy,  $Q$ , can be determined easily.

Figure 5.38 shows the  $\ln[\ln\{1/(1 - X)\}]$  vs  $\ln t$  plots for all the annealing temperatures. Expectedly, clear cut straight line relationships were obtained, and least square technique

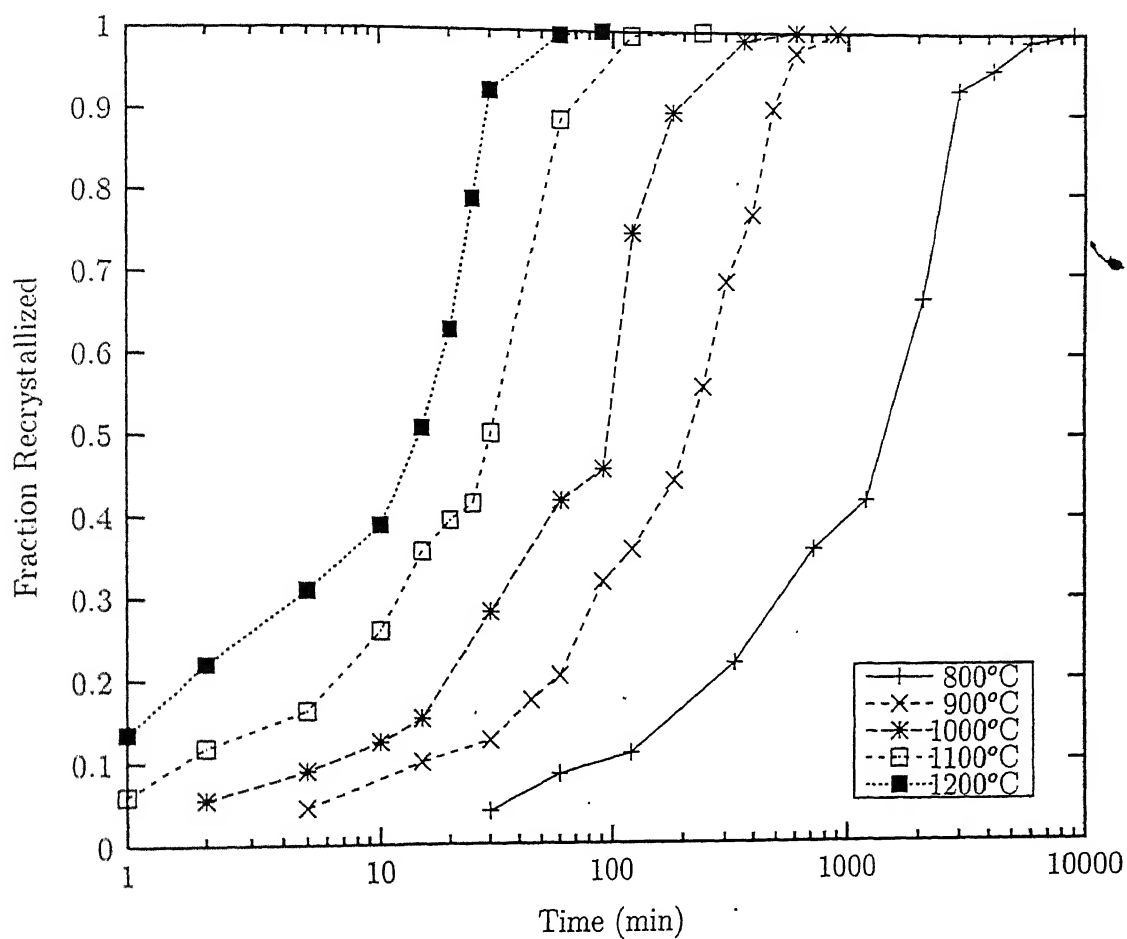


Figure 5.37 Plots of recrystallized volume fraction with annealing time at five annealing temperatures

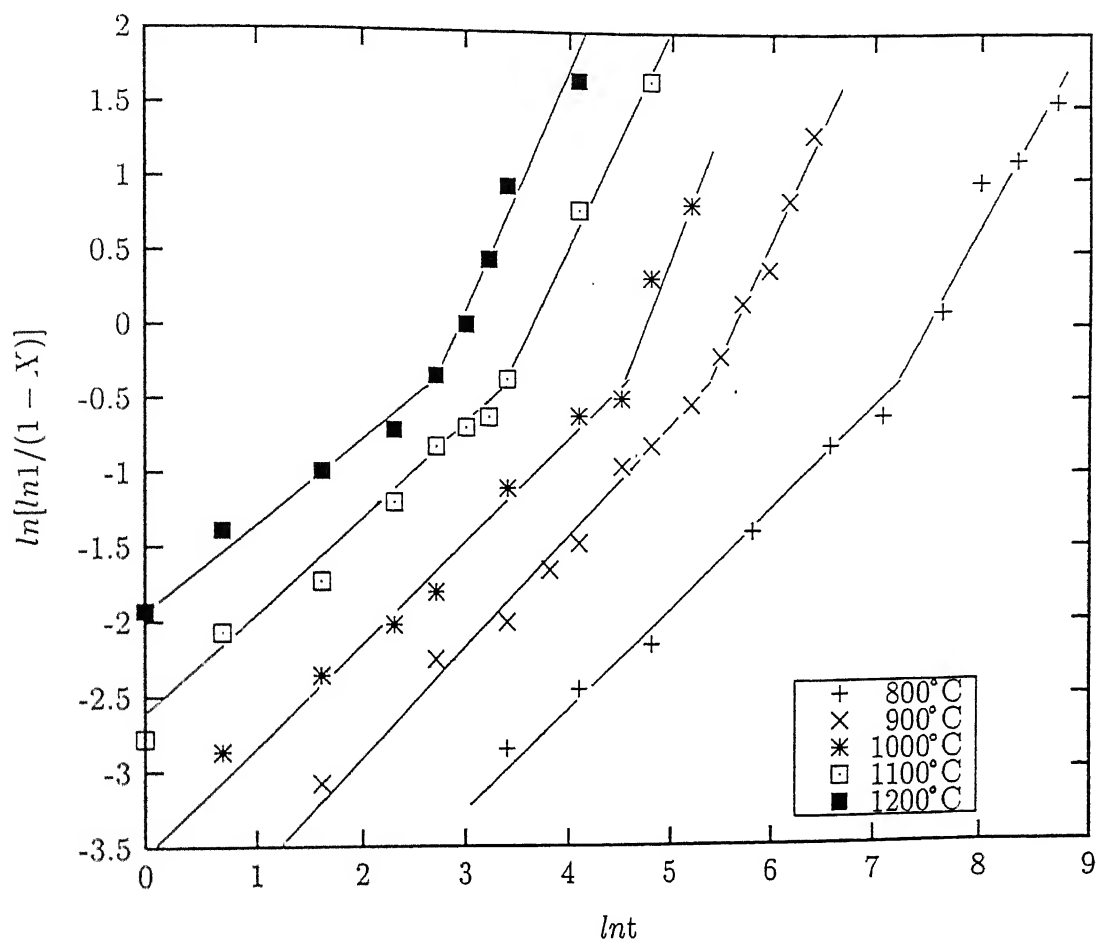


Figure 5.38 Plots of  $\ln[\ln\{1/(1-X)\}]$  versus  $\ln t$  at five annealing temperatures when  $X$  is the recrystallized volume fraction and  $t$  is the annealing time

was used to draw the lines. For a particular temperature, two straight lines were obtained at the two stages of recrystallization, and the abrupt change of slope was observed at around 50% recrystallization. Almost the same trend was maintained at all the five annealing temperatures. The  $n$  values determined from the slopes of these curves are listed in Table 5.2.

**Table 5.2**  $n$  values determined for all temperatures

Temperature	Stage 1 ( $X < 0.5$ )	Stage 2 ( $X > 0.5$ )
800°C	0.75	2.0
900°C	0.82	2.15
1000°C	0.81	2.0
1100°C	0.74	1.95
1200°C	0.68	1.95

The variation of  $n$  with temperature, at the two stages are shown in Figure 5.39. In the first stage, the value of  $n$  varied within 0.68 and 0.82, while in the second stage it varied between 1.95 and 2.15.

In order to determine the activation energy using equation 5.4, all the  $\ln k$  values determined from Figure 5.38 were plotted against inverse temperature. The  $\ln k$  values are listed in Table 5.3 and the corresponding plots are shown in Figure 5.40.

**Table 5.3** Calculated  $\ln k$  values at different temperatures

Temperature	Stage 1 ( $X < 0.5$ )	Stage 2 ( $X > 0.5$ )
800°C	-5.45	-14.33
900°C	-4.46	-11.12
1000°C	-3.64	-9.04
1100°C	-2.62	-7.63
1200°C	-1.83	-5.49

Plotting of the data points shown in Table 5.3 produced two curves which were nearly straight lines in nature. A close look at the data points of Stage 1 ( $X < 0.5$ ) in Figure 5.40 reveals that there is an abrupt change of slope at 1000°C. Therefore, actually two line

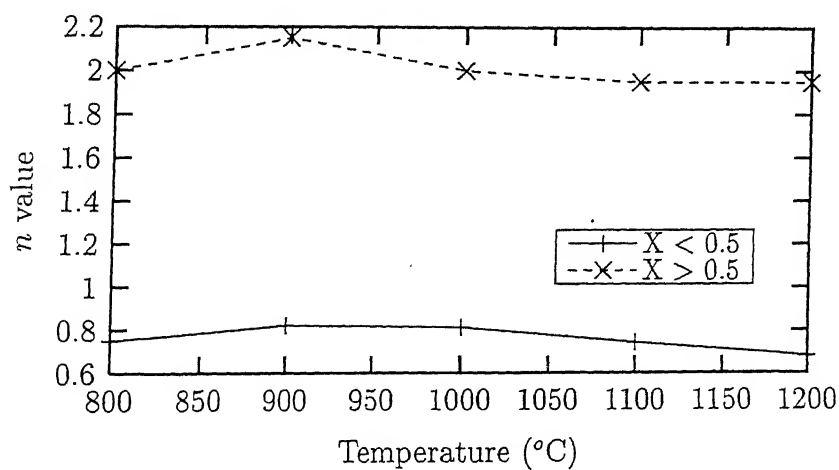


Figure 5.39 Variation of  $n$  (Avrami exponent) with temperature

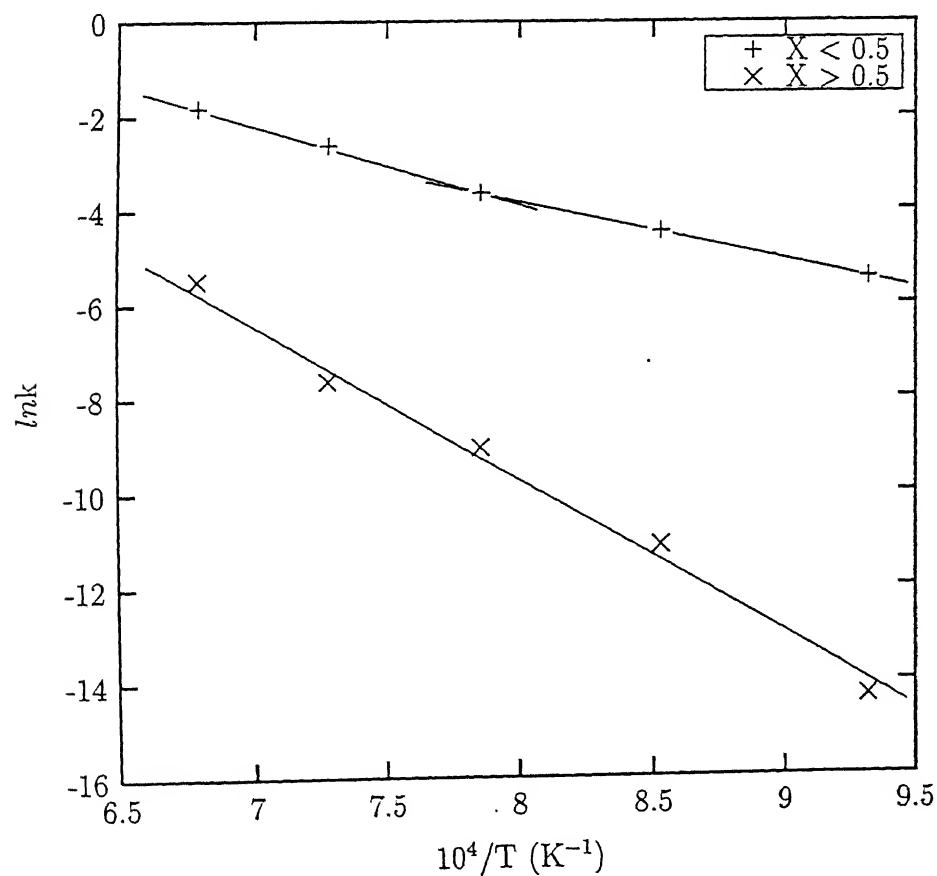


Figure 5.40  $\ln k$  versus  $1/T$  plots for the determination of activation energy



segments of different slopes were obtained for stage 1, whereas the stage 2 data points more or less followed a single straight line. The slopes of those lines were measured from which the activation energy values were calculated. These values are listed in Table 5.4. The temperature effect on the activation energy was not found to be very prominent. The  $Q$  value increased to some extent above  $1000^{\circ}\text{C}$  at stage 1, whereas it was almost constant throughout the temperature range at stage 2.

**Table 5.4** Activation energy ( $Q$ ) values at different stages

Stages	Temperature	$Q$ value (Activation energy)	
Stage 1 ( $X < 0.5$ )	$800^{\circ} - 1000^{\circ}\text{C}$	97.48 kJ/mole	Overall
	$1000^{\circ} - 1200^{\circ}\text{C}$	136.05 kJ/mole	117 kJ/mole
Stage 2 ( $X > 0.5$ )	$800^{\circ} - 1200^{\circ}\text{C}$	274.38 kJ/mole	

### 5.4.2 Analysis of Differential Scanning Calorimetry (DSC) Data

In order to isolate the heat effects due to the various reactions and transformations occurring in the alloy, samples cold rolled by different amounts were subjected to DSC measurements. All the DSC runs were carried out under identical conditions, and high purity well annealed platinum was used as the reference.

In the first run, platinum samples were used both in sample pan and reference pan. At this condition, the heat flow  $\dot{q}_1$ , to the reference relative to the sample pan can be expressed as

$$\dot{q}_1 = \frac{\phi}{E} [C_{h(R)} - C_{h(S)}] + \frac{\phi}{E} [C_{Pt(R)} - C_{Pt(S)}] \quad (5.5)$$

where,

$E$  is the calibration constant,

$\phi$  is the heating rate,

$C_{h(R)}$  and  $C_{h(S)}$  are the heat capacities of the reference and sample pans, respectively, and

$C_{Pt(R)}$  and  $C_{Pt(S)}$  are the heat capacities of Pt in the reference and sample pans, respectively.

In the second run, the Pt sample in the sample pan was replaced by the deformed  $Ni_3Al(B,Zr)$  specimen. At this situation, the heat flow  $\dot{q}_2$  can be expressed as

$$\dot{q}_2 = \frac{\phi}{E}[C_{h(R)} - C_{h(S)}] + \frac{\phi}{E}[C_{Pt(R)} - C_{A(S)}] + \frac{\dot{Q}M}{E} \quad (5.6)$$

where,

$C_{A(S)}$  is the heat capacity of the cold rolled sample,

$M$  is the mass of rolled sample, and

$\dot{Q}$  is the rate of heat evolution per unit mass due to transformation in the sample.

Subtraction of equation 5.5 from 5.6 gives

$$(\dot{q}_2 - \dot{q}_1) = \frac{\phi}{E}[C_{Pt(S)} - C_{A(S)}] + \frac{\dot{Q}M}{E} \quad (5.7)$$

When there is no reaction in the sample the rate of heat evolution,  $\dot{Q} = 0$ . The equation 5.7 then reduces to

$$(\dot{q}_2 - \dot{q}_1)_{\dot{Q}=0} = \frac{\phi}{E}[C_{Pt(S)} - C_{A(S)}] \quad (5.8)$$

Subtraction of equation 5.8 from 5.7 gives

$$\frac{\dot{Q}M}{E} = [(\dot{q}_2 - \dot{q}_1) - (\dot{q}_2 - \dot{q}_1)_{\dot{Q}=0}] \quad (5.9)$$

This equation is used to obtain the value of  $\frac{\dot{Q}M}{E}$  as a function of temperature. The thermograms of the DSC runs were recorded with the help of a standard software package.

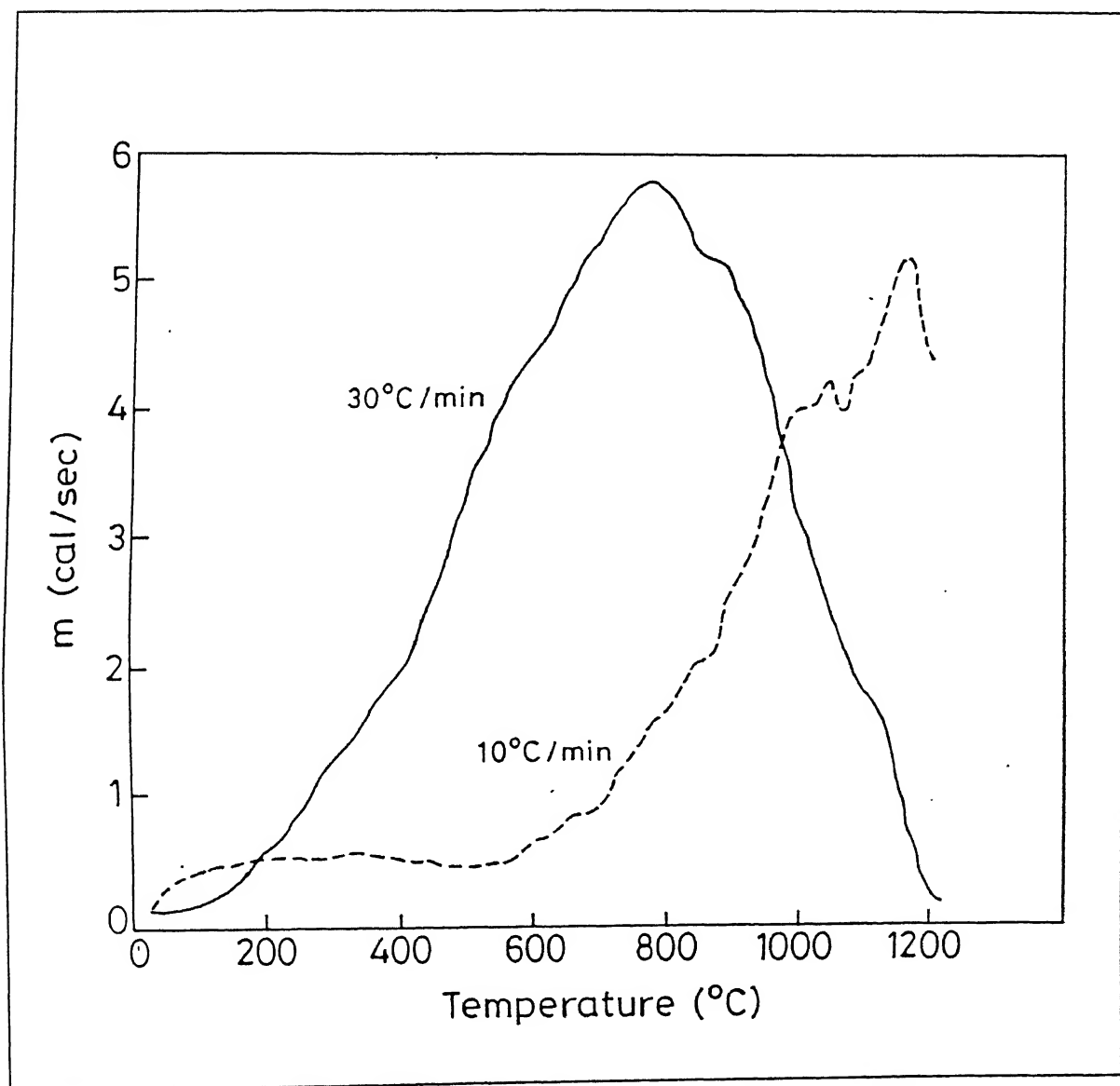


Figure 5.41 DSC thermograms of 73% cold rolled material at the two heating rates  $30^{\circ}\text{C/min}$  and  $10^{\circ}\text{C/min}$

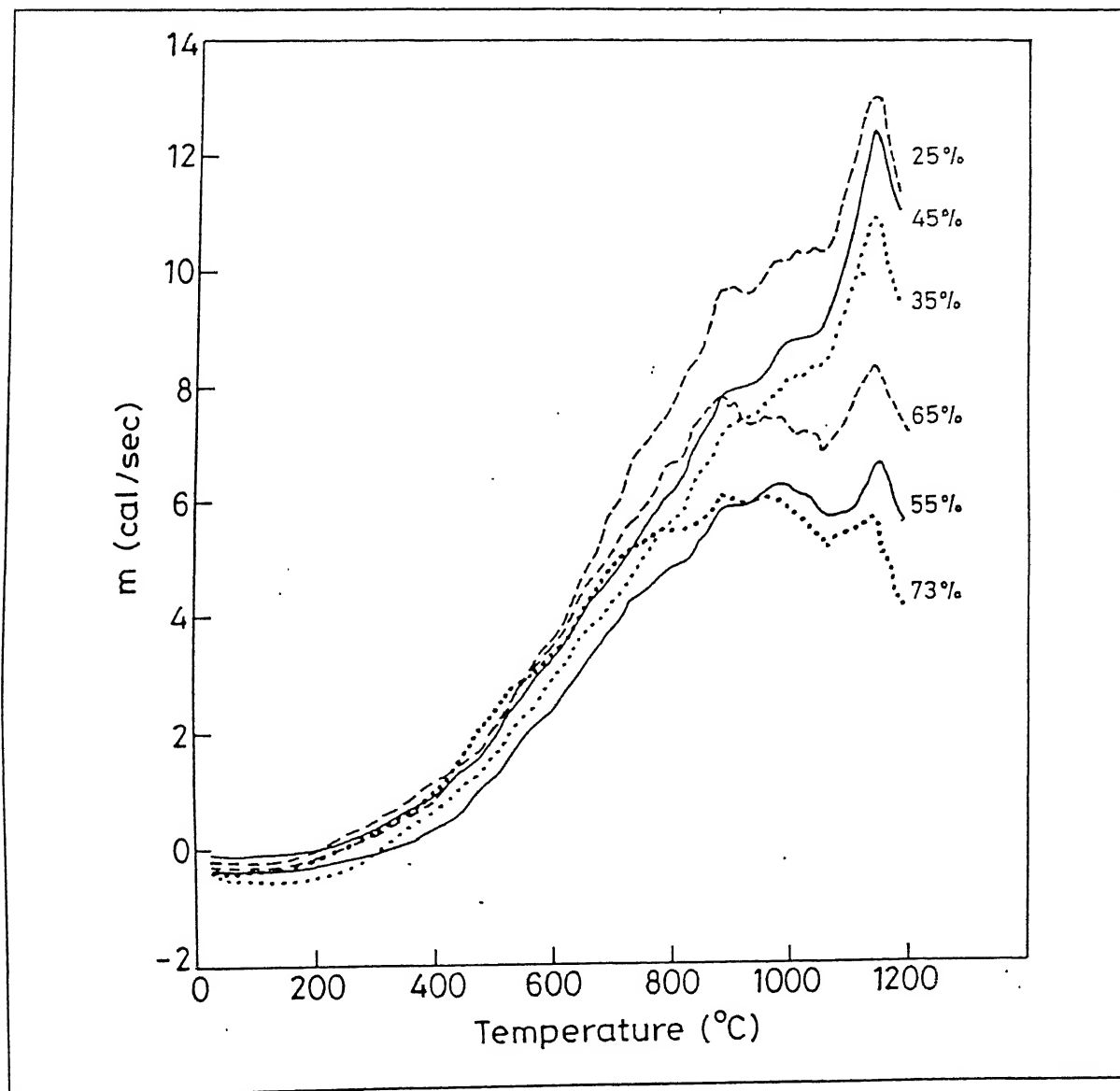


Figure 5.42 DSC thermograms of all the cold rolled samples at a fixed heating rate 20°C/min

To start with, two DSC runs were conducted on the 73% rolled sample, using two heating rates, namely, 30°C/min and 10°C/min respectively. These two thermograms are shown in Figure 5.41. At the higher heating rate, all the transformations took place abruptly. As a result, the  $\frac{\dot{Q}_M}{E}$  vs  $T$  curve appeared as a big hump from which the different stages could not be distinguished. At the lower rate of heating, the transformations were too sluggish, and the whole plot shifted towards the right end. An intermediate heating rate of 20°C/min was therefore chosen and all the subsequent DSC runs were carried out using this. The corresponding thermograms are shown in Figure 5.42.

A qualitative study of the thermograms reveals that there is a similarity in the shape for the 25%, 35% and 45% rolled materials; all three show a gradually increasing slope with temperature and a small peak at the end. The shapes of the thermograms for the 55%, 65% and 73% rolled materials are again similar among themselves, but somewhat different from the three previous ones. Instead of showing a single small peak at the end, they exhibit some kind of a plateau region containing a couple of short peaks. The temperature corresponding to the final peak in all the above thermograms lies between 1150° - 1175°C. Another interesting feature is that detectably smaller amount of heat evolution can be associated with the thermograms of the 55%, 65% and 73% rolled materials, as compared to the 25%, 35% and 45% rolled samples.

## 5.5 Textural Changes During Annealing

In an attempt to follow the texture development during annealing, both pole figure and ODF measurements were carried out from samples 73% cold rolled and then annealed at 900°C for various durations of time. In this way it was possible to characterize the texture as it developed during the entire range of recrystallization process. Figures 5.43a to 5.43g represent the (111) pole figures and the Figures 5.44a to 5.44g represent the corresponding ODFs for the seven different samples annealed at 900°C for time ranging between 4 min to

25 hr.

It is clear from the above Figures that the pole figures (Figures 5.43a to 5.43g) of all the annealed samples look quite similar and all of them signify a rather weak texture. In order to have more insight the ODFs were studied next. A strong Bs component, along with a Goss component could be identified in the ODF plot after 4 min of annealing (Figure 5.44a). These components weakened after 10 min (Figure 5.44b). A rotated Goss component with an orientation very near to  $\{011\} \langle 111 \rangle$  could be seen after 1 hr (at  $\phi_2 = 0^\circ$  of Figure 5.44c), which also weakened after 3 hr (Figure 5.44d). Another component  $\{123\} \langle 121 \rangle$  developed at the final stage (Figures 5.44e to 5.44g), which was basically a rotated variation of the S  $\{123\} \langle 634 \rangle$  component.

The variations of textural intensity with annealing time can be described with the help of the  $\beta$ -fibre plots. Figure 5.45 shows the  $\beta$ -fibre (maximum density) plots for the seven annealed samples as well as for the 73% rolled sample (starting material). Corresponding volume fractions of recrystallization are listed in Table 5.5. A simultaneous close inspection of Figure 5.45 and Table 5.5 reveals the following:

- Both Cu and Bs components decreased at the very initial stages, and a situation close to the equilibrium was achieved after 1 hr of annealing. Beyond that stage, the overall texture did not undergo any significant change.
- The intensity of the Cu component decreased more rapidly as compared to that of the Bs component. The intensity of the former became quite low after 4 min of annealing while the Bs component was not totally suppressed even after 1 hr of annealing.

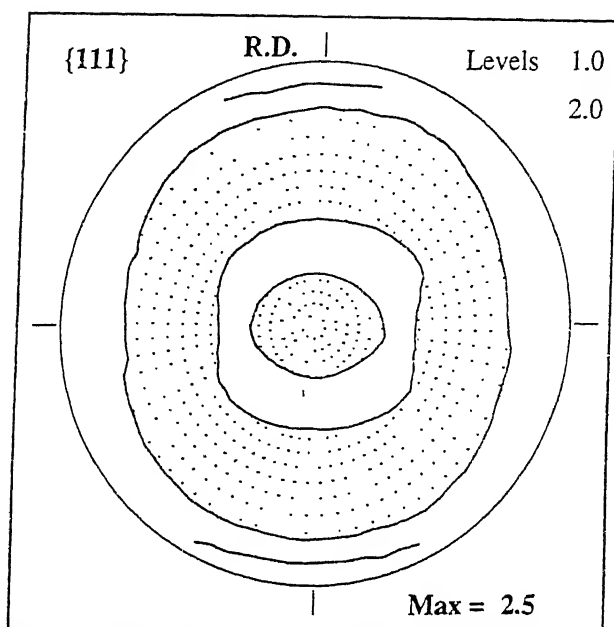


Figure 5.43a {111} pole figure after annealing at 900°C for 4 min

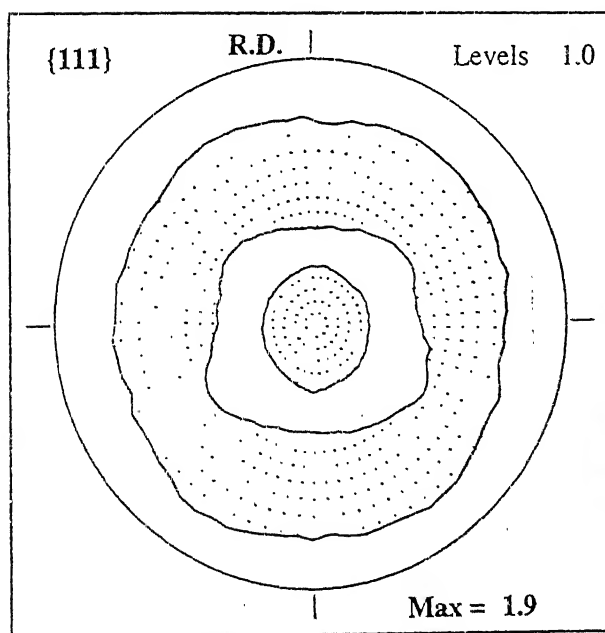


Figure 5.43b {111} pole figure after annealing at 900°C for 10 min

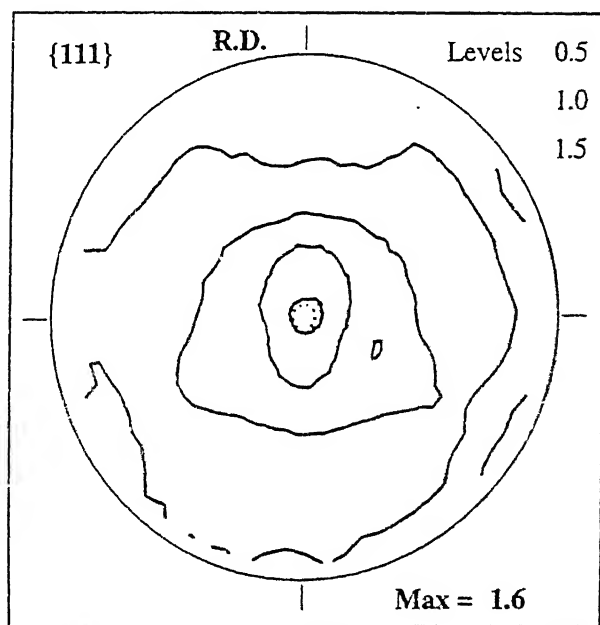


Figure 5.43c {111} pole figure after annealing at 900°C for 1 hr

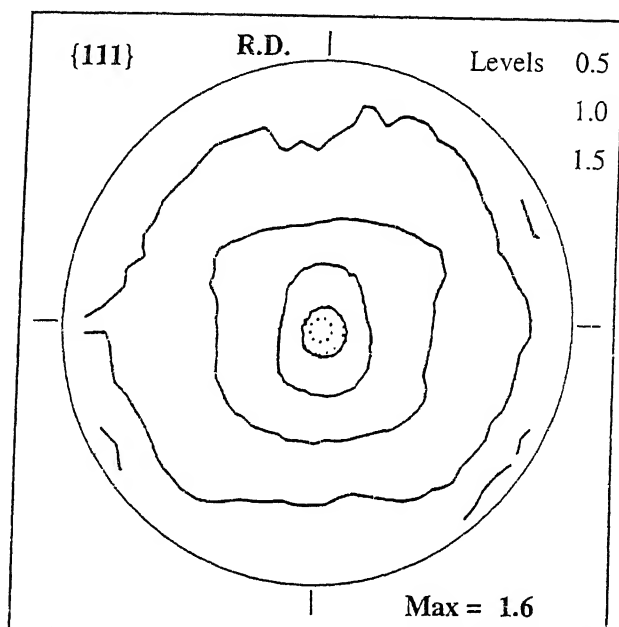


Figure 5.43d {111} pole figure after annealing at 900°C for 3 hr

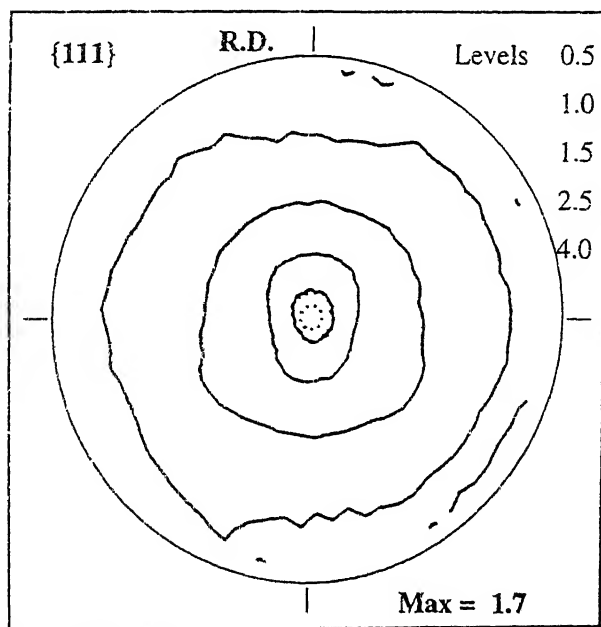


Figure 5.43e {111} pole figure after annealing at 900°C for 10 hr



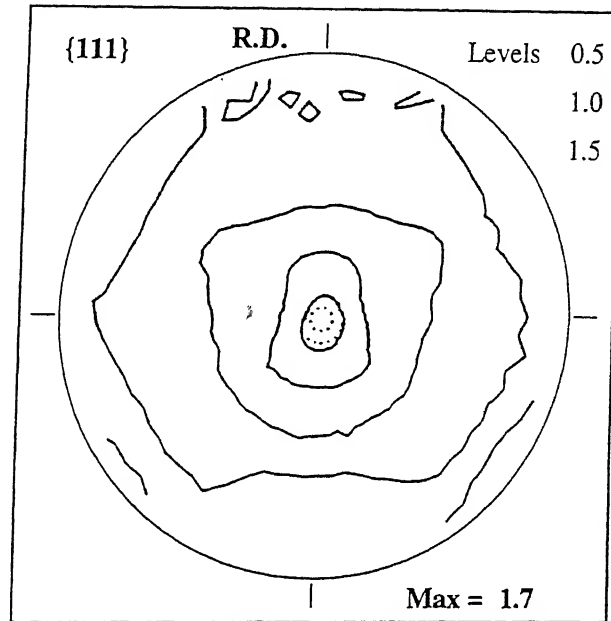


Figure 5.43f {111} pole figure after annealing at 900°C for 15 hr

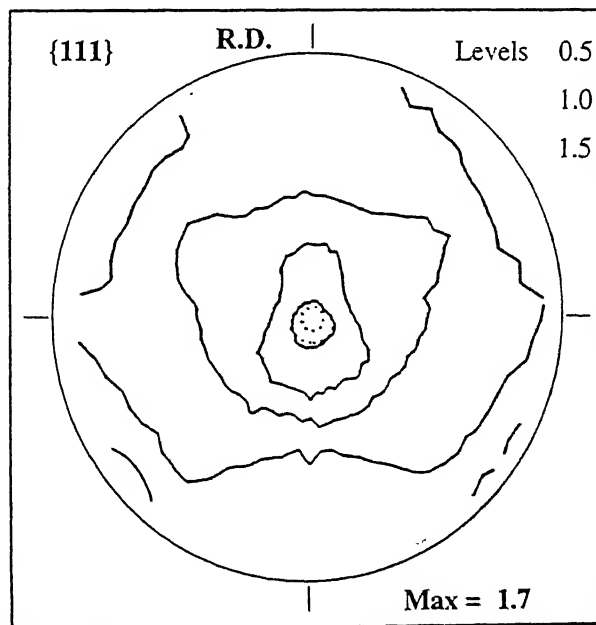


Figure 5.43g {111} pole figure after annealing at 900°C for 25 hr

52. E.M. Schulson, T.P. Weihs, I. Baker, H.J. Frost and J.A. Horton, *Scripta Metall.*, 19 (1985), p. 1497.
53. A. Fujita, T. Matsumoto, M. Nakamura and Y. Takeda, *MRS Symp. Proc.*, 133 (1989), p. 573.
54. T.P. Weihs, V. Zinoviev, D.V. Viens and E.M. Schulson, *Acta Metall.*, 35 (1987), p. 1109.
55. E.M. Schulson, T.P. Weihs, D.V. Viens and I. Baker, *Acta Metall.*, 33 (1985), p. 1587.
56. M. Takeyama and C.T. Liu, *Acta Metall.*, 36 (1988), p. 1241.
57. M.S. Kim, S. Hanada, S. Watanabe and O. Izumi, *Jr. Mater. Sci.*, 25 (1990), p. 1590.
58. T.S. Srivatsan and S. Sriram, *Jr. Mater. Sci.*, 27 (1992), p. 4974.
59. S. Ochiai, Y. Mishima, M. Yodogawa and T. Suzuki, *Trans. Jpn. Inst. Met.*, 27 (1986), p. 32.
60. Y. Mishima, S. Ochiai, M. Yodogawa and T. Suzuki, *Trans. Jpn. Inst. Met.*, 27 (1986), p. 41.
61. Y. Mishima, S. Ochiai, N. Hamao, M. Yodogawa and T. Suzuki, *Trans. Jpn. Inst. Met.*, 27 (1986), p. 648.
62. T. Srivatsan, S. Anand, S. Sriram and T.S. Sudarshan, *Jr. Mater. Sci.*, 27 (1992), p. 5939.
63. P.A. Flinn, *Trans. AIME*, 218 (1960), p. 145.
64. C. Lall, S. Chin and D. P. Pope, *Metall. Trans.*, 10A (1979), p. 1323.
65. Y. Umakoshi, D.P. Pope and V. Vitek, *Acta Metall.*, 32 (1984), p. 449.
66. B.H. Kear and H.G.F. Wilsdorf, *Trans. AIME*, 224 (1962), p. 382.
67. J.B. Cohen and M.B. Bever, *Trans. AIME*, 218 (1960), p. 155.
68. S. Takeuchi and E. Kuramoto, *Acta Metall.*, 21 (1973), p. 415.

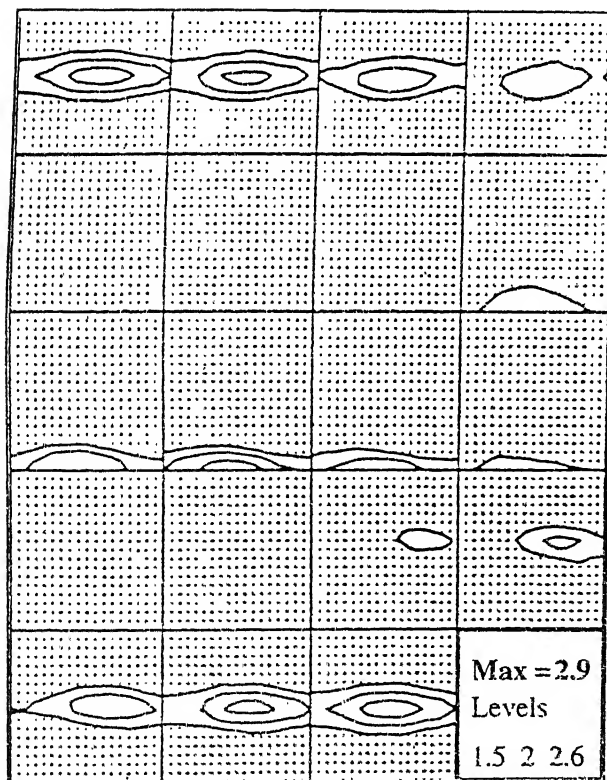
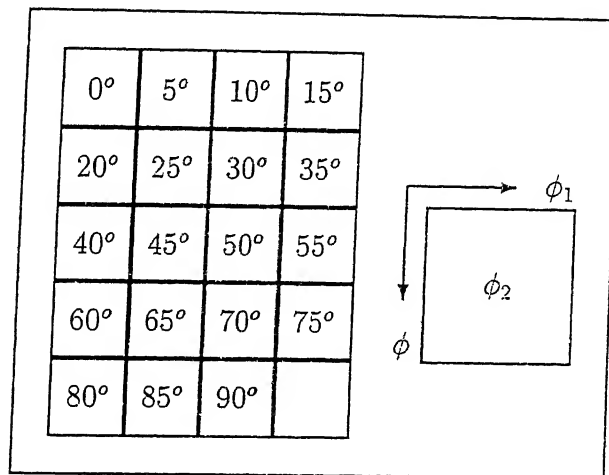


Figure 5.44b ODF after annealing at 900°C for 10 min

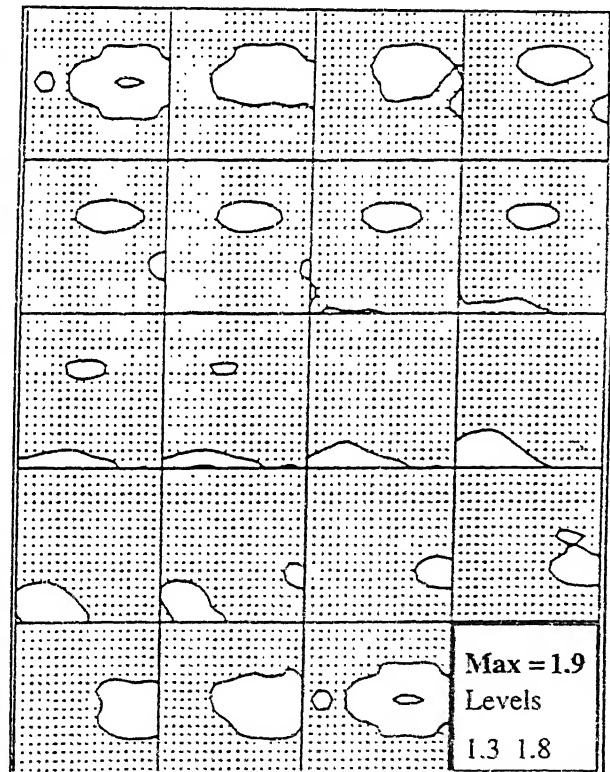


Figure 5.44c ODF after annealing at 900°C for 1 hr

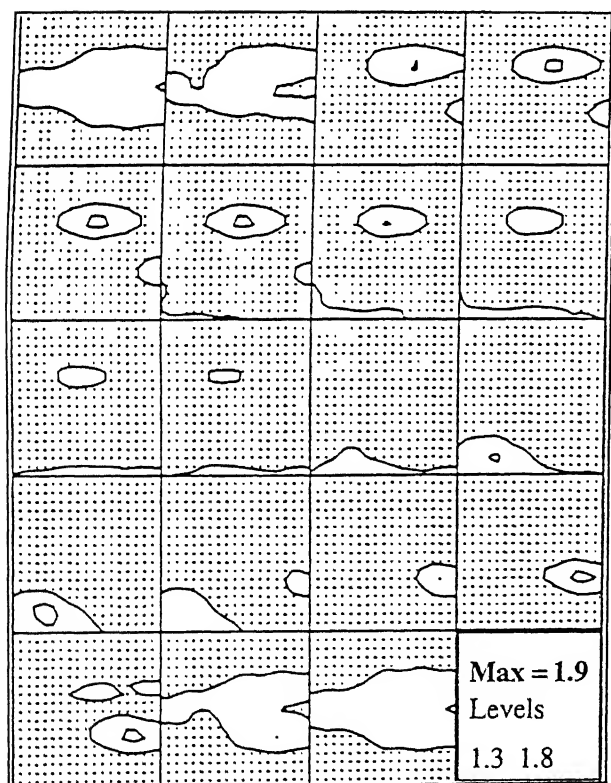
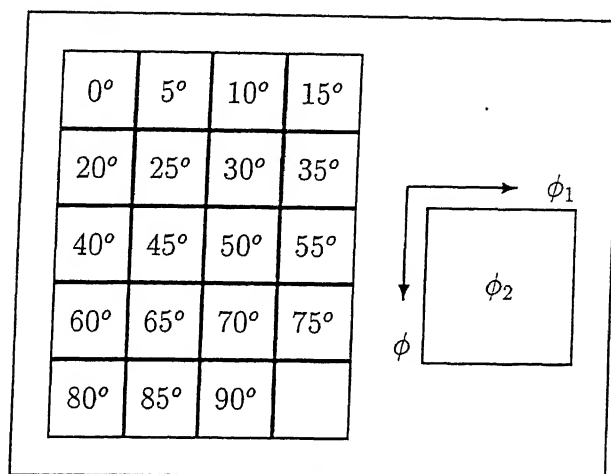


Figure 5.44d ODF after annealing at 900°C for 3 hr

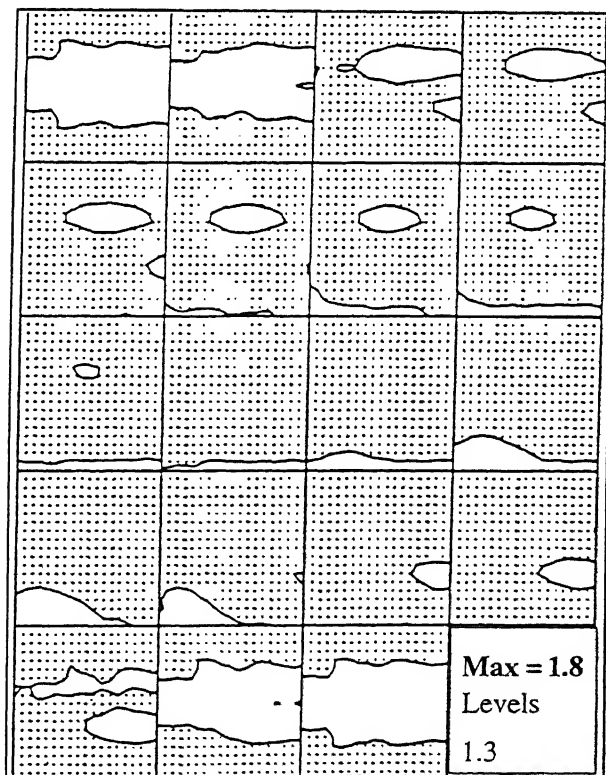


Figure 5.44e ODF after annealing at 900°C for 10 hr

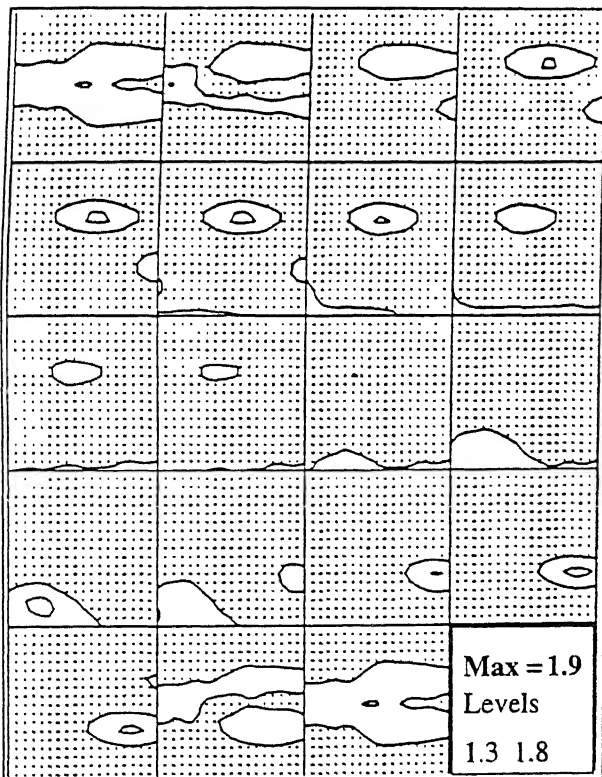
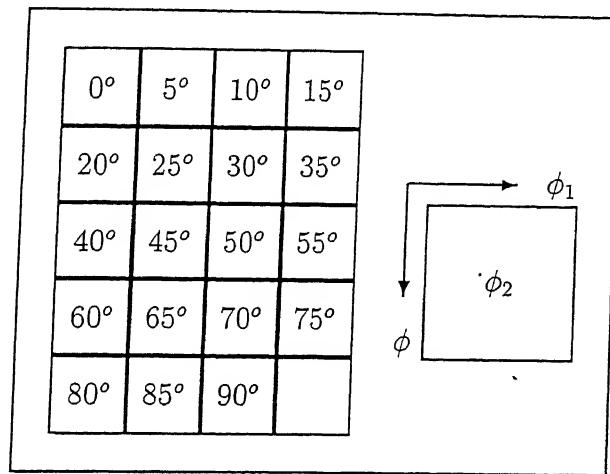


Figure 5.44f ODF after annealing at 900°C for 15 hr

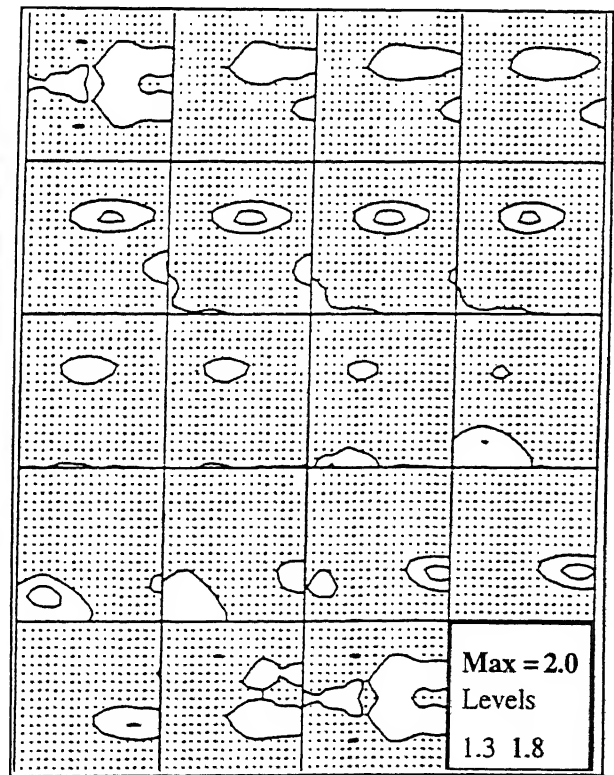


Figure 5.44g ODF after annealing at 900°C for 12 hr

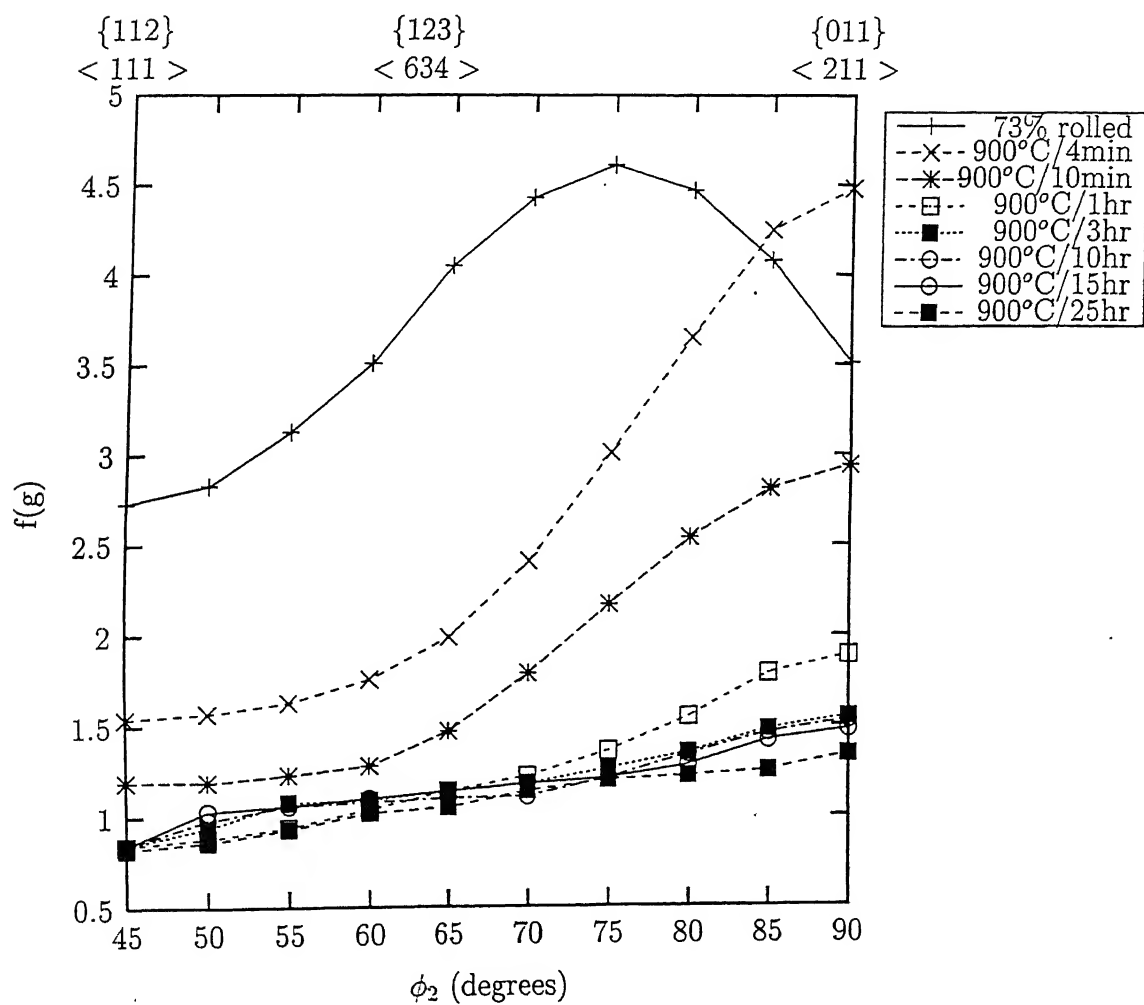
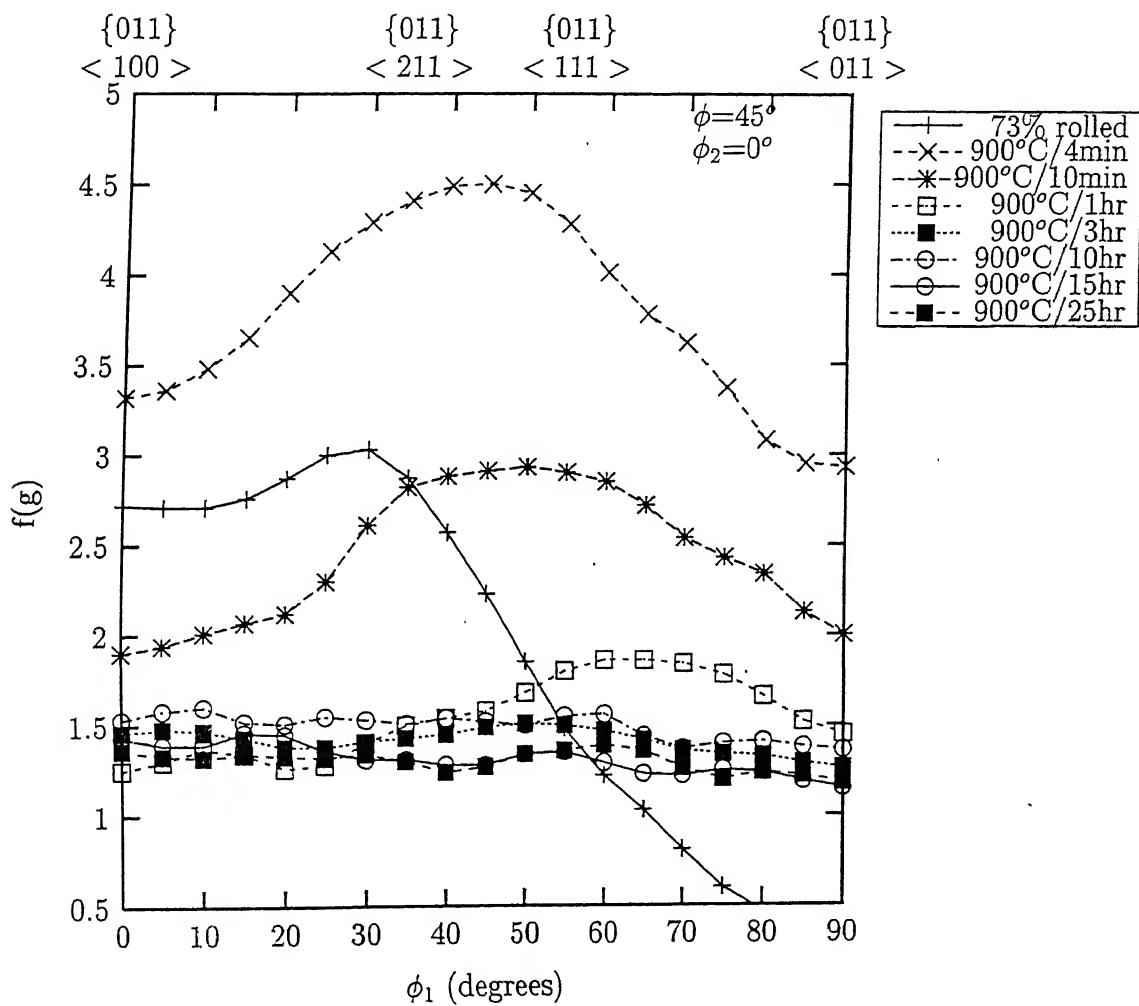
Figure 5.45  $\beta$ -fibre plots of the annealed samples

Table 5.5 Recrystallized volume fraction with annealing time at 900°C

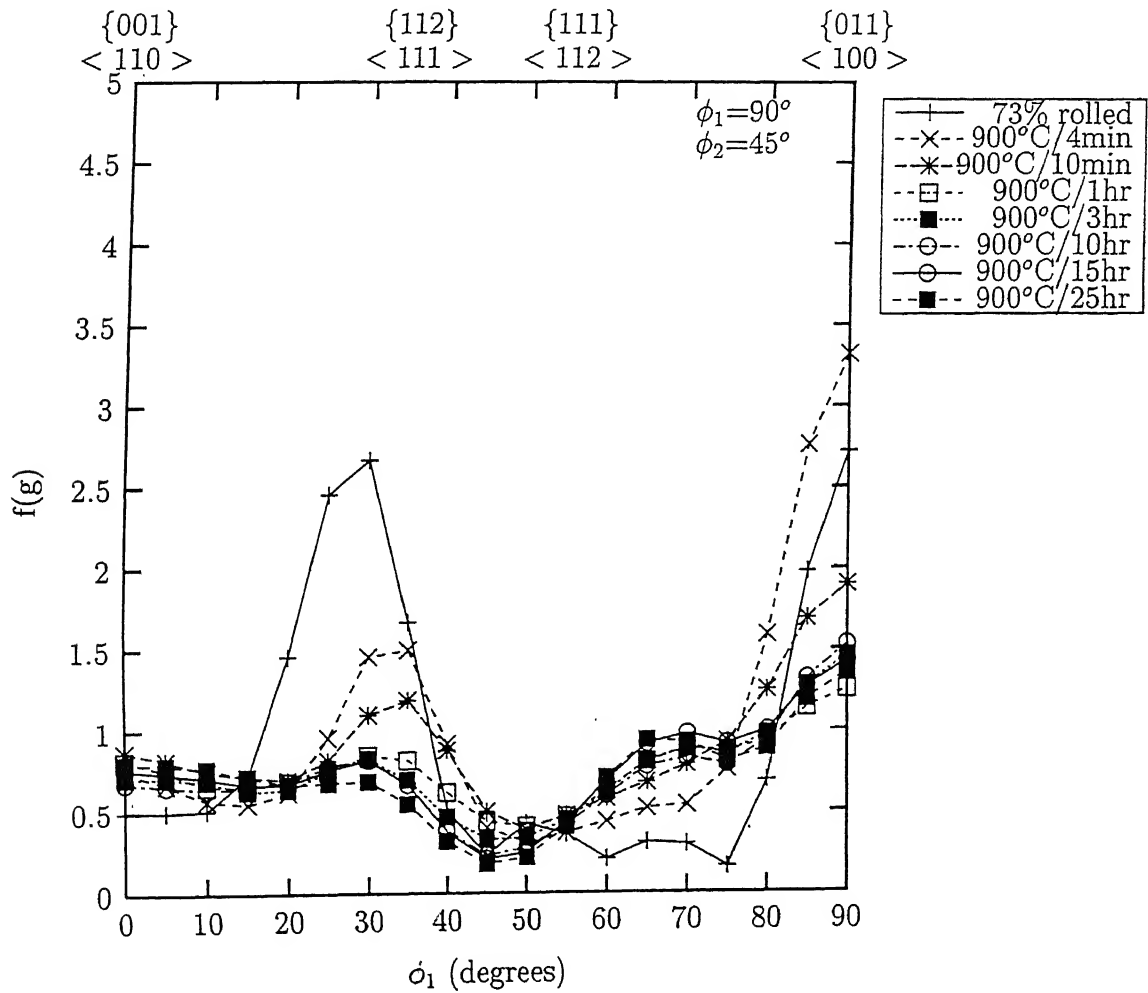
Time of annealing at 900°C	Fraction recrystallized
0 min	0%
4 min	4%
10 min	8%
1 hr	20%
3 hr	46%
10 hr	94%
15 hr	100%
25 hr	100%

The  $\alpha$ -fibre and  $\tau$ -fibre plots for all the samples are shown in Figures 5.46 and 5.47 respectively. Both the Figures indicate that the intensity of the Goss component increased at the early stage of annealing, followed by a gradual decrease after 1 hr of annealing. Another interesting point observed in Figure 5.46 is that the rotated Goss component  $\{011\}\langle 011 \rangle$  which was practically absent in the 73% rolled sample abruptly attained a reasonably high intensity after 4 min of annealing, and then gradually decreased after longer annealing time.

Figures 5.48a and 5.48b show the intensity variations with reference to the cube RD-rotation and the cube TD-rotation, respectively. These plots are obtained by plotting the  $f(g)$  values with respect to  $\phi$  (from 0° to 45°) in the section  $\phi_2 = 0^\circ$  when  $\phi_1$  is fixed at 0° (for RD-rotation) or at 90° (for TD-rotation). The significance of these plots is that they indicate a range of orientations in between the *cube* position (at  $\phi = 0^\circ$ ) and the *Goss* or *rotated Goss* position (at  $\phi = 45^\circ$ ). Therefore, the exact intensity values for cube or Goss components along with their rotated variations can be directly obtained from these plots. It is clear from both these Figures, that there was practically no cube component present at the start of annealing and no such component could be found anytime during the annealing process.

Figure 5.46  $\alpha$ -fibre plots of the annealed samples



Figure 5.47  $\tau$ -fibre plots of the annealed samples

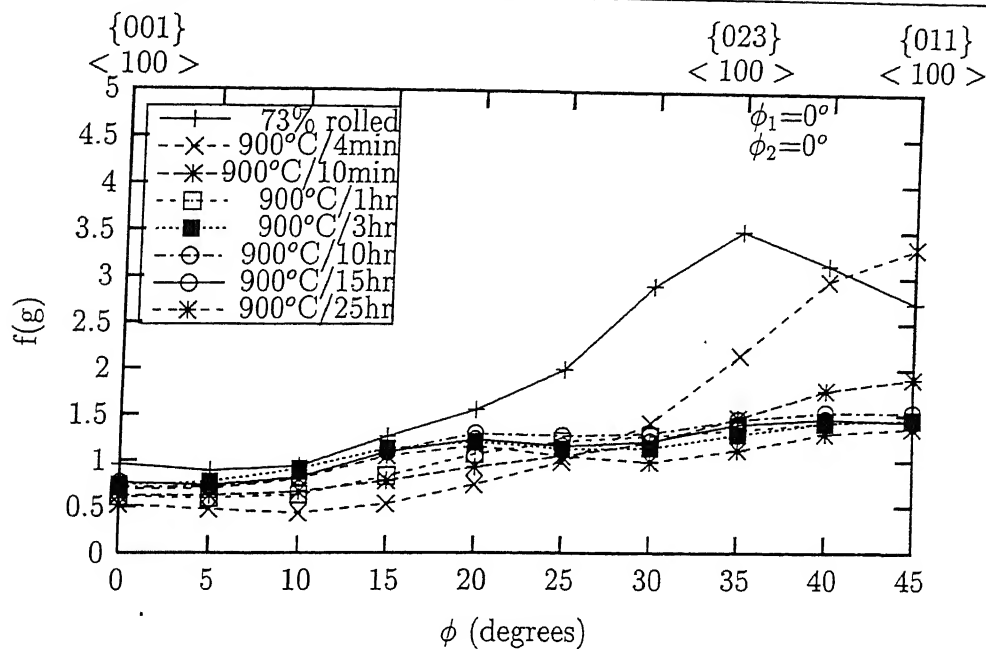


Figure 5.48a Cube RD-rotation plots of the annealed samples

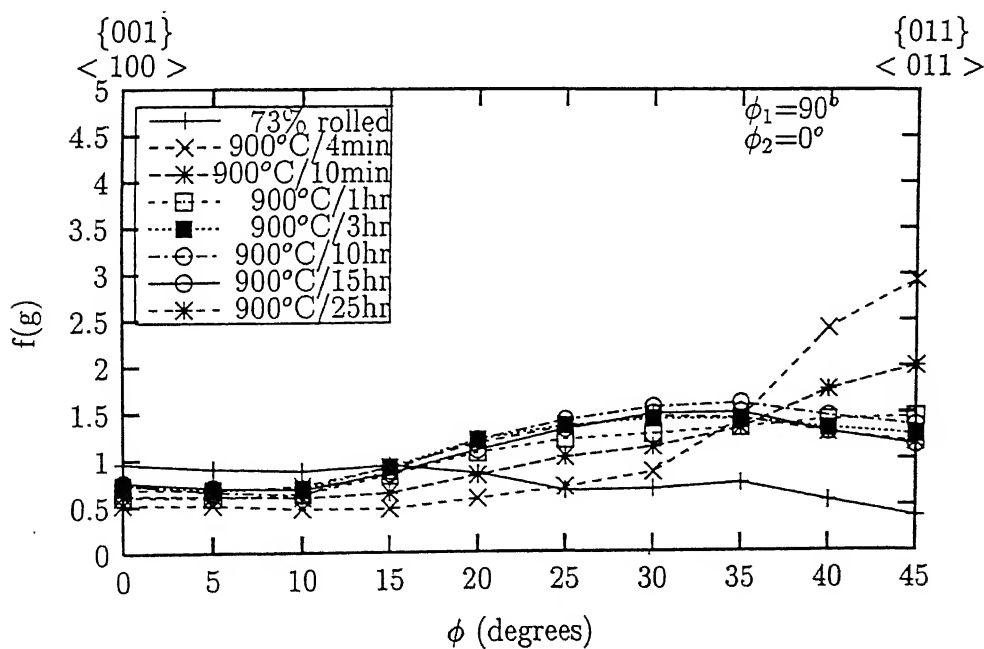


Figure 5.48b Cube TD-rotation plots of the annealed samples

## 5.6 Discussion of Annealing Results

Annealing of the cold rolled two-phase  $\text{Ni}_3\text{Al}(\text{B},\text{Zr})$  alloy has been found to lead to the following phenomena:

- recovery and reordering, and
- recrystallization and precipitation

### 5.6.1 Recovery and Reordering

A significant recovery stage was observed during the initial period of annealing, when the material was found to soften substantially. This is evident from the results of both the isochronal and isothermal annealing experiments (Figures 5.7 and 5.15).

Although recrystallization was yet to set in, some interesting changes in the microstructure of the cold rolled alloy were clearly noticed even after very short periods of annealing. The twins, which comprised a large volume fraction of the cold worked material, were found to decrease in density to a significant extent and eventually disappeared in the very early stages of recovery. Some of these disappearing twins can be seen in Figures 5.18a, 5.18b, 5.19a and 5.19b. The twins referred to above were part of the  $\text{DO}_{22}$  structure into which the original  $\text{L1}_2$  material transformed during cold rolling. The *de-twinning* phenomenon was therefore expected to indicate the reversal of the  $\text{L1}_2 \rightarrow \text{DO}_{22}$  transformation. This was indeed found out to be the case from the XRD results (Figures 5.11a and 5.11b) which indicated that both the (100) and (110) superlattice reflections, characteristic of the  $\text{L1}_2$  structure, were simultaneously present in the X-ray profiles even after short term annealing treatments, much before the start of recrystallization. Thus, the recovery stage is clearly accompanied by a *re-transformation* process (from  $\text{DO}_{22}$  to  $\text{L1}_2$  structure) in this material. The order parameter plots (Figure 5.13a to 5.13e) also indicate a rather quick establishment of  $\text{L1}_2$  ordering during the initial period of annealing. The order parameter values do not

show any significant change during subsequent recrystallization, indicating thereby that the level of ordering, characteristic of this material, is established essentially during the recovery stage.

A very interesting observation during the recovery stage was a significant change in the crystallographic texture from that in the cold rolled condition. The textures of the material after 4 min and 10 min of annealing at 900°C (Figures 5.43a, 5.44a, 5.44b and 5.45) will illustrate this point. The volume percent of recrystallization at these two conditions were found to be only 4% and 8% respectively. Therefore, any changes in the overall texture after 4 min and 10 min of annealing at 900°C cannot be ascribed to the phenomenon of recrystallization, but mainly to the recovery and retransformation (reordering) processes preceding recrystallization. Although the overall intensity of the texture does not change (from its value after 73% cold rolling) after 4 min annealing at 900°C (Figure 5.44a), the  $\beta$ -fibre plot (Figure 5.45) shows a drastic decrement of the intensities at the Cu  $\{112\} < 111 >$ , S  $\{123\} < 634 >$  and Bs/S  $\{168\} < 211 >$  locations and an increase in the Bs  $\{011\} < 211 >$  position. After 10 min of annealing at 900°C, the overall texture intensity also weakens drastically. As mentioned above, this weakening cannot be related to the recrystallization process, but to the atomic shuffling taking place during recovery and reordering and the back transformation from the DO<sub>22</sub> to L1<sub>2</sub> structure. In a way, therefore, the texture during the recovery stage is a kind of *transformation* texture.

Although Gottstein *et al* [114] and Ball and Gottstein [125] investigated the textural changes in single phase Ni<sub>3</sub>Al(B) and two phase Ni<sub>3</sub>Al(B,Zr,Fe) during deformation and recrystallization, they did not attempt measurement of textural change during the recovery stage. Ghosh Chowdhury *et al* [119] who made a systematic study of the structural and textural changes during the processing of a single phase Ni<sub>3</sub>Al(B) alloy, however, reported a marked weakening and change of the cold rolling texture during the very early stages of annealing prior to recrystallization.

### 5.6.2 Recrystallization and Precipitation

The 73% cold rolled material essentially consists of disordered  $\gamma$  ( $\sim 25\%$ ) and the rest ordered  $\gamma'$  ( $\text{DO}_{22}$ ). While  $\gamma$  is known to deform by slip,  $\gamma'$  with  $\text{DO}_{22}$  structure deforms essentially by twinning [145]. Therefore, the Cu component of the composite texture of the cold rolled material is expected to be derived significantly from the deformation of the former and much less from the deformation of the latter. The drastic weakening of the Cu component of the texture during the very initial period of recrystallization (Figure 5.45) therefore indicates changes in the deformed  $\gamma$  regions first. In fact, the initial recrystallized grains have been found to occur as clusters along the deformed  $\gamma$  regions adjacent to the  $\gamma'$  matrix (Figure 5.20b). Early recrystallization activity, preferably in the shear band regions, containing the deformed  $\gamma$  islands, was also noticed in optical micrographs (Figure 5.7).

Many of these earlier formed recrystallized grains are found to contain *discontinuous (cellular) precipitates* inside them (Figures 5.20a and 5.21a). The presence of plate-shaped precipitates at an inclined interface between a recrystallized grain and the adjacent deformed region (Figures 5.23a and 5.23b) indicate that the discontinuous precipitation could possibly have occurred by the well known *pucker mechanism* proposed by Tu and Turnbull [156]. This mechanism is schematically presented in Figure 5.49.

The interfaces mentioned above are thus the reaction fronts for both recrystallization and discontinuous precipitation (DP). Discontinuous precipitates could be seen in the cold rolled materials which were subjected to annealing at  $700^\circ\text{C}$  and  $800^\circ\text{C}$ . The morphology of the precipitates changed distinctly when higher annealing temperatures were employed. After annealing at  $900^\circ\text{C}$  isolated rod-shaped precipitates as well as plate-shaped and globular precipitates could be seen within recrystallized grains (Figures 5.27a and 5.27b). Only globular precipitate particles were observed when the cold rolled material was annealed at  $1000^\circ\text{C}$  (Figures 5.32 and 5.33a). It was further observed by TEM that whatever annealing temperature was used, only a fraction ( $\sim 50\%$  as a rough approximation) of the final

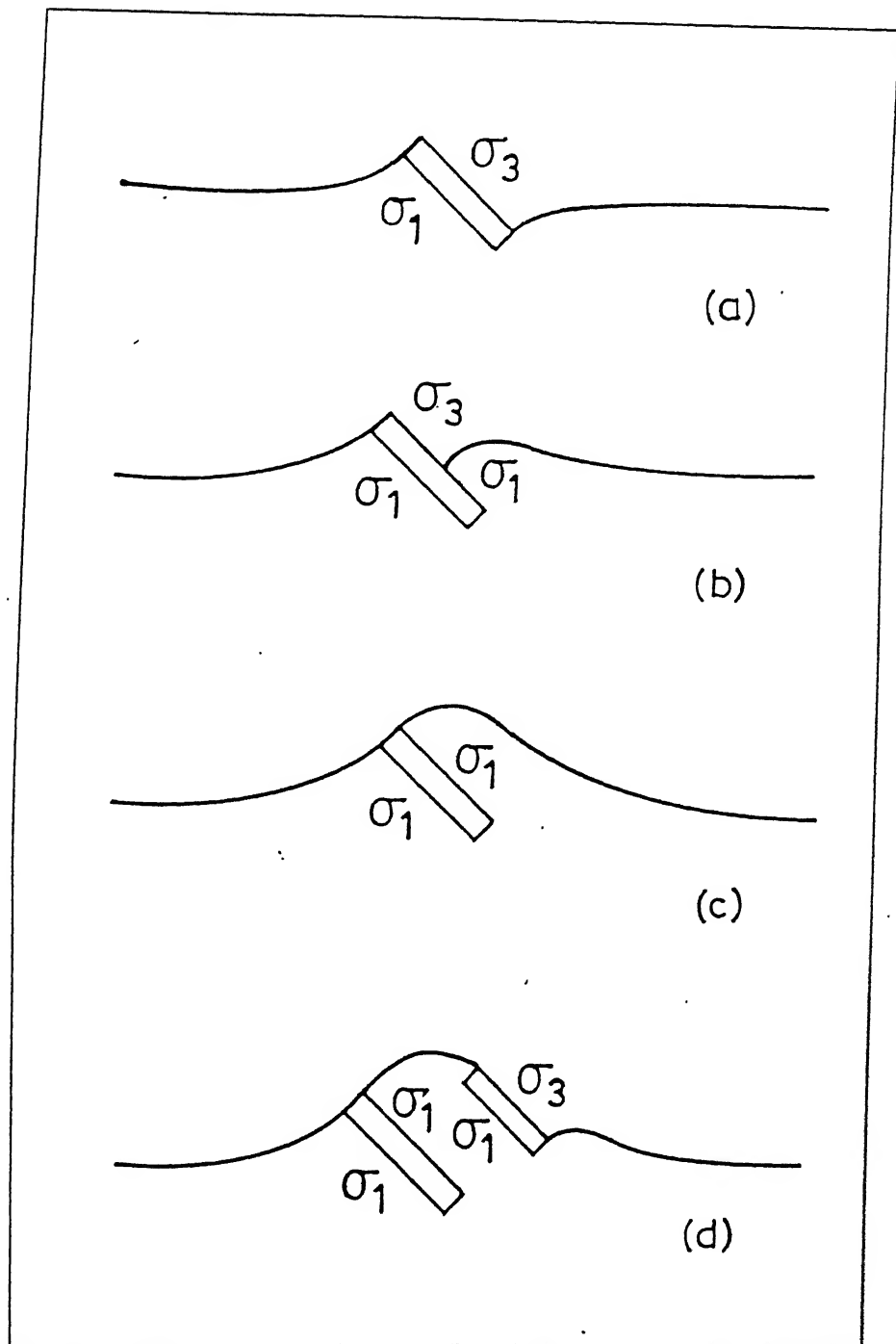


Figure 5.49 Schematic representation of the *pucker mechanism* of lamellar precipitation [156]

recrystallized grains contained precipitate particles inside, while others did not and appeared quite clean (even after tilting of the foils inside the TEM). The SAD patterns from both these types of grains, however, showed the superlattice spots in addition to the fundamental spots. XRD results indicated that with the progress of annealing, the volume fraction of the  $\gamma$  phase increased significantly from its initial value of  $\sim 25\%$  (Figure 5.3). This can be observed very clearly from a study of the XRD peaks for the isothermally annealed samples after prolonged heat treatment at higher temperatures (Figures 5.12a and 5.12b) where the  $\gamma$  phase peaks have been found to be even stronger as compared to the corresponding  $\gamma'$  peaks. That the volume fraction of the  $\gamma$  phase increases when a deformed two phase  $\text{Ni}_3\text{Al}$  base alloy is annealed at higher temperatures, has also been reported by Valiev *et al* [95]. Watanabe *et al* [103], who investigated the interface between  $\text{Ni}/\text{Ni}_3\text{Al}$  diffusion couples, detected the formation of a new  $\gamma$  phase on the  $\text{Ni}_3\text{Al}$  side of the couple. A higher volume fraction of the  $\gamma$  phase in this particular alloy composition at higher annealing temperatures can also be predicted from the relevant phase diagram (Figure 2.1).

The above discussion therefore points to the scenario that prolonged annealing of the cold worked material will produce a substantial volume fraction of the  $\gamma$  phase. Very careful TEM examination has revealed that SADs from pure disordered  $\gamma$  phase regions were very sparse and that the bulk of the  $\gamma$  regions containing precipitates which initially recrystallize from the cold rolled material give SAD patterns corresponding to the  $\gamma'$  phase. Thus these must be the recrystallized  $\gamma$  grains with  $\gamma'$  precipitate particles inside. Hornbogen and Kreye [157] also reported that during aging of severely deformed  $\text{Ni-Al}$  alloys in the two-phase field, ordered particles of  $\gamma'$  were formed in the  $\gamma$  behind the recrystallization front. Many of the recrystallized grains ( $\sim 50\%$  as a rough approximation) which appear at a somewhat later stage and do not show any precipitates inside, but at the same time exhibit SADs characteristic of  $\gamma'$ , must be the recrystallized  $\gamma'$  grains.

The microstructure of the highly annealed material is therefore expected to consist of

- about 50% by volume fraction of recrystallized disordered  $\gamma$  phase with dense precipitates of ordered  $\gamma'$  inside.
- another nearly 50% by volume fraction of recrystallized ordered  $\gamma'$  grains and
- an insignificant volume fraction of the pure disordered  $\gamma$  phase.

The fine size of the precipitate particles will preclude observation using an optical or a scanning electron microscope. Using these equipments therefore the fully recrystallized microstructure would appear as if there was only a single phase, as was the case observed in this investigation.

### 5.6.3 Mechanism of Recrystallization and Precipitation

On the basis of the experimental results described earlier in this chapter, an attempt will now be made to account for the recrystallization and precipitation reactions as were observed on annealing.

As stated in the previous chapter, the  $\gamma$  islands (many of which appeared to contain some  $\gamma'$  particles inside) of the homogenized material were deformed along with the  $\gamma'$  during cold rolling. These  $\gamma$  islands were also found to align themselves more and more within the macroscopic shear bands as the rolling progressed – the alignment being mostly complete after 73% rolling (Figure 4.4h). During the initial stages of annealing, major activity was noticed within these shear bands where the signs of initial nucleation of strain free grains were observed (Figures 5.7 and 5.8a). Transmission electron micrographs clearly showed the formation of the new recrystallized  $\gamma$  grains which formed in clusters (Figure 5.20b) indicating a high nucleation rate within the shear bands.

Simultaneously, along with the nucleation of strain free  $\gamma$  grains within the shear bands, and quite likely even before the onset of recrystallization in those regions, some atomic shuffling must be taking place in the nearby deformed  $\gamma'$  regions, as evident from the drastic



changes of the  $\gamma'$  order parameter during the early stages of annealing. The atomic shuffling, coupled with the *de-twinning* process, that was clearly observed, led to a change in the structure of  $\gamma'$  from  $\text{DO}_{22}$  back to  $\text{L1}_2$ . Much of the strain energy of the cold work must have been released from the deformed  $\gamma'$  regions during this transformation process; this is also evident from the strain parameter plots (Figure 5.14). As a result there may not be sufficient amount of strain energy left in these regions to trigger a fast recrystallization process.

The recrystallized grains of the  $\gamma$  solid solution will now grow at the expense of the deformed  $\gamma'$  regions by the movement of the  $\gamma/\gamma'$  interface towards the  $\gamma'$ . At the lower temperatures of annealing ( $700^\circ\text{C}$  and  $800^\circ\text{C}$ ) a combined recrystallization and discontinuous precipitation reaction will occur giving rise to the typical cellular morphology of the precipitates within the  $\gamma$  grains, as observed (Figures 5.21a and 5.23a). The morphology of the precipitates changes at higher temperatures, and at  $1000^\circ\text{C}$  instead of the cellular precipitation, globular particles precipitate within the  $\gamma$  grains (Figure 5.32). The precipitate particles at certain stage could exert a retarding force on the advancing recrystallization front thereby bringing the recrystallization of the  $\gamma$  grains to a stop. Annealing beyond this stage will possibly allow the deformed  $\gamma'$  grains, which could not recrystallize earlier due to insufficient driving force, to start recrystallizing.

#### 5.6.4 Discontinuous Reactions

Discontinuous precipitation is a well known phenomenon which occurs, more commonly, during the recrystallization of two phase alloys. As an essential pre-requisite, a supersaturated matrix should be available and this should decompose at the advancing reaction front. Basically it is an autocatalytic reaction [158] and the term *discontinuous* refers to the composition of the matrix lattice which changes discontinuously across the reaction front. There may be several kinds of discontinuous reactions [158]:

- Recrystallization, in which the boundary of a strain free subgrain moves into the deformed matrix.
- Phase transformation, in which the newly formed stable phase spontaneously grows and consumes the parent phase.
- Discontinuous precipitation from a supersaturated matrix, in which nucleation occurs at the advancing reaction front, as a result of which the precipitates assume a cellular appearance.
- Eutectoid reaction, which is basically a kind of phase transformation. The product phases nucleate at the reaction front thereby giving rise to a lamellar structure.
- Combined recrystallization and precipitation, in which the recrystallization front itself acts as the reaction front. A supersaturated deformed matrix is likely to trigger this kind of combined reaction on annealing.
- Dissolution of a metastable phase may take place at an advancing reaction front (after a grain boundary) and reprecipitation of a stable phase may occur subsequently.
- Crystallization of an amorphous mixture of atoms, in which a crystallized phase grows discontinuously at an advancing reaction front.

The interaction between recrystallization and precipitation as a function of the temperature of annealing is shown schematically in Figure 5.50 [159]. Four different zones can be identified in this diagram, viz,

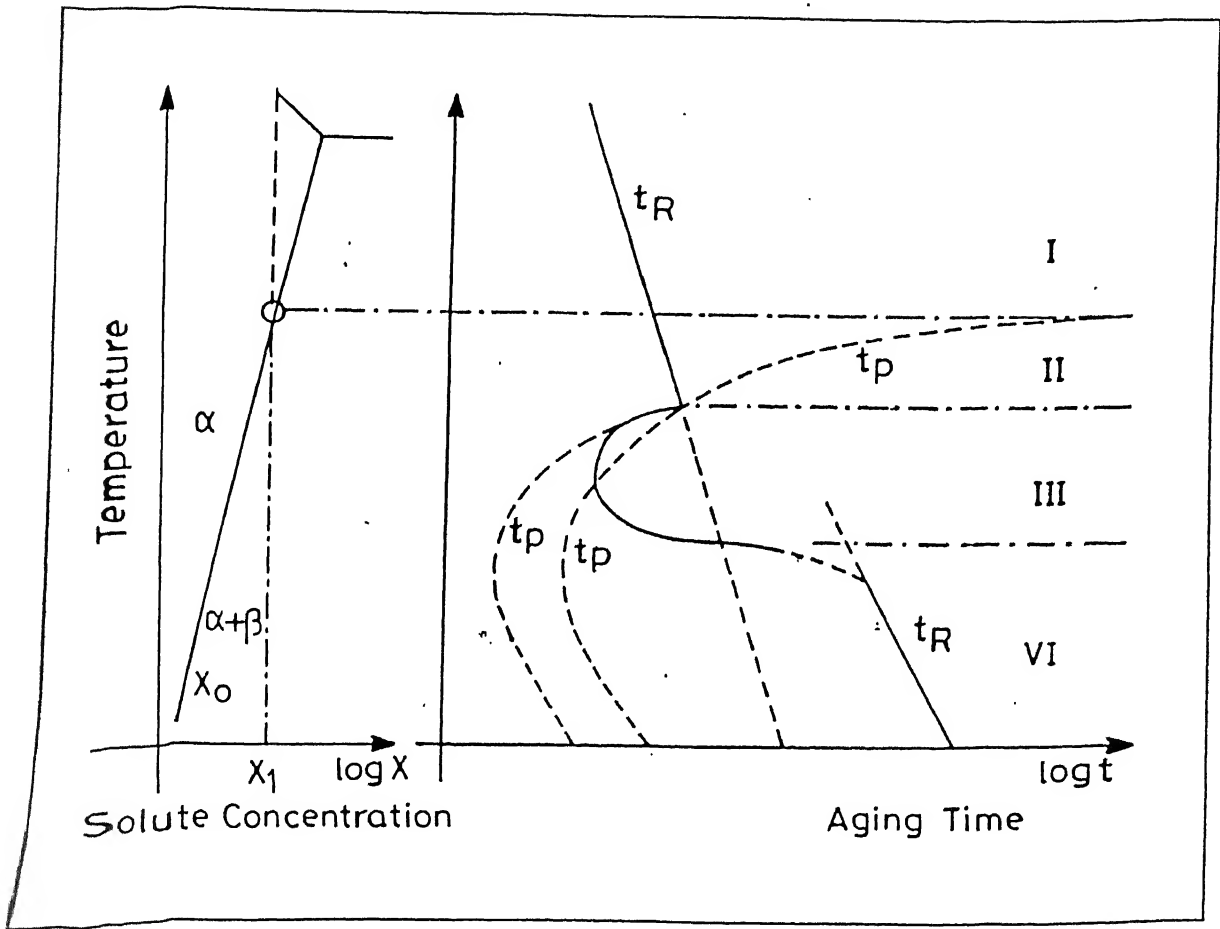


**Figure 5.50** Schematic diagram showing the interaction between recrystallization and precipitation as a function of the temperature of annealing [159]

Zone I : Recrystallization only

Zone II : Recrystallization followed by precipitation

Zone III : Combined recrystallization and precipitation

Zone IV : Continuous precipitation followed by recrystallization

It is apparent that annealing at lower temperatures of 500°C or 600°C would correspond to the zone IV of this diagram. Continuous precipitation will occur throughout the matrix and this will cause an inordinate delay in the start of recrystallization. In fact it was noticed in the present investigation that annealing for very long period of time ( $\sim 50$  hr) failed to reveal any recrystallization in the samples annealed at 600°C.

The structural changes in the samples annealed at 700°C and 800°C corresponded to the zone III of Figure 5.50 where a combined recrystallization and precipitation occurred. As mentioned earlier, the interface between highly deformed disordered  $\gamma$  and ordered  $\gamma'$  acted as the reaction front in this case. Work by Böhm [160] led to the suggestion that in an alloy system where  $r_A$  and  $r_B$  are the radii of the solvent and the solute respectively, discontinuous precipitation will be possible if  $(r_B - r_A)/r_A > 0.11$ . In the Ni-Al system, atomic radii of Ni and Al are 0.125 nm and 0.143 nm respectively and this yields an  $(r_B - r_A)/r_B$  ratio of  $\sim 0.14$ , which clearly indicates that discontinuous precipitation is quite likely in this system. In Cu-base alloys discontinuous precipitation is found to be favoured if the second solute element deviates in its atomic radius in the same direction as the first solute element [160, 161]. In the present material, the second solute element, Zr has an atomic radius of 0.16 nm and hence this may be favourable for discontinuous precipitation in this system.

As mentioned earlier, Watanabe *et al* [103] found out from their experiments on Ni/Ni<sub>3</sub>Al diffusion couple that during diffusion anneal, a Ni-rich  $\gamma$  phase is produced from the  $\gamma'$  (Ni<sub>3</sub>Al) as a consequence of atom exchange, with Al being diffused out and Ni atoms being diffused in the Ni<sub>3</sub>Al. In the present material, the adjacent  $\gamma/\gamma'$  regions should behave in

a similar manner. The only difference is that the disordered  $\gamma$  will be in a recrystallized condition right at the initial stages of annealing, while  $\gamma'$  will still be in a deformed condition. The formation of new  $\gamma$  from the  $\gamma'$  will create an interface between the two and the movement of this interface into the deformed  $\gamma'$  will enlarge the  $\gamma$  regions. Presumably this interface is populated by small  $\text{Ni}_3\text{Al}$  particles (Figure 5.23b) which could initiate the lamellar discontinuous precipitation as the interface (recrystallization front) moves. In this way the already recrystallized  $\gamma$  grains will grow, eating into the  $\gamma'$  regions and at the same time these will be covered by copious cellular precipitation inside.

Recrystallization of the  $\gamma'$  regions will start later presumably because of less strain energy in them and therefore less driving force as mentioned earlier. The process is also expected to be quite sluggish as the mechanism of recrystallization in the ordered state might involve migration of only low or medium angle boundaries [112]. When  $\gamma'$  recrystallization will also be complete, the microstructure will consist of recrystallized  $\gamma$  with discontinuous (cellular) precipitates of  $\text{Ni}_3\text{Al}$  inside plus recrystallized  $\gamma'$ . Both types of grains will therefore show the superlattice spots in addition to the fundamental spots in SAD; the superlattice spots from the essentially  $\gamma$  matrix grains will be weaker as compared to those from the  $\gamma'$  grains. This has actually been observed in the present investigation.

The structural changes in the samples annealed at  $900^\circ\text{C}$  clearly corresponded to the boundary region between zone III and zone II since both discontinuous precipitation and globular precipitation were observed in different grains simultaneously (Figure 5.29b). The structural features in the material annealed at  $1000^\circ\text{C}$  apparently corresponded to the zone II of Figure 5.50 where the process of recrystallization starts first and this is followed by precipitation. It is quite likely that due to the highly deformed microstructure of the disordered  $\gamma$  (with  $\gamma'$  particles inside) and the higher annealing temperatures used, the fine  $\gamma'$  particles will dissolve into the  $\gamma$  matrix simultaneously with the recrystallization of  $\gamma$ . As the  $\gamma/\gamma'$  recrystallization front will move into the  $\gamma'$  regions flux of Al atoms will preferentially flow

from  $\gamma'$  to  $\gamma$  regions [103]. The supersaturation of the  $\gamma$  phase with respect to Al and the availability of Ni atoms locally will lead to the precipitation of  $\text{Ni}_3\text{Al}$  particles inside the  $\gamma$  grains, as has been observed (Figures 5.21a and 5.21b). This phenomenon will then be followed by a second stage when deformed  $\gamma'$  regions will recrystallize.

### 5.6.5 Recrystallization Kinetics

The Avrami exponent  $n$  gives a general idea regarding the kinetics of transformation, as it depends on the relative flatness or steepness of the fraction transformed versus time curves. The values of  $n$  determined in the present investigation exhibit considerable difference in magnitude below and above the 50% recrystallization level. Few other investigators also measured the  $n$  values for recrystallization in  $\text{Ni}_3\text{Al(B)}$  alloy [114, 119]. These values have been presented in Table 2.6 in chapter 2. Ball and Gottstein, from their work on the recrystallization of single phase  $\text{Ni}_3\text{Al(B)}$ , measured the value of  $n$  and found that it varied between 1.8 and 0.3 as the temperature of annealing was increased from 800°C to 1000°C. In a recent study, Ghosh Chowdhury *et al* [119] detected a two stage kinetics during recrystallization of a deformed  $\text{Ni}_3\text{Al(B)}$  single phase alloy. According to their report, below 60% recrystallization an  $n$  value of 2.2 at 800°C was obtained. The value of  $n$  varied with the temperature of annealing and finally attained a value of nearly 0.7 at 950°C. Above 60% recrystallization, however, a constant value of 3.0 was obtained for all annealing temperatures.

A two stage kinetics was also observed in the present investigation. In the first stage (below a recrystallization volume percent of 50), the value of  $n$  varied within a narrow range (between 0.68 and 0.82) and was found to be rather independent of the annealing temperature. In the second stage (above 50% recrystallization) the value of  $n$  was found to be nearly 2.0 (between 1.95 and 2.15, to be more precise), which was again temperature independent.

The relative insensitivity of  $n$  towards annealing temperature, and its strong dependence

on the volume fraction recrystallized as has been observed in the present investigation, is a feature quite different from the observations of earlier works on single phase  $\text{Ni}_3\text{Al(B)}$ . This could be due to the fact that unlike in the previous investigations the present one deals with a two phase  $\gamma'/\gamma$  alloy rather than single phase  $\gamma'$ . The changes taking place in both the phases  $\gamma'$  and  $\gamma$  will therefore be reflected in the overall transformation kinetics and obviously  $n$  values, characteristic of the single phase  $\gamma'$  alloys, cannot be expected to be obtained in this case.

Two distinct activation energy values were obtained for the two stages of recrystallization in the present case. Below the recrystallization volume fraction of about 50%, the average value of the activation energy was found to be 117 kJ/mole, while it more than doubled to a value of 274 kJ/mole for recrystallization volume fractions above 50% (Table 5.4). The activation energy, just like  $n$ , was also found to be rather insensitive to the annealing temperature. Gottstein *et al* [114] reported an activation energy value of 120 kJ/mole during annealing of a heavily cold rolled  $\text{Ni}_3\text{Al(B)}$  single phase alloy within the temperature range of 650° - 675°C. Ghosh Chowdhury *et al* [119], who also worked on a single phase  $\text{Ni}_3\text{Al(B)}$  alloy, reported an activation energy of 110 kJ/mole below 900°C and more than 400 kJ/mole above 900°C.

Although the  $Q$  value of 117 kJ/mole obtained for the first stage of recrystallization in the present case, is quite comparable to the values of 120 kJ/mole and 110 kJ/mole, as reported by Gottstein *et al* [114] and Ghosh Chowdhury *et al* [119] respectively, it is difficult to figure out the reasons for this similarity. On the other hand, the low  $Q$  value of 117 kJ/mole below 50% recrystallization and the high  $Q$  value of 274 kJ/mole above 50% recrystallization, in the present case, can be correlated well with the initial comparatively fast recrystallization of the disordered  $\gamma$  phase followed by a rather sluggish recrystallization of the ordered  $\gamma'$  phase, as revealed by the microstructural studies. The  $Q$  value at the second stage (274 kJ/mole) agrees well with that for self diffusion of Ni, which is 293 kJ/mole [162]. It can

also be mentioned here that the activation energy for diffusion of Ni in hypostoichiometric  $\text{Ni}_3\text{Al}$  was reported to be 309 kJ/mole [96] which is also quite close to the value observed in the second stage of recrystallization in the present case.

The DSC thermograms (Figure 5.42) clearly show that for the 25%, 35% and 45% rolled materials, most of the heat is evolved during the recovery stage which is quite extensive, leaving only a small fraction of the heat to be evolved during recrystallization. Jena *et al* [115] confirmed the presence of extensive recovery from their calorimetric study of 35% cold rolled hypostoichiometric  $\text{Ni}_3\text{Al(B)}$ . Due to recovery, the subsequent recrystallization kinetics was found to be slow. They also found that nucleation started by *strain induced boundary migration (SIBM)* as well as at deformation bands and grain boundaries.

The shapes of the DSC thermograms for the 55%, 65% and 73% rolled samples appear quite similar to those of the less deformed ones upto a temperature of about 700°C. The heat evolved till then is due to the recovery of defects as well as the *re-transformation* from the  $\text{DO}_{22}$  to the original  $\text{L1}_2$  structure. The extensive plateau region in these thermograms, beyond 700°C, can be ascribed to the first stage of recrystallization involving the disordered  $\gamma$  regions which should produce a peak in the corresponding thermogram plus an endothermic precipitation reaction producing either the cellular or the globular precipitates. The final small peak appearing at temperatures between 1150° - 1175°C could be associated with the second stage of the recrystallization process involving the  $\gamma'$  regions.

### 5.6.6 Textural Changes

The crystallographic texture of the 73% cold rolled material was found to change significantly right after 4 min annealing at 900°C when only 4% of the alloy was found to recrystallize. Both the Goss  $\{011\} \langle 100 \rangle$  and the rotated Goss  $\{011\} \langle 011 \rangle$  components were found to sharpen at this stage and at least part of it could be related to the newly emerging recrystallized grains of the disordered  $\gamma$  phase appearing primarily in the shear band regions.



The Goss  $\{011\} < 100 >$  oriented grains are known to nucleate in the deformation/shear bands. Hence initial nuclei of this orientation and its rotated version are quite likely to form. The fine  $\gamma'$  particles present inside the deformed  $\gamma$  regions could act as heterogeneous nucleation sites producing randomly oriented grains during the recrystallization of  $\gamma$ . This could suppress the formation and growth of the cube  $\{100\} < 001 >$  oriented grains which otherwise would have been expected to form from the heavily deformed disordered FCC  $\gamma$  during recrystallization. Cube oriented grains were practically absent in the recrystallization texture of the present experimental alloy. Ball *et al* [125] who worked on an alloy of similar composition also could not find any cube component in the annealing texture. However, some rotated variations of the cube and another component  $\{123\} < 121 >$  could be detected in the final annealing texture in the present investigation. These results have been corroborated by the work of Ball *et al* [125]. These results are also in general agreement with the results obtained by Ghosh Chowdhury *et al* [119] who determined the annealing texture of a heavily cold rolled  $\text{Ni}_3\text{Al(B)}$  alloy.

It may be recalled that a drastic weakening of the texture occurs in this material during the recovery stage itself when the  $\text{DO}_{22}$  structure reverts back to the  $\text{L1}_2$  giving rise to a *transformation texture*. Before any significant recrystallization takes place, the material already possesses a weak texture. The very first recrystallization nuclei to appear were the ones in the disordered  $\gamma$  regions within the shear bands. The small size of these grains (figure 5.20b) can be attributed to the high nucleation rate in the shear bands and low grain boundary mobility due to the presence of Zr. With the progress of recrystallization, numerous such grains will appear which will lack any growth selection and as a result the overall texture will be very weak, as has been found to be the case. Finally, the  $\gamma'$  regions will also recrystallize by an essentially *in-situ* phenomenon leading to a final very weak (nearly random) texture.

# CHAPTER 6

## CONCLUSIONS

## ● *Conclusions*

1. The initial homogenized material possesses a solidification texture showing a strong (200) fundamental peak and a reasonably strong (100) superlattice peak. The imperfect  $L1_2$  structure of the initial material changes into a fully disordered state after filing. The filed powder, after annealing shows the perfect  $L1_2$  structure.
2. The homogenized alloy shows a two-phase microstructure, consisting of disordered FCC Ni-rich  $\gamma$  phase islands randomly distributed over ordered  $\text{Ni}_3\text{Al}$  ( $\gamma'$ ) grains. The lattice parameters of the  $\gamma$  and the  $\gamma'$  phases are 0.3574 nm and 0.3565 nm respectively. The Zr atoms preferentially partition into the  $\gamma'$  phase. Many of the  $\gamma$  islands appear to contain fine  $\gamma'$  particles inside.
3. On cold rolling, the (100) superlattice line weakens substantially after 25% reduction and totally disappears after 35% deformation. The (110) superlattice line shows the first sign of appearance after 35% rolling and can be distinctly seen in the XRD pattern after 45% reduction. The order parameter ( $S$ ) based on the 100/200 reflection pair becomes zero after 35% rolling, whereas the order parameter ( $S$ ) based on the 110/220 reflection pair starts rising at this level, reaches a maximum value of nearly 0.55 after 55% deformation, followed by a decrease on further deformation.
4. Distinct splitting of the XRD lines after 45% rolling indicates the presence of an additional tetragonal ordered phase with a  $c/a$  ratio of 2.004. The strain parameter and microhardness values show significant drops within 35% and 45% deformation levels.

All these observations indicate a structural transformation taking place in the ordered  $\gamma'$  phase from  $L1_2$  to  $DO_{22}$  as a result of cold rolling.

5. TEM micrographs show the incidence of twinning in the 35% rolled material. The density of twins increases with increase in the amount of cold rolling. Since the  $L1_2$  structure deforms by slip only, whereas the  $DO_{22}$  structure deforms essentially by twinning, the presence of twins in the microstructure is an indirect proof of the  $L1_2 \rightarrow DO_{22}$  transformation during rolling.
6. The change of the deformation mode from slip to twinning in the  $\gamma'$  phase leads to a textural transition from *pure metal* type after 25% to *alloy* type after 35% - 45% reduction. The overall texture intensity comes down after 55% reduction followed by a rise again after 65% reduction. The final deformation texture after 73% cold rolling consists of the components such as Cu  $\{112\} \langle 111 \rangle$ , Bs  $\{011\} \langle 211 \rangle$  and S  $\{123\} \langle 634 \rangle$ , while the peak intensity at this stage, as well as during the intermediate transition stage appears at the Bs/S  $\{168\} \langle 211 \rangle$  position. The Bs component of texture is mainly due to the twinning deformation mode in  $\gamma'$  phase, whereas the  $\gamma$  phase, undergoing slip deformation, significantly contributes to the Cu component.
7. Annealing of the 73% cold rolled material comprises two main stages, namely, recovery and recrystallization. The recovery stage is accompanied by the reverse structural transformation of the  $\gamma'$  phase from  $DO_{22}$  to  $L1_2$ , whereas the recrystallization stage is accompanied by a precipitation phenomenon. Reordering is essentially complete within the recovery period; order parameter values show only a marginal increase after recrystallization.
8. On prolonged annealing, the  $\gamma$  phase peaks strengthen considerably with respect to the  $\gamma'$  phase peaks, indicating increase in the volume fraction of the  $\gamma$  phase at the expense of  $\gamma'$ . Although optical and SEM micrographs do not show a two phase microstructure

after full recrystallization, TEM micrographs reveal nearly 50% of the grains with precipitates inside and remaining grains without any precipitates. The SAD patterns from both types of grains show  $L1_2$  diffraction spots.

9. On annealing, the highly strained  $\gamma$  regions (with fine  $\gamma'$  particles inside) are the first to recrystallize. Discontinuous (cellular) precipitates are seen inside these grains after annealing at 700° and 800°C. Both lamellar and globular precipitates inside the grains are seen after annealing at 900°C, whereas only a fine globular precipitation is observed after annealing at 1000°C. The precipitates – whether cellular or globular type are likely to be of  $Ni_3Al$  ( $\gamma'$ ).
10. After the recrystallization of the deformed  $\gamma$  regions is almost over, the deformed  $\gamma'$  regions start to recrystallize. The final microstructure of the annealed material consists of (i) nearly 50% by volume of recrystallized  $\gamma$  grains with fine  $\gamma'$  precipitate particles inside, (ii) nearly 50% by volume of recrystallized  $\gamma'$  grains and (iii) a very small fraction of recrystallized pure  $\gamma$  grains without any precipitate inside.
11. Both the Avrami exponent ( $n$ ) and the activation energy ( $Q$ ) are somewhat independent of temperature of annealing, but very much dependent on the volume fraction of material recrystallized. Below 50% recrystallization  $n$  varies between 0.68 and 0.82, whereas above 50% recrystallization it varies between 1.95 and 2.15. The average activation energies in these two stages are 117 kJ/mole and 274 kJ/mole respectively.
12. The overall texture at the beginning of recrystallization is weak and remains so till recrystallization is complete. This appears to be due to a high density of randomly oriented nuclei at the beginning of recrystallization. The final recrystallized material has a texture not much different from the random.

# REFERENCES

## ● *References*

1. K. Aoki and O. Izumi, *Jr. Jpn. Inst. Met.*, **43** (1977), p. 1190.
2. C.T. Liu, C.L. White and J.A. Horton, *Acta Metall.*, **33** (1985), p. 213.
3. C.T. Liu and C.L. White, *MRS Symp. Proc.*, **39** (1985), p. 365.
4. C.T. Liu and J.O. Stiegler, in *ASM Metals Handbook*, vol.2 (1990), p. 913.
5. S.H. Avner, *Introduction to Physical Metallurgy*, McGraw - Hill Book Company (1987).
6. *Binary Alloy Phase Diagram*, vol.1, eds. T.B. Massalski *et al*, ASM, Metals Park, Ohio (1986).
7. C. Barrett and T.B. Massalski, *Structure of Metals*, McGraw - Hill Book Company (1966).
8. *ASTM Powder Diffraction File*, JCPDS, USA (1985).
9. A.H. Cottrell, *Theoretical Structural Metallurgy*, Edward Arnold Ltd., ELBS edition (1964).
10. R.W. Guard and J.H. Westbrook, *Trans. AIME*, **215** (1959), p. 871.
11. C.L. Corey and B. Lisowskey, *Trans. AIME*, **239** (1967), p. 239.
12. G.R. Stoeckinger and J.P. Newmann, Jr. *Appl. Cryst.*, **3** (1970), p. 32.
13. D.P. Pope and J.L. Garin, Jr. *Appl. Cryst.*, **10** (1977), p. 14.
14. O. Noguchi, Y. Oya and T. Suzuki, *Metall. Trans.*, **12A** (1981), p. 1647.

15. N. Masahashi, T. Takasugi and O. Izumi, *Acta Metall.*, **36** (1988), p. 1815.
16. R. Ramesh, R. Vasudevan, B. Pathiraj and B.H. Kolster, *Jr. Mater. Sci.*, **27** (1992), p. 270.
17. M. Yamaguchi, S.R. Nishitani and Y. Shirai, in *High Temperature Aluminides and Intermetallics*, eds. S.H. Whang *et al*, TMS, Warrendale, PA (1990), p. 63.
18. C.L. Corey and D.I. Potter, *Jr. Appl. Phys.*, **38** (1967), p. 3894.
19. J.P. Clark and G.P. Mohanty, *Scripta Metall.*, **8** (1974), p. 959.
20. A.L. Ward and D.F. Mikkola, *Metall. Trans.*, **3A** (1972), p. 1479.
21. J.S.C. Jang and C.C. Coch, *Jr. Mater. Res.*, **5** (1990), p. 498.
22. S. Gialanella, R.W. Cahn, J. Malagelda, S. Surinach and M.D. Baro, in *Kinetics of Ordering Transformation in Metals*, eds. H. Chen and V.K. Vasudevan (1992), p. 161.
23. I. Baker, D.V. Viens and E.M. Schulson, *Jr. Mater. Sci.*, **19** (1984), p. 1799.
24. J. Ball and G. Gottstein, *Intermetallics*, **1** (1993), p. 171.
25. S. Ghosh Chowdhury, R.K. Ray and A.K. Jena, *Scripta Metall. et Mater.*, **32** (1995), p. 1501.
26. G. Wassermann, *Z. Metallkunde*, **54** (1963), p. 61.
27. G.E. Dieter, *Mechanical Metallurgy*, McGraw - Hill Book Company (1986).
28. M. Yamaguchi and Y. Umakoshi, *Prog. Mater. Sci.*, **34** (1990), p. 1.
29. Y. Umakoshi, in *Materials Science and Technology*, vol.6, eds. R.W. Cahn *et al*, VCH Publishers Inc., NY (1993), p. 251.
30. B.H. Kear, J.M. Oblak and A.F. Giamei, *Metall. Trans.*, **1A** (1970), p. 2477.
31. J. Douin, P. Veyssi re and P. Beauchamp, *Phil. Mag.*, **A54** (1986), p. 375.
32. S.H. Foils and M.S. Daw, *Jr. Mater. Res.*, **2** (1987), p. 5.



33. S.P. Chen, A.F. Voter and D.J. Srolovitz, *Scripta Metall.*, **20** (1986), p. 1389.
34. K.J. Hemker and M.J. Mills, *Phil. Mag.*, **A68** (1993), p. 305.
35. K.J. Hemker and M.J. Mills, *ibid*, cf Fu, Ye and Yoo (1992)
36. A.T. Paxton, in *Electron Theory and Alloy Design*, eds. D. Pettifor and A. Cottrell, Oxford Alden Press (1992), p. 158.
37. P. Veyssi re and J. Douin, *Phil. Mag. Lett.*, **51** (1985), p. L1.
38. M.J. Markinkowski, N. Brown and R.M. Fisher, *Acta Metall.*, **9** (1961), p. 129.
39. B.H. Kear, A.F. Giamei, J.M. Silcock and R.K. Ham, *Scripta Metall.*, **2** (1968), p. 287.
40. M. Yamaguchi, V. Vitek and D.P. Pope, *Phil. Mag.*, **A43** (1981), p. 1027.
41. J.A. Horton, I. Baker and M.H. Yoo, *Phil. Mag.*, **A63** (1991), p. 319.
42. P. Beauchamp, J. Douin and P. Veyssi re, *Phil. Mag.*, **A55** (1987), p. 565.
43. I. Baker, E.M. Schulson and J.A. Horton, *Acta Metall.*, **35** (1987), p. 1553.
44. L.M. Hsiung and N.S. Stoloff, *MRS Symp. Proc.*, **133** (1989), p. 261.
45. P. Veyssi re, J. Douin and P. Beauchamp, *Phil. Mag.*, **A51** (1985), p. 469.
46. I. Baker and E.M. Schulson, *Phys. Stat. Sol. (A)*, **89** (1985), p. 163.
47. P. Veyssi re, M.H. Yoo, J.A. Horton and C.T. Liu, *Phil. Mag. Lett.*, **57** (1988), p. 17.
48. P.H. Thorton. R.G. Davies and T.L. Johnston, *Metall. Trans.*, **1A** (1970), p. 207.
49. M.H. Yoo, Jr. *Mater. Res.*, **4** (1989), p. 50.
50. S. Ghosh Chowdhury, R.K. Ray and A.K. Jena, *Scripta Metall. et Mater.*, **32** (1995), p. 213.
51. E.M. Grala, in *Mechanical Properties of Intermetallic Compounds*, ed. J.H. Westbrook, John Wiley & Sons (1960), p. 358.

52. E.M. Schulson, T.P. Weihs, I. Baker, H.J. Frost and J.A. Horton, *Scripta Metall.*, **19** (1985), p. 1497.
53. A. Fujita, T. Matsumoto, M. Nakamura and Y. Takeda, *MRS Symp. Proc.*, **133** (1989), p. 573.
54. T.P. Weihs, V. Zinoviev, D.V. Viens and E.M. Schulson, *Acta Metall.*, **35** (1987), p. 1109.
55. E.M. Schulson, T.P. Weihs, D.V. Viens and I. Baker, *Acta Metall.*, **33** (1985), p. 1587.
56. M. Takeyama and C.T. Liu, *Acta Metall.*, **36** (1988), p. 1241.
57. M.S. Kim, S. Hanada, S. Watanabe and O. Izumi, *Jr. Mater. Sci.*, **25** (1990), p. 1590.
58. T.S. Srivatsan and S. Sriram, *Jr. Mater. Sci.*, **27** (1992), p. 4974.
59. S. Ochiai, Y. Mishima, M. Yodogawa and T. Suzuki, *Trans. Jpn. Inst. Met.*, **27** (1986), p. 32.
60. Y. Mishima, S. Ochiai, M. Yodogawa and T. Suzuki, *Trans. Jpn. Inst. Met.*, **27** (1986), p. 41.
61. Y. Mishima, S. Ochiai, N. Hamao, M. Yodogawa and T. Suzuki, *Trans. Jpn. Inst. Met.*, **27** (1986), p. 648.
62. T. Srivatsan, S. Anand, S. Sriram and T.S. Sudarshan, *Jr. Mater. Sci.*, **27** (1992), p. 5939.
63. P.A. Flinn, *Trans. AIME*, **218** (1960), p. 145.
64. C. Lall, S. Chin and D. P. Pope, *Metall. Trans.*, **10A** (1979), p. 1323.
65. Y. Umakoshi, D.P. Pope and V. Vitek, *Acta Metall.*, **32** (1984), p. 449.
66. B.H. Kear and H.G.F. Wilsdorf, *Trans. AIME*, **224** (1962), p. 382.
67. J.B. Cohen and M.B. Bever, *Trans. AIME*, **218** (1960), p. 155.
68. S. Takeuchi and E. Kuramoto, *Acta Metall.*, **21** (1973), p. 415.

69. V. Paidar, D.P. Pope and V. Vitek, *Acta Metall.*, **32** (1984), p. 435.
70. P.B. Hirsch, *Scripta Metall. et Mater.*, **25** (1991), p. 1725.
71. K. Aoki and O. Izumi, *Trans. Jpn. Inst. Met.*, **19** (1978), p. 203.
72. C.T. Liu and J.O. Stiegler, *Science*, **226** (1984), p. 636.
73. C.T. Liu and V.K. Sikka, Jr. *Met.*, May, **38** (1986), p. 19.
74. A. Choudhury, A.K. mukherjee and V.K. Sikka, Jr. *Mater. Sci.*, **25** (1990), p. 3142.
75. T. Takasugi and O. Izumi, *Acta Metall.*, **33** (1985), p. 1247.
76. T. Takasugi, O. Izumi and N. Masahashi, *Acta Metall.*, **33** (1985), p. 1259.
77. A.I. Taub and C.L. Briant, *MRS Symp. Proc.*, **81** (1987), p. 343.
78. A.H. King and M.H. Yoo, *Scripta Metall.*, **21** (1987), p. 1115.
79. V. Vitek, J.J. Kruisemana and J. Th. M. DeHosson, in *Interfacial Structure, Property and Design*, eds. M.H. Yoo *et al*, (1988), p. 139.
80. A. Chiba S. Hanada and S. Watanabe, *Acta Metall. et Mater.*, **39** (1991), p. 1799.
81. R.P. Messmer and C.L. Briant, *Acta Metall.*, **30** (1982), p. 457.
82. K. Aoki and O Izumi, *Nippon Kinzoku Gakkaishi*, **43** (1979), p. 1190.
83. C.T. Liu, C.L. White and M. Chang, *Unpublished Results*, ORNL (1983).
84. C.C. Koch, J.A. Horton, C.T. Liu, O.B. Kavin and J.O. Scarborough, *Proc. 3rd Int. Conf. on Rapid Solidification*, ed. R. Mehrabian, NBS, Gaithersburg, Maryland (1982), p. 264.
85. E.M. Schulson, T.P. Weihs, I. Baker, H.J. Frost and J.A. Horton, *Acta Metall.*, **34** (1986), p. 1395.
86. H.J. Frost, *Acta Metall.*, **36** (1988), p. 2199.
87. I. Baker and E.M. Schulson, *Scripta Metall.*, **23** (1989), p. 1883.

88. W. Yan, I.P. Jones and R.E. Smallman, *Scripta Metall.*, **21** (1987), p. 1511.
89. T.K. Chaki, *Phil. Mag. Lett.*, **61** (1990), p. 5.
90. E.P. George, C.T. Liu and D.P. Pope, *Scripta Metall. et Mater.*, **27** (1992), p. 483.
91. Y. Gu, D. Lin (T.L. Lin) and J. Guo, *Scripta Mater.*, **35** (1996), p. 609.
92. A. Chiba, S. Hanada and S. Watanabe, *Scripta Metall. et Mater.*, **25** (1991), p. 303.
93. J. Mukhopadhyay, G. Kaschener and A.K. Mukherjee, *Scripta Metall. et Mater.*, **24** (1990), p. 857.
94. M.S. Kim, S. Hanada, S. Watanabe and O. Izumi, *Trans. Jpn. Inst. Met.*, **30** (1989), p. 77.
95. R.Z. Valiev, R.M. Gayanov, H.S. Yang and A.K. Mukherjee, *Scripta Metall. et Mater.*, **25** (1991), p. 1945.
96. G.F. Hancock, *Phys. Stat. Sol. (A)*, **7** (1971), p. 535.
97. M.B. Bronfin, G.S. Bulatov and I.A. Drugova, *Fiz. Met. Metalloved.*, **40** (1975), p. 363.
98. K. Aoki and O. Izumi, *Phys. Stat. Sol. (A)*, **32** (1975), p. 657.
99. K. Hoshino, S.J. Rothman and R.S. Averbach, *Acta Metall.*, **36** (1988), p. 1271.
100. L.N. Larikov, V.V. Geichenko and V.M. Fal'chenko, *Diffusion Processes in Ordered Alloys*, National Bureau of Standards and National Science Foundation, Armerind Publishing Company, New Delhi, (1981).
101. J. Sun and D. Lin (T.L. Lin), *Acta Metall et Mater.*, **42** (1994), p. 195.
102. T.C. Chou and Y.T. Chou, *MRS Symp. Proc.*, **39** (1985), p. 461.
103. M. Watanabe, Z. Horita, D.J. Smith, M.R. McCartney, T. Sano and M. Nemoto, *Acta Metall. et Mater.*, **42** (1994), p. 3381.

104. M. Watanabe, Z. Horita, T. Sano and M. Nemoto, *Acta Metall. et Mater.*, **42** (1994), p. 3389.
105. A.E. Vidoz, D.P. Lazarevic and R.W. Cahn, *Acta Metall.*, **11** (1963), p. 17.
106. T. Takasugi and O. Izumi, *Acta Metall.*, **33** (1985), p. 49.
107. M. Gagné and E.M. Schulson, *Metall. Trans.*, **7A** (1976), p. 1775.
108. R.W. Cahn, M. Takeyama, J.A. Horton and C.T. Liu, Jr. *Mater. Res.*, **6** (1991), p. 57.
109. B. Roessler, D.T. Novick and M.B. Bever, *Trans. AIME*, **227** (1963), p. 985.
110. N.S. Stoloff and R.G. Davies, *Prog. Mater. Sci.*, **13** (1966), p. 3.
111. M. Feller-Kniepmeier and F. Rückert, *Z. Metallkunde*, **66** (1972), p. 427.
112. W.B. Hutchinson, F.M.C. Besag and C.V. Honess, *Acta Metall.*, **21** (1973), p. 1685.
113. R.W. Cahn, in *High Temperature Aluminides and Intermetallics*, eds. S.H. Whang *et al*, TMS, Warrendale, PA (1990), p. 245.
114. G. Gottstein, P. Nagpal and W Kim, *Mater. Sci. & Engg.*, **A108** (1989), p. 165.
115. A.K. Jena, S.S. Sahay and R.P. Mathur, in *Structural Intermetallics*, eds. R. Darolia *et al*, TMS (1993), p. 425.
116. J. Ball and G. Gottstein, *Intermetallics*, **1** (1993), p. 191.
117. B. Zhou, Y.T. Chou and C.T. Liu, *Intermetallics*, **1** (1993), p. 217.
118. G. Gottstein and W. Kim, *MRS Symp. Proc.*, **133** (1989), p. 511.
119. S. Ghosh Chowdhury, R. K. Ray and A.K. Jena, *Communicated to Mater. Sci. & Engg.* (1996).
120. E. Aernoudt, P. Van Houtte and T. Leffers, in *Materials Science and Technology*, **vol.6**, eds. R.W. Cahn *et al*, VCH Publishers Inc. (1993), p. 89.

121. R.E. Smallman and D. Green, *Acta Metall.*, **12** (1964), p. 145.
122. J. Hirsch, K. Lücke and M. Hatherly, *Acta Metall.*, **36** (1988), p. 2905.
123. R.D. Doherty, in *Recrystallization of Metallic Materials*, ed. F. Haessner, Dr. Riederer Verlag GmbH, Stuttgart (1978), p. 23.
124. B. Bhattacharya and R.K. Ray, *Z. Metallkunde*, **86** (1995), p. 485.
125. J. Ball, B. Zeumer and G. Gottstein, *Intermetallics*, **3** (1995), p. 209.
126. V.K. Sikka, *MRS Symp. Proc.*, **133** (1989), p. 487.
127. J. Ball, B. Zeumer and G. Gottstein, *Textures and Microstructures*, vols.14-18 (1991), p. 653.
128. V.K. Sikka, in *High Temperature Aluminides and Intermetallics*, eds. S.H. Whang *et al*, TMS, Warrendale, PA (1990), p. 505.
129. B.D. Cullity, *Elements of X-ray Diffraction*, Addison - Weisely (1978).
130. M. Hatherly and W.B. Hutchinson, *An Introduction to Textures in Metals*, The Institute of Metallurgists, London (1979).
131. J. Hansen, J. Pospiech and K. Lücke, *Tables for Texture Analysis of Cubic Crystals*, Springer - Verlag, Berlin (1978).
132. R.K. Ray, J.J. Jonas, M.P. Butrón-Guillén and S. Savoie, *ISIJ International*, **34** (1994), p. 927.
133. H.J. Bunge, *Z. Metallkunde*, **56** (1965), p. 872.
134. R.J. Roe, Jr. *Appl. Phys.*, **36** (1965), p. 2024.
135. H.J. Bunge, *Mathematische Methodn der Texturanalyse*, Akademie Verlag, Berlin (1969).
136. H.J. Bunge, *Texture Analysis in Materials Science*, Butterworths, London (1982).
137. K. Lücke, H.J. Perlwitz and W. Pitsch, *Phys. Stat. Sol. (A)*, **7** (1964), p. 737.

138. J. Hirsch and K. Lücke, *Acta Metall.*, **36** (1988), p. 2863.
139. K.W. Andrews, D.J. Dyson and S.R. Keown, *Interpretation of Electron Diffraction Patterns*, Adam Hilger Ltd., London, (1968).
140. D.W. Pashley and M.J. Stowell, *Phil. Mag.*, **8** (1963), p. 1605.
141. B. Chalmers, *Trans. AIME*, **200** (1954), p. 519.
142. H. Sato and R.S. Toth, in *Alloying Behaviour and Effects in Concentrated Solid Solution*, ed. T.B. Massalski, Gordon and Breach (1965), p. 295.
143. H.J. Beattie, in *Intermetallic Compounds*, ed. J.H. Westbrook, Wiley and Sons Inc., NY (1967), p. 144.
144. M.H. Yoo, C.L. Fu and J.K. Lee, *MRS Symp. Proc.*, **133** (1989), p. 189.
145. M. Yamaguchi, Y. Umakoshi and T. Yamane, *Phil. Mag.*, **A55** (1987), p. 301.
146. S. Ghosh Chowdhury, *Doctoral Dissertation*, IIT Kanpur (1995).
147. R.E. Smallman, Jr. *Inst. Met.*, **83** (1955), p. 10.
148. G.Y. Chin, W.F. Hosford and D.R. Mendorf, *Proc. Roy. Soc.*, **A309** (1969), p. 433.
149. P. Van Houtte, *Acta Metall.*, **26** (1978), p. 591.
150. R.K. Ray, *Acta Metall. et Mater.*, **43** (1995), p. 3861.
151. J. Li and R.P. Wahi, *Acta Metall. et Mater.*, **43** (1995), p. 507.
152. R. Bonnet and A. Ati, *Acta Metall.*, **37** (1989), p. 2153.
153. W. Mao, J. Hirsch and K. Lücke, *Proc. ICOTOM-8*, eds. J.S. Callend and G. Gottstein, The Metallurgical Society (1988), p. 613.
154. B.J. Duggan, M. Hatherly, W.B. Hutchinson and P.T. Wakefield, *Metal Sci.*, **12** (1978), p. 343.
155. M. Avrami, Jr. *Chem. Phys.*, **7** (1939), p. 1103.

156. K.N. Tu and D. Turnbull, *Acta Metall.*, **15** (1967), p. 369.
157. E. Hornbogen and H. Kreye, *Z. Metallkunde*, **57** (1966), p. 122.
158. E. Hornbogen, *Metall. Trans.*, **3A** (1972), p. 2717.
159. E. Hornbogen, *Z. Metallkunde*, **69** (1978), p. 735.
160. H. Böhm, *Z. Metallkunde*, **52** (1961), p. 518.
161. B. Predel and H. Ruge, *Z. Metallkunde*, **59** (1968), p. 777.
162. G.B. Fedorov and E.A. Smirnov, in *Diffusion Process in Metals*, ed. V.N. Svechnikov, Academy of Sciences of the Ukrainian SSR (1970), p. 29.



**A 123608**

**Date Slip** **123608**

## Date Slip

This book is to be returned on  
date last stamped.

[illegible]

MME-1996-D-BAS-MIC